Improving the performance of façade systems

LEILA SOUFEIANI

The University of Melbourne

Improving the performance of façade systems

Leila Soufeiani

ORCID ID: 0000-0002-2604-8999

Submitted in total fulfilment for the degree of

Doctor of Philosophy

April 2021

Department of Infrastructure Engineering
Melbourne School of Engineering
The University of Melbourne

Abstract

The façade system is one of the most important components in a building. Beyond aesthetics, it provides the overall protection against weather and regulates thermal performance. Failures in the façade systems can be costly. Current cladding materials have several limitations related to durability, maintenance, corrosion, high thermal conductivity, high embodied energy, flammability, breathability, expansion and contraction, water ingress, cracks, heavy weight, and so on. Any of these can lead to façade failure, considerable financial loss, and pose a safety risk to the occupant. Thus, in developing the technology and introducing new materials and façade systems, façade failures and related costs are critical and need considerations.

Two potential issues within facade systems that could adversely affect performance are corrosion of steel components and fire performance of cladding. Approximately twenty percent of the world's annual steel production is lost because of corrosion. In Australia, corrosion may have cost up to $32 billion per annum, which is more than $1500 for every person in Australia each year. Two million fires are reported in Europe annually, and 70,000 people are hospitalised in Europe each year due to severe injuries caused by fire. Forty two percent of building fires start on the exterior wall surface and the rest are related to the items inside the façade system which also spread the fire.

Based on a comprehensive literature review on corrosion of steel in combination with moisture transfer simulations using Wärme Und Feuchte Instationar (WUFI) software, the risk of moisture penetration and the potential corrosion of steel in a rain screen façade system are found to be small. A detailed practical guidance to design and specify steel components against corrosion is presented.

With regards to improving the cladding fire performance, this thesis focused on the development and fabrication of a new type of cladding material (3D glass fibre reinforced polymer (GFRP) nanocomposite) with improved thermal stability, fire performance, and tensile properties. 3D GFRP nanocomposite samples were fabricated with 5% and 10% of sepiolite (Sep) and sepiolite-phosphate (SepP), and 5%, 10%, and 15% of ammonium polyphosphate (APP) flame retardant. Synthesis of SepP, dispersion

analysis of nanoparticles into the polymer, and fabrication process have been studied. The characterisation of materials was conducted using scanning electron microscopy (SEM), helium ion microscopy (HIM), transmission electron microscopy (TEM), thermogravimetric analysis (TGA), and X-ray diffraction analysis (XRD). The thermal stability, fire behaviour, and tensile properties of the 3D GFRP nanocomposite was studied via TGA, cone calorimeter tests, and tensile tests, respectively.

TGA results showed that the optimum amount of additives that improved the thermal stability and decomposition temperature is 15% flame retardants. According to the cone test, increasing the APP flame retardant percentage (between 0-15%) remarkably improved the fire reaction properties of 3D GFRP nanocomposite regardless of the presence of Sep/SepP nanoparticles. The effects of APP flame retardant in improving the fire performance of 3D GFRP nanocomposite are remarkably higher than those of Sep fibres and SepP nanoparticles. Among Sep, SepP, and APP, APP flame retardant is better in improving thermal and fire reaction properties while Sep fibres are better in improving tensile properties of the 3D GFRP nanocomposite. Furthermore, the Sep samples showed higher ultimate strength (6%-30%) and strain (2%-39%) than SepP samples. Also, higher percentages of Sep/SepP nanoparticles (10%) showed better tensile properties than lower percentages (5%) of them.

The cone calorimeter test results of the 3D GFRP nanocomposite indicated a prospective cladding that can benefit the construction industry. With more and properly instrumented full-scale façade system tests in the future and manufacturing optimisation, a more robust approach, e.g. using computational fluid dynamic modelling, need to be developed that allows the use of results from bench-tests such as those from the cone calorimeter tests to infer the fire performance of facades with alternative cladding materials in full-scale tests.

DECLARATION

I declare that this thesis comprises only my original work towards the degree of Doctor of Philosophy. The acknowledgement has been made in the text to all other materials used. The thesis is less than 100,000 words in length, exclusive of tables, figures, bibliographies, and appendices.

Leila Soufeiani

November 9th, 2020

Acknowledgements

I would like to acknowledge the support of people who helped me during this three-and a half-year journey.

My deepest gratitude to my supervisors, Professor Lu Aye, Professor Greg Foliente, and Dr Kate Nguyen, for their scholarly guidance, endless encouragement, continuous support, and invaluable advice throughout. Their constructive comments and accurate remarks have improved the quality of my PhD research and thesis. Thanks for being great supervisors, and wise mentors to me. I sincerely appreciate their valuable contributions.

I am also grateful to Professor Priyan Mendis (former supervisor), who initially provided the financial support through the CRC Project on Advanced Manufacturing of High-Performance Building Envelope Systems (CRC-P54018), and the ARC Centre for Advanced Manufacturing of Prefabricated Housing (IC150100023) and offering great opportunities to present my research to industry.

I would like to extend my gratitude to the industry partners of the project, CSR Limited, and Inhabit consultants.

I am also indebted to the following resources: the library database at the University of Melbourne, the laboratory testing facilities provided by the Department of Infrastructure Engineering, Department of Chemical and Biomolecular Engineering, Bio21 Institute, MCFP, and TrACEES platform at the University of Melbourne, Composite lab facilities at RMIT University, and CSIRO facilities for the cone calorimeter tests.

I am deeply grateful to Dr Thomas Loh who helped me in composite fabrication and gave valuable time, support, comments, and advice.

The proofreading service from John P. Mahony is highly acknowledged.

My heartful gratitude goes to my beloved family without whom I would not be standing where I am. To my beloved husband, I extend my appreciation for his love, patience, support, and informative feedback during my PhD that made me keep going even in the hardest time.

Finally, I wish to thank all my friends at The University of Melbourne for their encouragement and for sharing their times.

List of publications arising from the research

L. Soufeiani, K.T. Nguyen, G. Foliente, Use of resole sepiolite-phosphate nanocomposite for building facades, Proceedings of the 22nd International Conference on Composites Materials (ICCM22), 11-16 August, Melbourne (2019) 101759, https://doi.org/10.1016/j.jobe.2020.101759.

L. Soufeiani, G. Foliente, K. T. Nguyen, R. San Nicolas. Corrosion protection of steel elements in façade systems: a review, Journal of Building Engineering. 32(2020) 101759.

L. Soufeiani, K. Nguyen, N. White, G. Foliente, H. Wang, L. Aye. Fire safety performance of 3D GFRP nanocomposite as a cladding material, Composites Part B: Engineering, submitted.

Contents

List of Figures

List of Tables

Abbreviations*

$Al(OH)_3$	aluminium hydroxide
APP	ammonium dihydrogen phosphate
C	catalyst
CNT	cellulose nanofiber
DTA	differential thermal analysis
E	earthquake
E	Young's modulus
EHC	effective heat of combustion
FIGRA	fire growth rate
FPI	fire performance index
FR	flame retardant
FRP	fibre reinforced polymer
F^{tu}	maximum stress
GFRP	Glass fibre reinforced polymer
H_3PO_4	ortho-phosphoric acid
HCL	hydrochloric acid
HIM	helium ion microscopy
HR TEM	high-resolution transmission electron microscopy
ML	mass loss
MMT	montmorillonite
NH_4OH	ammonia solution
P	phenol
P_{max}	maximum load
POSS	polyhedral oligomeric silsesquioxane
PR	phenolic resin
PVC	polyvinyl chloride
SEA	specific extinction area
SEM	scanning electron microscopy
Sep	sepiolite
SepP	sepiolite-phosphate
TEM	transmission electron microscopy
T_{fo}	time to flame out
TGA	thermogravimetric analysis
THR	total heat release
TTI	time to ignition
W	wind
XRD	X-ray diffraction analysis
ξ	strain

*The nomenclature and abbreviations used in publications are included in the body of the published work.

Chapter 1

Introduction

1.1. Background

Façade systems consist of structural components and building envelope elements. Different types of facades are selected based on the building's scale and application. The façade system provides comfort requirements such as thermal control, moisture protection, hydrothermal control, acoustic control and so on. They also have to be designed for other requirements such as strength, stability, compatibility, durability, and fire resistance. In recent years, advanced glazing systems with different manufacturing and curing techniques have been introduced. Also, nowadays, buildings with lower energy consumption are desired. That is why modern façade systems with better thermal, visual, and safety performance have emerged. Double screen façade systems or rain screen façade system were introduced into modern buildings as an alternative to traditional glazing façade systems. They are composed of two layers of glazing, where the space between layers is called a cavity. The cavity helps in maintenance, and prevents heat loss in winter and heat gain in summer. Therefore, double skin façade systems provide better thermal performance, light, security, and moisture control. Several steel components such as steel frames and fasteners are used in the façade systems. Those elements are prone to corrosion which is one of the reasons for failure in façade systems that needs to be paid attention.

Two metal components which are widely used in the façade systems are steel and aluminium. They have superior durability and mechanical properties, but high

embodied energy. Nowadays, greener and advanced materials are more demanding such as fibre reinforced polymer composites (FRPCs). Metallic materials need a high amount of energy because of their manufacturing at high temperatures. FRPC materials are environmentally friendlier than aluminium and steel because of their lower weight and higher strength. FRPCs are a potential alternative to traditional metallic elements in buildings due to their excellent life cycle energy performance. However, greener and energy-efficient materials generally have fire issues which are very important performance failure criteria of façade systems. Façade failures due to cladding's fire are very critical and costly. Hence, cladding's material play a key role in spreading the fire and related uncompensated losses that need to be addressed carefully.

Even with developing the technology and introducing new materials and façade systems, façade failures and related costs are critical. When building owners and designers select a type of façade, they usually pay attention to the initial cost, function, and aesthetics. Even during the design of a building, less attention is paid to potential issues of the façade system, which may lead to future underlying failures that would be hard to detect. These failures lead to huge losses (due to replacement of a failed façade system and risk to human life) that are significantly more than the initial cost of a façade system. In addition, the loss of human life can never be restored.

1.2. Significance of the research

There are many failures in the current façade systems, from material failure to system failure. Current cladding materials have several drawbacks related to durability,

maintenance, corrosion, high thermal conductivity, high embodied energy, flammability, breathability, expansion and contraction, water damage, cracks, heavy weight, and so on. Any of these defects can lead to façade failure, considerable economic loss, and pose a risk to occupant safety. For instance, 2,000,000 fires are reported in Europe annually and €126 billion, equivalent to 1% of European GDP is lost by fire damage each year, and 70,000 people are hospitalised in Europe annually due to severe injuries caused by fire [1]. Forty two percent of building fires start on the exterior wall surface [2] and the rest are related to the items inside the façade system which also spread the fire. The combustibility of cladding materials in the façade system is the main issue in the building envelopes as combustible materials spread the fire rapidly. Also, 20% of world steel production is lost each year approximately because of corrosion. In Australia, corrosion may cost up to $32 billion each year, which is more than $1500 for each person in Australia each year [3]. However, corrosion cost is not only financial; it can also cause dangerous failures, waste of natural resources, and many other indirect costs. Therefore, it is very important to study the façade performance failures and address the issues with appropriate solutions.

In this regard, two main performance issues of façade systems, namely steel elements corrosion and cladding fire, are addressed. Steel elements corrosion and corrosion protection methods have been addressed in a journal paper (See Appendix A). Also, a case study for steel corrosion estimation in the CSR Inclose Rainscreen Façades' system is assessed (See Appendix B). Therefore, the main focus of the thesis will be on cladding fire and to develop a high-performance construction material as a safe and resilient alternative to many of the non-compliant façades.

1.3. Aim and objectives

This thesis aims to develop a new type of nanocomposite cladding material, (3D Glass Fibre Reinforced Polymer (GFRP)) to improve the performance of the façade system in a fire event. This new cladding material can be used to replace the cladding in existing façade system or be part of a new façade system design: it can be applied to both existing and new buildings. To achieve this goal, the specific research objectives are to:

1. Determine the appropriate contents mix and fabrication parameters for a new cladding panel with 3D GFRP phenolic nanocomposite;
2. Study the thermal stability and fire performance of 3D GFRP phenolic nanocomposite material samples; and
3. Investigate the tensile properties of the 3D GFRP phenolic nanocomposite material samples.

1.4. Research scope and methods

This thesis focuses on the most common façade performance failures which are corrosion of steel elements and combustible cladding. After critically reviewing the steel corrosion literature (Appendix A) and studying the durability of the selected system via numerical modelling (Appendix B), the major finding was that the possibility of failure caused by corrosion in Australia's climate is relatively negligible. But a comprehensive assessment of research findings and standards needed to be developed to underpin practice recommendations for façade system design and material specification. This was accomplished through the publication of the journal paper in Appendix A.

Thus, the remaining focus of the thesis is on developing a new and innovative cladding material to improve the fire performance. For this purpose, synthesis and application of sepiolite (Sep) and sepiolite-phosphate (SepP) nanoparticles in the 3D GFRP nanocomposite as a new cladding material in the façade system will be conducted and thermal and fire behaviour of the new cladding according to the National Construction Code of Australia performance requirements will be investigated. Also, the tensile properties of the 3D GFRP nanocomposite will be studied to examine the strength of the material under tension. The main steps for achieving the thesis aim and objectives are shown in Figure 1.1.

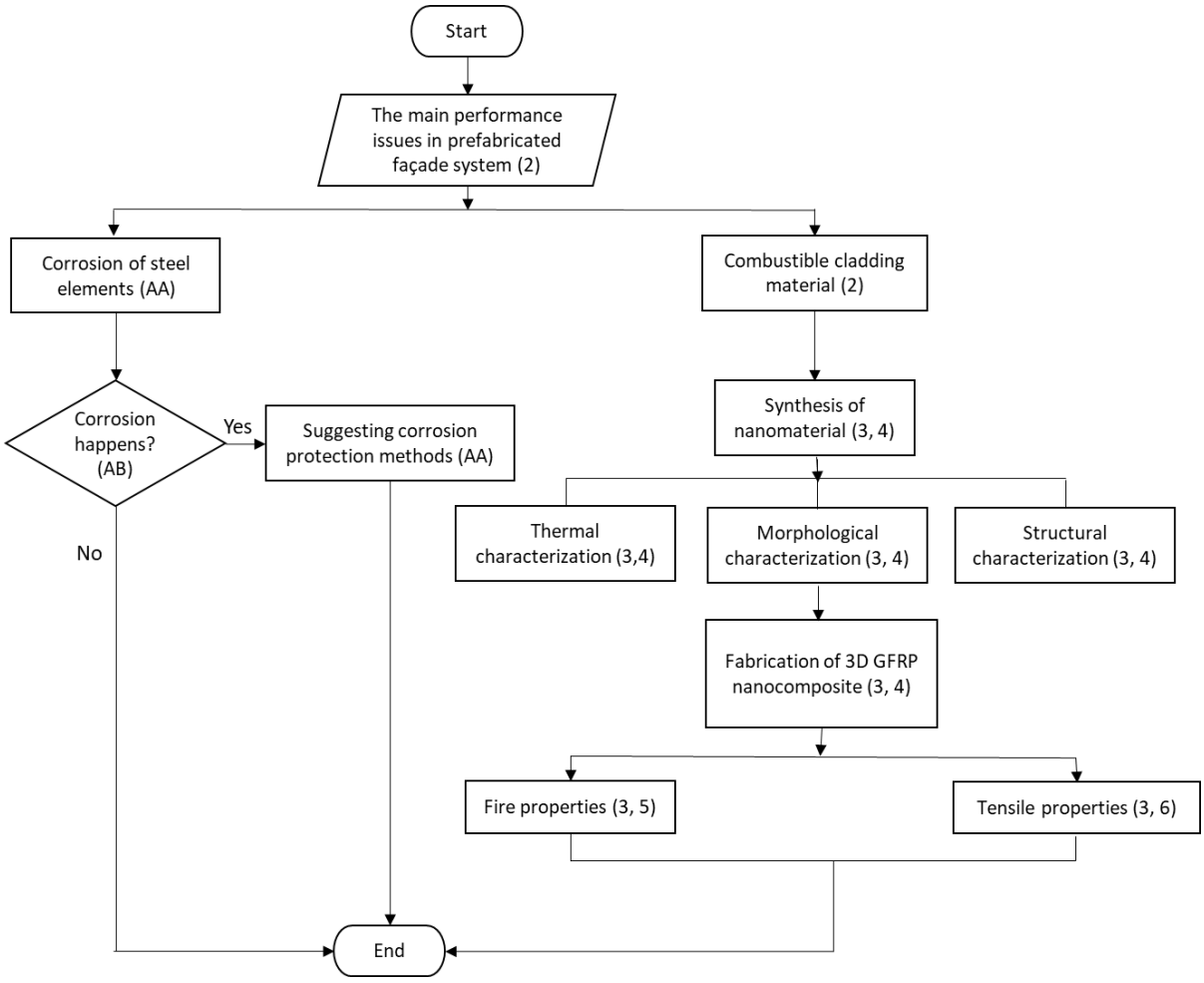

Figure 1.1. Main steps for achieving aims and objectives with (corresponding chapters) of the thesis

1.5. Thesis layout

The structure of the thesis is shown in Figure 1.2. The contents are presented in eight chapters, including this introduction (Chapter 1). Chapter 2 contains a comprehensive review of the literature. Chapter 3 contains the methods of research. Chapter 4 presents the synthesis of SepP and characterisations of Sep and SepP, dispersion analysis of nanoparticles, and fabrication of 3D GFRP nanocomposite. In Chapter 5, the thermal and fire behaviour of 3D GFRP nanocomposite cladding are investigated with thermogravimetric analysis and cone calorimeter tests, respectively. Chapter 6 studies the tensile properties of 3D GFRP material. Chapters 7 and 8 contain the results and discussions of all chapters and conclusions and future recommendations, respectively.

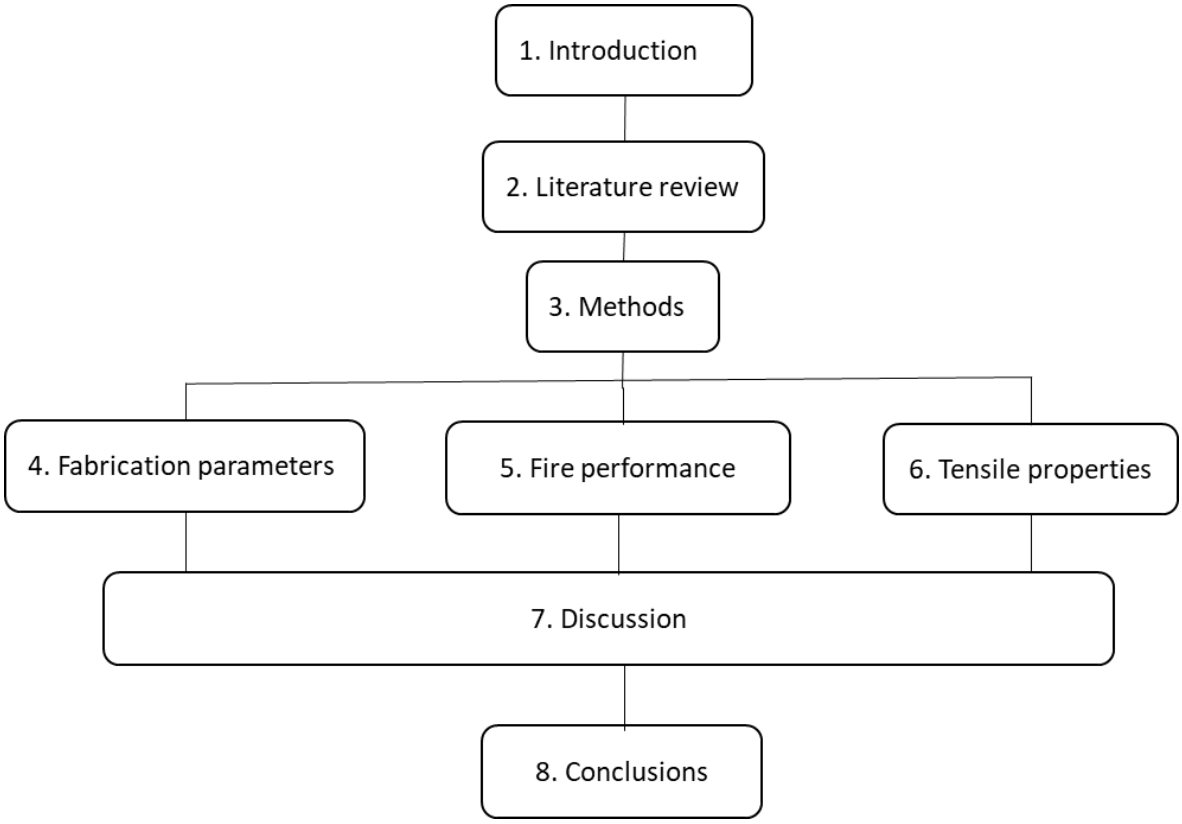

Figure 1.2. Structure of the thesis

1.6. References

[1] Fire Safe Europe. Europe is playing with fire. Fire Safe Europe; 2014. www.firesafeeurope.eu.
[2] White N, Delichatsios M. Fire hazards of exterior wall assemblies containing combustible components: Springer; 2015.
[3] Javaherdashti R. Research shows corrosion costs the local economy. 2009. https://news.curtin.edu.au/media-releases/research-shows-corrosion-costs-the-local-economy/.

Chapter 2

Literature review

This chapter summarises the importance of studies and research that have been done to date on façade systems and their failures, cladding materials, glass fibre reinforced polymers (GFRP), phenolic resins, nanocomposites, fire and tensile tests, which help identify knowledge gaps where more research is needed. To avoid repetition, some additional materials not covered in this chapter will be covered later in Chapters 3, 4, 5, and 6.

2.1. Introduction

Building failure is always a risk. A comprehensive assessment of building failures and related costs revealed that façade failure is one of the critical ones [1]. There is a variety of building facades today. Amongst them, only a few types of materials, support systems, or configurations are reliable and others are more prone to problems [2]. When building owners and designers select a type of façade, they usually pay attention to the initial cost, function, and aesthetic. Even during the design of a building, less attention is paid to potential issues of the façade system which may lead to future underlying failures that would be hard to detect [2]. This chapter reviews the pool of knowledge related to the performance of façade systems.

2.2. Common prefabricated façade systems

Prefabricated façade systems have advantages such as faster construction (panel making in a factory, no scaffolding at the site), better quality control, and lower cost. There are different prefabricated façade systems such as prefabricated brick systems, unitised curtain walling, precast concrete, panelised insulated render, and unitised rain screen façade system. The most common prefabricated façade systems and their main issues are mentioned in the following.

- Panelised insulated render system is composed of steel or timber stud frame, sheathing board, cavity, insulation board/alkali-resistant glass fibre scrim, leveling coating, silicon primer coat, and silicon finish coat as is shown in Figure 2.1 [3]. The common issue in this system is poor detailing and installation. Also, moisture can penetrate junctions and cause problems. Another issue is the cracking of cementitious renders because of temperature variation which causes expansion and contraction. Run-off of contaminated rainwater may lead to façade discoloration [4].

-

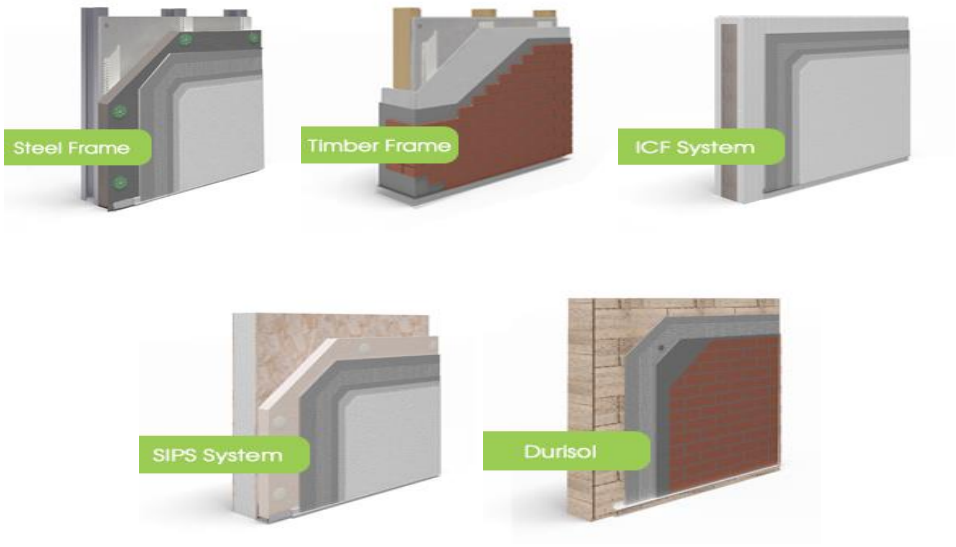

Figure 2.1. Panelised insulated render system [4]

- Prefabricated brick system is building panels with wood sections or steel stud framing and putting a thin brick on it. The prefabricated brick system is suitable for soffits and other places where lighter weight prefabricated elements are required. For attaching thin brick veneer, four elementary methods are used as follows: thin-set, thick-set, modular panel system, and prefabricated panels. Thin brick veneer provides better resistance to noise, minor impacts, abuse, heat, and vandalism than typical light-weight cladding systems. Thin brick system due to its nature can provide durability, fire resistance, security, and acoustic comfort. However, the main problem within this system is a differential movement because of the expansion of brick and substrate or shrinkage of mortar bed [5]. Figure 2.2 shows brick façade systems.

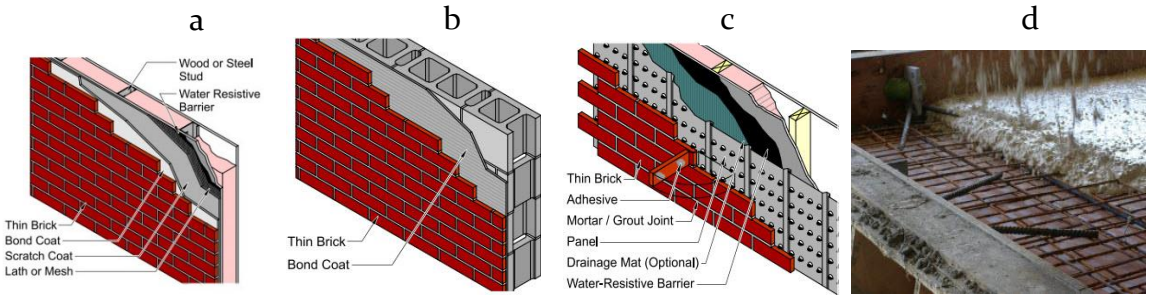

Figure 2.2. Brick façade system: a) thick set application on stud; b) thin set application on CMU; c) modular panel on suds; d) prefabricated panel [5]

- Unitised curtain wall system: composed of extruded aluminium infilled with glass. This system consists of anchors, mullion (vertical elements), horizontal rail, spandrel panel, and vision glass. Curtain walls can be classified based on their function, materials, place of assembly, glass attachments, configuration, heat transfer, and so on. The main issue in this system is fire performance. Building fires could reach 1100° C , which is beyond the melting point of aluminium (660° C). Other performance failures are condensation and frosting, glare, noise, leakage, glass breakage, corrosion, and so on. [6]. Figure 2.3 shows a unitised curtain wall system.

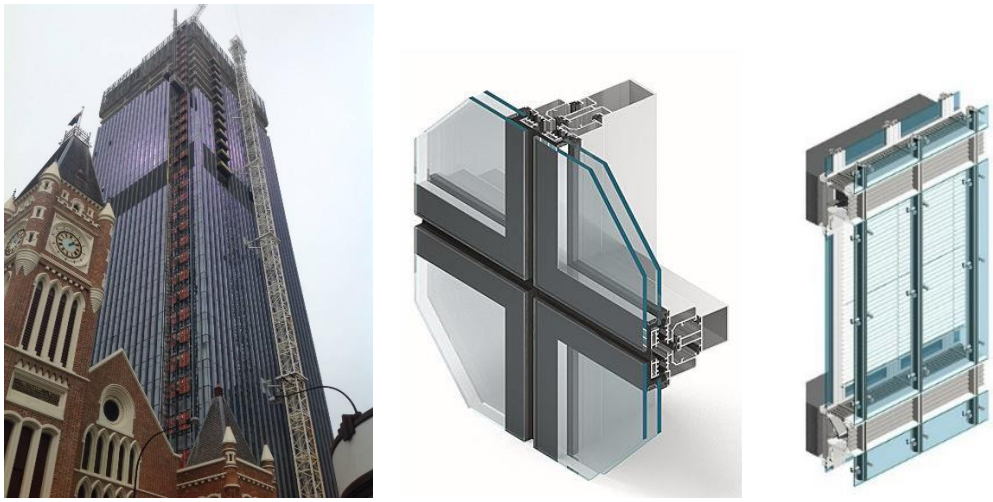

Figure 2.3. Unitised curtain wall system [7, 8]

- Prefabricated precast concrete panels: precast concrete panels are low cost and fire-resistant, but their weight, maintenance, thermal performance, and lack of design are the most common problems. Figure 2.4 shows these panels.

Figure 2.4. Prefabricated precast concrete cladding panel [9]

- Panelised rain screen façade system consists of cladding, air gap, mineral wool, membrane (vapour barrier), rigid sheathing (air tightness), steel frame, and plasterboard. The panels have protection from the direct effects of weather on the outside of the buildings. There also is a space between the panels and the outside of the building that prevents moisture accumulation, improves the weather-protecting features, and provides an insulating layer [10]. Figure 2.5 shows a unitised rain screen façade system.

Figure 2.5. Unitised rain screen façade system [12]

- Two extensive classifications of wall failures are stability failures and serviceability failures (cracks, water leakage, aesthetic degradation, and so on.) [13]. Since the facade of the building is not load-bearing, it must withstand different types of externally and internally imposed loads. External loads such as wind, earthquake, and vertical loads from the façade's self-weight and localised internal loads are applied by expanding elements embedded in the wall (e.g. reinforcement steel corrosion) or by differential movements between the facade component and the wall's substrate. Strength properties and connection systems of a façade could be designed in a way that resists those loads with an appropriate factor of safety. Also, internal loads are more complex and can vary extensively within the same structure or from structure to structure depending on the façade environments, materials, and configurations. Some other failures may come from water leakage, and material incompatibility [13]. Besides collapse, cracks, water, and moisture, facades that don't satisfy the project requirements, or building codes have also failed [14].

Some solutions to the above-mentioned failures can be a wall with cavities (fire and smoke spread through such cavity acting like a chimney), fire stops and cavity barriers in the façade assembly, drying and drainage, diffusive drying, air movement (leakage), and ventilation, or airflow through a space behind the cladding. Among the existing prefabricated façade systems, a panelised rain screen façade system has better design in terms of moisture control and water penetration [15]. It also increases the speed of enclosure and allows earlier interior finishing, greater site efficiency with fewer trades to manage, reduced safety, weather and quality risks, supply chain guarantee through local design and fabrication, and comprehensive façade warranty. This system was

developed in the USA and modified to suit Australian façade industry requirements. CSR (Inclose) [12] is a pioneer in the rain screen façade system in Australia from design to installation. Figure 2.6 shows the CSR factory and fabrication of a unitised rain screen façade system.

Figure 2.6. a) Rigid sheathing; b) steel frame; c) welded steel frame; d) perimeter extrusion and gasket applied; e) Rockwool installed; f) cladding installed; g) completed panel; h. i. j) installed façade system [11]

The main performance failures of façade systems are discussed in the next section.

2.3. In-service performance failure criteria for façade systems

Since the façade system materials are different based on the cost, design, application, low or high rise, climate requirements, and so on., the performance criteria may vary. The performance criteria for façade systems are air permeability, water penetration,

wind load resistance, thermal performance, acoustic performance, and fire safety [16]. One of the main issues in the façade system is moisture penetration into the wall assembly which causes many problems. The major sources of moisture are the condensation of water vapour carried by air movement or diffusion through the wall (from either interior or exterior); precipitation, particularly driving rain, both by penetration and capillary absorption; and stored and built-in moisture [17].

A wall is considered to be failed if water penetrates through the entire wall assembly. Also, the passing of rainwater into any delicate layers of a wall assembly can cause damage, reduce performance, and affect durability [17]. One of the major consequences of penetrating water or moisture through the wall assembly is the corrosion of steel elements which is examined in the current research. Corrosion and corrosion damage repair are multi–billion–dollar problems – the latest estimates show the United States spends annually approximately $423 billion ($52 billion in Canada) on metallic corrosion [18]. Nevertheless, corrosion cost is much more than financial, it can lead to hazardous failures, waste of natural resources, and many other indirect costs [18]. Corrosion of steel elements and protective coatings against corrosion in the façade system are explained comprehensively in a review article which is published [19] (Appendix A). Hence, it has not been further discussed in this thesis. Also, cut-edge corrosion estimation of the steel frame in the CSR panelised rain screen façade system has been carried out in Appendix B.

Another performance criterion which raised many issues recently is the fire performance of the façade system, specifically cladding material. Non-compliant façades are a risk to occupant safety and may produce significant financial loss in the

event of a fire. Many existing cladding materials are combustible and spread the fire rapidly. There is a lack of new cladding to prevent vertical fire spread and fulfil the fire safety requirements according to related standards. Cladding materials will be discussed more in the next Section.

2.3.1. Cladding materials

Building cladding is an important and typically applied activity area of the building sector. The main purpose of the cladding is a separation of indoor from the outdoor environment in a way that maintains the indoor environment at suitable conditions for occupants. In another way, cladding is a non-load bearing part of an exterior wall that protects the interior environment against water, wind, sun, light, heat, and cold, and other natural forces. Also, it must address the aesthetic, economic, and security considerations [20]. Cladding is commonly made from wood, metal, plastic (vinyl), masonry, or composite materials [21]. Modern facades are vulnerable to fire and this vulnerability clearly influences the safety of building occupants. In the latest façade fire incidents around the world, there was a fast fire spread along the exterior cladding because of the combustibility of the materials used. Combustible materials allow the flame to travel externally along the façades that cannot be extinguished by internal sprinklers and other active fire systems in buildings. The uncontrollable spread of fire through a façade has exposed buildings, especially high-rise structures with a large number of occupants, to a higher risk in a fire as it may limit egress routes and shorten the available evacuation time for occupants [22]. Figure 2.7 shows some building façade fires around the world.

Figure 2.7. Façade fire: a) Al Tyer tower fire in Sharjah, 2012; b) Lacross building fire in Melbourne, 2014; c) Grenfell tower fire in London, 2017; d) Torch tower fire in Dubai, 2015, 2017 [23-26]

After investigating the reason for recent fire incidents, a common issue was found. Combustible material that exists in façade cladding is the major contributor to the rapid spread of fire [27]. After a catastrophic incident, new rules and regulations are defined, but they usually apply only to new constructions. Hence, existing buildings are still vulnerable. Those buildings are even in a much worse condition because they were built before fire design regulations were introduced [27].

Existing cladding materials are reconstructed timber products, fibre cement, brick, plywood sheeting, timber weatherboards, steel, aluminium, PVC, composites, and so on. Some of them are not performing well in a fire, and those which are good in high temperatures have some other issues such as maintenance, aesthetics, durability, and so on [28]. Figure 2.8 compares cladding material performance requirements against some important criteria.

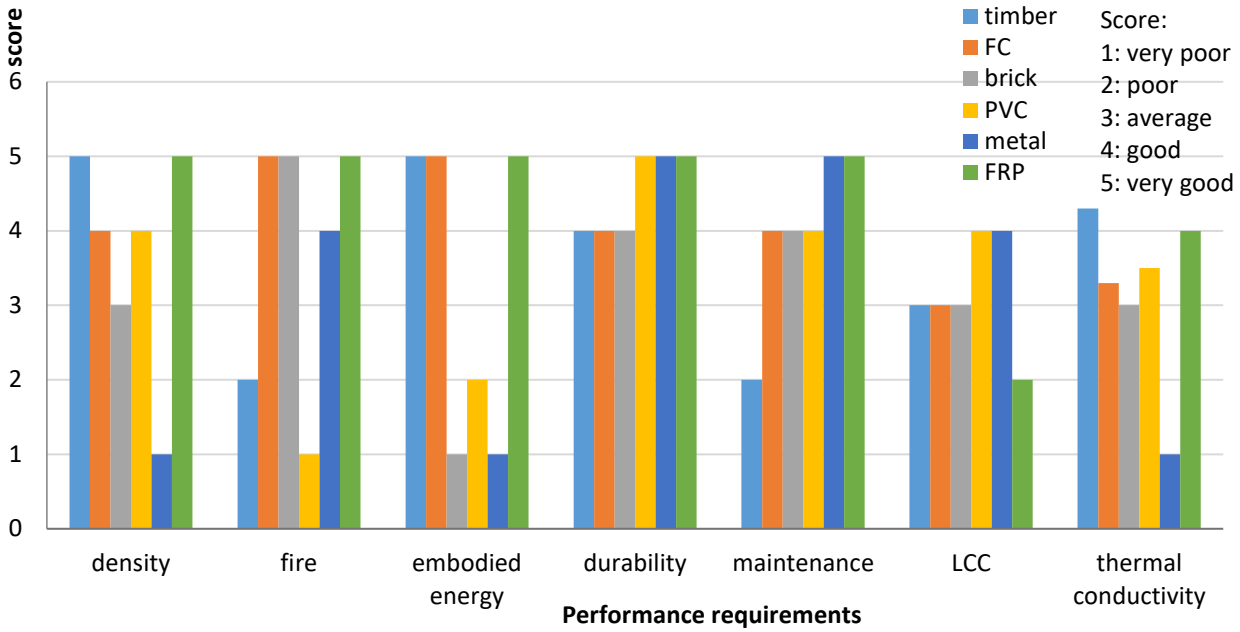

Figure 2.8. Comparison of cladding materials performance requirements (reproduced from [21])

Existing cladding materials have some defects which are as follows [21]:

- Timber cladding: fire issue, maintenance cost, durability (fade, warp, crack), paint and satin to prevent rot for 3-5 years, the moisture problem
- Metal cladding: damage, dent, difficult to repair, high thermal conductivity, steel corrosion, high embodied energy, need infill for sound insulation
- PVC or vinyl cladding: flammable (emits toxin), attracts dust, easily dented, not breathable, carcinogen, cracking in a cold climate, colour fading, difficulty of replacing panels, expansion and contraction, high embodied energy
- Brick cladding: cracks, needs repair, rising damp, water damage, bubbled paint inside, natural damage (W, E), at high temperatures mortar loses the adhesion
- Fibre cement: heavy, dust, health threat, pre-painted is pricey, need to repair after 10-15 years, installation needs professionals and high cost

Therefore, a new cladding material is needed to improve the fire performance and overcome the main issues of the existing cladding materials which will be discussed in the following sections.

2.3.2. GFRP

Fibre-reinforced composites possess two main components: the polymeric matrix and reinforcing fibre. The matrix keeps the fibres in their proper position, protecting the fibres from environmental impact, transferring loads to the fibres, and providing additional strength, whereas fibres mostly assure the strength and stiffness of the composite. Therefore, the selection of composite for individual applications depends on the type of matrix, reinforcing fibre, and fabrication process [22]. FRPs have been used in construction due to their high strength, light weight, and customised shape [29-34]. Also, FRPs are environmentally friendlier than metallic materials such as aluminium and steel due to their low embodied energy [22]. The fibres provide rigidity, strength, and elongation to the material as well as supporting mechanical stress. Hence, better mechanical properties are achieved with higher percentages of fibre in the FRP composites up to a certain limit. Fibres can be categorise in different types such as glass fibres, carbon fibres, aramid fibres, basalt fibres, boron, and hemp. The selection of fibres is based on their functional requirements and final application of the material [35].

Glass fibres are the most common reinforcement for composites. Glass fibres account for over 1.8 Mt consumed per year, which is 250 times higher than carbon fibre and Kevlar in total [36]. The advantages lie in their low cost and easy handling, with high tensile strength. The tensile strength of E-glass fibre is over 70% that of carbon fibre

strength, but the cost is only 10% that of carbon fibre [37]. Glass fibres have different chemical compositions, properties, and cost. They are used as reinforcement for 90% of structural applications [38]. Two types of glass fibres exist based on the silica content. The first type contains 46-75% of silica, and the second type contains over 96% of silica [36]. A high amount of silica fibre and quartz fibre means better performance at high temperatures, high toughness, stiffness, and strength. Moreover, the high purity of silica in these fibres will increase the cost of manufacturing of the fibre as well as tooling. However, the term “glass fibres” refers to the first type with lower silica content [37]. Glass fibres are classified in five categories, namely E-glass, S-glass, C-glass, D-glass, and A-glass. Each of them is used for a different purpose and application. For example, E-glass fibre shows a balance between cost and performance and is mainly used in structural applications which have been used in this research. S-glass fibre demonstrates higher strength and cost. C-, D-, and A-glass fibres are used in specific applications due to their excellent corrosion resistance, dielectric properties, and alkaline resistance [37].

Therefore, GFRP is an ideal product for façade cladding due to its low weight, elasticity, flexibility in design, high strength to weight ratio, faster installation, cost efficiency, resisting saltwater and chemicals, corrosion-free, seamless construction, low maintenance, and durability [37]. However, the main issue with FRP façade systems is fire performance which has not been consistently investigated yet. FRPs are sensitive to high temperatures and this issue which may lead to the failure of the composite structure needs to be studied comprehensively to protect the occupants' life in fire incidents. Therefore, it is important to examine new research to conduct the FRPs fire issues as a cladding material in the façade system. This research will offer a

solution for GFRP facades to meet the fire safety performance requirements based on the relevant standards.

2.3.3. 3D glass fabrics

The common usage of GFRP is as a face sheet in the sandwich panels with a lightweight core. The main issue with this system is the delamination or debonding of the GFRP face sheets from the core. To solve this issue, 3D glass fabrics are used in this research as shown in Figure 2.9. 3D composites have some advantages over 2D fabric laminates such as enhanced damage tolerance, superior impact, blast performance, and efficient delamination suppression. Also, these 3D composites have better strength and in-plane stiffness properties than “conventional” type 3D interlock weave composites [39]. 3D woven sandwich composites with their high skin–core debonding resistance emerged a new generation in the field of sandwich structures that is very helpful in increasing their lifetime [40]. These 3D glass fibres are a 100% woven E-glass material composed of two deck layers connected with vertical glass piles. When applying a thermoset resin, the fabric is compacted but then instantly returns to its original height. The final laminate is strong, stiff, durable, and lightweight [41].

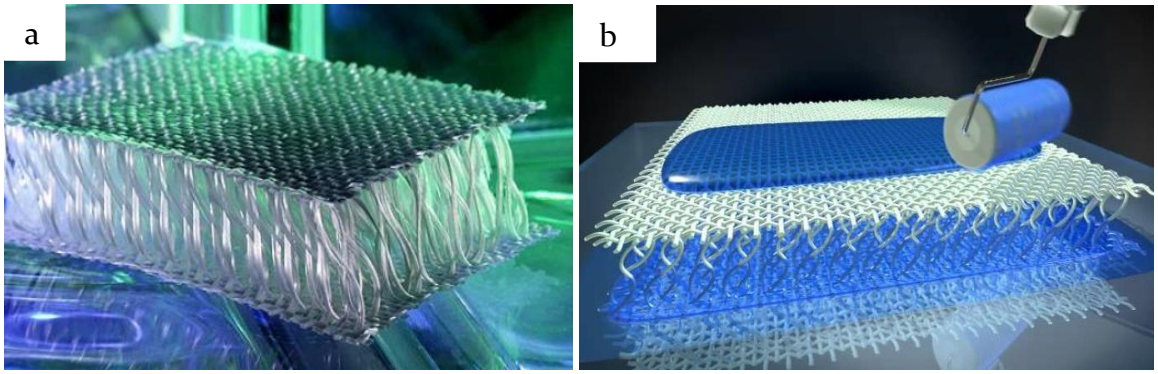

Figure 2.9. a) 3D glass fabric panel; b) applying resin [42]

The mechanical behaviour of 3D-fabric sandwich composites (considering their core structure) highly depends on skin thickness, pile diameter, resin content, sandwich thickness, the angle of piles, and fabric pattern. Van Vuure et al. [43] investigated that the mechanical behaviour of 3D woven composite panels improves with increasing resin ratio. Ductile properties of the panels have been studied by Fan et al. [44, 45]. It was found that thinner panels (8 mm) show higher maximum stress and compressive stiffness in flatwise compressive loading [40]. It means that panels with lower thickness have higher yield stress and shear modulus [40]. Compression properties of 3D woven composites have been studied by many researchers while less work has been conducted on tensile properties [46-49]. Microstructural properties and tensile failure of 3D woven composites have been conducted by Cox et al. [50-52]. The study of Cox et al. [51] was limited to several weave designs in one carbon/epoxy system. However, there are a variety of 3D designs and material arrangements which are of attraction to the composites industry.

2.3.4. Phenolic resin

A thermoset resin system encompasses the polymer and the hardener. The resin is rigidified as the result of an irreversible chemical reaction between the components of

the resin system to obtain a cross-linked structure. Therefore, the major difference between thermoset and thermoplastic matrices lies in the reversibility of the hardening process. In thermoplastics, the heating process can be reversed after a certain time of reheating. Owing to the limitations of large-sized products for façade applications and poor solvent resistance, thermoplastics are not suitable and are therefore not discussed in this work.

Thermoset resin and thermoset reinforced composites have a unique property. Because of the formation of a highly cross-linked web, they cannot be reformed or reshaped on curing [53]. In addition, thermoset resins cannot be re-cured by the aid of temperature, pressure, and light irradiation. There are a variety of thermoset resins such as phenol-formaldehyde, urea-formaldehyde, melamine-formaldehyde, resorcinol formaldehyde, polyurethane, polyesters, and epoxies [54, 55]. Among the thermosets, phenolic resin, due to its high thermal stability and mechanical properties, has been of industrial and commercial interest [56, 57].

Two important parameters that must be considered in selecting thermoset matrices are the gel time and curing time of the resin system. The gel time is the time during which the resin can be processed because of its low viscosity. The curing time is the time needed for the resin system to be hardened to a certain extent [22]. Phenol has better properties against fire and smoke among thermoset resins as can be seen in Table 2.1.

Table 2.1. Comparison of thermoset resins [58]

Polyimides	Very high-temperature resin system (280-310° C), hard handling
Polyesters	Widely used in industrial applications because of low cost and handling flexibility, used in both continuous and discontinuous composites
Vinyl Esters	Comparatively like polyesters but are tougher and have improved moisture resistance
Bismaleimides	Epoxy-like handling, high-temperature resin matrix for usage in the temperature of 135-180° C and retains elevated-temperature post-cure
Cyanate esters	Epoxy-like handling, high-temperature resin matrix for use in the temperature between 180-275° C and retains elevated-temperature post-cure
Epoxies	High-strength resin systems for main continuous fibre composites may be utilised at temperatures up to 250-275° F, improve temperature function than polyesters and vinyl esters
Phenolics	Although difficult to process, resin system with better thermal stability with great smoke and fire properties, mainly used for aircraft products

Phenolic possesses very high working temperature in comparison with other thermosets and, therefore, is particularly attractive in structural applications at high temperatures. It is an excellent flame retardant, with low flammability and low smoke production. These properties make it feasible in applications prone to high temperatures and requiring minimum smoke release. Another advantage of phenolic is its good adhesion and dimensional stability in varying temperatures. However, phenolic is a thermoset cured by condensation reactions (Figure 2.10). This reaction triggers water as a by-product. Therefore, if the cured phenolic does not get rid of the newly formed by-product, it causes a decrease in the mechanical strength at room temperature and results in structural damage at elevated temperature. The issue of water elimination should be paid attention to, but once overcome, the fire performance is excellent. Also, the complexity of manufacturing phenol and its brittleness is another noticeable disadvantage of the cured phenolic system [22]. It is common to use additives and fillers to reach their desired properties and features [59].

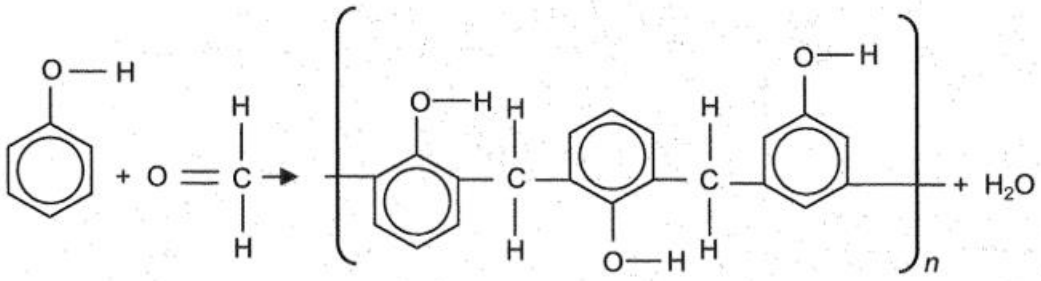

Figure 2.10. Example of the condensation reaction during the curing process of phenolic [58]

Phenol-formaldehyde resins (phenolic resins, PR) are considered to be the first fabricated commercially accessible plastic resins [59]. From the chemical reaction of phenols and formaldehyde liquids, phenol-formaldehyde resins are produced [59]. However, the reaction mechanism is not yet completely known. What is known is that the reaction is started by the activation of the benzene circle by the hydroxyl group like a methylol group (CH_2OH) connects the benzene nucleus at the ortho – and parapositions. From the reaction, resole and novalac are generated if an alkaline and acid catalyst are used, respectively [59]. A resole molecule has reactive methylol groups. By heating, the reactive resole molecules condense to form large molecules, without adding a hardener. Because of low viscosity and easy processability of resole phenolic resins, they are widely used in the composites [60]. Phenolics have very low flammability and this is due to the larger number of stable aromatic benzene rings in their natural structures which on heating crosslink and form stable char [60]. Polymer nanocomposites have not been utilised for commercial flame retardant products, because they cannot pass regulatory tests on their own due to slow burning and not extinguishment. Hence, they need to be merged with flame retardants to meet those tests [61]. By definition, the flame retardant is a material that retards flame growth,

and as polymer nanocomposites slow down flame expansion, they are a group of flame retardant materials [61].

According to literature, the more suitable resin in fire retardant applications is phenolic resin due to its high thermal stability. There are many types of phenolic resin and catalyst in the market. The selection of a suitable type of phenolic resin and catalyst for composite fabrication in civil engineering application is challenging and needs a deeper study of resin structure. However, after consulting with different suppliers and collecting information, a modified liquid phenolic resole resin (containing free phenol of less than 10% and free formaldehyde of less than 0.1%) was selected. In addition, Phencat 382 was selected due to its compatibility with selected resole phenolic resin and its longer pot life compared with other catalysts.

2.3.5. Phenolic nanocomposite

Different fibres such as glass, carbon, silicon dioxide, and refractory oxides are commonly added to phenolic resins. E-glass/phenolic composites have excellent properties and reasonable cost. That is why they are very popular in the marine, transportation, military, and construction industry [62].

One of the twenty-first century's key technologies is nanotechnology. Nanomaterials have functional properties such as self-cleaning capacity, fire resistance, and increasing tensile strength and potential of being used in the construction industry. They are also very useful in the façade system due to expanding design possibilities for indoor and outdoor spaces [63]. Nanostructured materials have an extremely high surface area to a given volume; the switch from micro to nanoscale yields dramatic alterations in physical and chemical properties [64]. Some research has been

conducted on the effects of nanomaterials such as nano clay, carbon nanotubes, graphite, graphene, and so on [65-67]. The results showed that adding nanomaterials increases the thermal and fire properties of the nanocomposite [68-74]. Nanocomposites reinforced with nano-sized fillers obtained from the polymeric matrix are a very demanding and active area of research [75]. There is much research on nano clays and their effects on the improvement of flame retardancy [22, 76, 77]. Recent research showed that using 5-10% organically modified clays in the polymer matrix can reduce the peak of heat release by 70% for many resins [60]. Polymer/clay nanocomposites, because of the low price of clay and enhanced mechanical, thermal, and gas barrier properties of the resultant nanocomposites, have received great interest nowadays [78].

Sepiolite (Sep) is a nano clay fibre that is called hydrated magnesium silicate ($Mg_8Si_{12}O_{30}(OH)_4(H_2O)_4{\cdot}8H_2O$), with a large specific surface area (about 320 m^2/g) [79]. The sepiolite structure is formed by a magnesium octahedral sheet in-between two layers of silica tetrahedrons which expand as a continuous layer with an reversal of the apical ends every six units. This reversal produces a discontinuous octahedral sheet which permits for the creation of a rectangular section, with tunnel-like holes (Figure 2.11), parallel to the fibre axis [80].

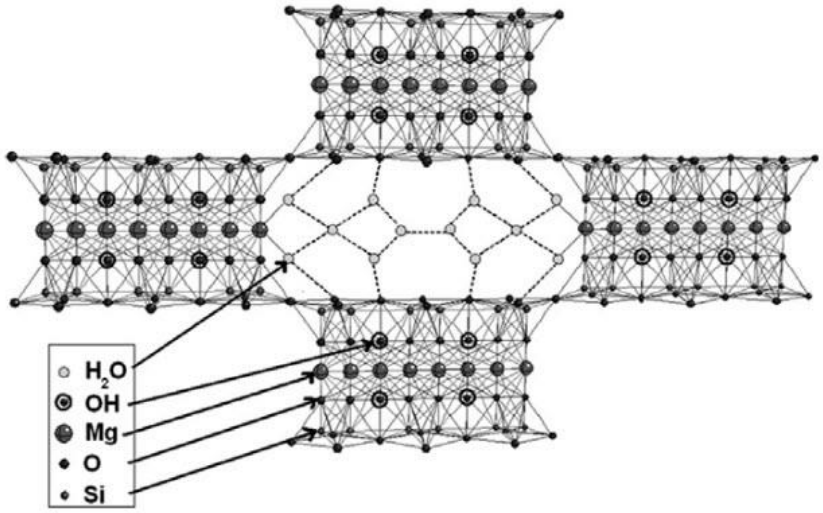

Figure 2.11. Sepiolite structure [80]

There is much research about the positive effects of sepiolite fibres on flame retardancy and smoke inhibition of polymer composites [80-88]. Sepiolite disperses easier in the polymer matrix than MMT due to its fibrous structure. Also, when sepiolite disperses in the polymer network, it prevents occurring of flocculation and agglomeration and results in good mechanical reinforcing effect [83]. The high tendency of sepiolite to absorb different materials is due to its high surface area, channels in the structure, and charge on the particles [89]. Alkan and Kizilcan [90, 91] showed sepiolite fibres could increase the thermal stability of the phenolic resole resin. Studying of flame retardancy properties of poly (methyl methacrylate) with MMT, sepiolite, and zirconium oxide in combination with ammonium polyphosphate (APP) revealed that composites composed of APP and sepiolite had the best fire behaviour [85].

In the development and usage of new materials, using flame retardant (FR) to decrease polymers' combustibility and smoke or toxic fume production turn out to be a key part [92]. Although halogen-containing flame retardants are useful in increasing the flame

retardancy of laminates, they emit toxic gases, which consequently pose a cancer risk to humans. Therefore, developing halogen-free flame retardants gained great attention [79]. Hence, flame retardant materials that connect efficiency with environmentally-friendly aspects are indisputable [79, 93-95]. Red phosphorus and ammonium polyphosphate (APP) are outstanding halogen-free flame retardants for all kinds of thermoset resins [60]. Also, phosphorous acts like a shield between the polymer surface and heat and air, and promotes char production in the condensed phase [92]. Palacios et al. [79] developed sepiolite-phosphate (SepP) which is a self-forming 3D core-shell ceramic nanostructure for halogen-free flame retardant materials. For this purpose, they synthesised nanometric and amorphous $AlPO_4$ with a low-cost and environmentally friendly process which is called precipitation synthesis. Moreover, sepiolite has been used as a support to manage the size and agglomeration of phosphate nanoparticles. According to Palacios's research [79] (which is the only research on SepP) and potential of SepP being used as flame retardant, SepP nanoparticles have been synthesised by the same method [96] to study its properties in the phenolic resin and 3D GFRP nanocomposite.

Using nano-modified phenolic resins in the FRPs is a promising way to maximise their flame retardant properties. Yet, this technology is in its infancy. There is some research on FRPs contain phenolic nanomaterials in literature [97-104]. Koo et al. [101] nano-modified resole resin with different nanofillers such as CNF, nano clay, and POSS. They used a cone calorimeter instrument with a heat flux of 75 kW/m^2 and found that the nanostructured system showed a 25% lower peak heat release rate (PHRR). In another study, Tate et al. [105] used nano clay and phenolic resin to make E-glass reinforced composite with a low-cost method. A mass loss calorimeter test was

performed with a heat flux of 35 kW/m^2. They observed that flammability properties increased by 33% with 7.5% loading of Cloisite Na+. These mineral fillers do not emit toxic gases on thermal decomposition and a high concentration of them significantly improves the flame retardancy, but negatively affects mechanical properties [60].

Considering the superior properties of nanomaterials, their dispersion into the resins is still challenging. Nanomaterials tend to agglomerate because of their fine particle size. This agglomeration prevents them from using their high surface area in reaction to other materials and negatively affects their properties [106, 107]. Tang et al. [108] showed that the same amount of reduced graphene oxide (RGO) when homogeneously dispersed in the matrix could become twice as effective. Dispersion methods for each nanomaterial depend on the type of nanomaterial, its shape, size, amount, and viscosity of the resin [109]. This would be found with experimental tests and study of the materials' chemistry. In addition, nanoparticles obtained from natural resources need to be treated to prevent the separation between discrete phases in the polymer nanocomposite [110, 111]. Poor physical interaction between organic and inorganic elements leads to poor thermal and mechanical properties [110]. Since the dispersion of nanomaterials in the polymer is a prerequisite for achieving desired properties, it will be studied in this research.

The literature review showed that no research on 3D GFRP integrated with flame retardants and nanomaterials for façade systems has been conducted. From this literature review, it is also concluded that thermosetting resins and glass fibre reinforcement are more suitable combinations against fire [22]. To develop a 3D GFRP nanocomposite which improves the fire performance, SepP will be synthesised based

on the Palacios et al. [79] work and accompanied by Sep will be used in the 3D GFRP phenolic panel for façade application.

2.4. Performance-based design for fire safety according to National Construction Code (NCC) Australia

According to the NCC, Section C, which deals with fire performance requirements, external walls including cladding must be non-combustible (AS 1530.1) or prevent the fire spread within a building and to adjacent buildings (AS 5113:2016). Also, the performance of materials and assemblies exposed to fire has been mentioned in Section C: CP4, which says that "different materials and assemblies must resist the spread of fire to limit the generation of smoke, heat, and toxic gases to different degrees, depending on the circumstances of their use". According to the NCC fire requirements, fire propagation testing (AS 5113:2016) needs to be conducted to investigate that wall assemblies (façade system materials) work well together and prevent the fire spread. Since the manufacturing of a full façade with new cladding material is very costly and facilities are beyond this research, it has not been conducted in this thesis and it will be an ongoing project. Instead, prediction of full-scale façade fire test cladding criteria has been carried out based on cone calorimeter test results to have an estimation of new material (3D GFRP nanocomposite) temperature in the full-scale fire test. Furthermore, the combustibility test (AS 1530.1) which is a requirement of performance-based design could not be conducted due to the COVID-19 pandemic. These two tests (combustibility and full-scale façade fire) may be conducted by the CSR company before introducing the new cladding into the market. However, a cone calorimeter test (AS/NZS 3837:1998) is conducted to investigate the heat and smoke release rate and other fire properties of new 3D GFRP

nanocomposite cladding material. Also, the fire safety rating of new cladding will be carried out based on cone calorimeter results.

In the next sections, the cone calorimeter test and tensile test which have been conducted in this thesis will be explained.

Cone calorimeter test (AS/NZS 3837:1998)

Cone calorimetry is recognised as the most accurate way of studying the flame retardant properties of reinforced polymers [62]. This test determines the ignitability, heat release rates, effective heat of combustion, mass loss rates, and smoke release. Cone calorimeter test shows the flammability of the material through the heat release rate per unit area of the horizontal specimen after being ignited by an external source. The sample size is 100 mm × 100 mm. The test apparatus is composed of: "(a) A conical-shaped radiant electric heater, capable of horizontal or vertical orientation. (b) Specimen holders, different for the two orientations. (c) An exhaust gas system with oxygen monitoring and flow measuring instrumentation. (d) An electric ignition sparkplug. (e) A data collection and analysis system. (f) A load cell for measuring specimen mass loss" [112].

To determine the amount of heat released per unit of time along with surface area, measurement of the reducing oxygen concentration in the burning gases of a sample exposed to a provided heat flux (typically between 0–100 kW/m^2) is used [62]. The gross heat of combustion of every organic material can be connected to the amount of oxygen needed for combustion. In a common cone calorimeter test, the heat release rate (HRR) is saved as a function of time: the amount of its PHRR is typically taken into account to estimate the fire behaviour [62]. Moreover, mass loss after burning is

another important parameter. Also, much other useful data can be achieved from cone calorimetry to understand the processes of material flammability [112]. Figure 2.12 shows a schematic of a typical cone calorimeter test.

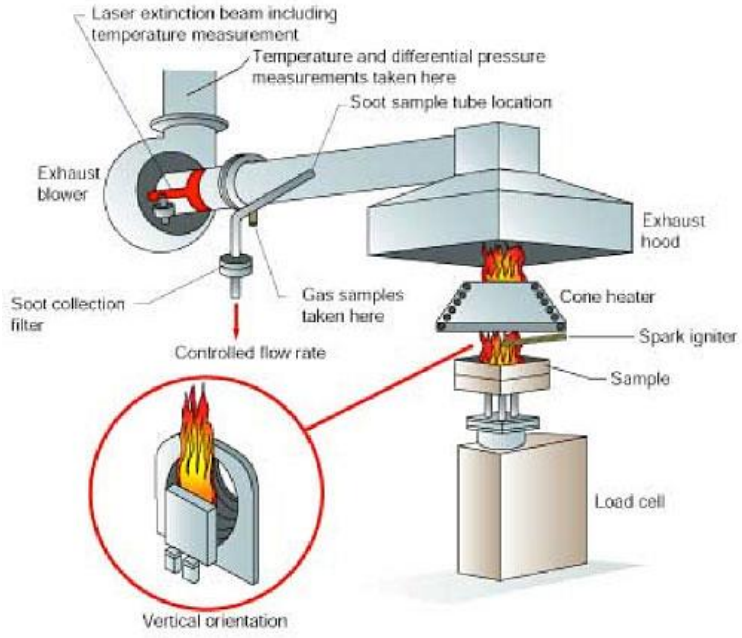

Figure 2.12. Cone calorimeter test [113]

Heat release rate is calculated by the following equations and procedure in [112]:

$$X_{o2}\,(t) = X_{o2}^{1}\,(t + t_d) \qquad Equation\ (2.1)$$

$$q(t) \dot{=} [\frac{\Delta h_c}{r_0}]\ (1.10) C \sqrt{\frac{\Delta P}{T_e}}\ \frac{(X_{o2}^{0} - X_{o2}(t))}{1.105 - 1.5 X_{o2}(t)} \qquad Equatin\ (2.2)$$

where the value of ($\Delta h_c/r_o$) for the test sample is taken to be 13.1 × 103 kJ/kg unless a more precise amount is known for the test material.

X_{o2}= oxygen analyser reading, mole fraction O_2
X_{o2}°= initial value of oxygen analyser reading
X_{o2}^{1}= oxygen analyser reading, before delay time correction

t_d = oxygen analyser delay time, s
t= time, s
Δh_c = net heat of combustion, kJ/kg
r_0 = stoichiometric oxygen/fuel mass ratio
C = calibration constant for oxygen consumption analysis, m1/2.kg1/2. K1/2
ΔP= orifice meter pressure differential, Pa
T_e= absolute temperature of the gas at the orifice meter, K

Then heat release rate per unit area is determined from Equation 2.3 [112]:

$$\dot{q}''(t) = \frac{q(\dot{t})}{A_s} \qquad \text{Equation (2.3)}$$

$\dot{q}$ = heat release rate, kW

Where A_s "is the initially exposed area, i.e. 0.0088 m^2 in the vertical orientation and in the horizontal orientation if the retainer frame is used, and 0.01 m^2 in the horizontal orientation if the retainer frame is not used".

Total heat released during combustion is determined from Equation 2.4 [112]:

$$q'' = \sum_i \dot{q_i''}(t)\Delta t \qquad \text{Equation (2.4)}$$

$\dot{q''}$= heat release rate per unit area, kW/m^2
Δt = sampling time interval, s

The peak heat release rate (PHRR) is the maximum quantity of heat released by a material throughout the combustion procedure, and it frequently happens over a very short period. The PHRR is assumed to be a key property managing the maximum temperature and flame spread ratio [114].

Mass loss rate (MLR) is associated with how quickly the sample is consumed during the combustion process. MLR_{ave} is estimated over a period starting once 10% of the ultimate sample mass loss has happened and ending at the time once 90% of the ultimate sample mass loss has happened in cone calorimeter tests [115]. The

calculation time of MLR_{ave} represents a relatively stable thermal decomposition process of the polymer [116].

The average effective heat of combustion is determined through Equation 2.5

$$\Delta h_{c,eff} = \frac{\sum_i q_i(\dot{t})\Delta t}{m_i - m_f} \qquad \text{Equation (2.5)}$$

m_i = initial specimen mass, kg
m_f = final specimen mass, kg

In principle, specific extinction area (SEA) is defined as "the product of the extinction coefficient and the volumetric flow rate, divided by the mass-loss rate of the tested sample" [117]. It is the effective optical obscuring area produced by 1 kg of mass loss of sample. The specific extinction area is applied to evaluate how much soot in smoke was released from the burning of different samples [112, 116, 118].

$$\sigma_{f(avg)} = \frac{\sum_i V_i \dot{K_i} \Delta t_i}{m_i - m_f} \qquad \text{Equation (2.6)}$$

V = volume exhaust flow rate, measured at the location of the laser photometer, m^3/s
K = smoke extinction coefficient, m^{-1}
Δt = sampling time interval, s
m_i = initial specimen mass, kg
m_f = final specimen mass, kg

Standard test method for tensile properties of polymer matrix composite materials, ASTM D3039

This test procedure is created to produce tensile properties for material qualifications, quality assurance, research and development, and structural design and analysis [119]. The test method defines the in-plane tensile properties of polymer composites

strengthened by high-modulus fibres. The composite material types are restricted to continuous fibre or discontinuous fibre-reinforced composites where the laminate is symmetric to the test direction [119]. A narrow flat strip of material with a constant rectangular cross-section is placed in the grips of a testing instrument and constantly loaded in tension as monitoring the force. The ultimate strength of the material can be calculated from the maximum force conducted before failure [119]. The ultimate strength of the material can be assessed from the maximum force taken before failure from Equation 2.7 [119].

$$F^{tu} = \frac{P^{max}}{A} \qquad \text{Equation (2.7)}$$

F^{tu} = ultimate tensile strength, MPa
P^{max} = maximum force before failure, N
A= cross-sectional area of the specimen

The module of elasticity can be calculated from Equation 2.8 according to Figure 2.13 [119]

$$E = \frac{\Delta\sigma}{\Delta\varepsilon} \qquad \text{Equation (2.8)}$$

E= tensile modulus of elasticity, GPa
Δσ = difference in applied tensile stress between the two strain points, MPa
Δ£ = difference between the two strain points

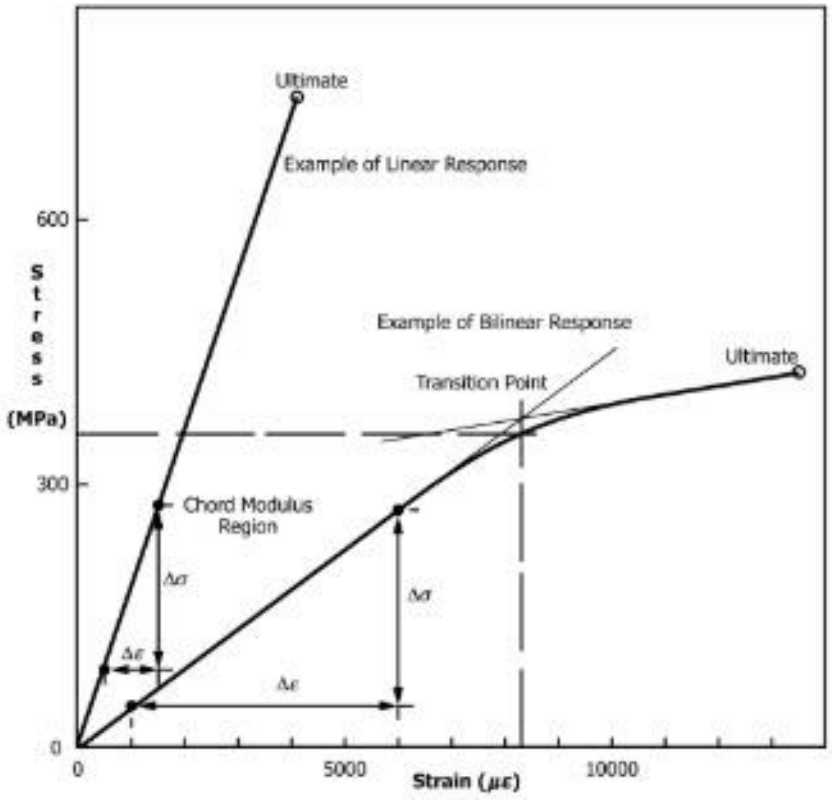

Figure 2.13. Typical stress-strain curves [119]

2.5. Chapter summary

Based on the literature reviewed, it can be concluded that there are three major gaps in the current pool of knowledge. There is a:

- lack of a new cladding material to improve the fire performance of façade systems
- lack of appropriate curing of phenolic resin in combination with Sep and SepP nanoparticles and a suitable method of dispersion of those nanoparticles into the phenolic resin
- lack of appropriate manufacturing of 3D GFRP phenolic nanocomposite as a new cladding material

- lack of study on fire behaviour of 3D GFRP nanocomposites for façade applications
- lack of tensile properties of 3D GFRP phenolic nanocomposite materials with Sep and SepP nanoparticles.

To fill these knowledge gaps, this study:

- developed a new cladding material which is called 3D GFRP phenolic nanocomposite and studied the synthesis of nanomaterials, their dispersion into the phenolic resin, curing time and temperature of phenolic resin, and manufacturing of 3D GFRP nanocomposite
- investigated the fire performance of 3D GFRP nanocomposite with studying of its thermal behaviour, the bench-scale fire test, and prediction of full-scale fire test criteria of cladding material
- examined the tensile properties of 3D GFRP nanocomposite cladding material by conducting a tensile test at ambient temperature.

Chapter 3 discusses all techniques and methods used in the thesis in detail. After studying the methods, developing the materials, their fire behaviour, and tensile properties will be discussed in the following chapters.

2.6. References

[1] Lin J, Scott D. Assessment of significances of building failure induced by foundation failure: facade failure, and moisture problem. Building Integration Solutions2006. p. 1-13.
[2] Beasley KJ. Latent building facade failures. Forensic Engineering 2012: Gateway to a Safer Tomorrow2013. p. 918-27.
[3] GreenSpec. Whole life costing: Insulated render. 2018.
[4] GreenSpec. 2020. https://www.greenspec.co.uk/.
[5] The brick industry association. Thin Brick Veneer. 2014. https://www.gobrick.com.
[6] Kazmierczak K, Hershfi M. Review of Curtain Walls, Focusing on Design Problems and Solutions. BEST2 Conference2010.

[7] Aluprof aluminium systems. 2020. https://aluprof.eu/us/manufacturers/offer/facades/mb-sg50#visualisation.
[8] Perth Photo Gallery. https://www.globalphotos.org/perth.htm.
[9] Designing Buildings Wiki. Precast concrete cladding. 2020. https://www.designingbuildings.co.uk/wiki/Precast_concrete_cladding.
[10] Smith S, Smith AD. Rain screen system. Google Patents; 2011.
[11] CSR. Inclose Unitised Rainscreen Facades. https://www.csrinclose.com.au/.
[12] CSR. A leading building products company in Australia and New Zealand. https://www.csrinclose.com.au/.
[13] Beasley KJ. Contemporary and traditional wall-system failures. Journal of performance of constructed facilities. 2001;15:42-5.
[14] Beasley KJ. Identification and Diagnosis of Building Façade Failures. Forensic Engineering 2009: Pathology of the Built Environment2010. p. 74-84.
[15] Kumar KS. Pressure equalization of rainscreen walls: a critical review. Building and Environment. 2000;35:161-79.
[16] In-service facade performance assessments. 2017. https://lccl.uk/in-service-facade-performance-assessnent-and-maintenance-requirements/.
[17] Straube J, Burnett E. Rain control and screened wall systems. Proc 7th Conf on Building Science and Technology Durability of Buildings Design, Maintenance, Codes and Practices Toronto1997. p. 20-1.
[18] American Galvanizers Association. Hot-dip galvanizing for corrosion protection. 2012.
[19] Soufeiani L, Foliente G, Nguyen KT, San Nicolas R. Corrosion protection of steel elements in façade systems–a review. Journal of Building Engineering. 2020;32:101759.
[20] Çıkış DT. The evolution and change of building facades: A research for developing alternative composite surface materials: İzmir Institute of Technology; 2007.
[21] Reardon C. Cladding systems. 2013. http://www.yourhome.gov.au/materials/cladding-systems.
[22] Nguyen T. Fire performance of GFRP facade systems. Thesis, 2015.
[23] Hanrahan J. Revealed: Cladding that 'fuelled London's tower inferno tragedy' is in more than HALF of Melbourne's high-rise apartments - as eerie pictures show similarity between 2014 Docklands blaze and Grenfell disaster. Daily mail Australa; 2017.
[24] Lee HWH, Keshavarz M. Nanocomposite materials with engineered properties. Google Patents; 2004.
[25] Egypt today. Large fire breaks out at Dubai's Torch Tower. 2017. https://www.egypttoday.com/Article/1/15464/Large-fire-breaks-out-at-Dubai-s-Torch-Tower.
[26] Sathish V. Families in fire-ravaged Al Tayer building face homeless night out. 2012.
[27] Nguyen KT, Weerasinghe P, Mendis P, Ngo T, Barnett J. Performance of modern building façades in fire: a comprehensive review. Electron J Struct Eng. 2016;16:69-86.
[28] Reardon C. Cladding systems. Australian Government; 2013.
[29] Devendra K, Rangaswamy T. Thermal conductivity and thermal expansion coefficient of gFRP composite laminates with fillers. Mech Confab. 2013;2:39-44.

[30] Wang S, Qiu J. Enhancing thermal conductivity of glass fiber/polymer composites through carbon nanotubes incorporation. Composites Part B: Engineering. 2010;41:533-6.
[31] Soufeiani L, Raman SN, Jumaat MZB, Alengaram UJ, Ghadyani G, Mendis P. Influences of the volume fraction and shape of steel fibers on fiber-reinforced concrete subjected to dynamic loading–A review. Engineering Structures. 2016;124:405-17.
[32] Soufeiani L. Dynamic Behavior of Fiber Reinforced Composite Slab Induced by Human Walking: Universiti Teknologi Malaysia; 2013.
[33] Sabamehr A, Soufeiani L, Ahmad Y. Computer simulation of bridge girder reinforced with FRP. Universiti Teknologi Malaysia; 2012.
[34] Soufeiani L, Ghadyani G, Kueh ABH, Nguyen KT. The effect of laminate stacking sequence and fiber orientation on the dynamic response of FRP composite slabs. Journal of Building Engineering. 2017;13:41-52.
[35] Jesus Cerezo Miguel Mand. Fiber Reinforced Polymer (FRP): A New Material Used in Façades of Tall Buildings. 2015.
[36] Barbero EJ. Introduction to composite materials design: CRC press; 2017.
[37] Nguyen TQ. Fire performance of GFRP façade systems. Thesis, 2015.
[38] Eckold G. Design and manufacture of composite structures: Elsevier; 1994.
[39] Lomov SV, Bogdanovich AE, Ivanov DS, Mungalov D, Karahan M, Verpoest I. A comparative study of tensile properties of non-crimp 3D orthogonal weave and multi-layer plain weave E-glass composites. Part 1: Materials, methods and principal results. Composites part a: applied science and manufacturing. 2009;40:1134-43.
[40] Sadighi M, Hosseini SA. Finite element simulation and experimental study on mechanical behavior of 3D woven glass fiber composite sandwich panels. Composites part b: engineering. 2013;55:158-66.
[41] Haufler Composites. Parabeam ParaGlass 8. 2019. https://www.compositeshop.de.
[42] Composites H. Parabeam ParaGlass 2018.
[43] Van Vuure A, Pflug J, Ivens J, Verpoest I. Modelling the core properties of composite panels based on woven sandwich-fabric preforms. Composites Science and Technology. 2000;60:1263-76.
[44] Fan H, Zhou Q, Yang W, Jingjing Z. An experiment study on the failure mechanisms of woven textile sandwich panels under quasi-static loading. Composites Part B: Engineering. 2010;41:686-92.
[45] Zheng J, Zhao L, Fan H. Energy absorption mechanisms of hierarchical woven lattice composites. Composites Part B: Engineering. 2012;43:1516-22.
[46] Chou S, Chen H-C, Chen H-E. Effect of weave structure on mechanical fracture behavior of three-dimensional carbon fiber fabric reinforced epoxy resin composites. Composites science and technology. 1992;45:23-35.
[47] Chou S, Chen H-C, Wu C-C. BMI resin composites reinforced with 3D carbon-fibre fabrics. Composites science and technology. 1992;43:117-28.
[48] Guess TR, Reedy E. Comparison of interlocked fabric and laminated fabric Kevlar 49/epoxy composites. Journal of Composites, Technology and Research. 1985;7:136-42.
[49] Rudov-Clark S. Experimental investigation of the tensile properties and failure mechanisms of three-dimensional woven composites. 2007.
[50] Cox B, Carter W, Fleck N. A binary model of textile composites—I. Formulation. Acta metallurgica et materialia. 1994;42:3463-79.

[51] Cox BN, Dadkhah MS, Morris W. On the tensile failure of 3D woven composites. Composites Part A: Applied Science and Manufacturing. 1996;27:447-58.
[52] Cox B. Failure models for textile composites. 1995.
[53] Raquez J-M, Deléglise M, Lacrampe M-F, Krawczak P. Thermosetting (bio) materials derived from renewable resources: A critical review. Progress in polymer science. 2010;35:487-509.
[54] Saba N, Jawaid M, Alothman OY, Paridah M, Hassan A. Recent advances in epoxy resin, natural fiber-reinforced epoxy composites and their applications. Journal of Reinforced Plastics and Composites. 2016;35:447-70.
[55] Vivaldo-Lima E, Saldívar-Guerra E. Handbook of polymer synthesis, characterization, and processing: Wiley Online Library; 2013.
[56] Mohammad Asim NS, Mohammad Jawaid, Mohammed Nasir. A review on Phenolic resin and its Composites. Current Analytical Chemistry ·. 2017.
[57] Nair CR. Advances in addition-cure phenolic resins. Progress in polymer science. 2004;29:401-98.
[58] Campbell FC. Structural composite materials: ASM international; 2010.
[59] Dodiuk HG, Sidney H. Handbook of thermoset plastics: Elsevier; 2014.
[60] Kandola B, Krishnan L. Fire performance evaluation of different resins for potential application in fire resistant structural marine composites. Fire Safety Science. 2014; 11:769-80.
[61] Morgan AB. Flame retarded polymer layered silicate nanocomposites: a review of commercial and open literature systems. Polymers for Advanced Technologies. 2006; 17:206-17.
[62] Monti M, Natali M, Petrucci R, Puglia D, Terenzi A, Valentini L et al. Composites Based on Nanocomposite Matrices. Wiley Encyclopedia of composites. 2011:1-18.
[63] Gammampila R, Mendis P, Ngo T, Aye L, Jayalath A, Rupasinghe R. Application of nanomaterials in the sustainable built environment. 2013.
[64] Khan ZM, Saleem MR. Multifunctional Polymer Nanocomposites in Next Generation Smart Structures. Development and Prospective Applications of Nanoscience and Nanotechnology: Nanomaterials and their Fascinating Attributes. 2016;1:51.
[65] Ghadyani G, Soufeiani L, Öchsner A. On the characterization of the elastic properties of asymmetric single-walled carbon nanotubes. Journal of Physics and Chemistry of Solids. 2016;89:62-8.
[66] Ghadyani G, Soufeiani L, Öchsner A. On a thickness free expression for the shear modulus of carbon nanotubes. Journal of Applied Physics. 2016;120:174302.
[67] Ghadyani G, Soufeiani L, Öchsner A. Angle dependence of the shear behaviour of asymmetric carbon nanotubes. Materials & Design. 2017;116:136-43.
[68] Ávila AF, Dias EC, Cruz DTLd, Yoshida MI, Bracarense AQ, Carvalho MGR et al. An investigation on graphene and nanoclay effects on hybrid nanocomposites post fire dynamic behavior. Materials Research. 2010;13:143-50.
[69] Kim M-J, Jeon I-Y, Seo J-M, Dai L, Baek J-B. Graphene phosphonic acid as an efficient flame retardant. ACS nano. 2014;8:2820-5.
[70] Lee JK, Song S, Kim B. Functionalized graphene sheets-epoxy based nanocomposite for cryotank composite application. Polymer Composites. 2012;33:1263-73.

[71] Li Y, Zhang H, Huang Z, Bilotti E, Peijs T. Graphite Nanoplatelet Modified Epoxy Resin for Carbon Fibre Reinforced Plastics with Enhanced Properties. Journal of Nanomaterials. 2017;2017.
[72] Ngo T, Nguyen Q, Nguyen T, Tran P. Effect of nanoclay on thermomechanical properties of epoxy/glass fibre composites. Arabian Journal for Science and Engineering. 2016;41:1251-61.
[73] Peeterbroeck S, Laoutid F, Swoboda B, Lopez-Cuesta JM, Moreau N, Nagy JB et al. How carbon nanotube crushing can improve flame retardant behaviour in polymer nanocomposites? Macromolecular rapid communications. 2007;28:260-4.
[74] Zhuge J, Gou J, Ibeh C. Flame resistant performance of nanocomposites coated with exfoliated graphite nanoplatelets/carbon nanofiber hybrid nanopapers. Fire and Materials. 2012;36:241-53.
[75] Saba N, Tahir PM, Jawaid M. A review on potentiality of nano filler/natural fiber filled polymer hybrid composites. Polymers. 2014;6:2247-73.
[76] Nguyen Q, Mendis P, Ngo T, Nguyen C, Bhattacharyya D. Effect of nanoclay on fire performance of hybrid nano composites. The 19th International conference on composite materials.
[77] Nguyen QT, Ngo TD, Tran P, Mendis P, Bhattacharyya D. Influences of clay and manufacturing on fire resistance of organoclay/thermoset nanocomposites. Composites Part A: Applied Science and Manufacturing. 2015;74:26-37.
[78] Huang W. Clay Nanopapers. Nanopapers: Elsevier; 2018. p. 59-86.
[79] Palacios E, Leret P, De La Mata MJ, Fernández JF, De Aza AH, Rodríguez MA et al. Self-Forming 3D Core–Shell Ceramic Nanostructures for Halogen-Free Flame Retardant Materials. ACS applied materials & interfaces. 2016;8:9462-71.
[80] Tartaglione G, Tabuani D, Camino G. Thermal and morphological characterisation of organically modified sepiolite. Microporous and Mesoporous Materials. 2008;107:161-8.
[81] Laoutid F, Bonnaud L, Alexandre M, Lopez-Cuesta J-M, Dubois P. New prospects in flame retardant polymer materials: from fundamentals to nanocomposites. Materials Science and Engineering: R: Reports. 2009;63:100-25.
[82] Marosfoi B, Garas S, Bodzay B, Zubonyai F, Marosi G. Flame retardancy study on magnesium hydroxide associated with clays of different morphology in polypropylene matrix. Polymers for Advanced Technologies. 2008;19:693-700.
[83] Mohd Zaini NA, Ismail H, Rusli A. Short Review on Sepiolite-Filled Polymer Nanocomposites. Polymer-Plastics Technology and Engineering. 2017;56:1665-79.
[84] Norouzi M, Zare Y, Kiany P. Nanoparticles as effective flame retardants for natural and synthetic textile polymers: application, mechanism, and optimization. Polymer Reviews. 2015;55:531-60.
[85] Vahabi H, Lin Q, Vagner C, Cochez M, Ferriol M, Laheurte P. Investigation of thermal stability and flammability of poly (methyl methacrylate) composites by combination of APP with ZrO2, sepiolite or MMT. Polymer Degradation and Stability. 2016; 124:60-7.
[86] Xu Z, Liu D, Yan L, Xie X. Synergistic effect of sepiolite and polyphosphate ester on the fire protection and smoke suppression properties of an amino transparent fire-retardant coating. Progress in Organic Coatings. 2020;141:105572.

[87] Carretier V, Delcroix J, Pucci MF, Rublon P, Lopez-Cuesta J-M. Influence of Sepiolite and Lignin as Potential Synergists on Flame Retardant Systems in Polylactide (PLA) and Polyurethane Elastomer (PUE). Materials. 2020;13:2450.
[88] Pan Y, Liu L, Cai W, Hu Y, Jiang S, Zhao H. Effect of layer-by-layer self-assembled sepiolite-based nanocoating on flame retardant and smoke suppressant properties of flexible polyurethane foam. Applied Clay Science. 2019;168:230-6.
[89] Murray HH. Overview—clay mineral applications. Applied clay science. 1991;5:379-95.
[90] Alkan ÜB, Kızılcan N. Characterization of nanocomposite resol resins: Individual/synergist effects of alendronic acid and sepiolite. Journal of Applied Polymer Science. 2016;133.
[91] Alkan ÜB, Kızılcan N. In situ preparation of resol/sepiolite nanocomposites. Procedia-Social and Behavioral Sciences. 2015;195:2067-75.
[92] Lu S-Y, Hamerton I. Recent developments in the chemistry of halogen-free flame retardant polymers. Progress in polymer science. 2002;27:1661-712.
[93] Cho JH, Vasagar V, Shanmuganathan K, Jones AR, Nazarenko S, Ellison CJ. Bioinspired catecholic flame retardant nanocoating for flexible polyurethane foams. Chemistry of Materials. 2015;27:6784-90.
[94] Carosio F, Fontaine G, Alongi J, Bourbigot S. Starch-based layer by layer assembly: efficient and sustainable approach to cotton fire protection. ACS applied materials & interfaces. 2015;7:12158-67.
[95] Chen M-J, Shao Z-B, Wang X-L, Chen L, Wang Y-Z. Halogen-free flame-retardant flexible polyurethane foam with a novel nitrogen–phosphorus flame retardant. Industrial & engineering chemistry research. 2012;51:9769-76.
[96] Soufeiani L, Nguyen KT, Foliente G. Use of resole sepiolite-phosphate nanocomposite for building facades. ICCM22 2019. 2019:2480.
[97] Chiang CL, Ma CCM, Wu DL, Kuan HC. Preparation, characterization, and properties of novolac-type phenolic/SiO2 hybrid organic–inorganic nanocomposite materials by sol–gel method. Journal of Polymer Science Part A: Polymer Chemistry. 2003;41:905-13.
[98] Jiang W, Chen SH, Chen Y. Nanocomposites from phenolic resin and various organo-modified montmorillonites: Preparation and thermal stability. Journal of applied polymer science. 2006;102:5336-43.
[99] Kato M, Tsukigase A, Usuki A, Shimo T, Yazawa H. Preparation and thermal properties of resole-type phenol resin–clay nanocomposites. Journal of applied polymer science. 2006;99:3236-40.
[100] Kaynak C, Tasan CC. Effects of production parameters on the structure of resol type phenolic resin/layered silicate nanocomposites. European polymer journal. 2006;42:1908-21.
[101] Koo JH. Polymer nanocomposites: McGraw-Hill Professional Pub.; 2006.
[102] Srikanth I, Daniel A, Kumar S, Padmavathi N, Singh V, Ghosal P et al. Nano silica modified carbon–phenolic composites for enhanced ablation resistance. Scripta Materialia. 2010;63:200-3.
[103] Wang H, Zhao T, Yan Y, Yu Y. Synthesis of resol–layered silicate nanocomposites by reaction exfoliation with acid-modified montmorillonite. Journal of applied polymer science. 2004;92:791-7.

[104] Wu Z, Zhou C, Qi R. The preparation of phenolic resin/montmorillonite nanocomposites by suspension condensation polymerization and their morphology. Polymer composites. 2002;23:634-46.
[105] Tate J, Kabakov D, Koo J, Lao S. Nanomodified phenolic/E-glass composites. SAMPE. 2009.
[106] Guo D, Xie G, Luo J. Mechanical properties of nanoparticles: basics and applications. Journal of physics D: applied physics. 2013;47:013001.
[107] Horzum N, Arik N, Truong YB. Nanofibers for fiber-reinforced composites. Fiber Technology for Fiber-Reinforced Composites: Elsevier; 2017. p. 251-75.
[108] Tang L-C, Wan Y-J, Yan D, Pei Y-B, Zhao L, Li Y-B et al. The effect of graphene dispersion on the mechanical properties of graphene/epoxy composites. Carbon. 2013;60:16-27.
[109] De Cicco D, Asaee Z, Taheri F. Use of Nanoparticles for Enhancing the Interlaminar Properties of Fiber-Reinforced Composites and Adhesively Bonded Joints—A Review. Nanomaterials. 2017;7:360.
[110] Gacitua W, Ballerini A, Zhang J. Polymer nanocomposites: synthetic and natural fillers a review. Maderas Ciencia y tecnologia. 2005;7:159-78.
[111] Hou K, Ouyang J, Zheng C, Zhang J, Yang H. Surface-modified sepiolite fibers for reinforcing resin brake composites. Materials Express. 2017;7:104-12.
[112] AS/NZS 3837. Method of test for heat and smoke release rates for materials and products using an oxygen consumption calorimeter. 2016.
[113] NIST. Cone Calorimeter. 2018. https://www.nist.gov/laboratories/tools-instruments/cone-calorimeter.
[114] Mouritz AP, Gibson AG. Fire properties of polymer composite materials: Springer Science & Business Media; 2007.
[115] Hurley MJ, Gottuk DT, Hall Jr JR, Harada K, Kuligowski ED, Puchovsky M et al. SFPE handbook of fire protection engineering: Springer; 2015.
[116] Shen R, Hatanaka LC, Ahmed L, Agnew RJ, Mannan MS, Wang Q. Cone calorimeter analysis of flame retardant poly (methyl methacrylate)-silica nanocomposites. Journal of Thermal Analysis and Calorimetry. 2017;128:1443-51.
[117] Myllymäki J, Baroudi D. Prediction of smoke production and heat release by convolution model. VTT TIEDOTTEITA. 1999.
[118] Barakat M, Souil J-M, Breillat C, Vantelon J-P, Knorre V, Rongère F-X. Smoke data determination for various types of fuel. Fire safety journal. 1998;30:293-306.
[119] ASTM D3039. Standard test method for tensile properties of polymer matrix composite materials. ASTM International; 2008.

Chapter 3

Methods

3.1. Introduction

In this chapter, comprehensive methods of the research from the synthesising of nanomaterial to a bench-scale fire test as well as tensile properties are explained. The first step in fabricating 3D GFRP phenolic composite as a new cladding material is the synthesis of nanoparticles. Sepiolite-phosphate (SepP) has been synthesised according to Palacios et al. [1], and morphological, structural, and thermogravimetric analyses have been carried out. Then a comprehensive study on the dispersion of SepP in the phenolic composite has been conducted. Also, dispersion analysis of both Sepiolite (Sep) and SepP nanoparticles in the phenolic resin with high shear mixing instrument was carried out. Also, thermogravimetric analysis of Sep/SepP phenolic composite has been conducted to study the percentage of weight loss of nanocomposite while recording temperature. After the fabrication of Sep/SepP phenolic composite, 3D GFRP composite was fabricated manually and morphological characterisation has been carried out. Prepared 3D GFRP composite has cut to required dimensions for cone calorimeter (AS/NZS 3837:1998 [2]) and tensile tests (ASTM D3039 [3]) which will be explained in detail in Chapters 5 and 6. Figure 3.1 shows the step by step process of the current chapter.

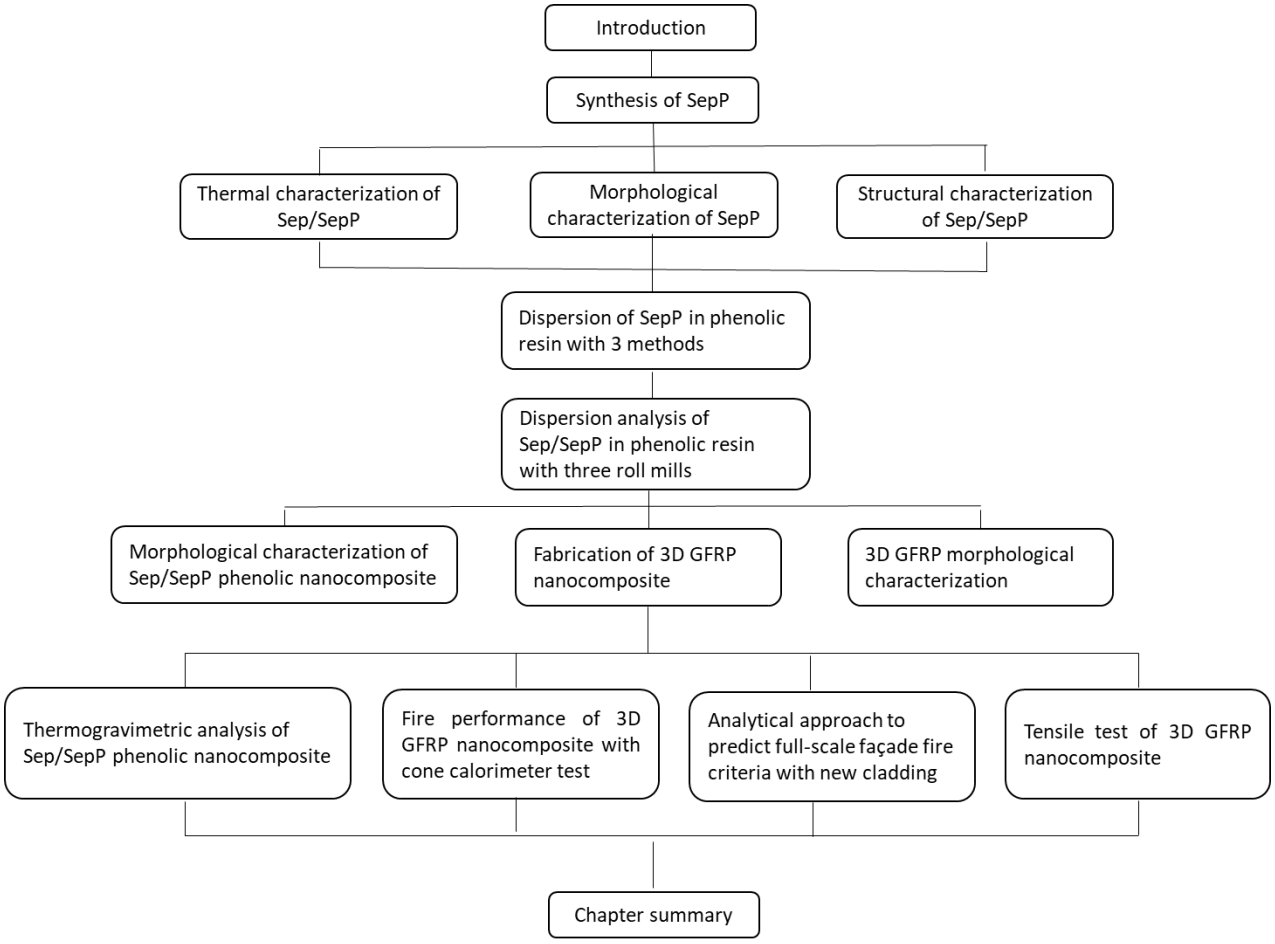

Figure 3.1. Flowchart of method chapter

In the previous chapter, in-service performance failures for façade systems have been identified which were moisture penetration and corrosion of steel elements in the façade system, and combustible cladding materials. Corrosion of steel elements and corrosion protection methods are discussed in the published journal paper (Appendix A). Moreover, cut-edge corrosion of the steel frame in the CSR rain screen façade system has been modelled with WUFI 1D and WUFI 2D software (see Appendix B). The second performance failure criterion (cladding fire) is discussed in the rest of the thesis.

3.2. Materials

Sepiolite [Sep] powders (>95%, Pangel S9) were kindly provided from TOLSA S.A. Spain. Aluminium hydroxide powder [Al $(OH)_3$], hydrochloric acid [HCl] fuming 37%, ammonia solution [NH_4OH] 28-30%, and ammonium dihydrogen phosphate [APP] powder were purchased from Merck, Australia. Ortho-phosphoric acid [H_3PO_4] 85% was purchased from Sigma-Aldrich, Australia. Phenolic resin (Cellobond J2027X01) and catalyst (Phencat 382) were purchased from Hexion Pty Ltd, UK. 3D woven glass fibre fabric (ParaGlass 8 mm, width 127 cm) were supplied from Haufler Composites GmbH& Co. KG, Germany.

3.3. Synthesis of sepiolite-phosphate

To obtain the 6% sepiolite, 6 g of sepiolite powder was dispersed in deionised water under high shear mixing for 5 min. Then HCl solution was added to adjust the pH to around 2 under stirring. Also, 2.33 g of Al $(OH)_3$ was dissolved in the aqueous solution of 17.33 g of H_3PO_4 (Al/P:1/3 molar ratio) and stirred at room temperature to reach a uniform solution. Then, this uniform solution was added to the initial sepiolite solution and stirring was continued for 30 min. Thereafter, an NH_4OH solution was added dropwise to the solution until a pH of 4.8 to produce the phosphate precipitation. Then, synthesised powders were filtered under vacuum, washed with deionised water, and dried at 80^o C for several hours. The final product is SepP nano powders. In this way, 6 g of SepP can be produced each time. Figures 3.2 and 3.3 show the SepP synthesis procedure and final produced SepP nanoparticles, respectively.

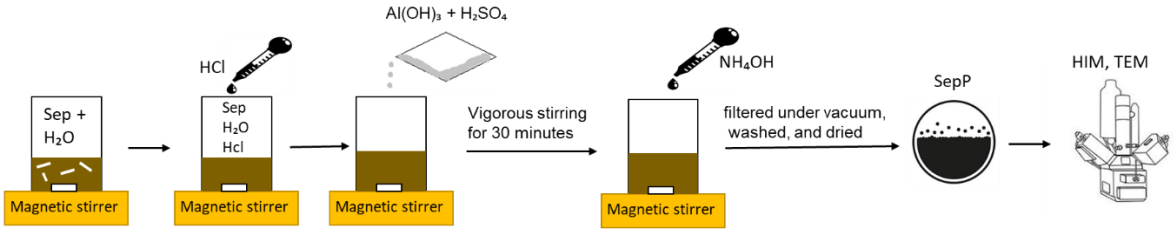

Figure 3.2. Synthesising of SepP

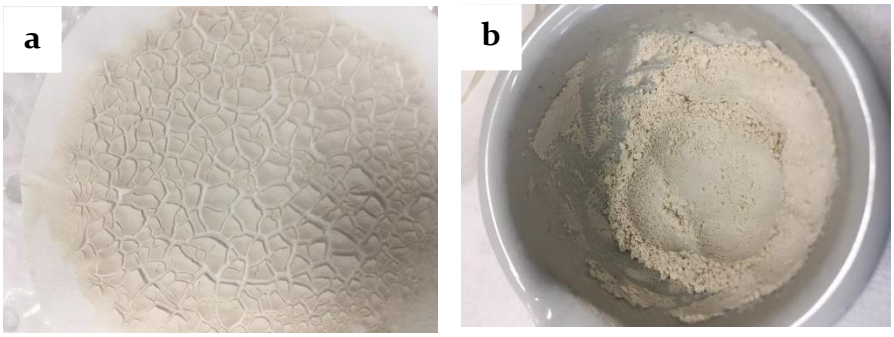

Figure 3.3: a) Cured SepP in the oven; b) crushed SepP nanoparticles

3.4. Thermal characterisation

Measurement of changes in the physical and chemical properties of a material as a function of temperature (ASTM E1131 and ISO 11358) is called thermogravimetric analysis (TGA) [4]. In TGA, a sample is heated under a controlled program and weight changes with respect to temperature are monitored. To study curing reactions or degradations during heating the sample, this quantitative method is very useful. A thermobalance (with a sensitivity of 1 µg for recording weight and a few hundred milligrams capacity) and a furnace which is conducted in the temperature range 50-800 °C with a heating rate up to 100 °C/min are two elements of the TGA instrument. A material's thermal stability can be examined in an inert or oxidative environment. TGA curves demonstrate the mechanism of decomposition. Thermogravimetric analysis of Sep and SepP composite has been conducted with PerkinElmer, TGA 8000 following a heating rate of 10 °C/min. TGA curves were recorded with a flow rate of

0.04 L/min over the temperature range 30-1200 ^{o}C under the air atmosphere. Figure 3.4 shows the TGA instrument which has been used in this research.

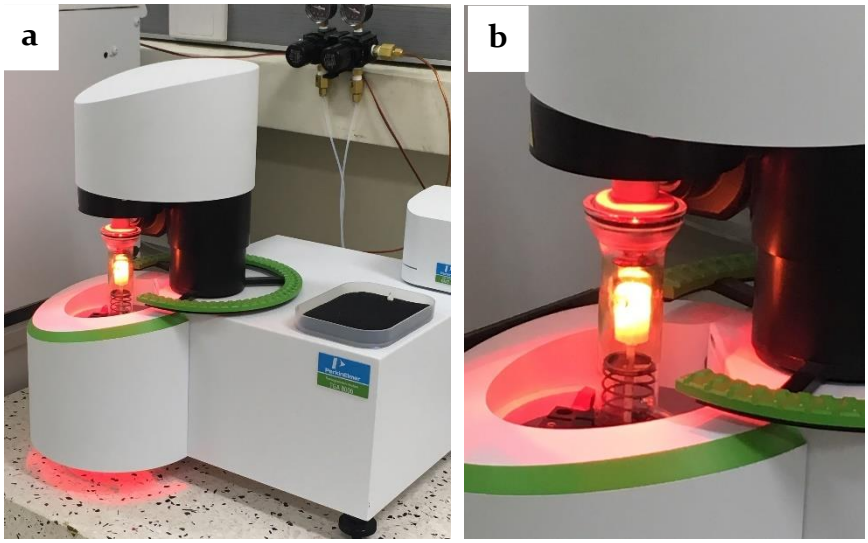

Figure 3.4: a) TGA instrument; b) furnace, (TrACEES platform – University of Melbourne)

3.5. Morphological characterisation

To evaluate the morphology and particle size of the SepP composites, both helium ion microscope (HIM – Zeiss Orion NanoFab) and transmission electron microscope (TEM/FEI Tecnai F30) have been used at the Materials Characterisation and Fabrication Platform (MCFP) and Bio 21 (Advanced Microscopy Facility) at the University of Melbourne. HIM has been used over SEM due to its better resolution at high magnification.

TEM is also used to examine morphology, especially to study nano-scale distribution of inorganic fillers or other polymeric elements in the thermoset resin. The resolution of modern TEM is up to 0.1 nm. By concentrating a beam of electrons onto a very thin sample, images are produced. The transmitted electrons transmit information about the internal structure, which is taken to create an image. Therefore, the thickness of

the specimen should be very low (<80 nm) to guarantee transmittance [5]. Also, TEM equipped with an energy dispersive spectroscopy (EDS) has been used to determine the composition of the SepP composite. For TEM sample preparation, a 300-mesh copper TEM grid with carbon film support has been used for particles. Figure 3.5 shows the TEM samples preparation and instrument.

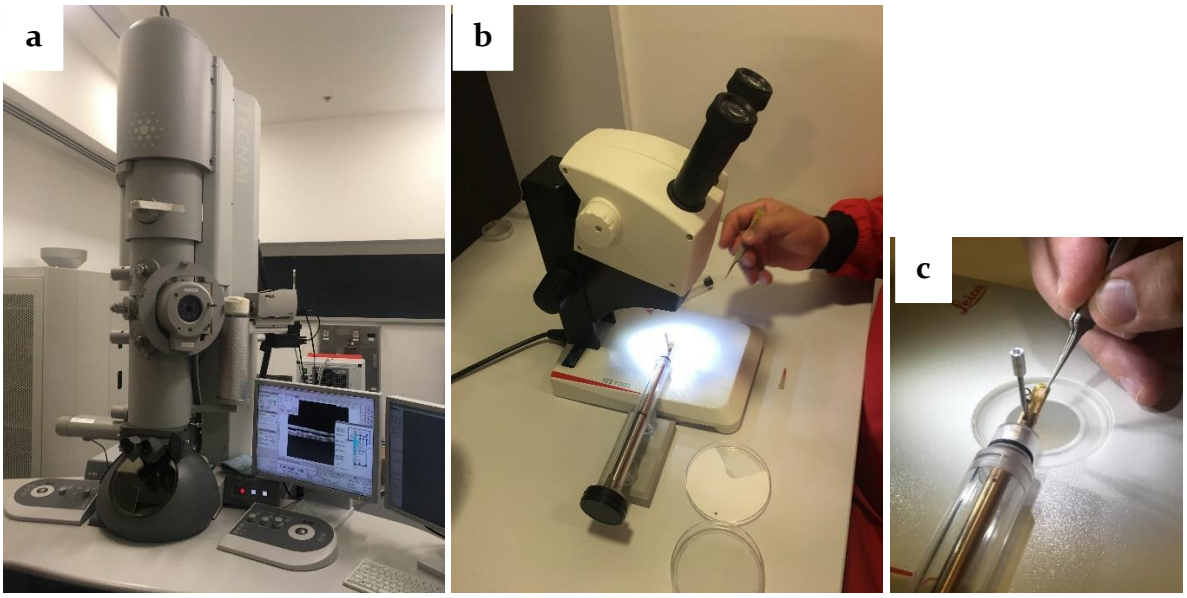

Figure 3.5: a) TEM instrument; b) looking at the sample under a microscope; c) sample preparation (Bio21 institute – University of Melbourne)

3.6. Structural characterisation

The Sep and SepP samples were backloaded into a standard sample holder (without any additional sample preparation) for analysis by X-ray diffraction. Diffraction information were gathered applying a Bruker D8 Advance X-ray diffractometer with Ni-filtered Cu kα radiation (1.54 Å). Information were gathered between 5-85° 2θ, with a step size of 0.02° and a scan ratio of 1.0 s per step. An anti-scatter blade was utilised to shrink the diffracted background concentration at low angles. An incident beam deviation of 1.0° was employed with a 2.5° Soller split in the diffracted beam. The sample was rotated at 15 revolutions per minute. Phase detection was achieved

utilising Diffrac. EVA V4.1 software with the ICDD PDF4+ 2018 databank and Quantitative Rietveld assessment for the quantification of known crystalline phases was conducted using Bruker Diffracplus Topas software.

3.7. Dispersion and curing of SepP-phenolic nanocomposite with three different methods

To study the phenolic resin (PR) curing process, and SepP dispersion in the resin, 2 g of SepP phenolic resin consisting of 5% of SepP and 100% of PR has been prepared and investigated in three different methods as follows:

Method 1: SepP added into the phenol and mixed on a magnetic stirrer at a temperature of 80° C for 10 min. Then, put the solution in a sonicator with the same temperature for 10 min followed by adding 5% catalyst and stirring for 2 more minutes. Thereafter, cure the sample in an oven at 80° C for an hour. After that crush the sample, followed by gold coating for HIM characterisation. Figure 3.6 shows Method 1.

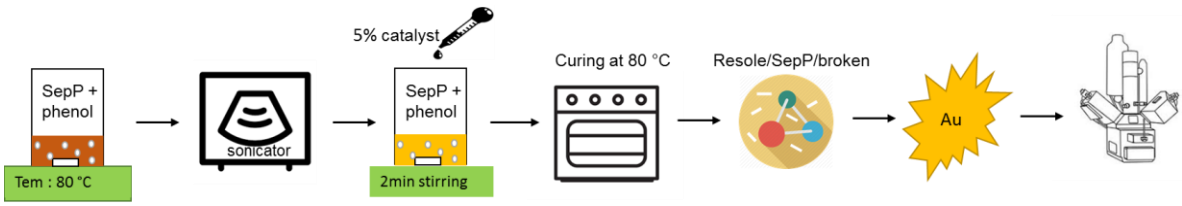

Figure 3.6. SepP-phenolic nanocomposite – Method 1

Method 2: In this method, SepP is added into the phenolic resin, followed by 10 min magnetic stirring at 80° C. Then 5% catalyst is added and stirred for 2 more minutes. Thereafter, putting the sample in the vacuumed oven with a temperature of 40° C for 20 min, and increasing the temperature to 80° C for an hour to cure. The sample has

been taken from the oven, crushed and prepared for HIM. Figures 3.7 shows Method 2.

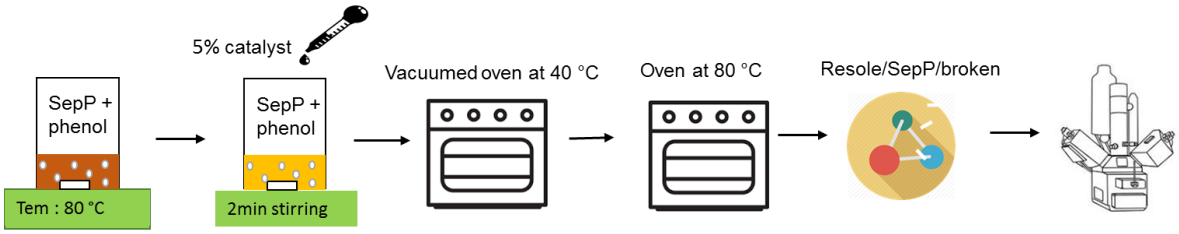

Figure 3.7. SepP-phenolic nanocomposite – Method 2

Method 3: In this method, SepP is added into the phenolic resin, followed by 10 min magnetic stirring at 80° C. Then 5% catalyst is added and stirred for 2 more minutes. Thereafter, put the sample in the vacuum desiccator at room temperature for half an hour which is the gel time of the phenolic resin. Then cure the sample in the oven at 80° C for an hour followed by crushing the sample for HIM. Figure 3.8 shows Method 3.

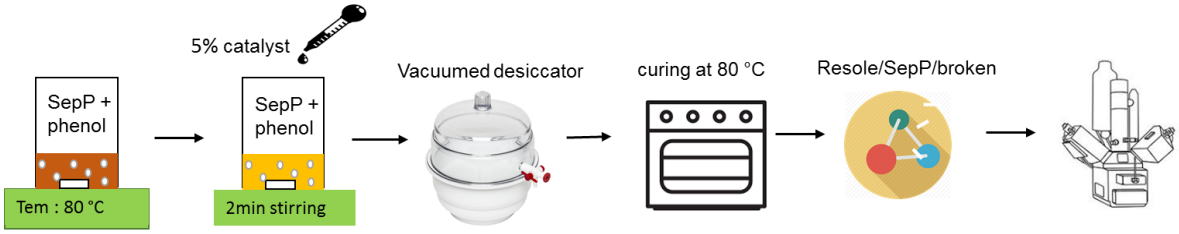

Figure 3.8. SepP-phenolic nanocomposite – Method 3

The results of the above three methods will be discussed in Chapter 4.

3.8. Dispersion of Sep/SepP in the phenolic resin nanocomposite with three roll mills

3.8.1. Three roll mills adjustments

The 50 g mixture of SepP (5%) and phenol have been prepared. Seven samples were tested under different speeds and roller spaces of three roll mills for 10 min. The

speeds of 50, 70, and 90 are considered. Also, front, and back roller spaces were changed to find an appropriate space. The back roller mainly controls the dispersion of nanoparticles in the phenol. Table 3.1 shows the different scenarios. Samples taken from each configuration are observed with microscope Leica DMC2900. They will be discussed in Chapter 4.

Table 3.1. Adjustments of three roll mill for dispersion analysis

Sample no	Front roller	Back roller	Speed	Time sample was taken (min)
1	3	4	70	10, 15
2	1	4	70	10
3	1	3	70	10
4	1	3	90	5, 10
5	1	3	50	10
6	1	2	70	5, 10
7	1	1	70	5, 10

After adjusting the front and back roller, and speed of three roll mill instrument, it is time to start the process of Sep/SepP dispersion in the phenolic resin.

3.8.2. Dispersion analysis of Sep/SepP in the phenolic resin

Five samples of Sep/SepP phenolic resin (50 g) with different compositions have been prepared for morphological characterisation as is shown in Table 3.2.

Table 3.2. Composition of samples

No	Samples	Sep/SepP	APP	Aerosil
1	SepP +PR	5%		
2	SepP +APP + PR	5%	5%	
3	Sep +PR	5%		
4	Sep +APP+PR	5%	5%	
5	Sep + APP + Aerosil + PR	5%	5%	1%

APP, ammonium polyphosphate flame retardant; PR, phenolic resin

Moreover, two more Samples (6, 7) have been prepared composed of Sep, APP, acetone, and PR. The reason for making these two samples was to study the dispersion

of sepiolite fibres and viscosity of the nanocomposite with the presence of acetone. Table 3.3 shows the composition of Samples 6 and 7.

Table 3.3. Composition of samples

No	Samples	Sep	APP
6	Sep +APP+ PR + Acetone	10%	10%
7	Sep +APP+ PR + Acetone	10%	10%

Preparation of Samples 1-5: Sep/SepP, APP, and Aerosil added to the phenol, mixed with three roll mill instrument for 10 min, followed by adding 5% of catalyst, stirring until the colour stabilised. Then vacuum pump the samples for 30 min at room temperature to remove air bubbles. After that, a 1 mm thickness of the sample is taken and cured in an oven at 80° C for an hour. Figure 3.9 shows the procedure.

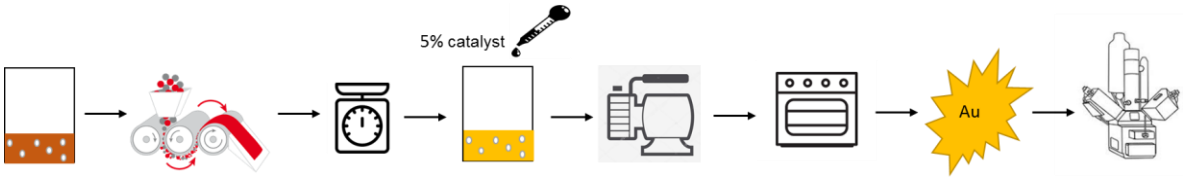

Figure 3.9. Preparation of Samples 1-5

Cured samples are prepared in two ways for SEM/HIM characterisation. In the first method, samples were crushed, followed by gold coating. In the second method, samples were prepared in epoxy in a cylindrical shape and cured at room temperature. Then samples were polished to a diameter of 12 mm and a height of 6 mm to be appropriate for HIM analysis. Figure 3.10 shows the preparation of samples.

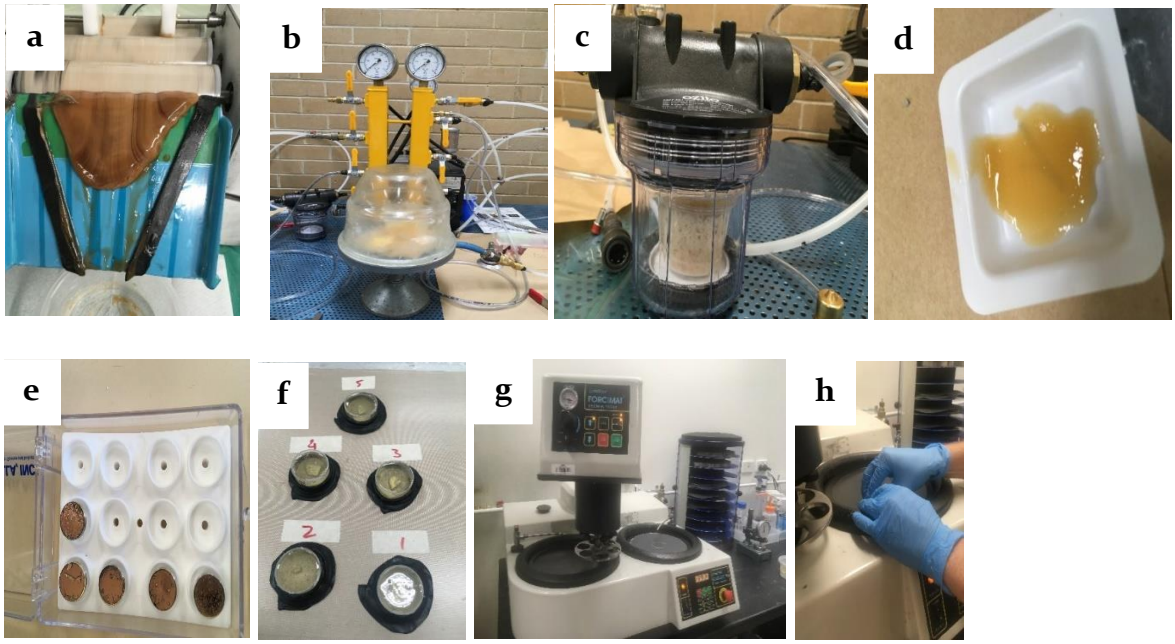

Figure 3.10: a) Mixing materials with three roll mill; b. c) samples in the vacuum pump; d) prepared sample, Method 1; e) gold-coated samples; f) preparing samples, Method 2; g) polishing instrument; h) polishing samples in Method 2

Preparation of Sample 6: 10% of Sep mixed with acetone, followed by adding phenol, and APP. The sample is weighted, then, put in the oven at 30° C overnight to evaporate acetone. The day after, the sample is vacuum pumped several times (each time half an hour) to remove the remaining acetone. Catalyst is added, followed by an extra half an hour in a vacuum pump, and curing in the oven for an hour at 80° C.

Preparation of Sample 7: Sep, APP, phenol, and acetone are mixed, putt in the oven at 30° C overnight to evaporate acetone, followed by several times vacuum pumping. Then materials are mixed with mechanical mixing for 10 min with a speed of 650 rpm, adding a catalyst, putting in vacuum pump for 30 min. Then cured in an oven at 80° C for an hour.

The morphological characterisation of samples is carried out and will be discussed in Chapter 4.

3.9. Fabricating of 3D GFRP nanocomposite samples

3D GFRP nanocomposite was fabricated with 5% and 10% of Sep and SepP, 5%, 10%, and 15% of APP, 95% of phenol, 5% of catalyst, and parabeam®3D woven E-glass fabric. The phenol with viscosity 180-270 cPs, pH: 7-8, and water content 14-16%, and a catalyst with viscosity 150-350 cP and water content 20-28% were used in this study. Table 3.4 shows the 3D GFRP nanocomposite samples composition.

Table 3.4. Composition of 3D GFRP phenolic composite samples

Samples	Composition	Sep (%)	SepP (%)	APP (%)	P (%)	C (%)
1	Sep (0%) + APP(0%) +PR (100%)	0	0	0	95	5
2	Sep (0%) + APP(5%) +PR (100%)	0	0	5	95	5
3	Sep (0%) + APP(10%) +PR (100%)	0	0	10	95	5
4	Sep (0%) + APP(15%) +PR (100%)	0	0	15	95	5
S5	Sep (5%) + APP(5%) +PR (100%)	5	0	5	95	5
S6	Sep (5%) + APP(10%) +PR (100%)	5	0	10	95	5
S7	Sep (5%) + APP(15%) +PR (100%)	5	0	15	95	5
S8	Sep (10%) + APP(5%) +PR (100%)	10	0	5	95	5
S9	Sep (10%)+ APP(10%) +PR (100%)	10	0	10	95	5
SP5	SepP (5%) + APP(5%) +PR (100%)	0	5	5	95	5
SP6	SepP (5%) + APP(10%) +PR (100%)	0	5	10	95	5
SP7	SepP (5%) + APP(15%) +PR (100%)	0	5	15	95	5
SP8	SepP (10%) + APP(5%) +PR (100%)	0	10	5	95	5
SP9	SepP (10%) + APP(10%) +PR (100%)	0	10	10	95	5

Sep: sepiolite, SepP: sepiolite-phosphate, APP: ammonium polyphosphate, P: phenol, C: catalyst, PR: phenolic resin

Sample 1, which is neat phenolic resin, was made by stirring phenol with catalyst until a stabilised colour. Then it was vacuum pumped at room temperature for 20 min. A small amount was taken for characterisation and cured in an oven at a temperature of 80° C for an hour. The rest of the material is used for making 3D GFRP composite.

Samples 2, 3, and 4 were prepared as follows: adding APP into the phenol, followed by 10 min mechanical mixing with the speed of 463 rpm, adding a catalyst and stirred

until reaching a stabilised colour, then putting in the vacuum pump for 20 min. A small amount of resin was taken for characterisation and cured in an oven at a temperature of 80° C for an hour. The rest of the material is used for making 3D GFRP nanocomposite. Figure 3.11 shows the process.

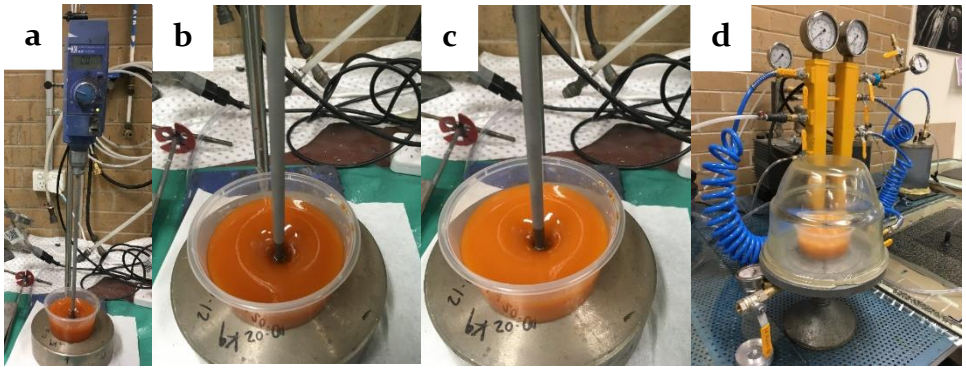

Figure 3.11. Making nanocomposite Samples 2-4: a) mechanical mixing; b) starting mechanical mixing; c) after a few minutes of mixing (brighter colour); d) vacuumed pumping

Preparation of Samples 5 to 14: firstly, phenol was weighted, followed by adding Sep/SepP, and APP flame retardant, followed by mixing materials with three roll mill instrument for 10 min (depends on the viscosity of the solution 2-4 run). Then the solution weighted, and added catalyst and stirred until the colour stabilises, followed by 20 min vacuum pumped to remove air bubbles. The prepared resin was used for making 3D GFRP nanocomposite. 3D fibreglass fabrics were cut to the required dimensions (450 mm x 350 mm x 8 mm, and 380 mm x 250 mm x 8 mm) with the Pathfinder cutting machine. Figure 3.12 shows the cutting machine.

Figure 3.12. Cutting 3D fibreglass fabrics

For the fabrication of 3D GFRP nanocomposite, apply 40% of the prepared resin on a cleaned plate, followed by putting the 3D fiberglass on the resin and roll until the fibres absorb all resin, then apply the rest of the resin and roll until a homogenous composite panel is obtained and make sure all glass fibres absorbed enough resin. The prepared composites are cured in the oven at a temperature of 80° C for 2 hours and cut with a water-cooled diamond blade to samples 200 × 25 mm for tensile test and 100 × 100 mm for cone calorimeter test. Figure 3.13 shows the fabrication of 3D GFRP samples.

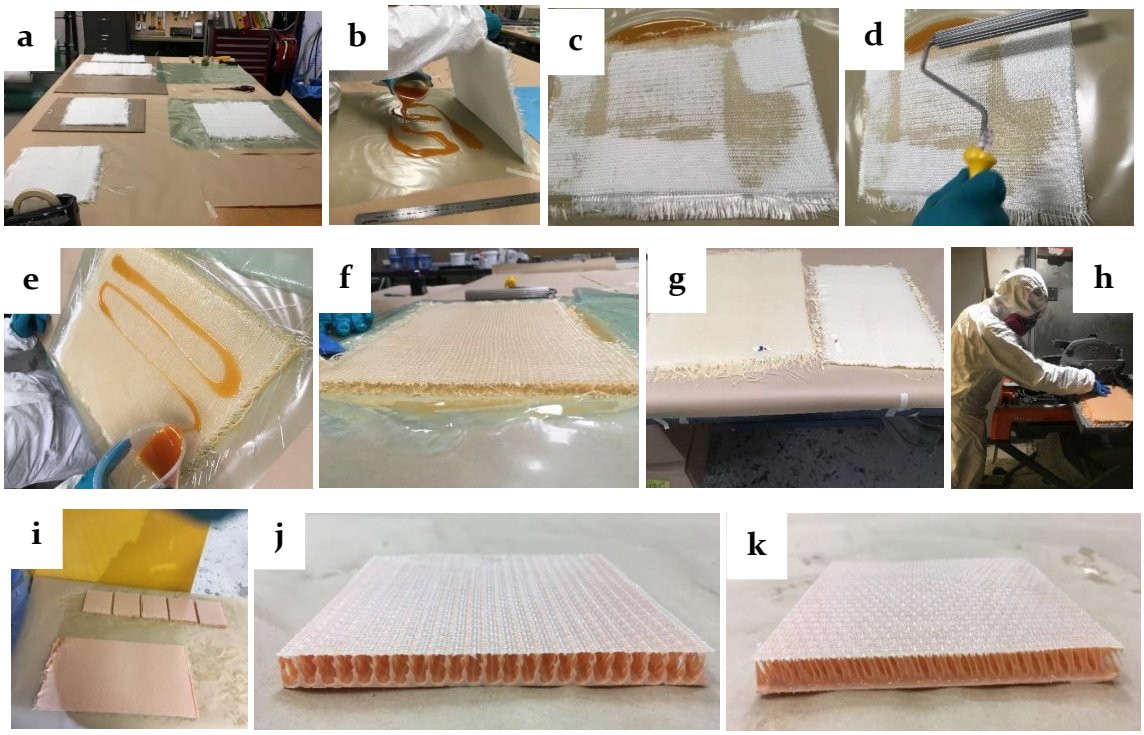

Figure 3.13. Fabrication of 3D GFRP nanocomposite: a) preparation of 3D glass fabrics; b) applying 40% of resin; c) putting glass fabrics on the resin; d) rolling the composite on the front and back face; e) applying the rest of resin and rolling; f) prepared composites; g) cured composites; h) cutting samples; i) cut samples; j) warp direction; k) weft direction

3.10. Morphological characterisation of Sep/SepP phenolic nanocomposite

Sep/SepP nanocomposite samples prepared for fabricating 3D GFRP nanocomposite have been observed with helium ion microscope (HIM- Zeiss Orion NanoFab) to study

the characterisation of nanocomposites. After curing, samples were crushed, to be observed with HIM. Table 3.5 shows sample compositions. HIM micrographs of Samples 1-14 will be discussed in Chapter 4.

Table 3.5. Sep/SepP phenolic nanocomposite compositions

No.	Sample's name	Sep (%)	SepP (%)	APP (%)	PR (%)
1	1	0	0	0	100
2	2	0	0	5	100
3	3	0	0	10	100
4	4	0	0	15	100
5	S5	5	0	5	100
6	S6	5	0	10	100
7	S7	5	0	15	100
8	S8	10	0	5	100
9	S9	10	0	10	100
10	SP5	0	5	5	100
11	SP6	0	5	10	100
12	SP7	0	5	15	100
13	SP8	0	10	5	100
14	SP9	0	10	10	100

3.11. 3D GFRP morphological characterisation with SEM

Morphological characterisations of 3D GFRP nanocomposites before performing the cone calorimeter test have been studied with SEM. Figure 3.14 shows a 3D GFRP nanocomposite structure, and the SEM micrograph of samples from the top, middle, and bottom surface will be discussed in Chapter 4.

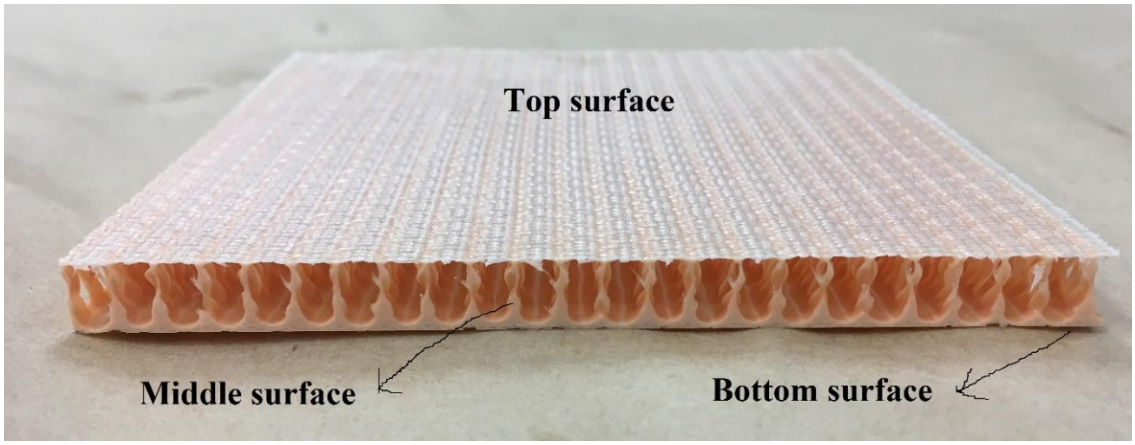

Figure 3.14. 3D GFRP nanocomposite structure

3.12. Thermogravimetric analysis of Sep/SepP phenolic composite

TGA can be used to examine the thermal stability and decomposition behaviours of the resins. Sep/SepP nanocomposite samples have been thermally characterised to study the thermal behaviour of the material. The thermal decomposition temperature of each sample of Sep/SepP phenolic nanocomposite was examined with PerkinElmer, TGA 8000 following a heating rate of 5 ^{o}C/min over the temperature range 30-850^{o} C under argon gas. The results will be discussed in Chapter 4.

3.13. Fire behaviour of 3D GFRP composite with cone calorimeter test

The cone calorimeter test [6] was built-up systematically to focus on the properties of materials [7] rather than to relate to a special full-scale scenario of an actual fire. A cone calorimeter can be used for comparing and ranking the fire reaction of materials. Hence, it plays an important role in the research and development of fire retardant polymeric materials [8]. The test approach is utilised to asses the ignitability, heat release rates, effective heat of combustion, mass loss rates, and smoke release of materials [2].

The cone calorimeter instrument used in this research is in accordance with ASTM E1345, ISO 5660, and AS/NZ 3837. The test was conducted in the CSIRO, Clayton, VIC. Specimens with dimensions of 100 mm by 100 mm with a thickness of 8 mm were exposed to a uniform heat flux of 50 kW/m^2 in the horizontal orientation. Figure 3.15 shows the cone calorimeter instrument and sample preparation.

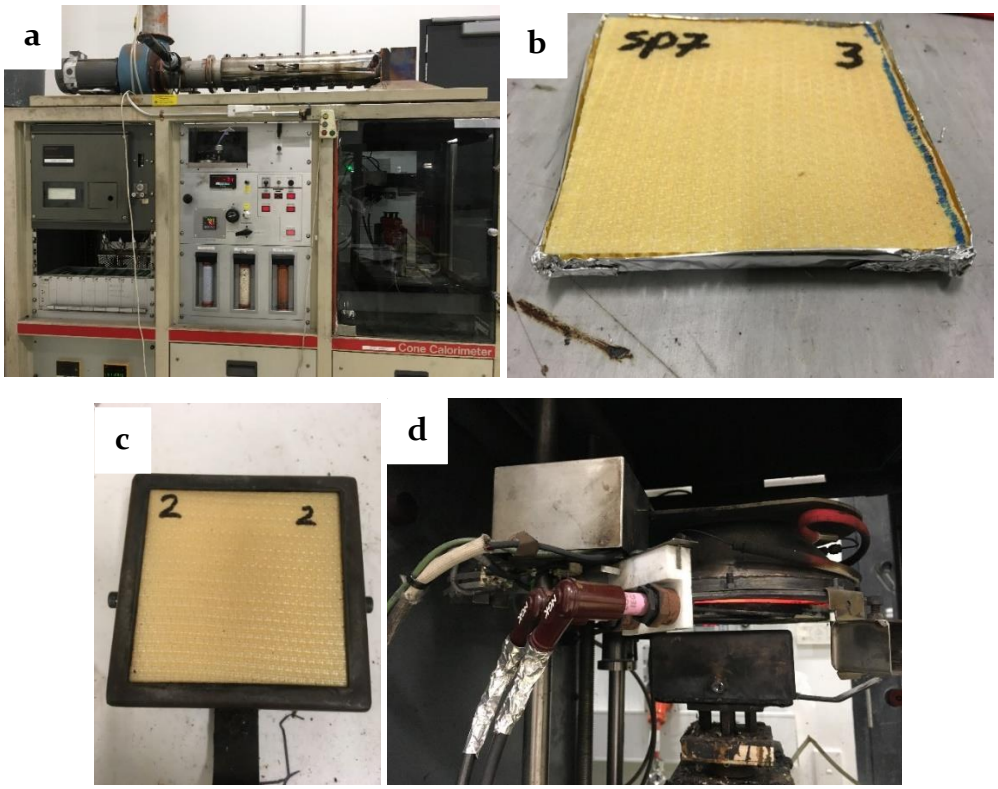

Figure 3.15: a) Cone calorimeter instrument at CSIRO; b) specimen's bottom surface and sides covered with aluminium foil; c) specimen holder; d) a sample is placed in the cone machine

3.14. Analytical approach to predict the full-scale façade fire classification criteria

The evaluation of the fire performance of a façade relies on the determination of the flame and smoke release and the possible damage. By experimentation, these criteria can be assessed in accordance with standard façade test techniques. Those tests would determine the temperature and flame height to give a holistic idea into how a certain

façade assembly will work under fire. In the NCC, Section C, which deals with fire performance requirements, fire propagation testing (AS 5113:2016) needs to be conducted to investigate wall assemblies (façade system materials) working well together and preventing the fire spread within a building and to the adjacent buildings. The importance of full façade fire test is also mentioned in other standards and codes such as the New Zealand building code [9], the UK building regulations and Approved Document B [10], Nordic countries and Europe [11], The USA International building code (IBC) [12], The National Fire Code of Canada [13], United Arab Emirates [14], and China and Japan [15]. However, since the performing of experimental full-scale façade fire tests with new cladding material is costly and such facilities are not available, it has not been carried out in this thesis. Instead, an analytical approach is developed to meet the full-façade fire test (AS 5113:2016) cladding classifications criteria with 3D GFRP nanocomposite cladding based on the cone calorimeter test results and the CSR full-scale façade fire test (AS 5113) with steel cladding material. The method is thoroughly discussed in Chapter 5.

3.15. Tensile properties of 3D GFRP composite

3.15.1. Preparation of samples for tensile test

3D GFRP nanocomposite samples were cut parallel to the warp direction of 3D fabric with water-cooled diamond blade (to avoid edge notches, undercuts, rough or uneven surfaces, or delamination) to 200 mm x 25 mm x 8 mm dimensions. Then specimens were measured with a micrometre at three places and the average were considered with a tolerance of ±1% of width and ±4% of thickness according to ASTM D3039 [3]. Since the 3D GFRP composite has a hollow core 3D structure, to avoid the gripping failure all samples were injected with filler (epoxy resin + 3% low-density fairing filler)

through thickness, 40 mm from both ends of specimens (gripping area). Filled specimens rest at room temperature for a few hours to cure, then are stored in the tensile test room until the test time. Figure 3.16 shows filled specimens and tensile instrument at RMIT University's Materials Testing Laboratory.

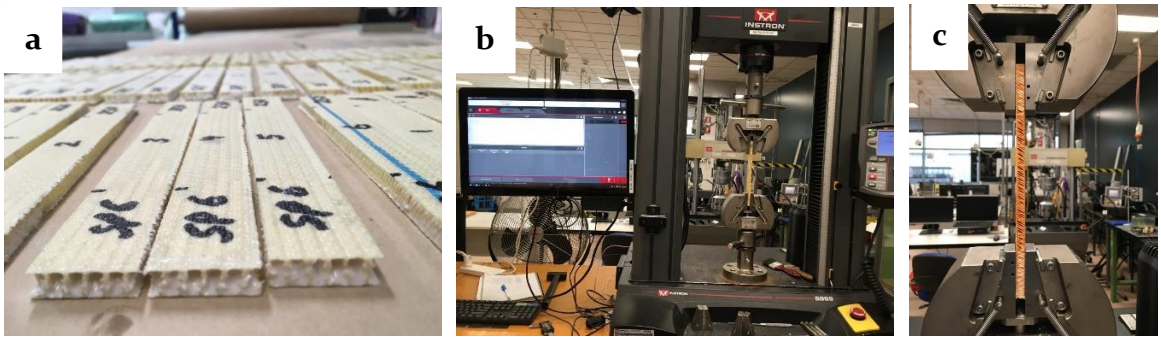

Figure 3.16. a) Filling through-thickness of samples 40mm from two ends (gripping area); b) INSTRON 50KN; c) placing the sample into grips

3.15.2. Experimental procedure

At least five samples were tested to failure for each composition under the same condition and the average reported. Each sample dimension has been measured accurately which was 200 mm x 25 mm x 8 mm. A tensile test has been conducted with INSTRON 50 KN at ambient temperature at the RMIT lab. Each specimen is mounted in the grips of the tensile testing machine with appropriate alignment and uniformly loaded in tension whilst recording the force versus displacement until failure. The ultimate strength of the material is calculated from the maximum force carried before failure as is shown in Equation 3.1.

$$F^{tu} = \frac{P^{max}}{A} \qquad \text{Equation (3.1)}$$

F^{tu} = ultimate tensile strength, MPa
P^{max} = maximum force before failure, N

A= cross-sectional area of the specimen

Figure 3.17 shows the cross-sectional area of the composite. The thickness of face sheets was about 0.60 mm and the average distance between neighbouring piles was 3.73 mm and 6.8 mm in weft and warp directions, respectively. The piles have an average diameter of 0.70 mm and roughly 86 degrees of stretching [16]. The A, the cross-sectional area, is calculated based on the glass fibre plies and hollow-core area deducted as is shown in Figure 3.17.

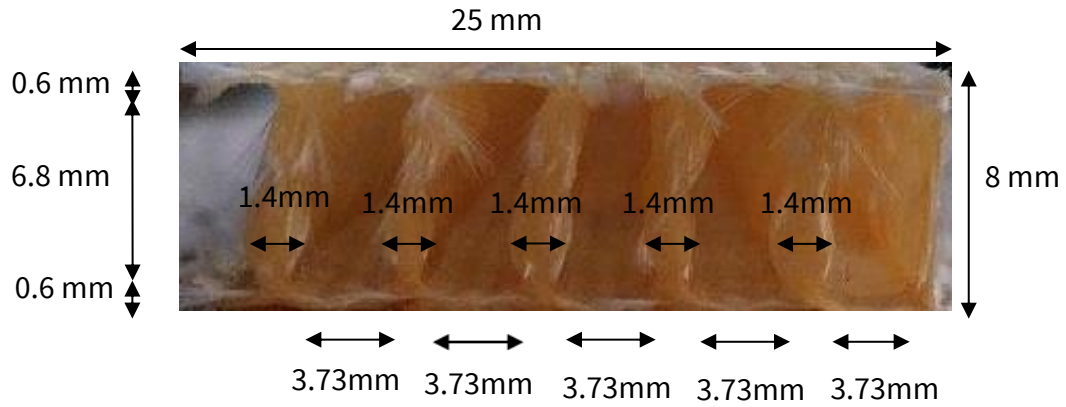

Figure 3.17. The cross-sectional area of samples

Due to the complex structure of the 3D GFRP nanocomposite, the modulus of elasticity is calculated from Equation 3.2 (ASTM D3039 [3]) and Figure 3.18 for the elastic part of the stress-strain curve for each specimen separately. The average of five specimens for each composition was reported as modulus of elasticity [3].

$$E = \frac{\Delta\sigma}{\Delta\varepsilon} \qquad \text{Equation (3.2)}$$

E= tensile modulus of elasticity, GPa
Δσ = difference in applied tensile stress between the two strain points, MPa
Δ£ = difference between the two strain points

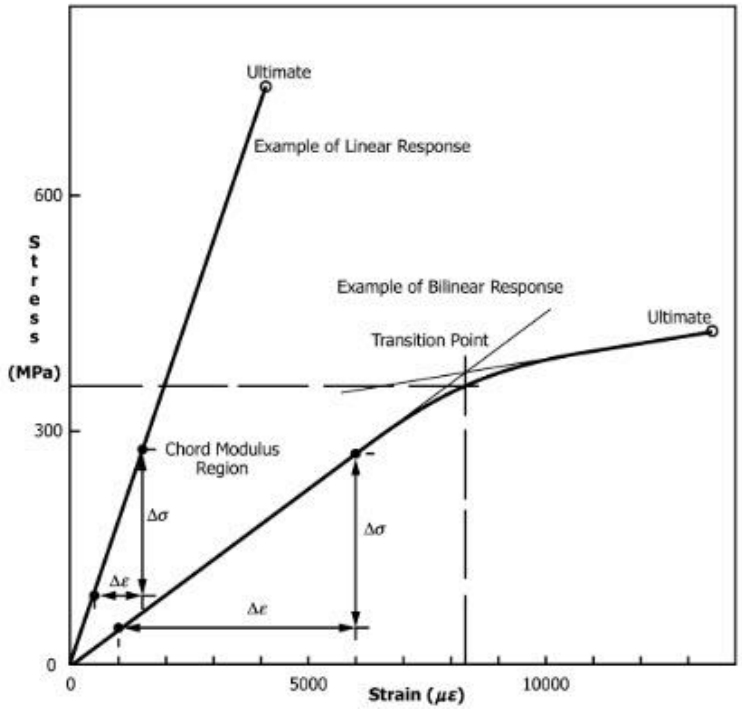

Figure 3.18. Typical tensile stress-strain curves [3]

3.16. Chapter summary

This chapter described the methods of the thesis step by step from the synthesising of SepP nanoparticles to be used in the 3D GFRP phenolic nanocomposite to the prediction of full-scale façade fire test criteria. A detailed procedure of the methods is as follows: making SepP nanoparticles in the lab and conducting thermal, morphological, and structural characterisation, studying dispersion analysis of SepP-phenolic nanocomposite and phenolic resin curing with different methods, dispersion analysis of Sep/SepP phenolic resin nanocomposite with three roll mill, fabrication of 3D GFRP phenolic composite as a new cladding and morphological characterisation of it, thermogravimetric analysis of Sep/SepP phenolic composite, studying of fire properties of 3D GFRP nanocomposite with cone calorimeter test, analytical approach to predict the cladding material behaviour in the full-scale façade test, and studying of tensile properties of 3D GFRP nanocomposite. Results and discussions of each method

will be discussed in the following Chapters 4, 5, and 6, respectively. In the next chapter, synthesis of SepP, dispersion analysis of Sep/SepP phenolic composite, microstructural analysis of materials, and fabrication of 3D GFRP nanocomposite will be discussed.

3.17. References

[1] Palacios E, Leret P, De La Mata MJ, Fernández JF, De Aza AH, Rodríguez MA et al. Self-Forming 3D Core–Shell Ceramic Nanostructures for Halogen-Free Flame Retardant Materials. ACS applied materials & interfaces; 2016;8:9462-71.
[2] AS/NZS 3837:1998. Method of test for heat and smoke release rates for materials and products using an oxygen consumption calorimeter; 2016.
[3] ASTM D3039. Standard test method for tensile properties of polymer matrix composite materials. ASTM International; 2008.
[4] Norouzi M, Zare Y, Kiany P. Nanoparticles as effective flame retardants for natural and synthetic textile polymers: application, mechanism, and optimization. Polymer Reviews; 2015;55:531-60.
[5] Ratna D. Handbook of thermoset resins: ISmithers Shawbury, UK; 2009.
[6] ASTM E1354-09. Standard test method for heat and visible smoke release rates for materials and products using an oxygen consumption calorimeter; 1999.
[7] Babrauskas V. Fire Test Methods for Evaluation of Fire-Retardant Efficacy in Polymeric materials. Chapter 3. Grand, A F and Wilkie, C A, Fire Retardancy of Polymeric Materials CRC Press, New York, USA; 2000.
[8] Schartel B, Bartholmai M, Knoll U. Some comments on the use of cone calorimeter data. Polymer degradation and stability; 2005;88:540-7.
[9] Ministry of Business, Innovation & Employment. Acceptable Solutions and Verification Methods: For New Zealand Building Code Clause B1 Structure; 2014. http://www.dbh.govt.nz/compliance-documents#C.
[10] HM Government. The Building Regulations 2010, Fire Safety Approved Document B; 2013. http://www.planningportal.gov.uk.
[11] Strömgren M, Albrektsson J, Johansson A, Almgren E. Comparative analysis of façade regulations in the Nordic countries. MATEC Web of Conferences: EDP Sciences; 2013. p. 01003.
[12] International Building Code (IBC). USA: International Code Council; 2012.
[13] NRC. National Fire Code of Canada (NFC) Ottawa, Ontario, Canada National Research Council Canada.; 2010.
[14] UAE Fire and Life Safety Code of Practice: Annexure. A.1.21. Fire stopping, exterior wall cladding and proofing systems United Arab Emirates: United Arab Emirates: General Headquarters of Civil Defence; 2013.
[15] Hokugo A, Hasemi Y, Hayashi Y, Yoshida M. Mechanism For The Upward Fire Spread Through Balconies Based On An Investigation And Experiments For A Multi-story Fire In High-riseapartment Building. Fire Safety Science. 2000;6:649-60.

[16] Hosseini SA, Sadighi M, Maleki Moghadam R. Low-velocity impact behavior of hollow core woven sandwich composite: Experimental and numerical study. Journal of Composite Materials. 2015;49:3285-95.

Chapter 4

Dispersion analysis of Sep/SepP phenolic nanocomposite, and fabrication of 3D GFRP nanocomposite

4.1. Introduction

SepP has been synthesised as explained in Chapter 3. Results of SepP characterisations are discussed in this chapter. Also, dispersion of Sep fibres and SepP nanoparticles in the phenolic resin was studied, as well as phenolic resin curing time and temperature. Then, Sep/SepP phenolic composite has been used to fabricate a 3D GFRP phenolic composite as a new cladding material. Also, morphological characterisation of Sep/SepP phenolic nanocomposite with and without 3D glass fabrics has been investigated to study the dispersion of nanoparticles and their sizes in the composite.

4.2. Thermal characterisation of Sep and SepP

Thermogravimetric analysis of SepP has been conducted as explained in Chapter 3, Section 3.4. Figure 4.1 shows the thermal behaviour of the Sep support and SepP composite.

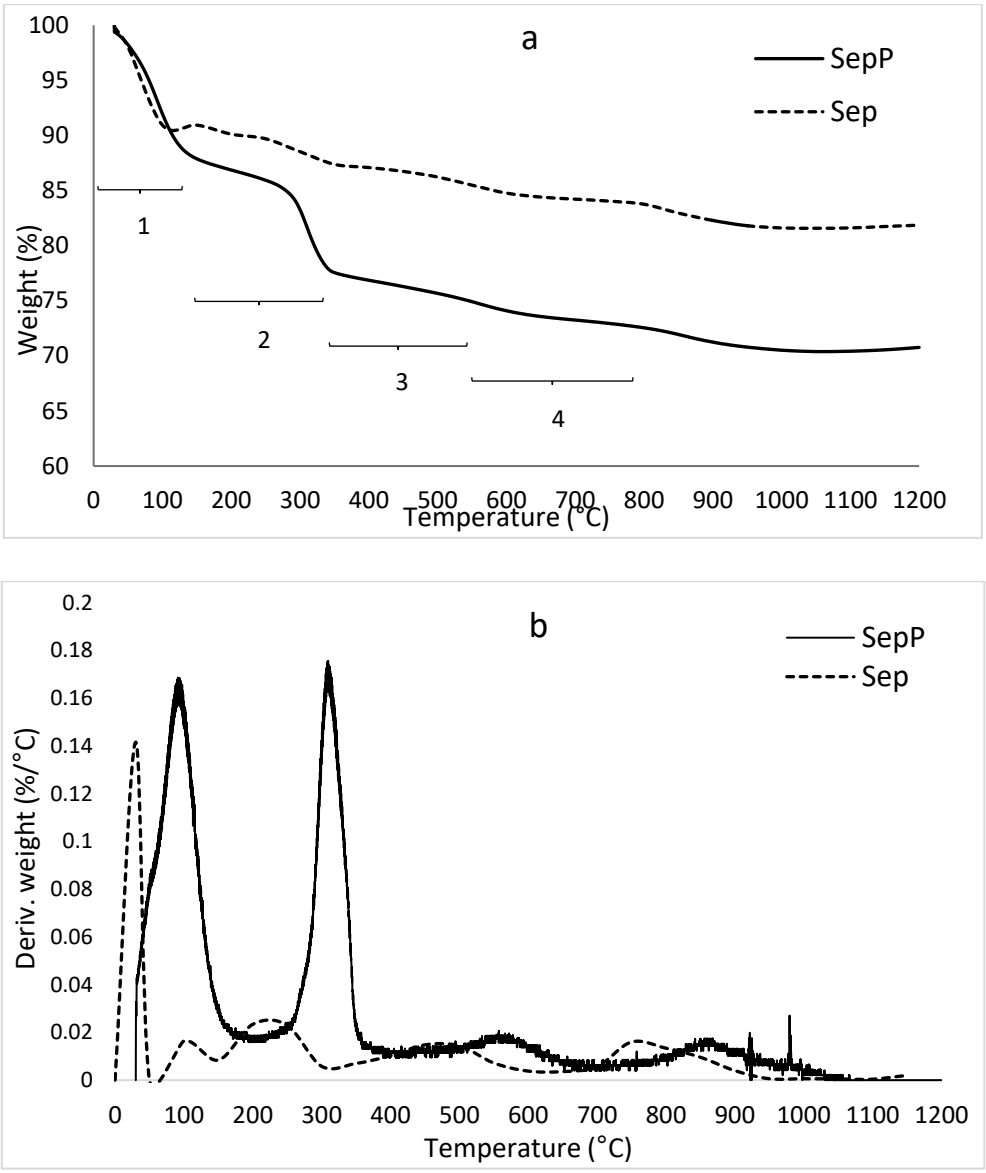

Figure 4.1. Thermal behaviour of Sep and SepP: a) TGA; b) DTA

From Figure 4.1a, numbers 1, 2, 3, and 4 represent four overlapping reactions at ~150 ° C, from 150° C to 350 ° C, from 350° C to 550 ° C, and from 550° C to 850 ° C, respectively. Point 1 shows the loss of adsorbed water, Point 2 corresponds to the loss of hydration water, Point 3 is related to the loss of co-ordination water, and Point 4 shows the sepiolite dihydroxylation process [1]. According to the TGAs, SepP has a steeper slope than Sep in the 100-250 and 250-350 ranges as is clear in the DTA curve as well (Figure 4.1b). The initial dehydration procedures are related to sepiolite and

phosphate and the next one is due to sepiolite dehydration and phosphate condensation.

4.3. Morphological characterisation of sepiolite-phosphate (SepP)

To observe the dispersion form of the phosphate on the sepiolite fibres, helium ion microscopy (HIM) characterisation has been conducted on the SepP composite. A HIM micrograph of SepP composite is shown in Figure 4.2.

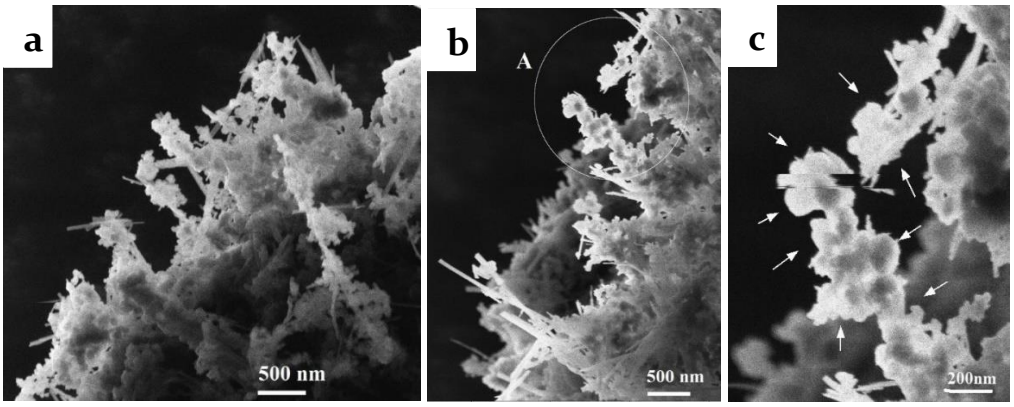

Figure 4.2. Micrograph of SepP composite: a, b) uniform distribution of phosphate nanoparticles on the surface of sepiolite fibres; c) section A at high resolution: sepiolite fibres are fully covered by P nanoparticles as is showed by arrows

From Figure 4.2, the phosphate particles covered the sepiolite fibres surface and distributed uniformly. Figure 4.2 shows the typical geometry of sepiolite fibres which are 15-50 nm in diameter. The micrograph shows that a uniform distribution of phosphate on the sepiolite fibres surface is a result of the direct precipitation process of aluminium phosphate on Sep nano fibres. To monitor the phosphate nanoparticles in detail, TEM and HRTEM micrographs are shown in Figures 4.3 and 4.4, respectively.

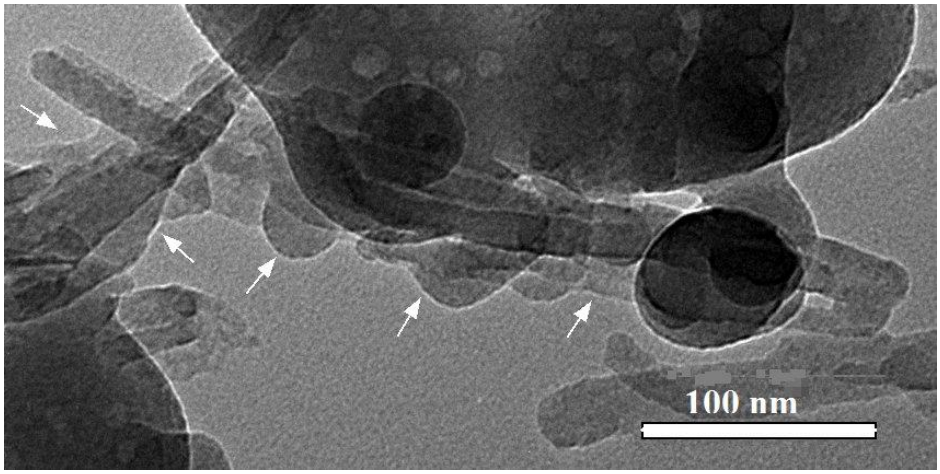

Figure 4.3. TEM micrograph of sepiolite fibre and phosphate coating on fibres surface

Figure 4.3 shows that sepiolite fibres are covered by phosphate nanoparticles with particle sizes of 40-80 nm. In addition, Figure 4.4a shows that phosphate nanoparticles are composed of primary nanoparticles with sizes below 20 nm as it is presented in Figure 4.4b.

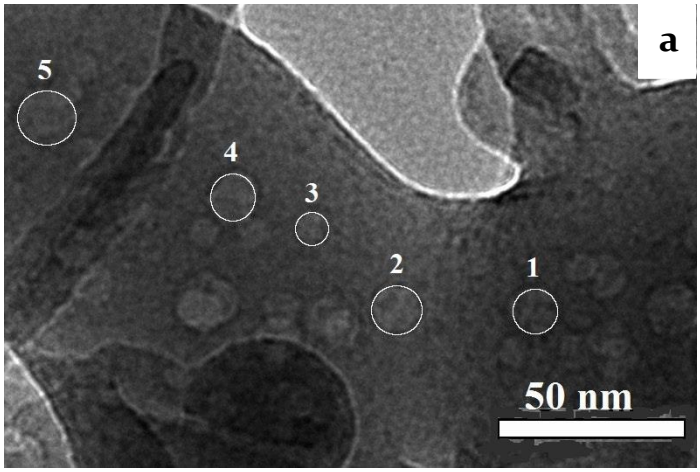

b

No	Diameter (nm)
1	12.242
2	13.281
3	8.307
4	12.122
5	15.64

Figure 4.4. a) HRTEM micrograph which shows phosphates are composed of spherical nanoparticles with diameter sizes between 8-20 nm; b) phosphate nanoparticles: diameter <20 nm.

TEM equipped with EDS has been carried out on the SepP from Figure 4.3 to find out the elemental composition of the SepP composite. The results have been shown in Figure 4.5, and Table 4.1.

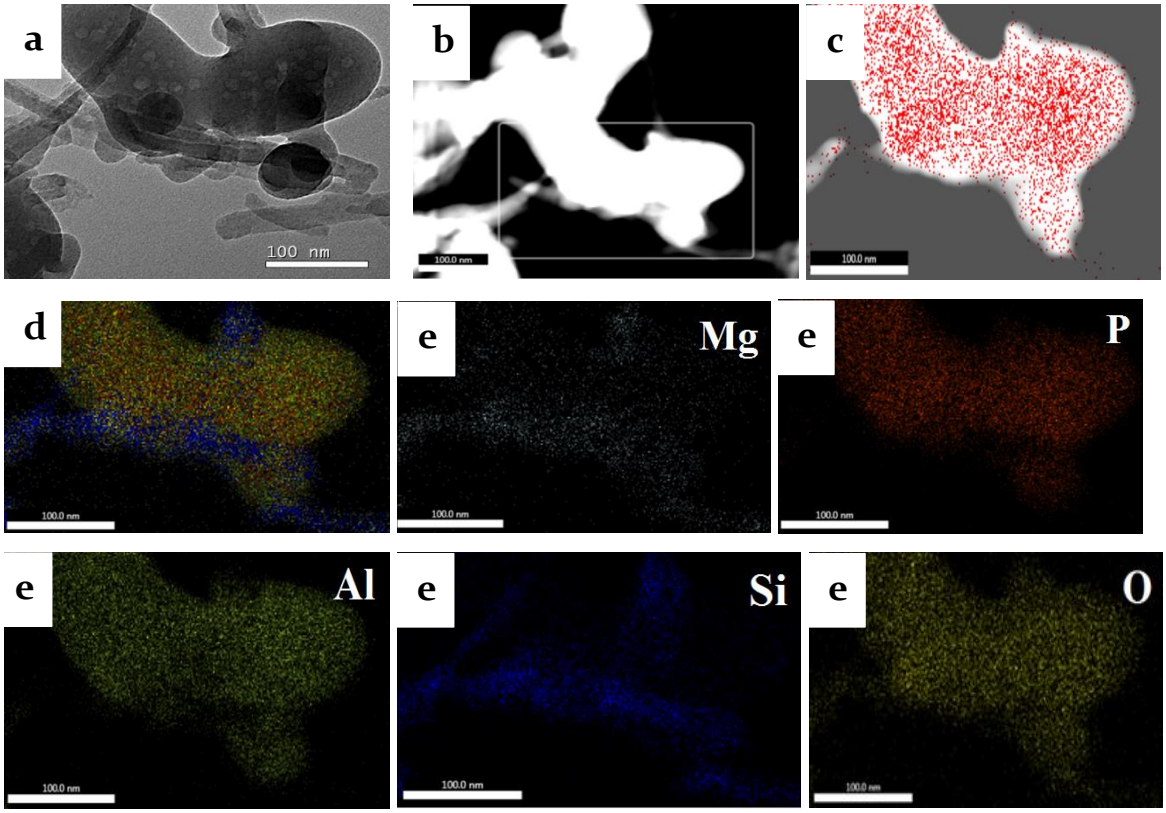

Figure 4.5. TEM-EDS images of SepP: a) TEM; b, c) EDS images; d, e) EDS mapping – elemental analysis.

Table 4.1. Elemental analysis of SepP nanoparticles: unallocated section

Element	Weight %	Atomic %	Net Int.	Net Error%
O	27.09	39.77	161.60	0.83
Mg	5.97	5.77	42.40	1.95
Al	25.16	21.90	201.10	0.79
Si	13.58	11.35	93.00	1.18
P	27.15	20.59	185.20	0.77
Ca	1.05	0.61	6.40	11.79

According to Figure 4.5 and Table 4.1, elemental analysis shows that both sepiolite elements and phosphate are available in the composite with different percentages.

4.4. Structural characterisation

An XRD characterisation has been done for Sep and SepP composite, examining the X-ray diffractograms to quantify the concentration of crystalline phases.

4.4.1. Phase identification

Table 4.2 and Figure 4.6 list the crystalline phases identified as the best match to the peaks in each sample and examples of the diffraction scans, respectively.

Table 4.2. Identified crystalline phases

Phase	Chemistry	ICDD PDF Number	Sample
Sepiolite	$Mg_4Si_6O_{15}(OH)_2.6H_2O$	00-013-0595	Sep and SepP
Illite	$Al_2Si_3AlO_{10}(OH)_2$	00-026-0911	Sep
Gibbsite	$Al(OH)_3$	01-070-2038	SepP

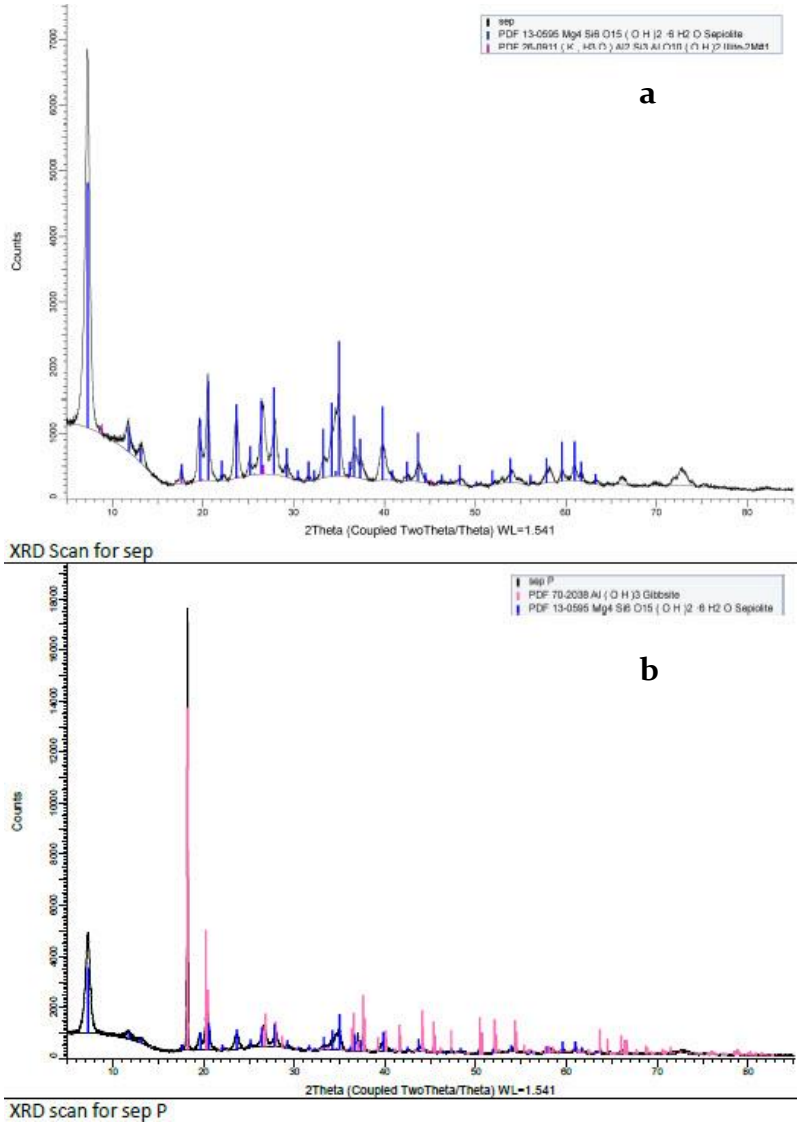

Figure 4.6. Examples of the diffraction scans: a) XRD scan for Sep; b) XRD scan for SepP

4.4.2. Crystalline phase quantification

Crystal structures for the recognised phases were taken from the ICDD PDF4+ 2018 archive and entered into Topas. The model factors were permitted to vary to provide the best match between the model and the measured data. Table 4.3 and Figure 4.7 show the diffraction refinement results for identified crystalline phases and examples of the diffraction refinement, respectively.

Table 4.3. Diffraction refinement results for identified crystalline phases

	Sep	SepP
Sepiolite	72%	65%
Illite	1%	
Gibbsite		6%
amorphous	27%	29%
Goodness of fit	2.48	3.03

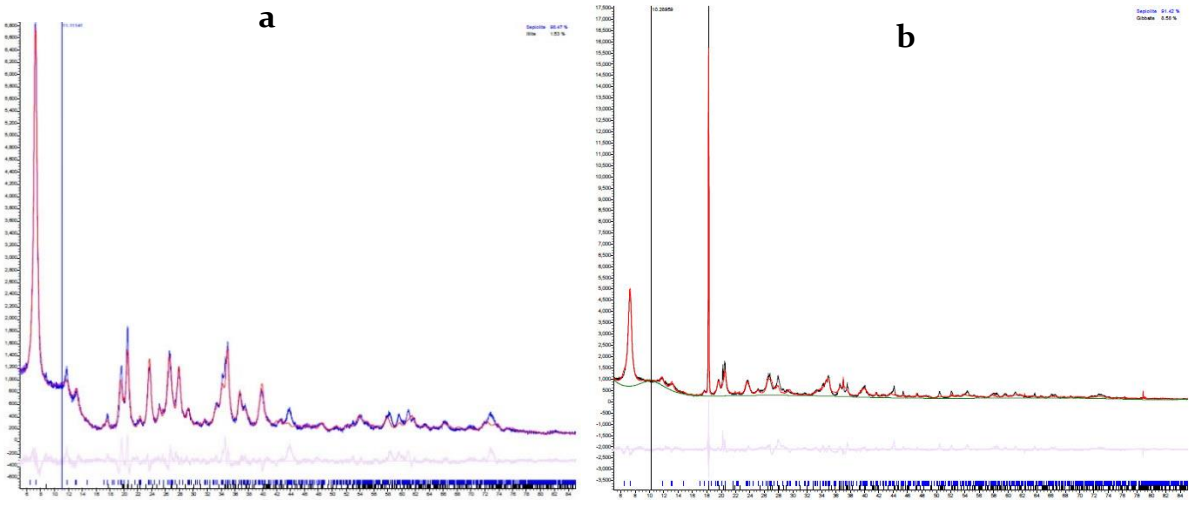

Figure 4.7. Examples of the diffraction refinement: a) XRD refinement of Sep; b) XRD refinement of SepP

The SepP sample crystallinity is lower than sepiolite even though no peaks of any phosphate are detected [2].

4.5. Morphological characterisation of phenolic resin

SEM produces a high-resolution image of a sample surface. Scanning electron microscopy (SEM-FEI Hitachi) analysis was conducted to understand the phenolic resin structure used in this research. A conductive coating of 20 nm of gold is used for analysis. The coating makes the phenolic resin surface conductive to prevent charging [3]. According to Figure 4.8 and further analysis of the micrograph with ImageJ software, there are micro voids on the phenolic resin surface with a diameter of less than 5 micrometres with an average diameter of 3.85 micrometres which are shown in Table 4.4.

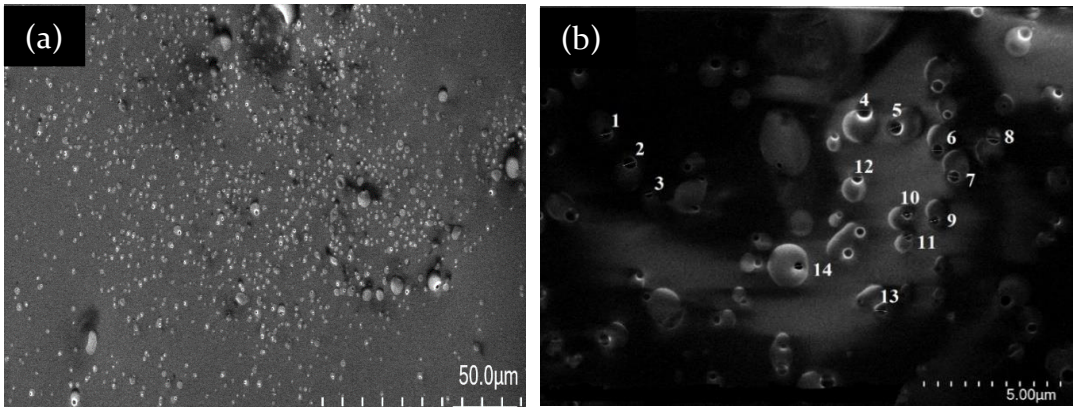

Figure 4.8: Phenolic resin structure: a) micro voids; b) micro voids diameter measurements which are less than 5 micrometres

Existence of micro voids is due to releasing by-product water molecules in the phenolic resin during polymerisation. Water vapour bubbles get trapped in the sample during curing and form macro and micro voids [4]. To reduce the number of defects and eliminate volatiles in the phenolic resin, accurate temperature control and gradual heating are needed [5]. However, this type of porosity may decrease the structural strength which is not our concern in this research because the proposed nanocomposite will be used as cladding material which is not load-bearing.

Table 4.4: Phenolic resin microvoids diameters

Voids	Area	Diameter (µm)
1	0.624	4.055
2	0.713	4.578
3	0.401	2.481
4	0.757	4.975
5	0.713	4.594
6	0.557	3.582
7	0.668	4.254
8	0.668	4.383
9	0.579	3.669
10	0.557	3.632
11	0.49	3.147
12	0.535	3.389
13	0.646	4.184
14	0.468	3.011
Mean	0.598	3.852

4.6. Studying of dispersion and curing of SepP-phenolic nanocomposite with three different methods

To study the phenolic resin (PR) curing process, and SepP dispersion in the resin, 2 g of SepP phenolic resin consisting of 5% of SepP, and 100% of PR, have been prepared and investigated in three different methods as explained in Chapter 3. Figures 4.9 and 4.10 show the cured sample and HIM micrograph of SepP-phenolic nanocomposite in Method 1, respectively.

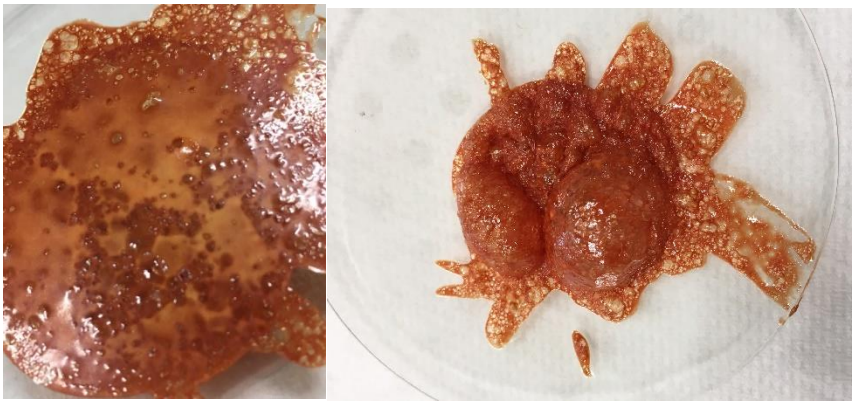

Figure 4.9. Cured sample – Method 1

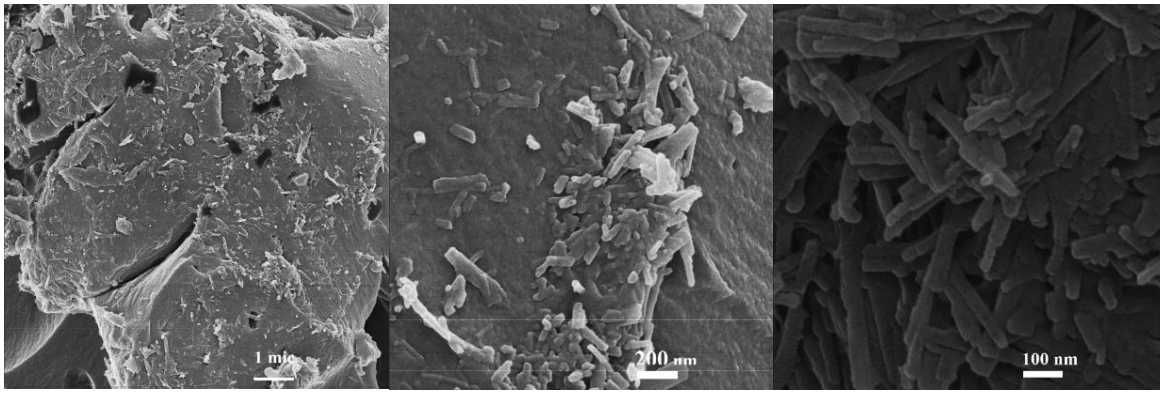

Figure 4.10. HIM micrograph of phenolic-SepP nanocomposite – Method 1

From Figure 4.9, there are macro and micro voids in the nanocomposite structure. Also, HIM micrographs in Figure 4.10 show the agglomeration of SepP nano powders in the resin. Moreover, it seems that phosphate coatings are removed from the surface of sepiolite fibres. Figures 4.11 and 4.12 show the cured sample and HIM micrograph of SepP-phenolic nanocomposite in Method 2, respectively.

Figure 4.11. Cured sample – Method 2

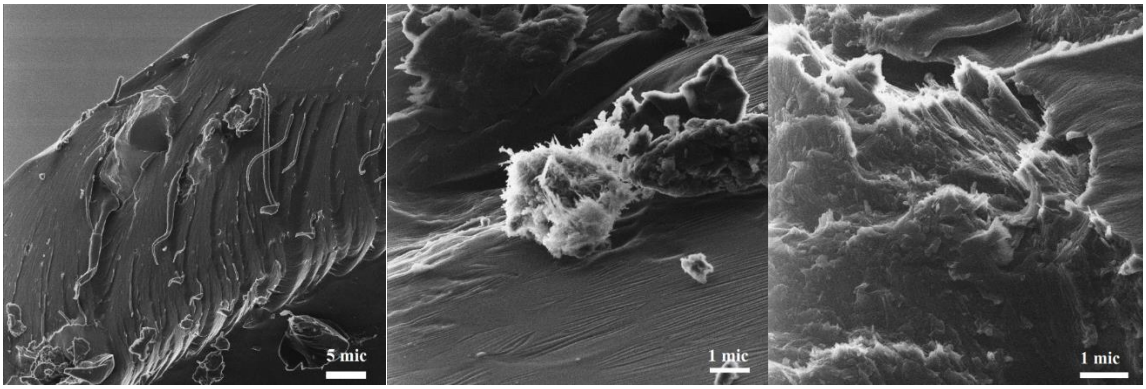

Figure 4.12. HIM micrograph of phenolic-SepP nanocomposite – Method 2

As can be seen in Figure 4.11, Macro and micro voids still exist in samples. The HIM micrograph of Figure 4.12 shows the agglomeration of SepP nanoparticles as well. Figures 4.13 and 4.14 show the cured sample and HIM micrograph of SepP-phenolic nanocomposite in Method 3 respectively.

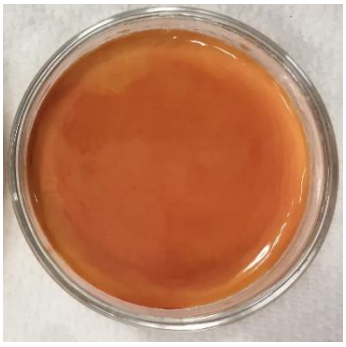

Figure 4.13. Cured sample – Method 3

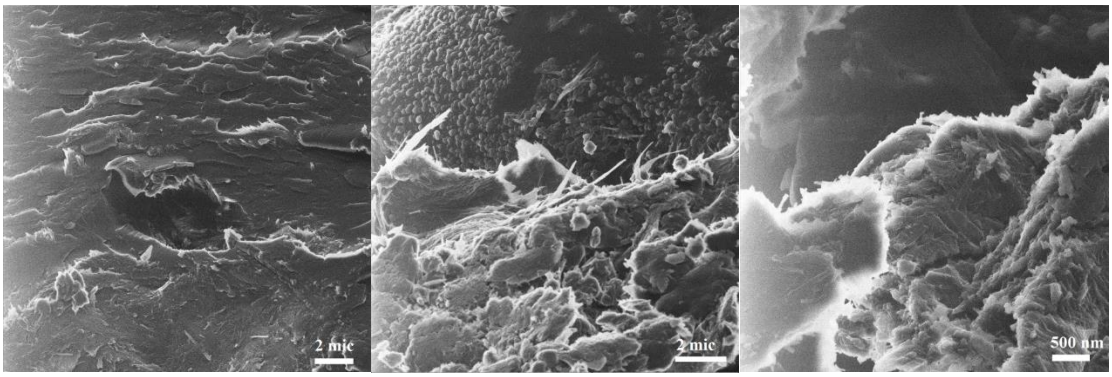

Figure 4.14. HIM micrograph of phenolic-SepP nanocomposite – Method 3

Figure 4.13 shows a very smooth and consistent structure of the nanocomposite. There have not been observed any micro voids in the nanocomposite. In terms of dispersion, HIM micrographs show the agglomeration of SepP in the resin in some sections.

The results of the above three different methods show that curing time and temperature of phenolic resin in Method 3 was appropriate to avoid air bubbles in the resin and have a void-free structure. The vacuum pump seems to be suitable for degassing the resin. However, it must be done at room temperature to obtain the desired structure. In terms of SepP nanoparticle dispersion in the phenolic resin,

magnetic stirring or sonication could not help as agglomeration happened in all three methods. Therefore, it seems that a high shear force instrument such as three roll mills is needed to disperse the SepP nanoparticles appropriately, which is studied in the next section.

4. 7. Dispersion of Sep/SepP in the phenolic resin with three roll mill instrument

4.7. 1. Three roll mills adjustments

To mix a Sep/SepP into the phenolic resin with a three roll mill machine, an appropriate adjustment of the instrument is needed. For this purpose, seven samples containing 5% SepP and 100% phenolic resin (about 50 g) have been prepared and tested under different roller spaces and speeds of three roll mills (Table 4.5) for 10 min as it is explained in Chapter 3. Then microscopic images have been taken which are shown in Figure 4.15.

Table 4.5. Adjustments of three roll mill for dispersion analysis

Sample no	Front roller	Back roller	Speed (m/s)	Time sample was taken (min)
1	3	4	70	10, 15
2	1	4	70	10
3	1	3	70	10
4	1	3	90	5, 10
5	1	3	50	10
6	1	2	70	5, 10
7	1	1	70	5, 10

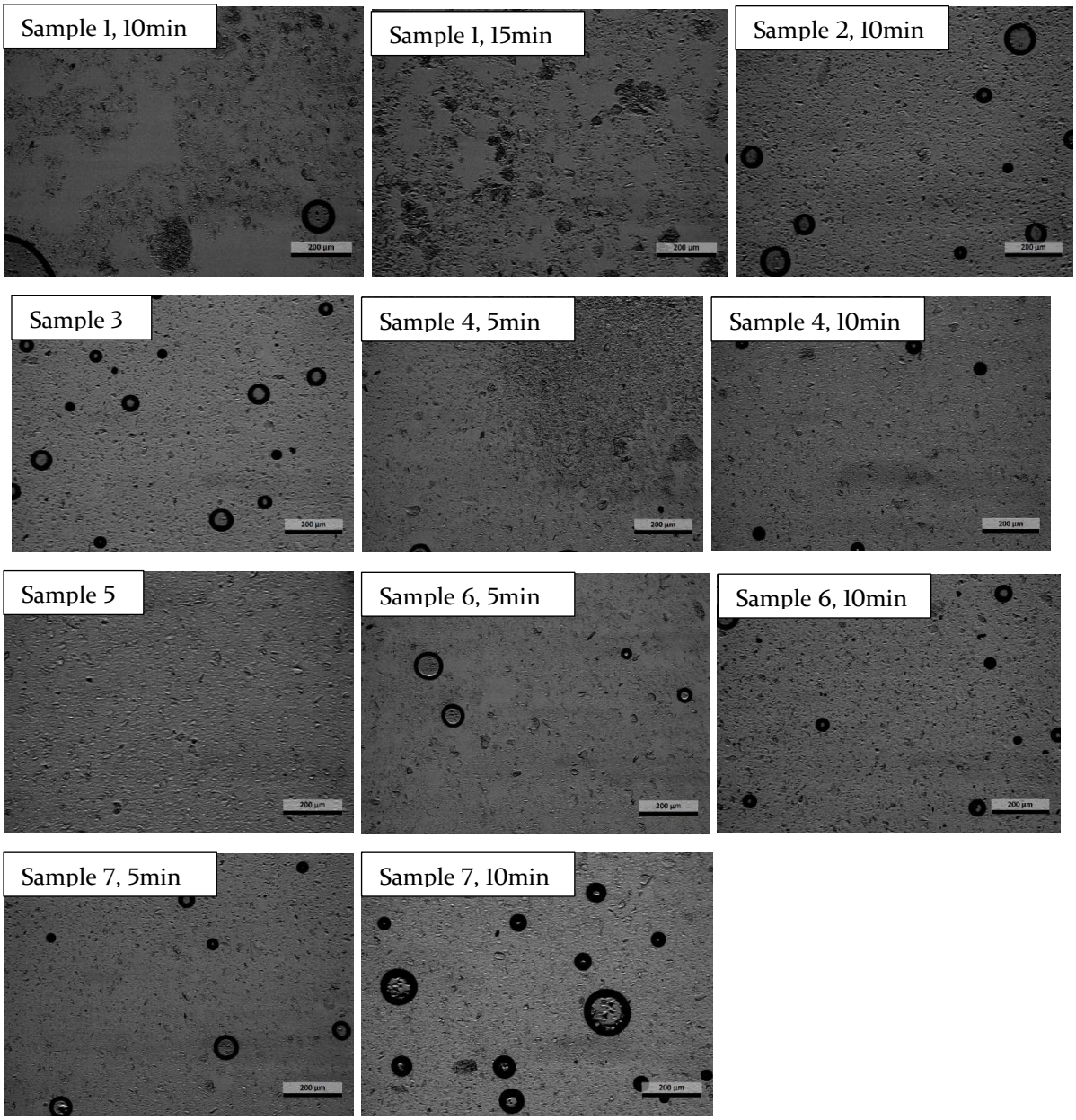

Figure 4.15. Microscopic image of Samples 1-7 from Table 4.5

As can be seen in Figure 4.15, Figures related to Samples 6 and 7 show better dispersion at 10 min. Hence, three roll mill adjustments for Sample 6, namely front and back rollers distance on 1 and 2, respectively, with a speed of 70, and 10 min time will be used for dispersion of Sep/SepP phenolic nanocomposite in this research.

4.7. 2. Dispersion analysis of Sep/SepP in the phenolic resin

Five samples of Sep/SepP phenolic resin (50 g) with different compositions have been prepared for morphological characterisation as is explained in Chapter 3. Samples 1-5 have been characterised by both SEM and HIM to observe the dispersion of the Sep/SepP in the nanocomposite. HIM has been conducted due to its better resolution at high magnification over SEM. Figure 4.16 (a-j) shows the micrograph of samples.

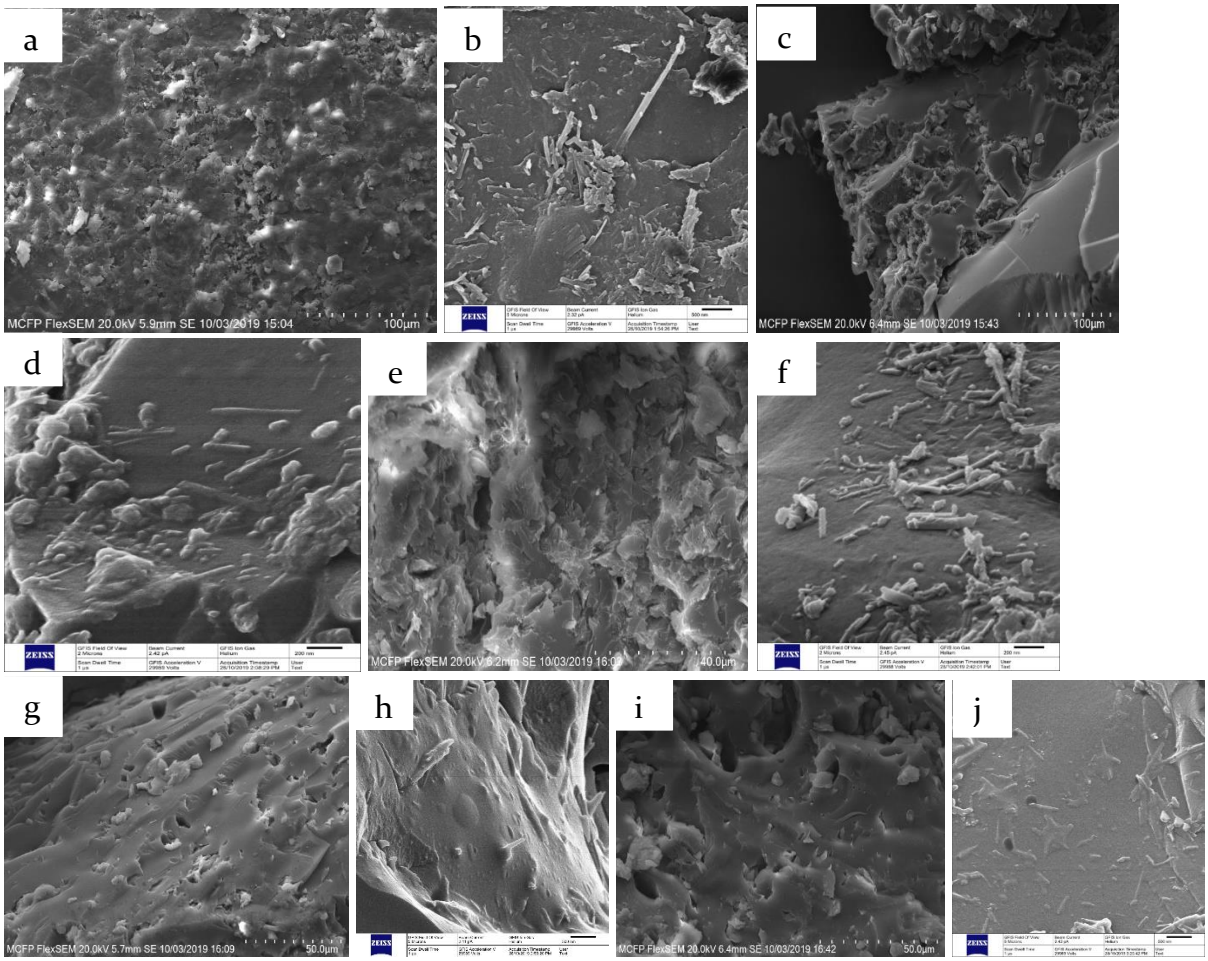

Figure 4.16. SEM and HIM micrographs of Samples 1-5: a) Sample 1 (SepP + PR)-SEM; b) Sample 1 (SepP+ PR)-HIM; c) Sample 2 (SepP+ APP + PR)-SEM; d) Sample 2 (SepP+ APP+PR)-HIM; e) Sample 3 (Sep +PR)-SEM; f) Sample 3 (Sep +PR)-HIM; g) Sample 4 (Sep+ APP+ PR)-SEM; h) Sample 4 (Sep+ APP+PR)-HIM; i) Sample 5(Sep+ APP+ Aerosil+ PR)-SEM; j) Sample 5(Sep+ APP+ Aerosil+ PR)-HIM

Figures 4.16(a, b) shows the SEM and HIM micrograph for Sample 1 (SepP + PR). SEM shows the dispersion of SepP nanoparticles in the phenolic resin on a 100 µm scale.

The image displays that SepP nanoparticles are sit in the phenolic resin voids and dispersed consistently. However, a closer look at the image with HIM (500 nm) showed a bit of agglomeration of SepP nanoparticles.

Figure 4.16(c, d) shows the micrograph of Sample 2. APP flame retardant can be seen in the SEM image, as a white chunk which sits mostly in the resin voids. HIM image at 200 nm displays the dispersion of SepP nano powders among APP chunks. Figure 4.16(e, f) shows sepiolite nano fibres dispersion in the phenolic resin. Sepiolite nano fibres dispersed very well as it clearly can be seen in the HIM image. Adding APP into the Sample 3 helped better dispersion of sepiolite nano fibres in the phenolic composite as is shown in Figure 4.16 (g, h). Also, a white chunk of APP sits in the phenolic resin micro voids. Adding a thixotropic agent (Aerosil R805) in Sample 5(i, j) helped the dispersion of sepiolite, decreased the viscosity of the sample significantly, and made the mixing easier. Figure 4.16(i, j) illustrates that sepiolite dispersed very well in the phenolic nanocomposite (HIM micrograph). However, during vacuum pumping of the sample, many air bubbles were observed which made the material splash out and lost as can be seen in Figure 4.17. Hence, using Aerosil R805 is not recommended with these materials.

Figure 4.17. Sample 5 (Sep + APP + Aerosil + PR)

Looking through the micrographs of Figure 4.16 shows the appropriate mixing method and adjustments of a three roll mill in terms of dispersion of Sep, and SepP nano powders. A HIM micrograph of prepared polished Samples 1-5 is shown in Figure 4.18.

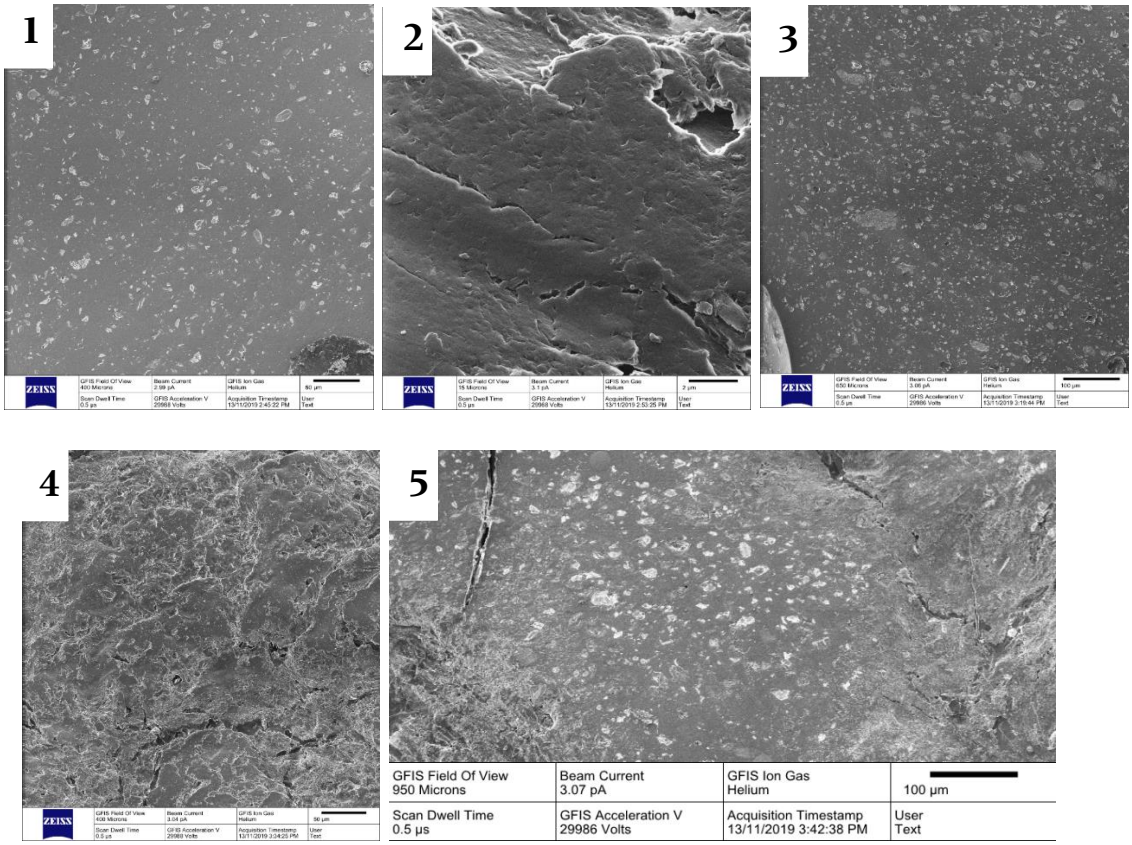

Figure 4.18. HIM micrograph of polished Samples 1-5

The dispersion of a bundle of nanoparticles can be seen in Figure 4.18. However, the dispersion of single nano powders has not been observed in the polished samples. Cured Samples 6 and 7 are shown in Figure 4.19.

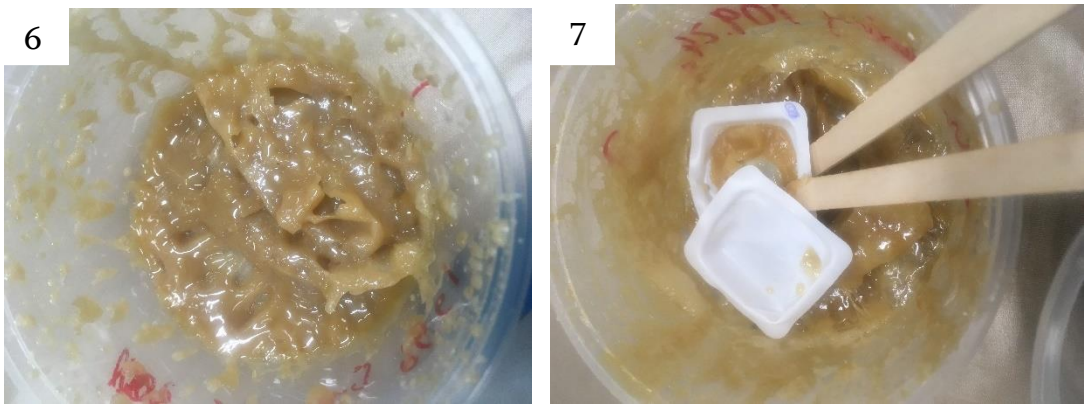

Figure 4.19. Cured Samples 6 and 7

As can be seen from Figure 4.19, acetone changed the structure of the nanocomposite and made a reaction with other materials. The samples did not cure properly, and a thin film has been observed on the top surface with a jelly material underneath. A HIM sample could not be taken from Sample 6 as it had a jelly structure. A small HIM sample was taken from Sample 7 for characterisation. A HIM micrograph of sample 7 has been displayed in Figure 4.20.

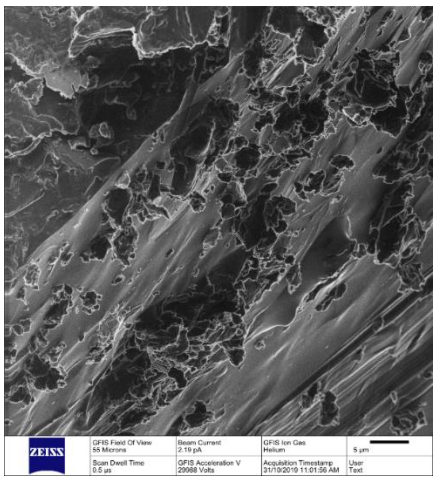

Figure 4.20. HIM micrograph of Sample 7

Figure 4.20 shows that acetone is not compatible with other materials since it changed the structure and texture of the nanocomposite as well as the agglomeration of sepiolite fibres.

4.8. Morphological characterisation of Sep/SepP phenolic composite

Sep/SepP phenolic composite samples prepared for fabricating 3D GFRP nanocomposite have been observed with a helium ion microscope (HIM- Zeiss Orion NanoFab) to study the characterisation of nanocomposites. Table 4.6 shows sample compositions. HIM micrographs of Samples 1-SP9 have been shown in Figure 4.21.

Table 4.6. Sep/SepP phenolic nanocomposite compositions

Sample's name	Compositions	Sep (%)	SepP (%)	APP (%)
1	Sep (0%) + APP (0%) + PR (100%)	0	0	0
2	Sep (0%) + APP (5%) + PR (100%)	0	0	5
3	Sep (0%) + APP (10%) + PR (100%)	0	0	10
4	Sep (0%) + APP (15%) + PR (100%)	0	0	15
S5	Sep (5%) + APP (5%) + PR (100%)	5	0	5
S6	Sep (5%) + APP (10%) + PR (100%)	5	0	10
S7	Sep (5%) + APP (15%) + PR (100%)	5	0	15
S8	Sep (10%) + APP (5%) + PR (100%)	10	0	5
S9	Sep (10%) + APP (10%) + PR (100%)	10	0	10
SP5	SepP (5%) + APP (5%) + PR (100%)	0	5	5
SP6	SepP (5%) + APP (10%) + PR (100%)	0	5	10
SP7	SepP (5%) + APP (15%) + PR (100%)	0	5	15
SP8	SepP (10%) + APP (5%) + PR (100%)	0	10	5
SP9	SepP (10%) + APP (10%) + PR (100%)	0	10	10

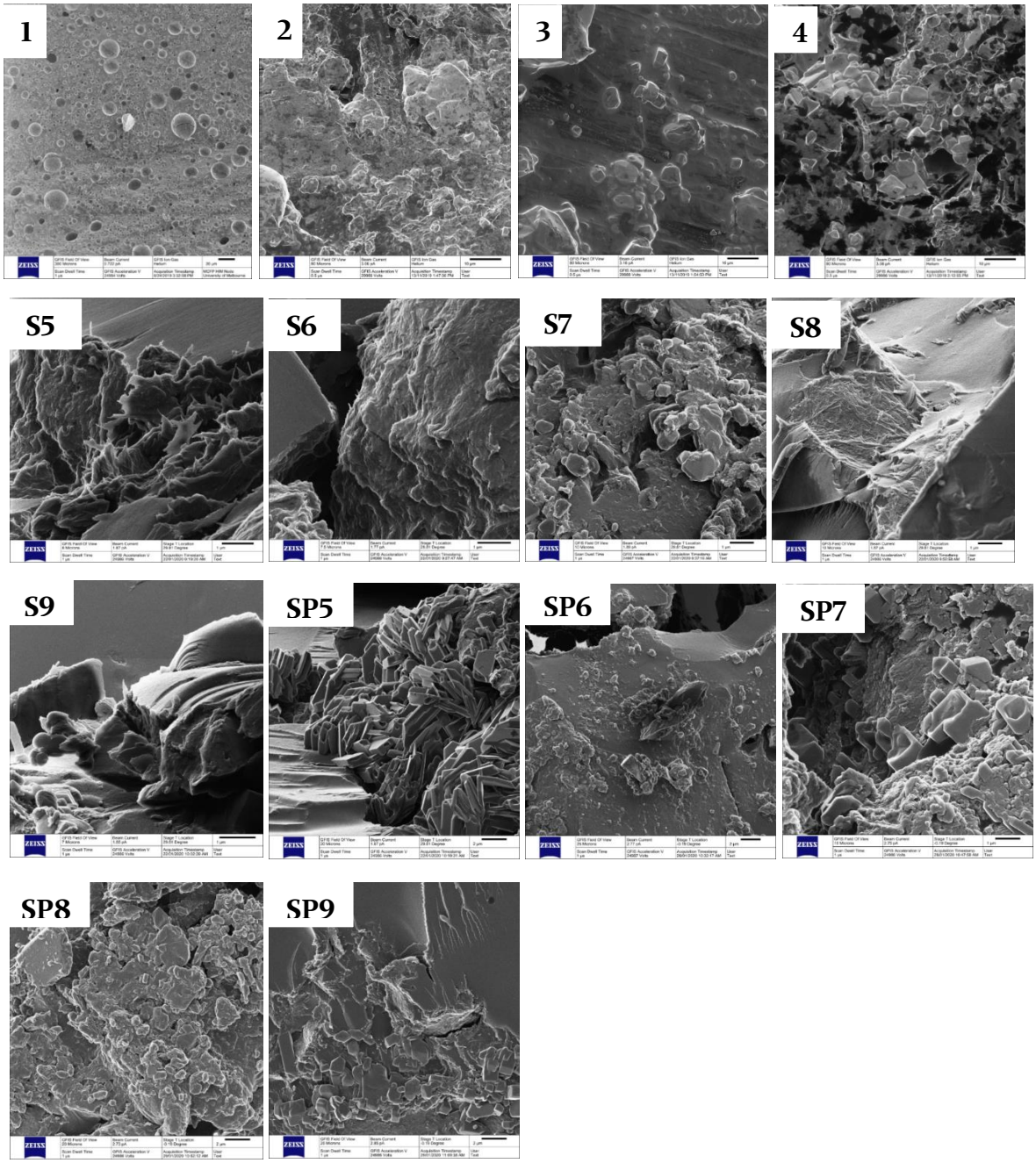

Figure 4.21. a-n) HIM micrographs of Samples 1-SP9

Figure 4.21(1) shows a neat phenolic resin structure. There are micro voids (<10 μm) due to the evaporation of water during curing. Figure 4.21(2) shows the structure of phenolic resin with a 5% APP. APP can be seen as a white chunk with a diameter of less than 10 μm both disperse and agglomerate consistently. Figure 4.21(3, 4) show dispersion of 10% and 15% of APP with different sizes in phenolic resin. 5% of sepiolite fibres with different percentages of APP can be seen in Figure 4.21(S5-S7). Sep fibres

are placed between APP chunks and dispersed consistently. Figure 4.21(S8, S9) represents sepiolite (10%) tendency to agglomeration particularly in regions among APP chunks in some parts. Figure 4.21(SP5) displays the crystallisation of the SepP in most parts of the sample. It seems that SepP reacted with phenolic resin. Chemical reaction separated the solid parts from the phenolic resin structure. This extent of crystallisation is observed mostly in the Sample SP5. However, crystallisation happened only in a small part of Samples SP6, SP7, SP8, and SP9. In other parts, APP and SepP nanoparticles dispersed properly. It also can be seen that by increasing APP percentage, crystallisation decreased significantly. 10% SepP with 5% and 10% APP in the phenolic resin have been shown in Figures 4.21(SP8 and SP9). The dispersion of SepP nanoparticles is consistent despite the percentage of the SepP (10%). The reason for crystallisation in SepP samples and the chemical reaction of materials is not clear and needs a deeper study of their chemical structure.

4.9. 3D GFRP morphological characterisation

Morphological characterisations of 3D GFRP nanocomposites before performing the cone calorimeter test have been studied with SEM-FEI Hitachi. The intention was observation of phenolic resin matrix around glass fibres rather than dispersion of nanoparticles in the matrix. SEM micrographs of samples are shown in Figure 4.22.

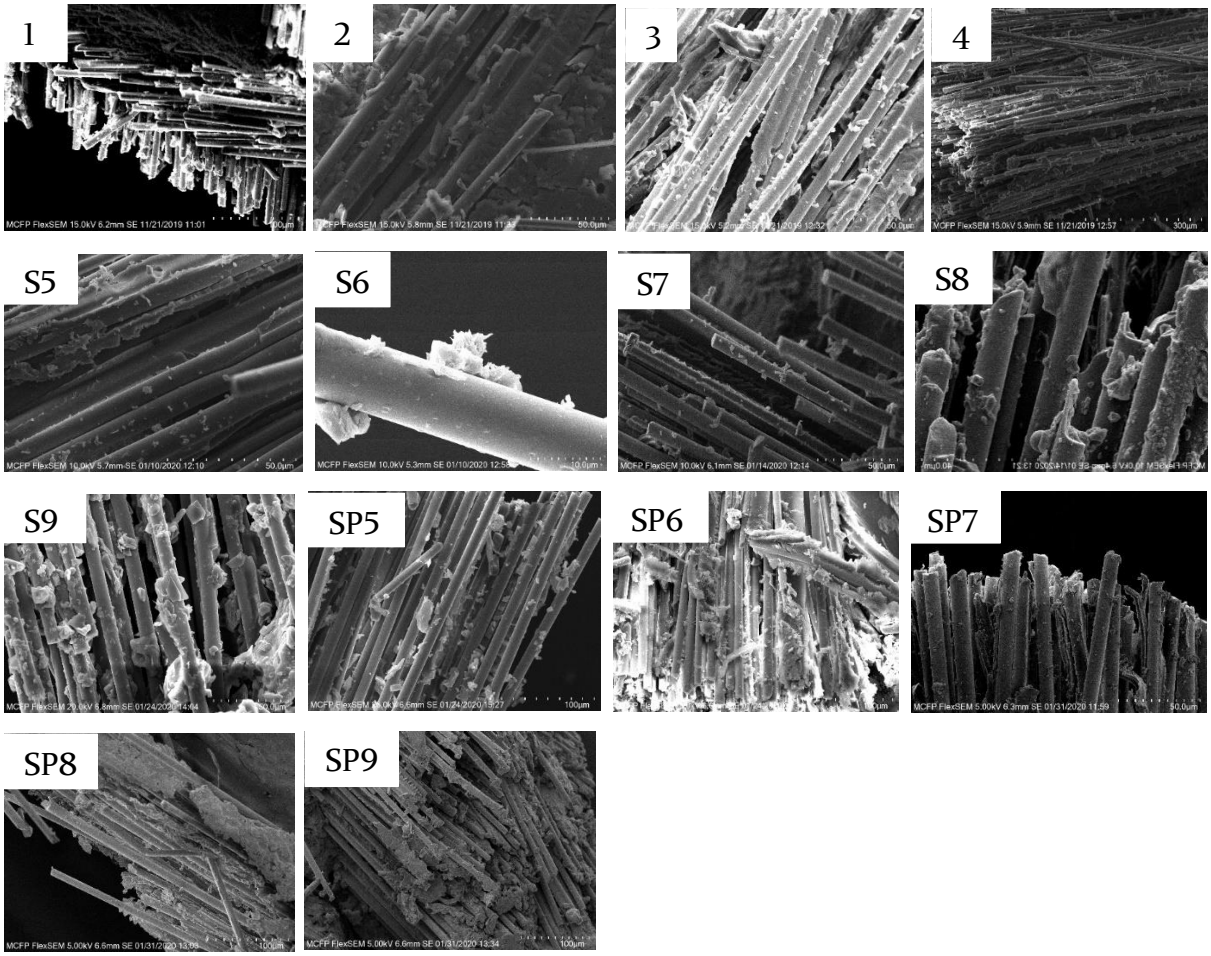

Figure 4.22. SEM micrograph of Samples 1-SP9

Figure 4.22(1) shows the uniform distribution of phenolic resin around glass fibres in the 3D GFRP; 5, 10, and 15% APP flame retardant can be seen as a white chunk up to 10 µm in Figure 4.22 (2-4). It also shows that APP is dispersed consistently around glass fibres. Figure 4.22 (SP5-SP7) shows samples with 5% sepiolite and 5%, 10% and 15% APP flame retardant. Sepiolite fibres are placed inside the matrix and between flame retardant chunks as it can be seen clearly in Figure 4.22 (S6). Increasing the sepiolite fibres to 10% shows a good interlock between APP chunks and dispersion with small agglomeration in some parts (Figure 4.22 (S8, S9)). In the samples with SepP nanoparticles (Figure 4.22 (SP5-SP9)), crystallisation can be observed in the

matrix in some parts around glass fibres. This crystallisation and chemical reaction between SepP nanoparticles, APP, and phenolic resin happened in most parts of the sample in a way that observing SepP nanoparticles in the sample was very hard due to their structural change. Overall, phenolic resin matrix consistently covered glass fibres.

4.10. Chapter summary

In this chapter, synthesis of SepP has been conducted and results of morphological, structural, and thermal characterisations show that SepP successfully meets its requirements and has the potential of using as a filler in the flame retardant as it is discussed in the Palacios et al. [2] research. Then, curing of phenolic resin was studied and appropriate curing time and temperature investigated. Also, dispersion of Sep fibres and SepP nanoparticles in the phenolic resin was studied and results showed that a high shear mixing machine is a good means of mixing materials with acceptable dispersion. Moreover, Sep and SepP phenolic nanocomposite were used with 3D glass fabrics to make a 3D GFRP phenolic nanocomposite. 3D GFRP phenolic nanocomposite has been fabricated successfully and cut to desired dimensions for further investigations. In the next chapter fire behaviour of 3D GFRP nanocomposite will be studied.

4.11. References

[1] Frost RL, Ding Z. Controlled rate thermal analysis and differential scanning calorimetry of sepiolites and palygorskites. Thermochimica Acta. 2003;397:119-28.
[2] Palacios E, Leret P, De La Mata MJ, Fernández JF, De Aza AH, Rodríguez MA et al. Self-Forming 3D Core–Shell Ceramic Nanostructures for Halogen-Free Flame Retardant Materials. ACS applied materials & interfaces. 2016;8:9462-71.
[3] Ratna D. Handbook of thermoset resins: ISmithers Shawbury, UK; 2009.

[4] Kaynak C, Tasan CC. Effects of production parameters on the structure of resol type phenolic resin/layered silicate nanocomposites. European polymer journal. 2006;42:1908-21.
[5] Munoz J-C, Ku H, Cardona F, Rogers D. Effects of catalysts and post-curing conditions in the polymer network of epoxy and phenolic resins: Preliminary results. Journal of Materials Processing Technology. 2008;202:486-92.

Chapter 5

Thermal and fire performance of 3D GFRP nanocomposite

5.1. Introduction

In this chapter, the fire properties of cladding panels based on different compositions of 3D GFRP nanocomposite are studied in a bench-scale test. For this purpose, first, thermogravimetric analysis of Sep/SepP phenolic nanocomposite is conducted to examine the thermal behaviour of material (weight loss versus temperature). Then, the fire properties of samples are obtained using cone calorimeter testing which is the most important bench-scale instrument in fire testing to examine the ignitability, heat release rates, effective heat of combustion, mass loss rates, and smoke release properties of a material. Thereafter, the fire safety of different compositions is compared and discussed. Finally, full-scale façade fire test classification criteria are evaluated based on the cone calorimeter results. The results of this chapter provide indications about the new material's fire behaviour, fire safety rating, and potential performance in medium-scale and full-scale fire tests.

5.2. Thermogravimetric analysis of Sep/SepP phenolic nanocomposite

Thermogravimetric analysis of Sep/SepP phenolic nanocomposite samples have been conducted as explained in Chapter 3. Table 5.1 shows specimens' number, compositions, and weight loss at 850°C. Figure 5.1 shows DTA graphs of all samples.

Table 5.1. Weight loss percentage of Samples 1-SP9

No	Composition (%)	Weight loss (%) & 850°C
1	PR	100.00
2	APP (5) +PR	50.34
3	APP (10) +PR	59.00
4	APP (15) +PR	40.28
S5	Sep (5) + APP(5) +PR	76.33
S6	Sep (5) + APP(10) +PR	43.88
S7	Sep (5) + APP(15) +PR	52.35
S8	Sep (10) + APP(5) +PR	49.49
S9	Sep (10) + APP(10) +PR	45.87
SP5	SepP (5) + APP(5) +PR	76.17
SP6	SepP (5) + APP(10) +PR	45.71
SP7	SepP (5) + APP(15) +PR	64.13
SP8	SepP (10) + APP(5) +PR	71.21
SP9	SepP (10) + APP(10) +PR	65.53

As can be seen in Figure 5.1, there is a three-stage decomposition in all the graphs. The first zone (150° C to 230° C) is related to the loss of weakly-bonded water from phenolic resin. The weight loss was between 9-26%. The second zone (350° C to 400° C) is related to the beginning of the thermal degradation and decomposition of cured resin by the scission reaction of the polymer and the weight loss is 17-45%. Finally, the carbonisation zone and char formation (520-560° C) occurs with the formation of H_2, CO, and CH_4. Neat phenolic resins complete decomposition happened at 680° C. The residual mass percentage or char formation tendency of samples can be ranked as:

4>S6>SP6>S9>S8>2>S7>3>SP7>SP9>SP8>SP5>S5> 1

The TGA graphs of categorised samples (Figure 5.2 (a-f)) with a detailed analysis are discussed next. Figure 5.2(a) shows the TGA graph for Samples 1 to 4. Sample 4 (15% APP) lost less weight (40.28%) than the other samples; this is followed by Samples 2 (50.34%), 3 (59%), and 1 (100%), respectively.

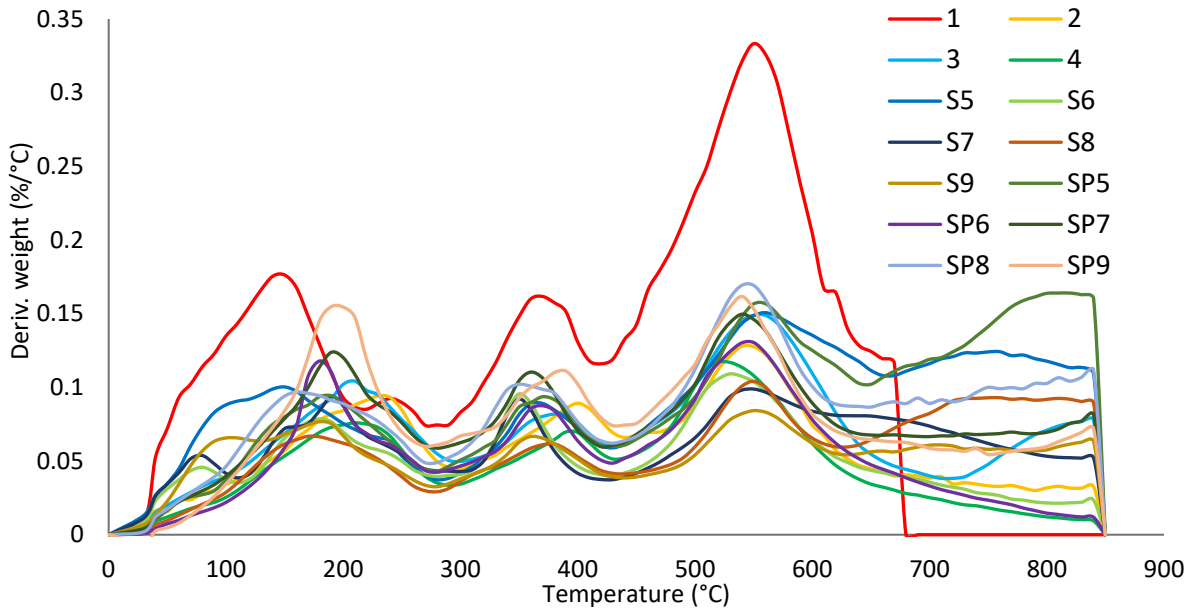

Figure 5.1. DTA of Samples 1-SP9

This means that the APP flame retardant protects the polymer by forming a char layer on the polymer surface and remains higher residual mass compared with the neat phenolic resin sample [1, 2]. The graphs of Samples 1, 2, and 3 follow a similar trend between 30-800° C with a different mass loss at the end. It is also seen that Sample 4 lost less weight than the other samples between 200° C and 850° C. In terms of weight loss at each peak, Sample 4 lost less weight (6.61%, 17.47%, 33.91%) than Samples 2 (7.88%, 21.79%, 40.24%), 3 (8.72%, 23.40%, 43.83%), and 1 (26.34%, 45.17%, 88.83%), respectively. From Figure 5.2(b) and Table 5.1, in the Samples 2, S5, SP5, S8, and SP8, with a constant 5% APP and 0, 5, and 10% of Sep, and SepP, the higher mass concentration of Sep and SepP (S8: 49.49%, SP8: 71.21%) lost less weight than the lower concentration of them (S5: 76.33%, SP5: 76.17%). However, adding Sep/SepP nanoparticles increased the mass loss percentage in both Sep and SepP samples except in the Sample S8. By looking at Figure 5.2b, all samples follow the same trend until 550° C (Sample S8 lost less weight), but behaved differently after 600° C.

From Figure 5.2(c), in the samples with a constant amount of APP (10%), and 0, 5, and 10% of Sep/SepP nanomaterials, the higher mass concentration of Sep and SepP (S9: 45.87%, SP9: 65.53%) lost more weight than the lower mass concentration (S6: 43.88%, SP6: 45.71%) of them at 850° C. It means that a combination of 10% APP with 5% nanoparticles protects the polymer by absorbing heat and creating a protective layer on the surface of the polymer. Also, all samples show a similar trend between 30-850° C and have almost similar weight loss percentages except Sample SP9 which lost more weight than the other samples. Figure 5.2(d) shows a constant higher percentage of APP (15%) with and without 5% of Sep and SepP nanoparticles. As can be seen from Figure 5.2 (d) and Table 5.1, Sample 4 lost less weight (40.28%) than the other samples followed by Sample S7 (52.35%) and SP7 (64.13%) at 850° C. The TGA graph of three samples followed the same trend until 600° C. According to Table 5.1 and Figure 5.2(e), between Samples S5, S6, S7, SP5, SP6, and SP7 including a constant 5% Sep/SepP and 5, 10 and 15% of APP, Sep and SepP samples showed a same trend weight loss percentage at 850° C.

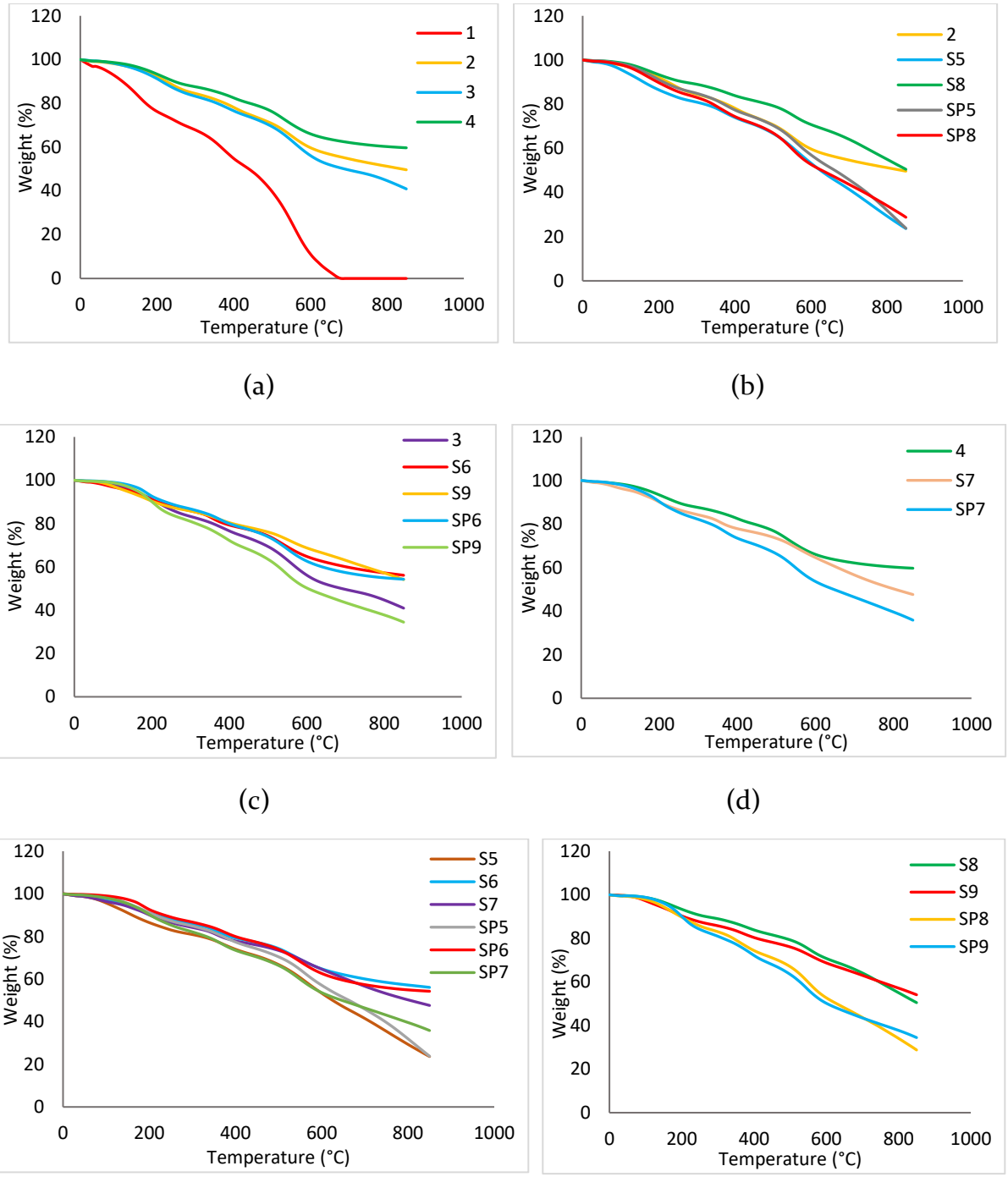

Figure 5.2. TGA graphs of samples: a) 1, 2, 3, 4; b) 2, S5, S8, SP5, SP8; c) 3, S6, S9, SP6, SP9; d) 4, S7, SP7; e) S5, S6, S7, SP5, SP6, SP7; f) S8, S9, SP8, SP9

Increasing APP from 5% to 10% decreased the weight loss percentage at 850° C while increasing APP from 10% to 15% increased WL%. It means that samples containing 10% APP had the lowest value. Samples S5 and SP5 lost more weight than the other

samples (76%). Moreover, all graphs follow a similar trend until 600° C with a small change after that. In the samples with 10% of Sep/SepP, and 5%, and 10% of APP flame retardant (Figure 5.2(f)), increasing APP from 5% to 10% reduced weight loss percentages. Also, sepiolite samples lost less weight than SepP samples.

From the results of the thermogravimetric analysis of Sep/SepP phenolic composite samples, the following conclusions can be drawn:

- In the samples with a constant amount of Sep/SepP, by adding APP flame retardant, the %WL decreased. The lowest value was observed in samples with 10% and 15% APP flame retardant.
- In the samples including a constant 5% and 15% of APP, by adding Sep/SepP, %WL increased (except Sample S8). However, in the samples including a constant 10% of APP, by adding Sep/SepP (5% to 10%), WL% decreased (except Sample S9).
- In samples containing APP without nanoparticles (Samples 2, 3, and 4), Sample 4 (15% APP + PR) lost less weight than the other samples.
- In samples including both APP and nanoparticles, samples with 10% APP lost less weight than the other samples followed by 15% and 5% APP regardless of Sep/SepP percentages.

Altogether, the above means that APP flame retardant significantly reduced the weight loss percentages and increased the thermal stability. However, increasing the Sep and SepP nanoparticles into the phenolic composite didn't follow a constant trend and showed some fluctuations.

5.3. Cone calorimeter test

The cone calorimeter test method and the associated fire reaction properties from the test have been explained in Chapter 3. The test results are summarised in Table 5.2. The values are averages of, typically, six runs each tested under the same conditions. The time interval between each data measurements were 2 seconds. Higher standard deviation can be observed in some compositions and it may be due to the inconsistent presence of APP flame retardant, dispersion of nanoparticles and their percentages in each specific sample, and small variations in specimen dimensions. Therefore, in materials containing flame retardant, more than 5-6 samples need to be tested to reduce the standard deviation and obtain more reliable values. Figure 5.3 shows the sample ignition.

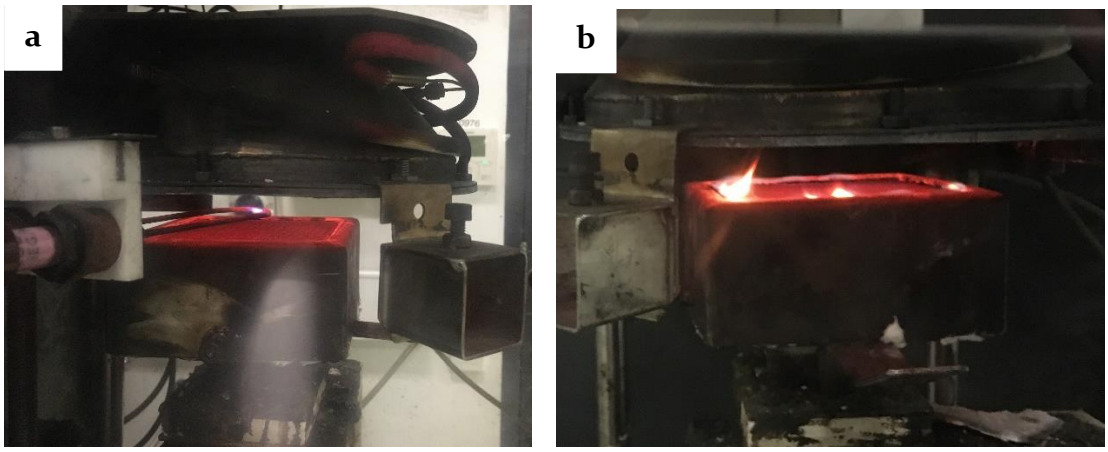

Figure 5.3: Cone calorimeter test: a) spark ignition; b) start of ignition

Table 5.2. Cone calorimeter test results

Sample	Composition	ML% [SD]	TTI [SD]	T_{fo} [SD]	THR - MJ/m^2 [SD]	PHRR- KW/m^2 [SD]	EHC- MJ/kg [SD]	SEA (m^2/kg) [SD]	FIGRA- MJ/m^2s	FPI- (m^2s/KW)
1	Sep (0%) + APP(0%) +P (100%)	25.3 [6.6]	154.2 [16.6]	302.6 [30.9]	7.59 [1.1]	72.5 [10.4]	10.1 [1.8]	2.8 [1.6]	0.47	2.12
2	Sep (0%) + APP(5%) +P (100%)	25.2 [4.4]	153.2 [10.9]	272.5 [35]	7.23 [1]	56.1 [12.6]	10.8 [1.4]	0.4 [0.5]	0.36	2.73
3	Sep (0%) + APP(10%) +P (100%)	24.1 [3]	141.2 [6.7]	245 [17.3]	5.63 [0.8]	41.6 [9.8]	9.6 [1.7]	0.0 [0.02]	0.29	3.39
4	Sep (0%) + APP(15%) +P (100%)	24.2 [1.7]	150.4 [18.9]	253.8 [4.8]	6 [0.9]	44.2 [6.4]	9.6 [1.1]	0.1 [0.1]	0.29	3.40
S5	Sep (5%) + APP(5%) +P (100%)	24.6 [1]	97.5 [21.8]	210.8 [24.1]	8.06 [2]	66.8 [20.6]	12.6 [2.9]	3.3 [3]	0.68	1.45
S6	Sep (5%) + APP(10%) +P (100%)	26.1 [2.4]	108 [15]	217.5 [13.3]	7.53 [1.3]	60.3 [18.6]	11.3 [1.5]	2.3 [2.5]	0.55	1.79
S7	Sep (5%) + APP(15%) +P (100%)	27 [2.3]	149.3 [37.6]	246.3 [24.4]	7.21 [1.5]	53.4 [9.1]	10.3 [2.5]	0.4 [0.8]	0.35	2.79
S8	Sep (10%) + APP(5%) +P (100%)	22 [3.2]	107.6 [25.3]	208.3 [19.4]	8.29 [1.1]	60.8 [18.8]	13.9 [2.9]	0.3 [0.4]	0.56	1.76
S9	Sep (10%)+ APP(10%) +P (100%)	25.9 [1.3]	141.6 [35.3]	236 [23.2]	7.75 [1.4]	50.2 [7.7]	11.1 [2.2]	0.6 [0.9]	0.35	2.82
SP5	SepP (5%) + APP(5%) +P (100%)	26.5 [2.8]	112.6 [8.6]	219.6 [22.6]	9.26 [1.1]	69.6 [8.5]	13.6 [1.2]	1.2 [1.1]	0.61	1.61
SP6	SepP (5%) + APP(10%) +P (100%)	24.9 [1.5]	137 [10.6]	245.1 [11]	8.54 [0.9]	75.3 [10.5]	12.1 [0.6]	2.9 [1.8]	0.54	1.81
SP7	SepP (5%) + APP(15%) +P (100%)	26.65 [3.3]	163.5 [35]	257.5 [18.9]	6.06 [1.3]	44.2 [7.6]	8.4 [1.8]	0.1 [0.1]	0.27	3.69
SP8	SepP (10%) + APP(5%) +P (100%)	25.69 [2.1]	106 [18.1]	218 [17.1]	8.73 [1.6]	64.3 [13.1]	13.1 [1.4]	1.3 [0.9]	0.6	1.64
SP9	SepP (10%) + APP(10) +P (100%)	24.32 [4.6]	116.1 [25.6]	241.6 [5.1]	8.72 [2.2]	52.6 [13.3]	13.2 [1.8]	0.7 [1.3]	0.45	2.20

The parameter, time to ignition (TTI), shows the ignitability of materials. The lower TTI means that the testing material is more ignitable when tested in the similar fire scenario [27]. For 3D GFRP nanocomposite samples used in this research, TTI is directly connected to the pyrolysis temperature of the solid materials to generate enough volatiles at the lower flammable intensity, if the radiant heat flux is constant [3]. This means that samples with shorter TTI are easy to ignite and decompose at lower temperatures. It is important to note that, in the samples with the same composition including flame retardant, different TTI has been observed. Because ignition times are usually determined based on visual observations, this produces a

significant amount of ambiguity. Fire-retardant-treated materials usually display flashes and temporary flaming before sustained ignition [4]. Therefore, the presence of APP flame retardant makes the results inconsistent depending on its location and dispersion in the sample.

From Table 5.2, Sample S5 has the lowest time to ignition, followed by Samples SP8, S8, S6, SP5, SP9, SP6, 3, S9, S7, 4, 2, 1, and SP7. In samples with a constant amount of nanoparticles, increasing APP from 5% to 15% increased the TTI [1, 5]. Also, in the samples with a constant amount of APP, increasing the percentage of nanoparticles from 5% to 10% increased the TTI in the sepiolite samples, and decreased the TTI in the SepP samples.

In Samples 4, S7, and SP7, increasing nanoparticles from 0% to 5% increased TTI in the Sample SP7 significantly and decreased it slightly in the Sample S7. Furthermore, in Samples 1-4 (without nanoparticles), 10% APP (Sample 3) had the lowest TTI, followed by 15%, 5%, and 0% APP. This means that the pure phenolic resin Sample (Sample 1) had the highest TTI without any flame retardant, and APP decreased the pyrolysis temperature and reacted earlier than phenolic resin to produce char and protect the polymer. It can be further confirmed in Figure 5.4. This observation is consistent with previous research [3]. Figures 5.4 to 5.10 show HRR, MLR, and smoke production graphs of all samples and further discussion of cone calorimeter results.

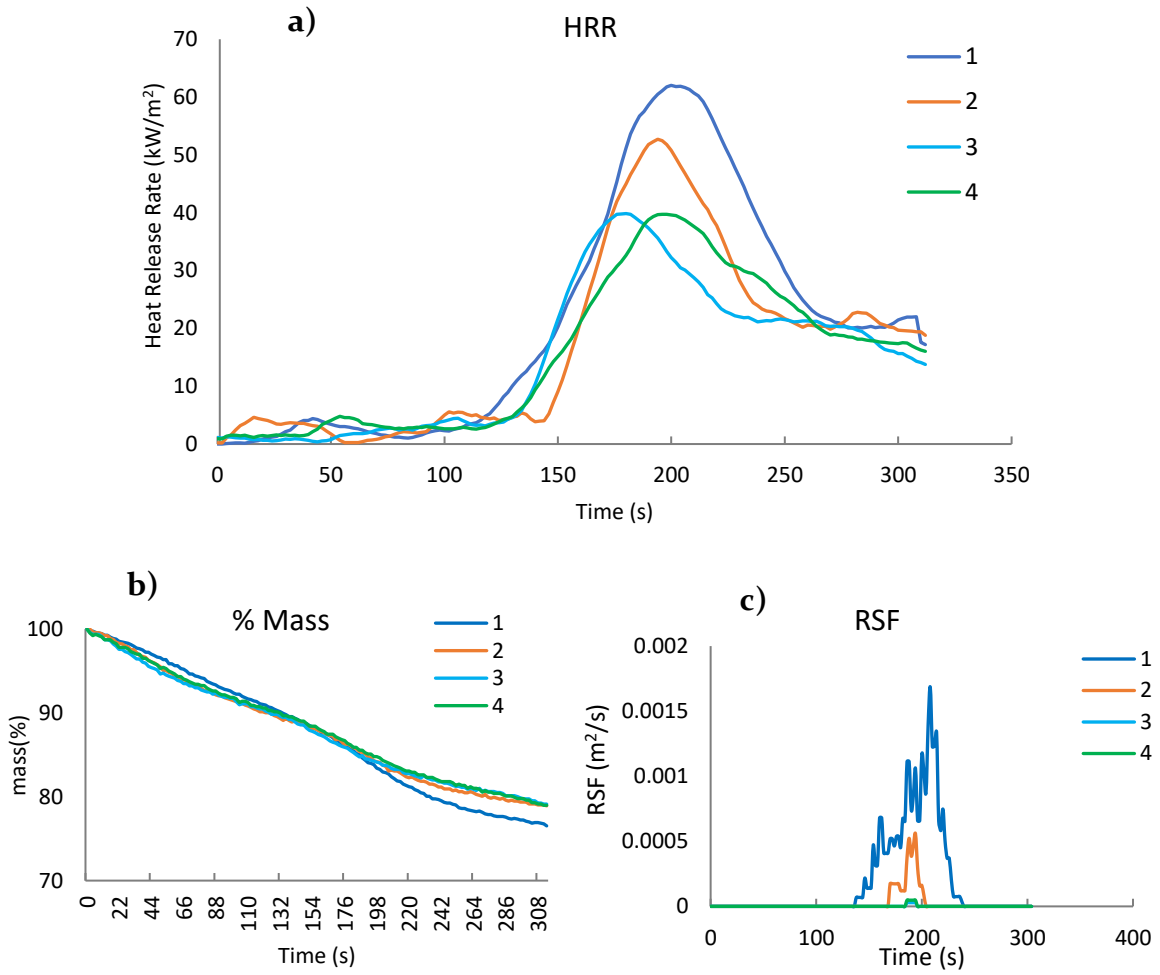

Figure 5.4. a) HRR; b) mass loss; c) rate of smoke formation versus time curves for Samples 1-4

According to Figure 5.4(a) and Table 5.2, in the samples without nanoparticles, all APP samples have lower values of PHRR compared with neat phenolic resin samples. Samples 2 (5% APP), 3 (10% APP), and 4 (15% APP) decreased the PHRR by 23%, 43%, and 39%, respectively compared with Sample 1 (neat phenolic resin). This means that adding APP flame retardant decreases the PHRR in phenolic composites. The main flame retardant mechanism of polymer composites is in the condensed phase, involving the char layer creation and nanoparticle-rich protective layer creation [34]. Both layers can perform as the mass transfer barrier and heat-proofing in the condensed stage. Also, the flame duration time of Sample 1 was more than Samples 2,

3, and 4. That means that Sample 1 had enough time to burn completely and increase more THR, and PHRR, than the other samples. It also means that increasing APP percentage decreased the flame duration time as well. Also, by increasing APP flame retardant, THR and EHC decreased by 21%, and 5%, respectively.

From Table 5.2 and Figure 5.4(b), by adding APP flame retardant from 5% to 15% in the Samples 1-4, %ML reduced to 25.2%, 24.1%, and 24.2%, respectively, that are less than a 5% drop. Also, according to Table 5.2 and Figure 5.4(c), the soot released reduced significantly (96%).

HRR, %ML and RSF of Samples 2, S5, S8, SP5, and SP8 with constant 5% APP and 0, 5, and 10% Sep, and SepP are shown in Figure 5.5(a-c).

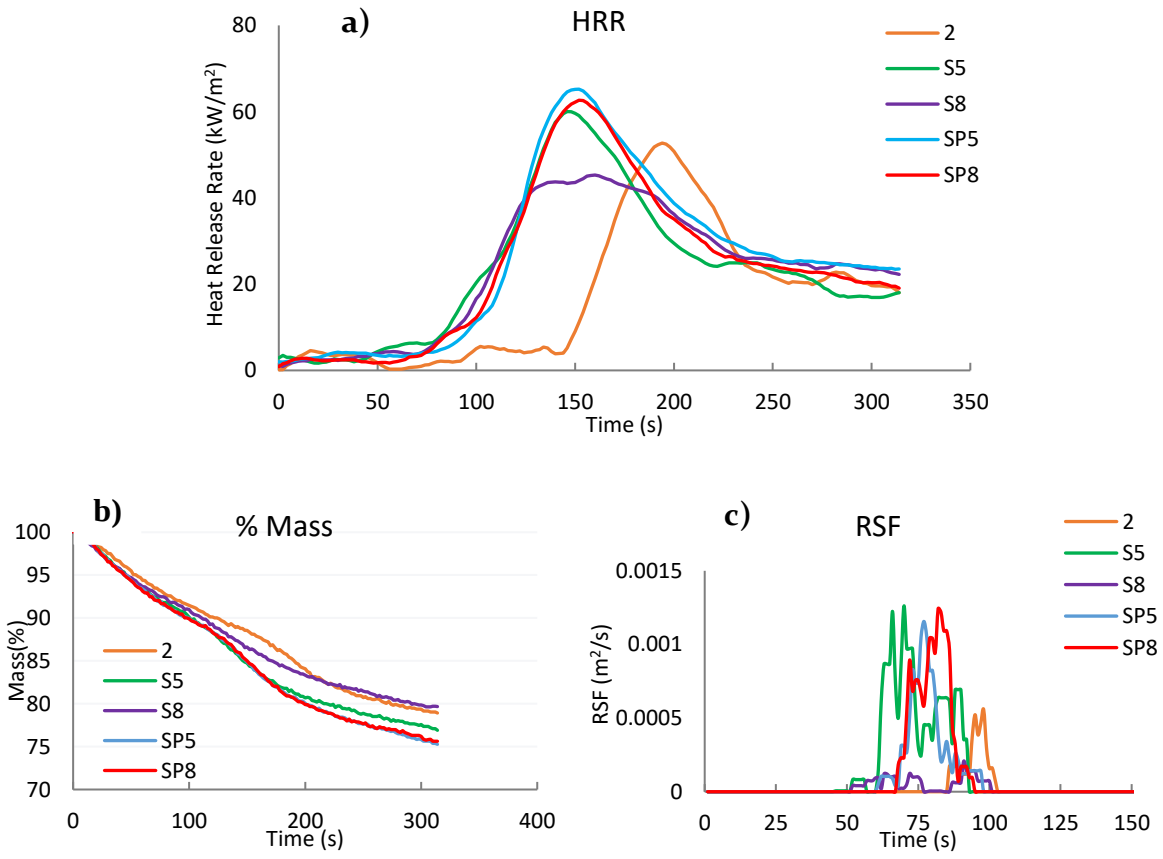

Figure 5.5. a) HRR; b) mass loss; c) rate of smoke formation versus time curves for Samples 2, S5, S8, SP5, and SP8

From Table 5.2 and Figure 5.5(a), Sample 2 has less THR, EHC, and PHRR than the other samples. This means that with a constant amount of APP flame retardant (5%), adding nanoparticles increased THR, EHC, and PHRR between 11% to 28%, 16% to 28%, and 8% to 24%, respectively. Also, higher percentages of Sep/SepP had a lower amount of THR, EHC, and PHRR than the lower percentages of them (exception: THR & EHC in Samples S5, and S8).

Moreover, the time to ignition of Sample 2 is much higher than the other samples. That means that the pyrolysis temperature in Sample 2 is higher than in the other samples. Furthermore, by adding Sep and SepP, mass loss decreased in Sep samples and increased slightly in SepP samples. Also, the higher mass concentration of Sep/SepP samples lost less weight than the lower concentrations of them. In terms of smoke production (Figure 5.5c), adding nanoparticles increased soot production except in the Sample S8 which released around the same amount of soot (0.3 m^2/kg) as Sample 2 (0.4 m^2/kg). Overall, Sample SP5 had the highest ML%, THR, and PHRR among the other samples. This can be due to the crystallisation of Sample SP5 and its structural change because of the reaction between SepP, APP and phenolic resin which decreased TTI and released more heat with a higher peak. Figure 5.6 (a-c) shows samples with a constant amount of APP (10%) and various amounts of Sep, and SepP nanoparticles. According to Table 5.2 and Figure 5.6, adding Sep/SepP nanoparticles increased ML%, THR, PHRR, EHC, and SEA. It also can be seen that higher mass concentration of nanoparticles has lower values of PHRR, ML%, and SEA compared with a lower mass concentration of them. By adding nanoparticles, THR

increased between 33-54%. The higher mass concentration of Sep, and SepP increased the THR slightly compared with the lower mass concentration of them.

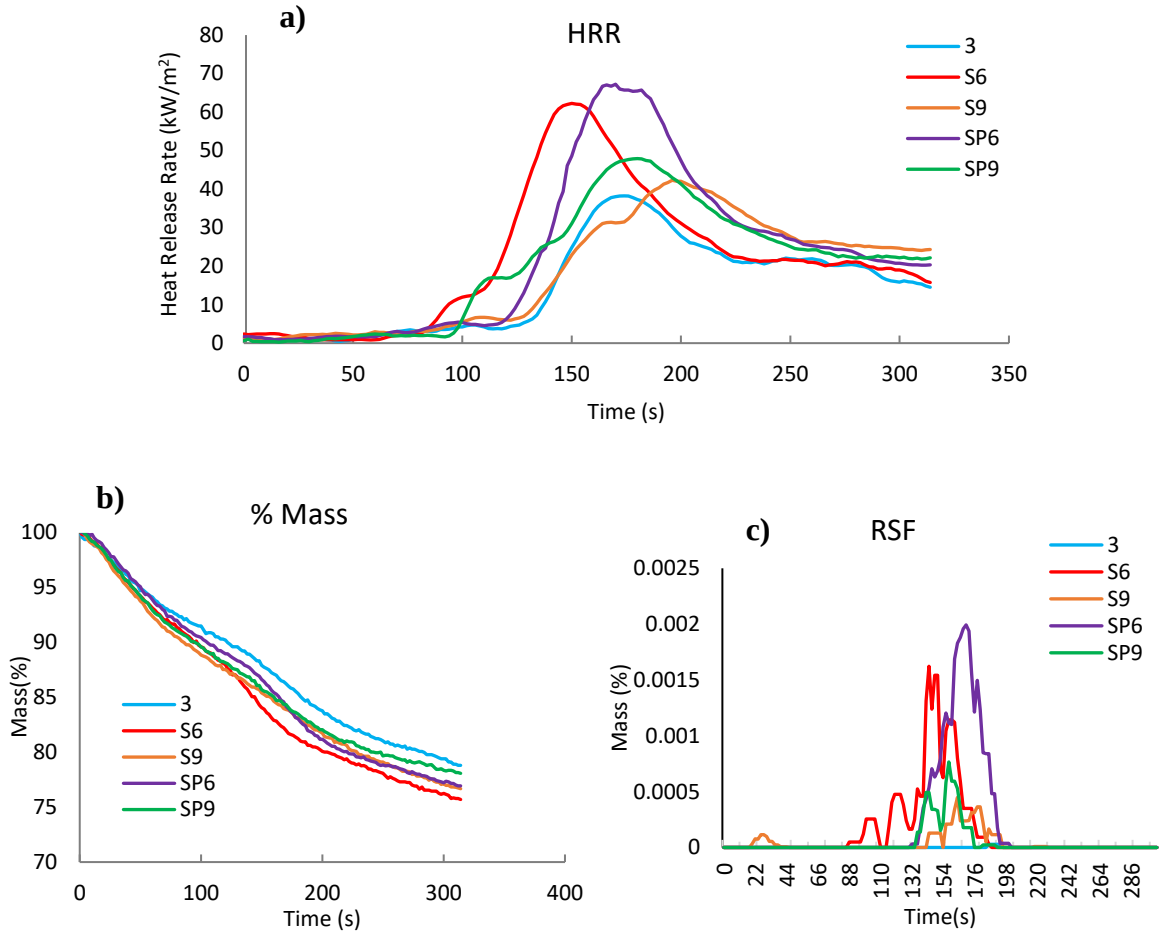

Figure 5.6. a) HRR; b) mass loss; c) rate of smoke formation versus time curves for Samples 3, S6, S9, SP6, and SP9

From Table 5.2, Sample S6 had the lowest TTI, and Sample S9 had the highest. This means that a low concentration of sepiolite samples needs a lower temperature to decompose and a high concentration of sepiolite needs a high temperature to pyrolysis than the other samples. However, a high percentage of SepP in the sample needs less time to ignite and decompose at a lower temperature than the low percentage of SepP sample. This inconsistency may happen due to inconsistent dispersion of APP flame

retardant in combination with Sep, and SepP nanoparticles which affect the time of ignition and time to flame out. In terms of weight loss (Table 5.2 and Figure 5.6.b), by adding Sep/SepP nanoparticles, mass loss percentage increased slightly between 0% to 8%. The higher mass concentration of Sep/SepP samples (10%) lost less weight than the lower mass concentration (5%) of them. Looking through Figure 5.6.c and Table 5.2, adding nanoparticles increased the soot amount. Lower mass concentration of Sep/SepP (S6: 2.3 m^2/kg, SP6: 2.9 m^2/kg) produced higher smoke than the higher concentration (S9: 0.6 m^2/kg, SP9: 0.7 m^2/kg).

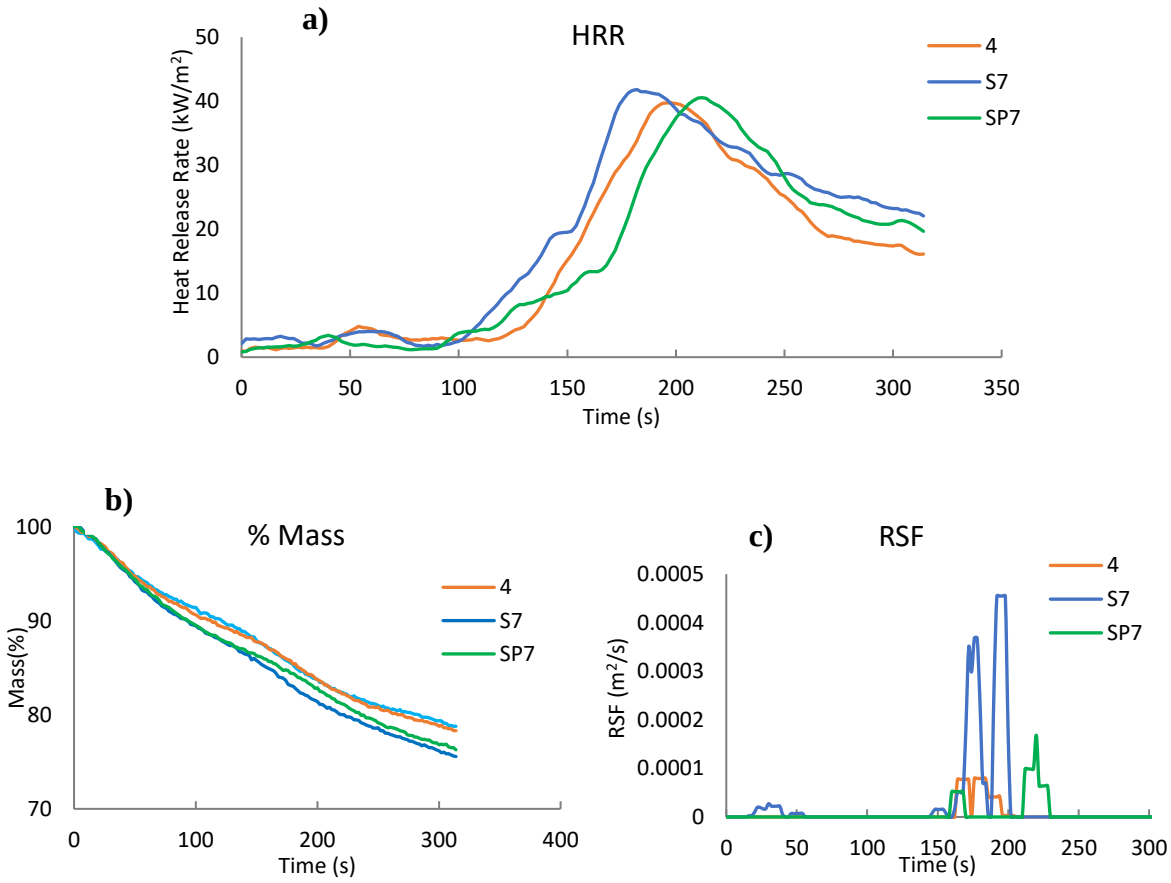

Figure 5.7. a) HRR; b) mass loss; c) rate of smoke formation versus time curves for Samples 4, S7, and SP7

Figure 5.7a shows the heat release rate of samples with a constant 15% of APP and 5% of Sep, and SepP. From Table 5.2 and Figure 5.7a, adding 5% of Sep increased THR,

PHRR, EHC, and SEA while adding 5% SepP into Sample 4 did not change those parameters and decreased EHC by 12%. In addition, TTI of Samples 4 and S7 is almost the same while the TTI of SP7 increased by 8%. It means that SepP nanoparticle samples need more time to ignite and have higher decomposition temperatures and protect the polymer by absorbing heat and increasing the TTI. Also, adding Sep/SepP increased the weight loss percentages by 11% and 9%, respectively, compared with the Sample 4 (Figure 5.7.b). Looking through RSF and SEA (Figure 5.7c), Sample S7 produced slightly more soot than other samples (0.4 m^2/kg). In total, Sample S7 had the highest PHRR, THR, %ML, EHC, and SEA than other samples. It also can be derived adding 5% SepP does not change the fire reaction properties of the polymer (refer to Table 5.2).

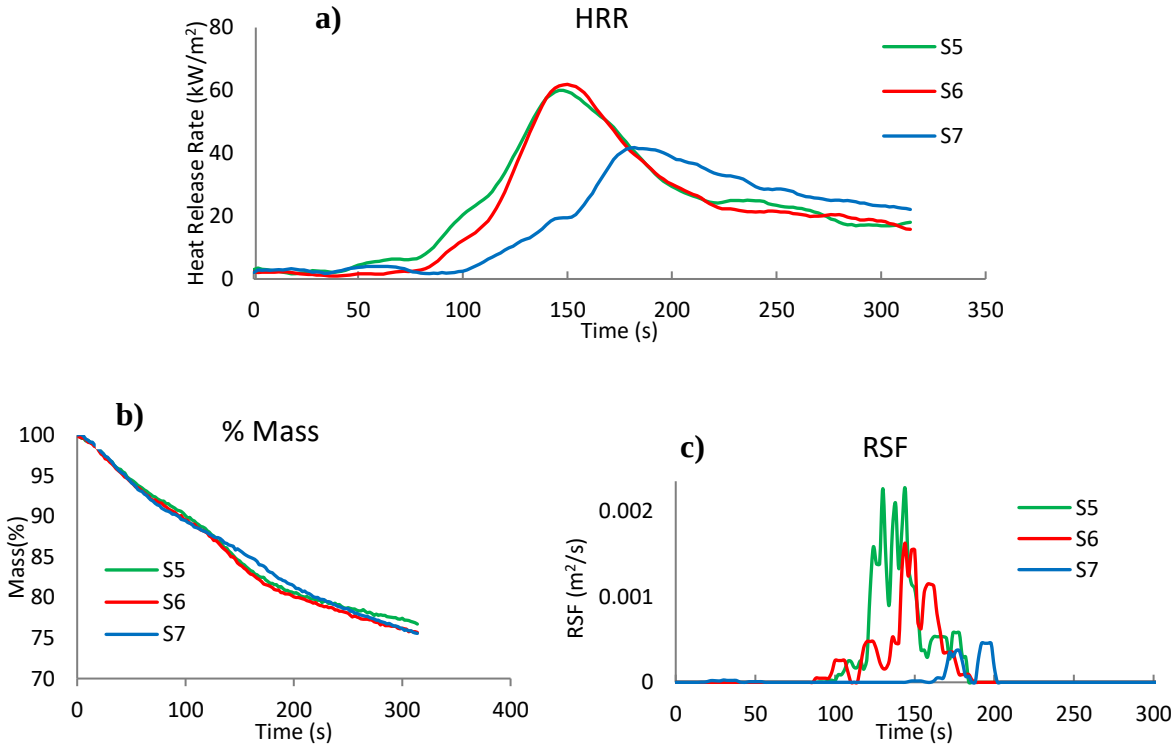

Figure 5.8. a) HRR; b) mass loss; c) rate of smoke formation versus time curves for Samples S5, S6, and S7

Figure 5.8a shows samples with a constant 5% of Sep, and 5, 10, and 15% of APP. By increasing the amount of APP flame retardant from 5% to 15%, THR, EHC, PHRR, SEA (Table 5.2) and flame duration decreased. However, TTI and ML% increased. Sample S7 had the highest TTI. It means that Sample S7 with 15% APP performed better in terms of fire properties than the other samples.

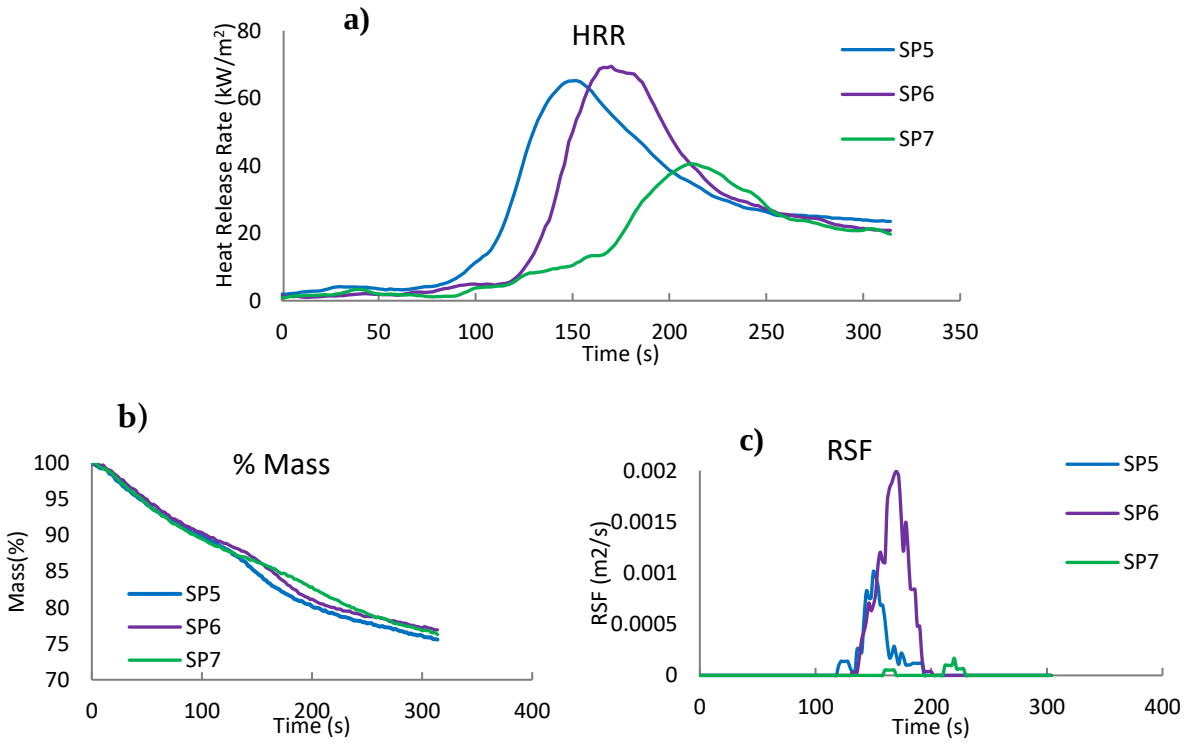

Figure 5.9 a) HRR; b) mass loss; c) rate of smoke formation versus time curves for samples SP5, SP6, and SP7

From Figure 5.9a, by increasing APP in the SepP samples, THR and EHC decreased while TTI increased. That means that Sample SP7 samples need a higher temperature to decompose. Sample SP7 has the lowest PHRR, THR, EHC, SEA, and flame duration than the other two samples. Sample SP7 showed the lowest soot production (0.1 m^2/kg) followed by Samples SP5 (1.2 m^2/kg) and SP6 (2.9 m^2/kg). By adding APP percentages, the weight loss percentage decreased in the Sample SP6 by 6% and remained the same in the Sample SP7.

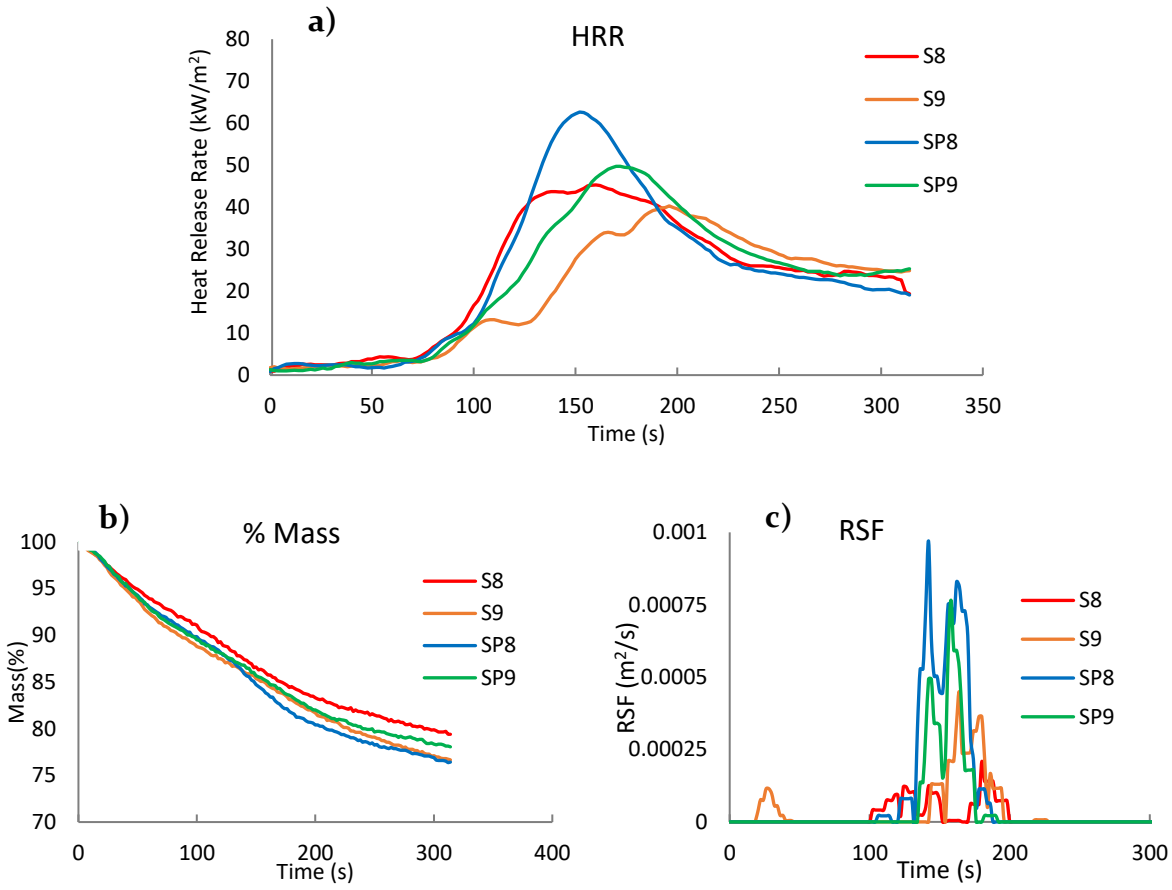

Figure 5.10. a) HRR; b) mass loss; c) rate of smoke formation versus time curves for Samples S8, S9, SP8, and SP9

According to Table 5.2 and Figure 5.10(a-c), higher percentages of APP(10%) samples have lower PHRR, THR and EHC than the lower percentages of APP samples in both Sep and SepP samples with an exception of EHC in the Sample SP9 that has the same value. However, SEA, flame duration, and ML% showed a different trend in the Sep and SepP samples. By increasing the APP percentage, the flame duration in Sep samples decreased by 6% while the smoke production was doubled. However, in SepP samples flame duration increased by 10% while smoke production was decreased by 46%.

Also, TTI in both samples increased by increasing APP percentage and this is more significant in Sep samples. In terms of weight loss percentage (Figure 5.10b), by adding

APP percentage, ML% in Sep sample increased by 17% while in SepP sample it slightly decreased (5%).

Therefore, Sep/SepP with 10% of APP performed very well together in the condensed phase and char formation layer. It also needs a higher temperature to decompose and form a protective layer on the polymer surface. Through comparison of fire properties of all samples, Sample 3, followed by Samples 4 and SP7 showed better fire performance properties (low THR, PHRR, EHC, and smoke production) than the other samples. That means that adding 10% or 15% APP into the phenolic resin significantly improves the flame retardancy performance.

From the cone calorimeter test results for all samples, the following conclusions can be drawn:

Effects of APP:

- Increasing APP flame retardant from 0% to 15% in the samples without the presence of Sep/SepP nanoparticles (Samples 1-4) decreased THR, PHRR, EHC, and SEA by 20%, 39%, 4%, and 96%, respectively.
- Increasing APP flame retardant from 5-15% in the samples including 5% of Sep nano fibres (Samples S5, S6, and S7) decreased THR, PHRR, EHC, and SEA by 10%, 20%, 18%, and 87%, respectively.
- Increasing APP flame retardant from 5% to 15% in the samples including 5% of SepP nanoparticles (Samples SP5, SP6, and SP7) decreased THR, PHRR, EHC, and SEA by 34%, 36%, 38%, and 91%, respectively.

- Increasing APP flame retardant from 5% to 10% in the samples including 10% of Sep nano fibres (Samples S8, and S9) decreased THR, PHRR, and EHC by 6%, 17%, and 20%, respectively. However, SEA increased by 50%.
- Increasing APP flame retardant from 5% to 10% in the samples including 10% of SepP nanoparticles (Samples SP8, and SP9) decreased PHRR, and SEA by 18%, and 46%, respectively, while these did not change THR and EHC.

Altogether, the above means that increasing the APP flame retardant percentage from 5% to 15% significantly improves the fire reaction properties of 3D GFRP nanocomposite regardless of Sep/SepP nanoparticles.

Effects of sepiolite fibres:

- Increasing sepiolite fibres from 0% to 10% in the samples including 5% of APP (Samples 2, S5, and S8) increased THR, PHRR, and EHC by 14%, 8%, and 28% respectively, while this decreased SEA by 25%.
- Increasing sepiolite fibres from 0-10% in the samples including 10% of APP (Samples 3, S6, and S9) increased ML%, THR, EHC, and SEA by 2%, 7%, 2%, and 50%, respectively, while this decreased PHRR by 10%.
- Increasing sepiolite fibres from 0% to 5% in the samples including 15% of APP (Samples 4, and S7) increased ML%, THR, PHRR, EHC, and SEA by 10%, 20%, 20%, 7%, and 300%, respectively.

Altogether, the above means that increasing the Sep fibres percentage from 0% to 10% slightly increased the fire reaction properties of 3D GFRP nanocomposite with some fluctuations in the smoke production values.

Effects of SepP nanoparticles:

- Increasing SepP nanoparticles from 0% to 10% in the samples including 5% of APP (Samples 2, SP5, and SP8) increased THR, PHRR, EHC, and SEA by 20%, 15%, 22%, and 225%, respectively.
- Increasing SepP nanoparticles from 0% to 10% in the samples including 10% of APP (Samples 3, SP6, and SP9) increased THR, PHRR, EHC, and SEA by 55%, 26%, 37%, and 70%, respectively.
- Increasing SepP nanoparticles from 0% to 5% in the samples including 15% of APP (Samples 4, and SP7) decreased EHC by 12%, and did not change the other fire properties.

Altogether, the above means that increasing the SepP nanoparticles percentage from 0% to 10% increased the fire reaction properties of 3D GFRP nanocomposite.

5.4. Fire safety rating

Some research has been conducted to predict the full-scale fire behaviour of materials from the results of a bench-scale test like the cone calorimeter test [6]. Among them, Babrauskas [7] used the PHRR/TTI to demonstrate the propensity to flashover. In this system, higher values of PHRR/TTI show a propensity to flashover [6] and the lower the PHRR/TTI value, the lower the fire growth in the material. The ratio of PHRR/TTI is called the fire growth rate (FIGRA) and is used to rate the fire safety of materials [8]. In designing construction materials, FIGRA value is important as it shows the speed rate of a material combustion and therefore; the maximum time for the safe

evacuation of the occupants [9]. Based on FIGRA values in Table 5.2, the fire safety of phenolic nanocomposites can be ranked as:

SP7<4=3 <S7=S9<2<SP9<1<SP6<S6<S8<SP8<SP5<S5

Another parameter that is utilised to rate the fire safety of materials is the fire performance index (FPI). It is described as the ratio of TTI to PHRR. There is a connection between FPI and time to flashover (a lower FPI value means an accelerated flashover event [8]). Hence, materials with low FPI values have elevated fire risks. According to the FPI values in Table 5.2, the fire safety of different 3D GFRP composites can be ranked as:

SP7<4<3<S9<S7<2<SP9<1<SP6<S6<S8<SP8<SP5<S5

The total heat released (THR) from a cone calorimeter test can be used to measure full-scale fire behaviour. THR is the total amount of heat discharge when a material burns. It is the value of the integral under the heat release vs time curve. A better understanding of potential full-scale fire behaviour is obtained when the flashover (FIGRA) is combined with THR [6]. A higher value of THR means a large amount of heat the material releases as it burns. An X-Y scatterplot is provided for all material compositions in Figure 5.11. Fire-safe materials are those which have low THR and FIGRA values and fall close to the coordinate (0;0). Short fire duration relates to materials with low HRR and slow-growing fire relates to the lower PHRR/TTI [8].

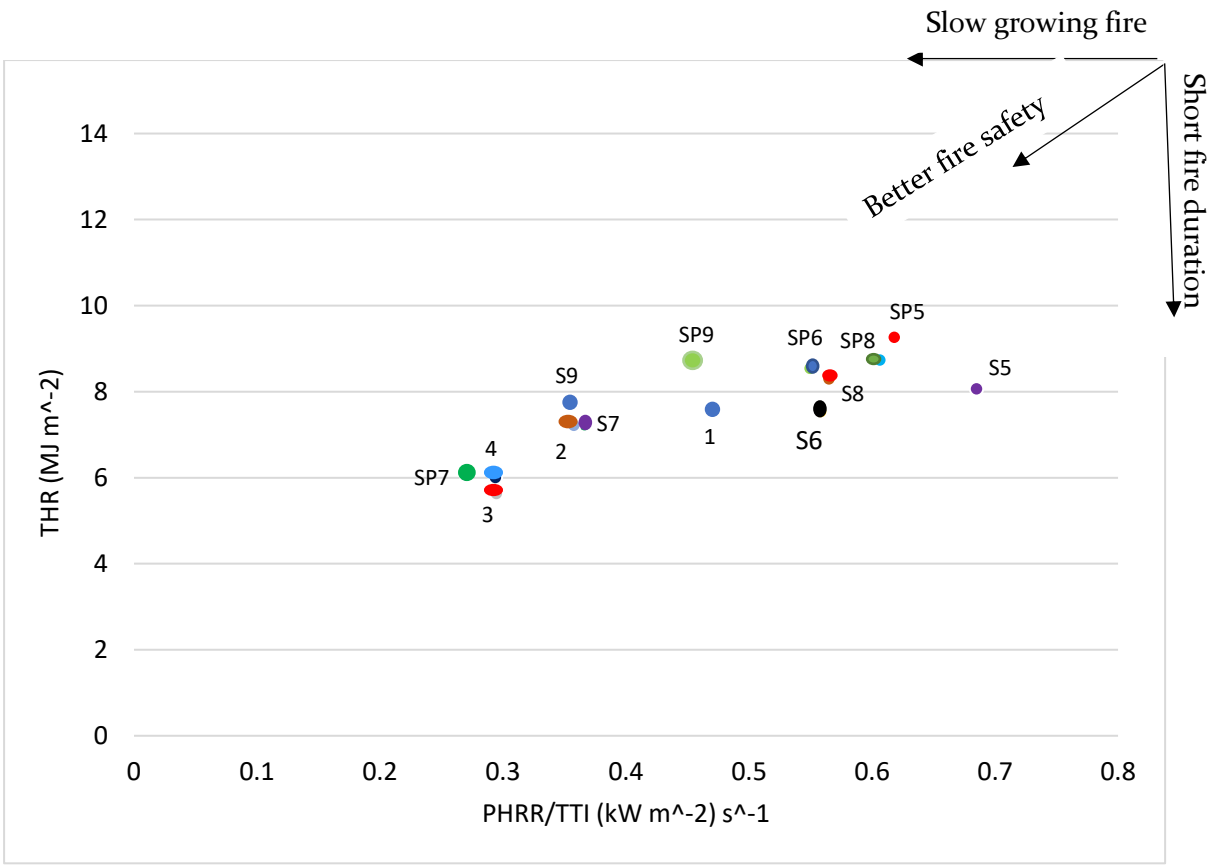

Figure 5.11. The flashover potential and total heat release for all materials

All samples have a PHRR/TTI less than 1 and THR of less than 10 MJ/m^2. Due to the cross-linked structure of phenolic resin, using APP flame retardant, Sep/SepP nanomaterials, and char formation during burning, all samples have a very low THR and high fire safety. In terms of comparison between samples, Samples SP7, 3, and 4 show quite similar fire safety behaviour and performed better than the other samples. These samples contain a high percentage of APP with and without the presence of Sep/SepP nanoparticles.

5.5. An analytical approach to predict the full-scale façade fire test cladding criteria

Standards Australia established AS 5113: “Fire propagation testing and classification of external walls of buildings (Standards Australia 2016)”. AS 5113 was adopted from ISO 13785-2 (International Organisation for Standardisation 2002) and BS 8414 (British Standard Institute 2015). This standard measures fire spread via all exterior vertical or near-vertical surfaces and includes all kinds of external wall systems, involving façades, outer skins, core materials, cavities, and attachments. AS 5113 uses the same sample size as ISO 13785 or BS 8414 along with their corresponding thermocouple locations. AS 5113 classification criteria for external wall fire-spread are mentioned in Section 5.4.5 [10]. Among these criteria, the most relevant to the cladding material is criteria (a) that says, “Temperatures 5 m above the opening measured 50 mm from the exposed specimen face shall not exceed 600°C for a continuous period more than 30 s”. Since conducting the full-scale façade fire test with 3D GFRP cladding is not possible for this research because of constraints on costs and availability of facilities (especially in a pandemic period), a conservative analytical method is presented in this section to infer whether the most relevant criteria of cladding of AS 5113 can be met by the 3D GFRP cladding based on the cone calorimeter test results. The proposed conservative analytical method can only evaluate criteria (a) of Section 5.4.5 AS 5113. An actual full-scale façade fire test is required to confirm the predictions from the analytical method and meet the other criteria such as debris mass and flaming, the temperature at cavity and unexposed face, and flame spread, which are not considered in this analytical method.

Herein, the time-temperature curve of 3D GFRP cladding is estimated using the cone calorimeter test results from the test materials and the full-scale façade fire test results from a "standard" cladding material (in particular, the CSR façade fire test) to address criteria (a) of Section 5.4.5 AS 5113.

The CSR façade fire test, which was cladded with steel, has been conducted according to AS 5113:2016 at Exova Warringtonfire in Victoria. Softwood timber (*Pinus Radiata*) was used as crib material with a moisture content of 14.8% and a density of 0.63 kg/dm^3. The test setup and instrumentation was in accordance with AS 5113:2016 [10] and BS 8414-2:2015 [11]. The place of thermocouples for assessment of criteria (a) (5 m above the opening) and CSR full-façade fire test in accordance with AS 5113 and BS 8414-2 test method are shown in Figures 5.12 and 5.13, respectively.

According to the cone calorimeter test results and the fire safety analysis in Sections 5.3 and 5.4, Sample 3 of the 3D GFRP nanocomposite samples has been selected for this hypothetical evaluation of full-scale façade cladding material in the alternate CSR façade system. This means that, in the following analysis, we replace the actual cladding used in the CSR full-façade test [12] with a cladding material following the composition of Sample 3 of the 3D GFRP nanocomposite panel.

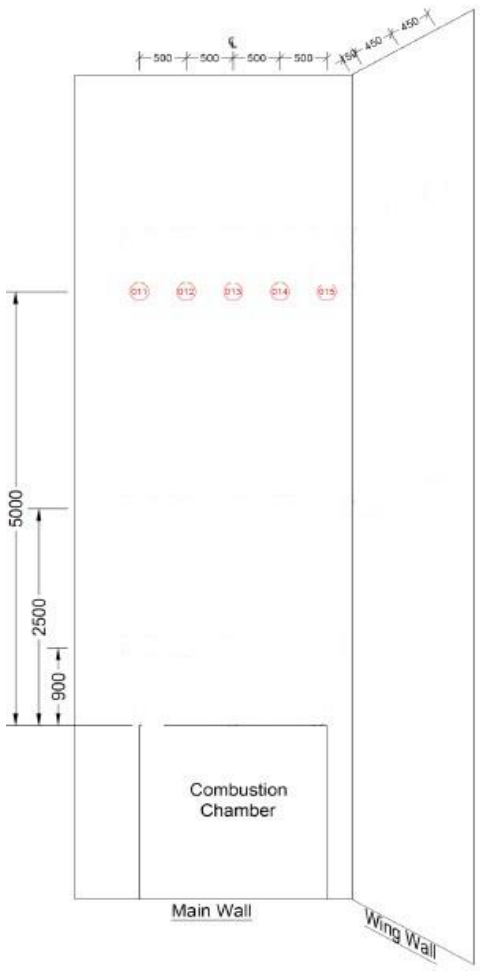

Figure 5.12. Place of thermocouples for assessment of criteria (a) from CSR report [12]

The cladding surface area of 1000 mm × 500 mm around each thermocouple is considered by assuming that each point receives heat from the assigned surrounding area and all material burns (no heat loss). Based on Sample 3's surface area and mass, and cladding surface area, the mass of the 3D GFRP nanocomposite cladding is calculated and presented in Table 5.3.

Figure 5.13. CSR full-façade fire test in accordance with AS 5113 and BS 8414-2 test method

Table 5.3. Calculation of cladding mass based on Sample 3's cone test results

	Length (m)	Width (m)	Area (m^2)	Mass (kg)
Cone calorimeter/Sample 3	0.100	0.101	0.01	0.02
Cladding (small section)	1	0.5	0.5	1
Full cladding			28.8	57.6

Note: Sample 3's values are an average of 5 samples

The fuel load is calculated based on the effective heat of combustion from the cone calorimeter test for Sample 3 (9.6 MJ/ kg) and the 3D GFRP nanocomposite cladding mass around the thermocouple (1 kg), which is 9.6 × 1= 9.6 MJ.

By having the specific heat capacity of GFRP (1028 J/kg°C), the cladding's mass, and fuel load Q(9.6 MJ), ΔT can be calculated from Equation 5.1, which is equal to 162° C.

$$Q = mc\Delta T \ \rightarrow \Delta T = \frac{Q}{mc} \qquad Equation\ 5.1$$

Q= heat transfer
m= mass of cladding (kg)
c= specific heat capacity (J/kg°C)
ΔT= temperature difference(°C)

The time-temperature curve (at 5 m above the opening) from the actual CSR test is shown in Figure 5.14. The peak point of maximum curves has been extracted (dot points in Figure 5.14) as initial temperature (T_1) for the 3D GFRP nanocomposite cladding. Obtaining ΔT from Equation 5.1 and T_1 from Figure 5.14, the T_2 curve which is the final maximum temperature in the new cladding system is calculated. Figure 5.15 shows the initial and final temperature curve at level 2 (5 m above the opening) of the 3D GFRP nanocomposite cladding. As can be seen in Figure 5.15, the maximum temperature is 502° C which is less than 600° C. This meets the criteria (a) of Section 5.4.5 AS 5113. The result is summarised in Table 5.4.

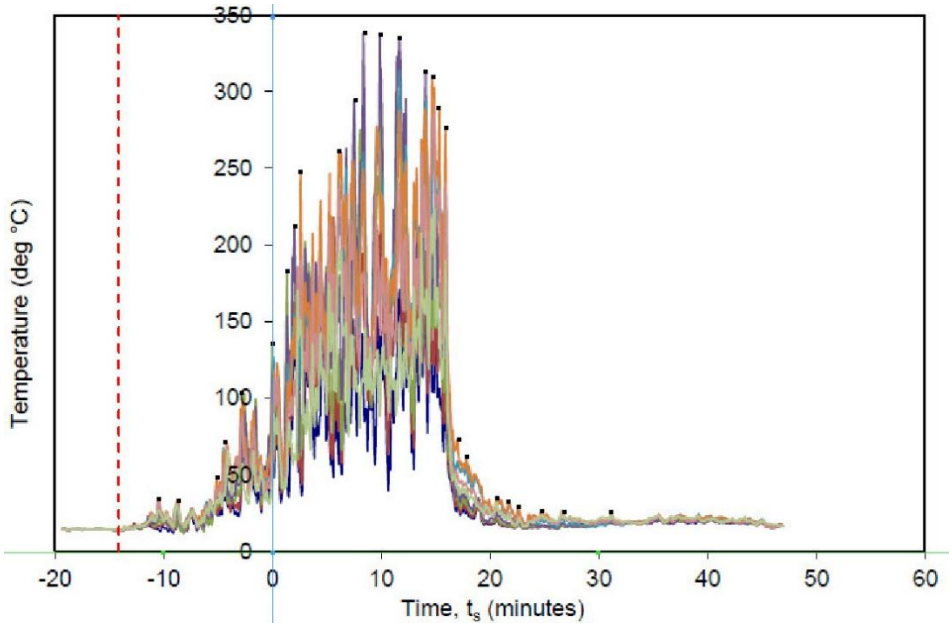

Figure 5.14. External temperature versus time at level 2, CSR test [12]

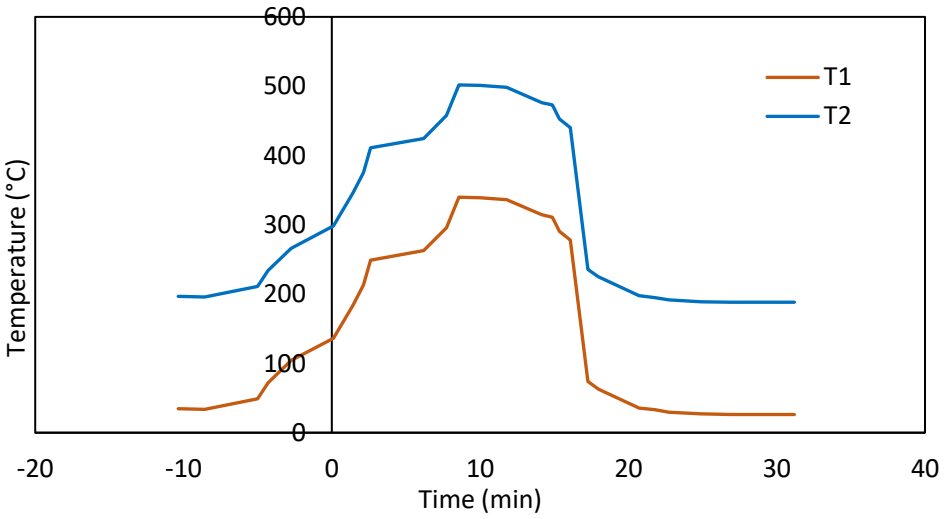

Figure 5.15. External time-temperaure curve (worst case scenario), for the 3D GFRP nanocomposite cladding (Sample 3)

Table 5.4. The AS 5113 EW classification criteria (a) as related to a BS 8414 test

Classification criteria	Related classification measure	Result in analytical approach	Pass/fail
5.4.5 (a) T_{w5m}	$\leq 600^\circ C$	Maximum 502° C at 19 min after crib ignition	Pass

According to Table 5.4, the 3D GFRP nanocomposite cladding (with Sample 3 composition) in the worst-case scenario (i.e., assuming all the heat is absorbed by the cladding; there is no heat loss) is estimated to pass the cladding criteria (a) of AS 5113.

Accepting the above procedure as a simplified preliminary way of estimating the potential full-scale fire test performance of new alternative cladding materials, the final temperature curves for all the other compositions of the 3D GFRP nanocomposite (Table 5.2) have also been computed.

In this way, the maximum final temperature of all compositions were calculated and found to be less than 600° C. In other words, all the new panel compositions meet criteria (a) of Section 5.4.5. AS 5113. This means that if the 3D GFRP nanocomposite cladding is used to replace the original cladding material in the same CSR façade system, the new 3D GFRP/Inclose system is likely to pass clause 5.4.5 (a) of AS 5113.

However, the approach presented herein can only be considered as a preliminary evaluation before a proper full-scale façade system test is undertaken in order to verify the results and evaluate the other criteria such as debris mass and flaming, temperature at cavity and unexposed face, and flame spread. With more and properly instrumented full-scale façade system tests in the future, a more robust approach, e.g. using computational fluid dynamic modelling, needs to be developed that allows the use of results from bench-tests such as those from the cone calorimeter tests to infer the fire performance of claddings with alternative cladding materials in full-scale tests.

5.6. Chapter summary

In this chapter, the thermal behaviour and fire performance of 3D GFRP phenolic composite panels have been studied. Results of TGA showed that Sample 4

(containing 15% of APP flame retardant) enhanced the thermal stability of the polymer more than the other compositions. In addition, cone calorimeter test results showed that Sample 3 (containing 10% of APP flame retardant), followed by Samples 4 and SP7, had lower fire reaction properties and better fire performance than the other samples. Also, these same samples showed higher fire safety as well. This means that adding 10% or 15% APP into the phenolic resin significantly improved the flame retardancy performance. Furthermore, the results of a simple analytical approach showed that an alternative cladding with 3D GFRP nanocomposite could potentially meet the AS 5113:2016 clause 5.4.5 (a) in full-scale façade system tests. However, this approach can only be considered as a preliminary evaluation. A proper full-scale façade system test needs to be undertaken in order to verify the results and evaluate the other fire performance criteria such as debris mass and flaming, temperature at cavity and unexposed face, and flame spread.

The tensile properties of the 3D GFRP nanocomposite panel are reported in the next chapter.

5.7. References

[1] Bar M, Alagirusamy R, Das A. Flame retardant polymer composites. Fibers and polymers. 2015;16:705-17.
[2] Zhang ZX, Zhang J, Lu B-X, Xin ZX, Kang CK, Kim JK. Effect of flame retardants on mechanical properties, flammability and foamability of PP/wood–fiber composites. Composites Part B: Engineering. 2012;43:150-8.
[3] Shen R, Hatanaka LC, Ahmed L, Agnew RJ, Mannan MS, Wang Q. Cone calorimeter analysis of flame retardant poly (methyl methacrylate)-silica nanocomposites. Journal of Thermal Analysis and Calorimetry. 2017;128:1443-51.
[4] Janssens M. Challenges in fire testing: a tester's viewpoint. Advances in Fire Retardant Materials: Elsevier; 2008. p. 233-54.
[5] Chen X, Jiao C. Study on flame retardance of co-microencapsulated ammonium polyphosphate and pentaerythritol in polypropylene. Journal of fire sciences. 2010;28:509-21.

[6] Petrella R. The assessment of full-scale fire hazards from cone calorimeter data. Journal of fire sciences. 1994;12:14-43.
[7] Babrauskas V. Bench-scale methods for prediction of full-scale fire behavior of furnishings and wall linings: Society of Fire Protection Engineers Boston, MA; 1984.
[8] Kandola B, Krishnan L. Fire performance evaluation of different resins for potential application in fire resistant structural marine composites. Fire Safety Science. 2014;11:769-80.
[9] Nguyen QT, Tran P, Ngo TD, Tran PA, Mendis P. Experimental and computational investigations on fire resistance of GFRP composite for building façade. Composites Part B: Engineering. 2014;62:218-29.
[10] AS 5113. Fire propagation testing and classification of external walls of buildings. 2016.
[11] BS 8414-2. Fire performance of external cladding systems: Part 2: Test method for non-loadbearing external cladding systems fixed to and supported by a structural steel frame. 2015-2017.
[12] Hebel E-C. Fire propagation testing of a 297mm thick external wall system clad with 0.55mm thick Lysaght DominionTM cladding in accordance with AS5113: 2016. 2017.

Chapter 6

Tensile properties of 3D GFRP nanocomposite

6.1. Introduction

In this chapter tensile properties of 3D GFRP phenolic nanocomposite, a non-load bearing cladding, are investigated. The 3D GFRP nanocomposite cladding is supposed to withstand self-weight when it is under tension in the façade system. That is the reason for studying its tensile properties. Materials, fabrication process, preparation of samples, experimental procedure, and calculations were explained in Chapter 3. In this chapter, results, and discussions of the tensile test at ambient temperature, are addressed.

6.2. Tensile properties of 3D GFRP phenolic nanocomposite

Table 6.1 shows tensile properties of different compositions of 3D GFRP phenolic nanocomposite specimens including strain percentage at failure(%ξ), maximum force before failure (P_{max}), ultimate tensile strength (F^{tu}), and modulus of elasticity (E) with their standard deviation calculated according to Section 3.14.2 of Chapter 3. The numbers are an average of five samples per composition tested under the same conditions. Standard deviations in Table 6.1 are quite similar with a bit of variation in some compositions. Higher standard deviation may be due to inconsistent presence of APP flame retardant, dispersion of nanoparticles and their percentages in each specific sample, small variations in specimen dimensions, and the percentages of resin absorbed by each glass fibres that may affect the sample dimension.

The behaviour of different compositions of 3D GFRP nanocomposite in the elastic region will be addressed first, following by the transition to plastic deformation, ultimate stress and strain, and their results and discussions.

Table 6.1. Average tensile properties of 3D GFRP nanocomposite

Sample	P_{max} (kN) [SD]	F^{tu} (MPa) [SD]	E (GPa) [SD]	%ξ at failure [SD]
1 [PR]	3.8 [0.03]	46.7 [0.62]	1.71 [0.46]	3.2 [0.08]
2 [5%APP + PR]	3.6 [0.12]	45.0 [1.26]	1.65 [0.28]	3.6 [0.1]
3 [10%APP + PR]	3.1 [0.04]	41.6 [0.78]	1.62 [0.09]	4.2 [0.5]
4 [15%APP + PR]	3.1 [0.42]	39.1 [7.20]	0.67 [0.13]	4.7 [0.6]
S5 [5%Sep +5%APP +PR]	3.5 [0.11]	44.1 [2.5]	1.02 [0.29]	3.9 [0.3]
S6 [5%Sep +10%APP + PR]	3.1 [0.35]	41.0 [5.54]	0.83 [0.17]	3.9 [0.7]
S7 [5%Sep+ 15%APP + PR]	3.3 [0.28]	43.3 [4.33]	1.19 [0.22]	3.6 [0.2]
S8 [10%Sep + 5%APP +PR]	3.6 [0.28]	47.5 [5.93]	0.75 [0.04]	4.5 [0.2]
S9 [10%Sep +10%APP +PR]	3.1 [0.16]	44.7 [3.32]	1.06 [0.16]	4.2 [0.2]
SP5 [5%SepP + 5%APP +PR]	3.3 [0.28]	41.2 [3.12]	1.25 [0.19]	3.5 [0.5]
SP6 [5%SepP +10%APP +PR]	2.5 [0.19]	32.1 [2.22]	1.29 [0.23]	2.8 [0.1]
SP7 [5%SepP +15%APP +PR]	2.4 [0.23]	30.0 [3.51]	1.92 [0.68]	2.2 [0.3]
SP8 [10%SepP +5%APP +PR]	3.3 [0.15]	43.8 [2.20]	1.24 [0.26]	3.6 [0.3]
SP9 [10%SepP + 10%APP +PR]	3.1 [0.22]	39.2 [2.20]	1.58 [0.42]	4.1 [0.2]

6.2.1. Tensile stress-strain response

A typical plot of a tensile stress-strain curve for one of the five samples of composition 1 (neat phenolic resin composite) is presented in Figure 6.1 with key features labelled. The curve shows three zones before failure. The first zone is called the “elastic phase” and was considered by a linear rise in the curves until a slight kink happened at a strain of 0.5% for the current sample (transition point). For other compositions, the elastic region varies between 0.2% and 1% strain with some fluctuations in different compositions (Figure 6.2). The region above the bend is called the “hardening phase” when, by increasing the strain, the curves continued to rise linearly up to 2.5% in the current curve (in other compositions hardening phase varies between 1.40% to 3%), but at a lower rate than in the elastic region. Above the strain of 2.5%, the third region

happened, in which the composite faced continuous softening until failure at a strain rate of 3.12% (in other compositions failure strain is between 2.5% to 5%). Further softening happened at higher strains through inelastic straightening of all the tows. In addition, some form of initial damage is generated after the elastic phase until failure as a string of jagged peaks and small load falls owing to the rupture of individual tows in almost all compositions of 3D GFRP composite samples. This is shown with arrows in Figure 6.1. The tensile failure occurs during the non-linear phase and this damage relates to mostly fibre failure in the warp yarns.

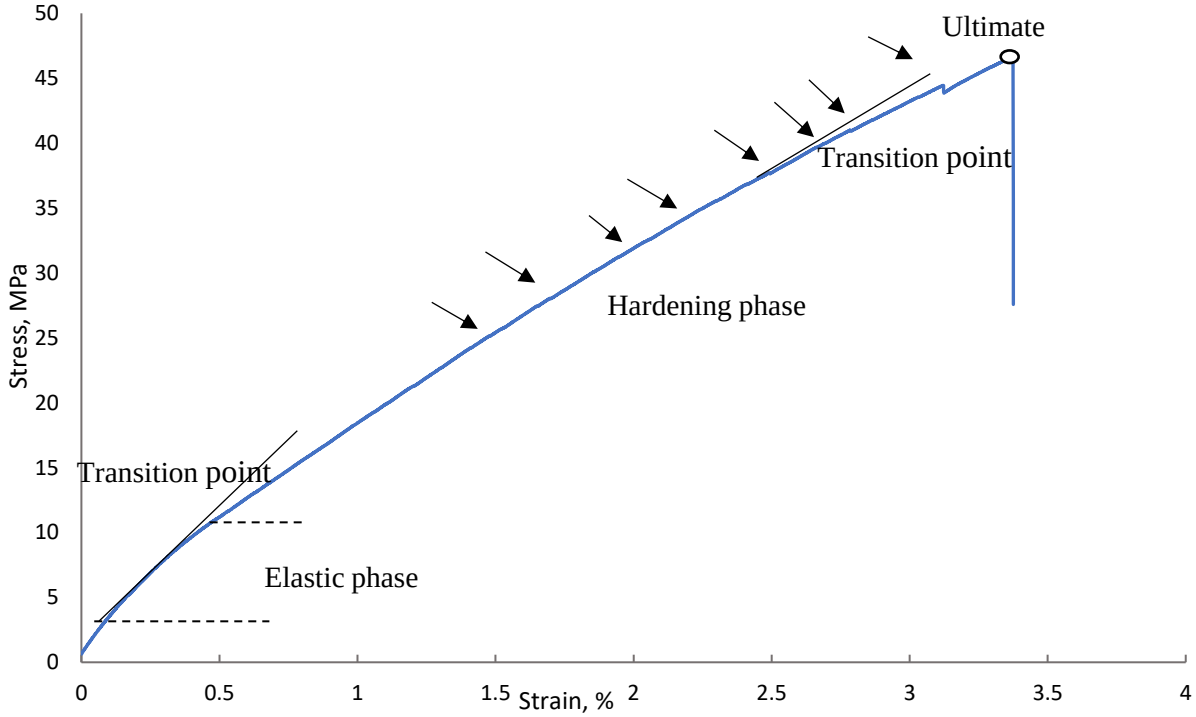

Figure 6.1. Stress-strain curve of one of the samples of composition 1

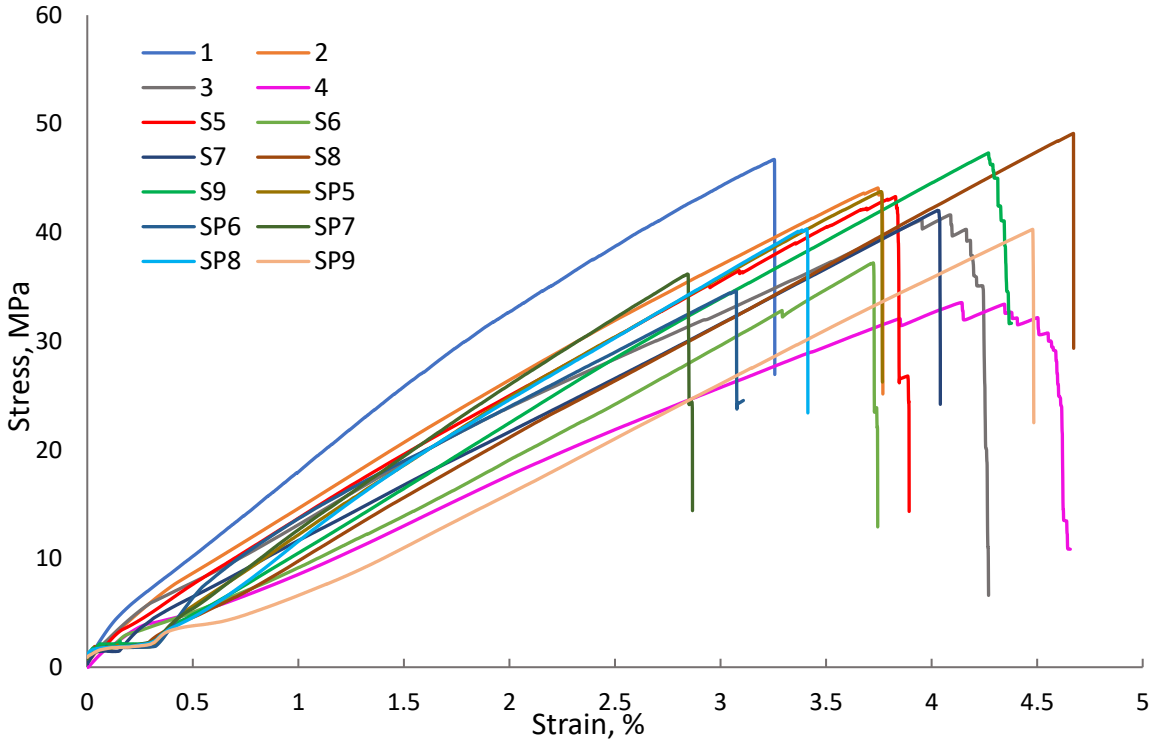

Figure 6.2. Stress-strain curve of Samples 1-SP9 (1 sample out of 5 samples per composition)

6.2.2. Young's modulus of 3D GFRP composites

Table 6.1 gives the average Young's modulus values for different compositions of 3D GFRP nanocomposite. The elastic modulus was measured from the linear section of the stress-strain curve for each sample according to ASTM D3039 [1]. The data shows that among Samples 1-4, with 5, 10, and 15% of APP flame retardant, stiffness decreased by 3%, 5%, and 60%, respectively. It means that adding 15% APP reduced the stiffness significantly.

In the samples with a constant 5% APP and 0, 5, and 10% of Sep/SepP nanoparticles (Samples 2, S5, S8, SP5, and SP8), adding 5% and 10% of Sep and SepP reduced the stiffness by 38%, 54%, 24%, and 24%, respectively. Sep samples reduced the modulus of elasticity more than SepP samples. Also, higher percentages of nanoparticles (10%)

had a lower value of elastic modulus than lower percentages of them (5%). In Samples 3, S6, S9, SP6, and SP9 containing a constant 10% of APP and 0, 5, and 10% of Sep/SepP nanoparticles, by adding Sep/SepP nanoparticles, stiffness decreased and this reduction is more significant in the sepiolite samples. Also, higher percentages of Sep/SepP samples had a higher value of E than the lower percentages of them. However, in the samples with a constant 15% of APP and 5% of Sep/SepP (Samples 4, S7, and SP7), adding 5% of Sep and SepP increased the stiffness by 77% and 186%, respectively. Also, Sample SP7 has the highest amount of stiffness (1.92 GPa).

Moreover, in the samples with a constant 5% of Sep fibres and 5, 10, and 15% of APP (Samples S5, S6, and S7), Sample S6 had the lowest value (0.8 3 GPa) followed by Sample S5 (1.02 GPa), and Sample S7 (1.19 GPa). However, in the Samples SP5, SP6, and SP7, with increasing APP from 5 to 15%, stiffness increased by 53%. In this case, Sep samples behaved differently from SepP samples. Looking through the Samples S8, S9, SP8, and SP9 including 10% of nanoparticles and 5% and 10% of APP, by increasing APP from 5% to 10%, the modulus of elasticity increased by 41% and 27% in the Sep and SepP samples, respectively. For a better comparison of samples, average E values are shown in Figure 6.3.

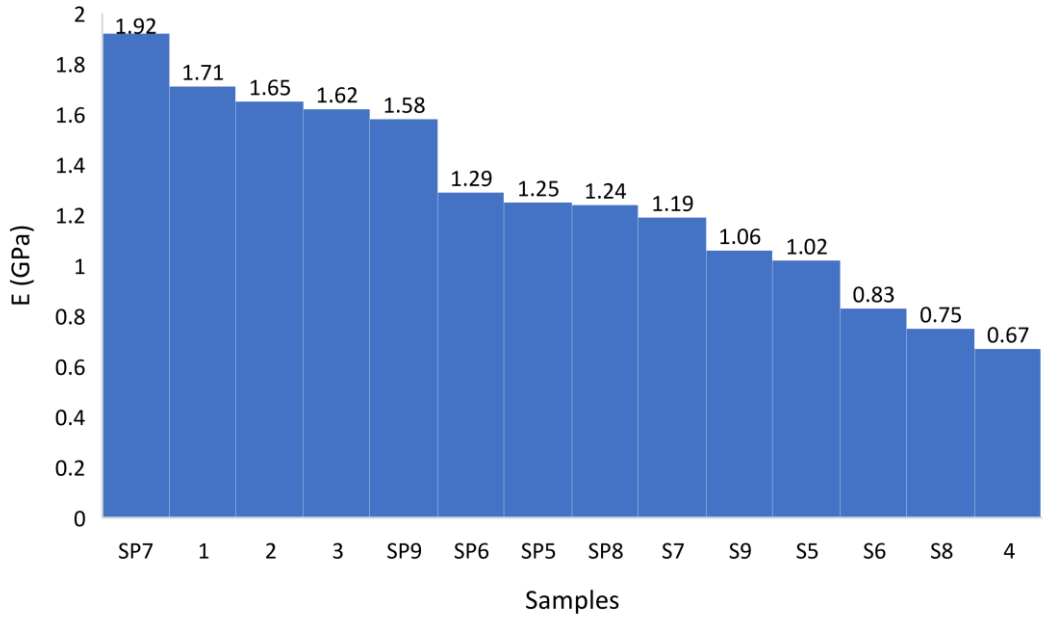

Figure 6.3. Young's modulus average values for 3D GFRP nanocomposite samples

From Figure 6.3, Sample SP7 (5% SepP + 15% APP) had the highest stiffness while Sample 4 (15% APP) has the lowest stiffness. It means that adding only 5% of SepP into Sample 4 significantly increased the stiffness from the bottom to the top. Other observations are:

- Neat phenolic resin and 5 and 10% of APP without the presence of nanoparticles showed the highest values of E.
- SepP samples showed a higher modulus of elasticity than sepiolite samples.
- In samples including both APP and Sep/SepP nanoparticles, higher stiffness was observed in samples with 15% APP, followed by 10%, and 5%.

6.2.3. Transition to plastic deformation

The transition point as it is shown in Figure 6.1 is when the stress-strain curve deflects from the linear phase to the non-linear phase. The mechanism for transition to the

non-linear phase is attributed to plastic tow straightening in which the initially wavy warp yarns straighten.

6.2.4. Ultimate stress and strain

The average of maximum tensile load, ultimate tensile strength, and ultimate strain percentage are compared in Table 6.1 for all samples with their standard deviations. From Table 6.1, by adding 5, 10, and 15% APP into the neat phenolic resin (Samples 1, 2, 3, and 4), ultimate strength decreased by 3%, 10%, and 16%, respectively, while corresponding strain percentage increased by 12%, 31%, and 46%, respectively. It means that adding APP flame retardant made the polymer more ductile.

In samples including a constant 5% of Sep/SepP and 5, 10, and 15% of APP, by increasing APP percentages in SepP samples, both ultimate strength and strain% decreased (F^{tu} = 22% and 27%, and %ξ = 20%, and 37%, respectively). Also, in Sep samples, ultimate strength decreased more in Sample S7 (43.3 MPa) than Sample S6 (41 MPa). Strain percentage remained the same for Samples S5 and S6 but decreased slightly in Sample S7 (7%).

Looking through Samples S8, S9, SP8, and SP9 containing constant 10% of Sep/SepP and 5%, and 10% of APP, by increasing APP percentage from 5% to 10%, ultimate strength decreased by 5% and 10% in Sep and SepP samples, respectively. Also, the ultimate strain% decreased in the Sep sample by 6% while it increased in the SepP sample by 13%.

In the samples with a constant 5% of APP and different percentages of Sep/SepP (Samples 2, S5, S8, SP5, and SP8), ultimate strength decreased except in Sample S8

which had a slight increase (5%). Also, higher percentages of Sep/SepP samples had higher ultimate strength than lower percentages. In terms of ultimate strain%, by adding Sep/SepP nanoparticles, ductility increased except in Sample SP5 (2% fall) and this rise was more in higher percentages of nanoparticle samples than lower percentages of them. In samples with 10% of APP and different percentages of Sep/SepP nanoparticles (Samples 3, S6, S9, SP6, SP9), by adding Sep fibres, ultimate strength decreased slightly (1%) in Sample S6 while it increased 7% in Sample S9. However, the ultimate strength in SepP samples (Samples SP6 and SP9) decreased by 22% and 5%, respectively. Failure strain% remained the same for Sample S9 while it reduced in other samples and this was more significant in Sample SP6 (33%). Also, higher percentages of Sep/SepP nanoparticles had a higher ductility than lower percentages. There are several studies on the positive effect of Sep fibres on the tensile properties of polymer composites [2-4].

In the samples with a constant 15% APP and 5% of Sep/SepP (Samples 4, S7, and SP7), Sample S7 had the highest ultimate strength (43.3 MPa) followed by Sample 4 (39.1 MPa), and Sample SP7 (30 MPa). However, Sample 4 had the highest %strain (4.7%) than Sample S7 (3.6%) and Sample SP7 (2.2%).

6.3. Results of the tensile test

From the discussion of Section 6.2, the following conclusions can be drawn:
Increasing the APP flame retardant content from 0% to 15% into the 3D GFRP composite (without nanoparticles) decreased the ultimate strength and elastic modulus by 16% and 61%, respectively. Increasing APP content in the Sep/SepP samples increased the elastic modulus while decreasing the tensile strength.

Increasing the Sep/SepP contents from 0% to 10% in samples with 5% or 10% of APP decreased elastic modulus while it increased the tensile strength in Sep samples and decreased it in the SepP samples. Also, increasing the Sep/SepP nanoparticles from 0% to 5% in the samples containing 15% APP, increased the tensile modulus while it decreased the ultimate strength in SepP samples, and increased it in Sep samples. Furthermore, Sample S8 showed the highest ultimate tensile strength, and Sample 4 showed the highest ultimate strain among the other samples.

6.4. Chapter summary

In this chapter, the tensile properties of 3D GFRP nanocomposite have been studied. Results show that adding APP into the neat phenolic resin sample decreased tensile properties while it increased ductility. Also, adding APP into the Sep/SepP samples decreased tensile properties. Moreover, in the samples with a constant percentage of APP flame retardant, and different percentages of Sep/SepP, tensile properties did not follow a consistent trend and some fluctuations in values were observed. It was also found that higher percentages of Sep/SepP nanoparticles (10%) showed higher load capacity, ultimate strength, and ductility than lower percentages (5%). In the next chapter, the results of Chapters 4, 5, and 6 will be further discussed.

6.5. References

[1] ASTM D3039. Standard test method for tensile properties of polymer matrix composite materials. ASTM International; 2008.
[2] Bidsorkhi HC, Mohamad Z. Effect of Sepiolite Content on Mechanical and Flammability Properties of Ethylene Vinyl Acetate Nanocomposite. Advanced Materials Research: Trans Tech Publ; 2014. p. 259-62.
[3] Kaymakci A. Effect of sepiolite clay nanofibers on physical, mechanical, and thermal properties of wood-plastic nanocomposites. Journal of Thermoplastic Composite Materials. 2020:0892705720939171.

[4] Manchanda B, Kakkarakkal Kottiyath V, Kapur GS, Kant S, Choudhary V. Morphological studies and thermo-mechanical behavior of polypropylene/sepiolite nanocomposites. Polymer Composites. 2017;38:E285-E94.

Chapter 7

Discussion of results

7.1. Introduction

This chapter presents the results of Chapters 4, 5, and 6 and discusses their significance and implications. The key topics include the characterisations of Sep and SepP, morphological characterisation of phenolic resin, studying of dispersion and curing of SepP-phenolic nanocomposite, morphological characterisation and fabrication of 3D GFRP phenolic nanocomposite, thermal analysis, fire performance, fire safety rating and tensile properties of 3D GFRP phenolic nanocomposite samples.

7.2. Characterisations of Sep and SepP

The thermal, morphological, and structural characterisations of Sepiolite fibres (Sep) and sepiolite-phosphate (SepP) nanoparticles that were used in the 3D GFRP phenolic composite were presented in Chapter 4. Thermal analysis of Sep and SepP samples (Figure 4.1) showed four weight losses due to the dehydration process on the TGA curve. Also, the DTA curve (Figure 4.1b) displays an important weight loss corresponding to free and structural water losses. It is observed that there is an exothermic peak around 340°C which has an associated weight loss and is due to the polymerisation procedure by condensation of acid phosphate to create a polymeric phosphate [1]. A water molecule is released in this reaction corresponding to the

reaction of hydroxyl groups of acid phosphate with another hydroxyl group. This peak is overlapped with the sepiolite dehydration.

As the TGAs (see Figure 4.1a) display, the gradient of the SepP curve is steeper than the Sep one in 100-250° C and 250-350° C. The first dehydration processes are because of sepiolite and phosphate and the second is assigned to sepiolite dehydration and phosphate condensation [1]. The results are in good agreement with Palacios et al. 's research [1].

HIM micrographs of SepP in Figure 4.2 show a uniform distribution of phosphate particles on the sepiolite fibres surface as a result of the direct precipitation process of aluminium phosphate on Sep nano fibres [1]. Observations from HIM, TEM, and HRTEM (Figures 4.2, 4.3, and 4.4, respectively) showed that the sepiolite fibres and phosphate nanoparticles sizes are 15-50 nm and 40-80 nm, respectively. Palacios et al. [1] found similar observations with SEM and TEM on SepP nanoparticles. An XRD characterisation has been done (see Section 4.4, Chapter 4) for Sep and SepP composite, studying the X-ray diffractograms to quantify the concentration of crystalline phases which were explained in Section 4.4, Chapter 4. It is found that the SepP sample's crystallinity is lower than that for the sepiolite even though no peaks of any phosphate are detected [1]. Also, the Palacios et al. [2] research on the homogeneous synthesis of aluminium phosphate showed that the synthesised phosphate is amorphous at the same reaction situations. A deeper study of SepP nanoparticles, their characterisations, and potential for being used as a filler in flame retardant systems has been conducted only in the Palacios et al. [1] research. However,

discovering a potential technological application of the SepP composite as a flame retardant is still missing.

7.3. Morphological characterisation of phenolic resin

Scanning electron microscopy (SEM-FEI Hitachi) analysis was conducted to understand the phenolic resin structure used in this research. According to Figure 4.8, there are micro voids [3, 4] on the phenolic resin surface with a diameter of less than 5 micrometres with an average diameter of 3.85 micrometres. The reason for this porosity is the long and complicated polymerisation process, producing the water and formaldehyde as by-products. The mechanical properties of phenolic resin may be compromised by porosity and controlling the porosity to the desired level still poses a scientific and industrial challenge [4]. A long heating cycle is needed to produce a void-free phenolic resin which is not desirable for many industries due to time and energy intake issues [5]. To reduce the number of defects and eliminate volatiles in the phenolic resin final product, accurate temperature control, and gradual heating are needed [6]. Hamad et al. [4] produced a phenolic resin with a void-free microstructure and optimising the size and distribution of voids throughout the choice of different catalysts. They showed that instead of minimising or avoiding void contents, achieving a homogenous void distribution is vital. However, this type of porosity is not a concern in this research since the proposed cladding will be used in a non-load-bearing façade system.

If the phenolic resin is used in applications in which mechanical properties of the final cured resin are important, further study on gelation time, temperature control, and catalyst type are needed.

7.4. Dispersion and curing of SepP-phenolic nanocomposite with three different methods

To study the phenolic resin (PR) curing process, and SepP dispersion in the resin, a mixture of 5% of SepP and 100% of phenolic resin was prepared and studied using three different methods as explained in Chapters 3 and 4.

The main differences between the three methods are: use of sonicator in Method 1, vacuumed oven in Method 2, and vacuumed desiccator in Method 3. Results of those three different methods showed that curing time and temperature of phenolic resin in Method 3 (using a vacuumed desiccator) was appropriate to avoid air bubbles in the resin and to have a void-free structure. The vacuum pumping needs to be done at room temperature to obtain the desired structure. In addition, the removal of phosphate coating from the sepiolite surface was not clearly observed in Methods 2 and 3. This may mean that sonication could be the reason for the removal of the phosphate coating in Method 1. However, since there is a lack of research in this area, further study is needed to understand the chemical reactions between the materials and the reason for the removal of the phosphate coating. In terms of SepP nanoparticle dispersion in the phenolic resin, magnetic stirring or sonication could not help since agglomeration happened in all three methods. Kahraman et al. [7] found that the sonication process is effective for the epoxy/nanoclay system while Sriraman et al. [8] find out that further homogeneous epoxy/clay dispersions may be achieved by shear mixing than sonication. Also, Natalie et al. [5] reached a good exfoliation of clays in a phenolic resin utilising a high shear mixer. Other methods of dispersion of clay in epoxy resin are mechanical stirring, ultrasonication, high-shear

mixing, ball milling, high-pressure mixing, and a slurry process [9]. However, the methods of dispersion of nanomaterials in a resin highly depend on the type of nanomaterial, it's shape, structure, percentages, and the type of resin and its viscosity. Therefore, it seems that a high shear force instrument [9, 10] is needed to disperse the SepP nanoparticles appropriately in this research. This is studied in the next section.

7.5. Dispersion analysis of Sep/SepP in the phenolic resin with three roll mills

Five samples of Sep/SepP phenolic resin (50 g) with different compositions were prepared for morphological characterisation as shown in Table 3.2, Chapter 3. Samples 1 to 5 were characterised by both SEM and HIM to observe the dispersion of the Sep/SepP in the nanocomposite. SEM and HIM micrographs of each composition are shown in Figure 4.16. It is observed that Sep and SepP in combination with APP flame retardant dispersed better than using only by itself in the resin.

In addition, using a thixotropic agent (Aerosil R805) and acetone showed a very good dispersion [10-12] but these also produced other issues such as air bubbles, splashing and wasting materials, chemical reaction, and structural change. Different solvents may affect the dissolvability and chain conformation of phenolic resin, and, as a result, alter its curing reaction and final properties [13]. The chain conformation of resole phenolic resin in the solution depends on the flexibility of the chain and the interaction between resin and solvent. Once the solvent is acetone, the interaction among resin and solvent is more powerful than that among the resin groups themselves, and the chain of resins tends to be open and extended. Therefore, the chain conformations of resin act as a loose coil, and viscosity decrease [13]. The curing time and temperature of acetone samples (Sep + APP + phenolic resin + acetone), and

the reason for their chemical reaction with other materials, need to examine carefully. Therefore, these two materials are not suitable to be used with Sep/SepP phenolic resin in the current study.

7.6. Morphological characterisation of Sep/SepP phenolic composite

Sep/SepP nanocomposite samples with different compositions of Sep, SepP and APP flame retardant prepared for fabricating 3D GFRP nanocomposite were observed with a helium ion microscope (HIM- Zeiss Orion NanoFab) to study the dispersion of nanocomposites. Table 4.6 and Figure 4.21 show sample compositions, and HIM micrographs of Samples 1 to 14, respectively.

Figure 4.21a shows a neat phenolic resin structure. Micrographs of 5, 10, and 15% APP flame retardant into the phenolic matrix can be seen in Figure 4.21 (b, c, and d). APP can be seen as a white chunk with a diameter of less than 10 μm in the phenolic resin which is dispersed uniformly. 5% of sepiolite fibres with 5, 10 and 15% APP can be seen in Figure 4.21 (e, f, and g). It is apparent that sepiolite possesses a fibrous and needle-like morphology and sepiolite nanofillers are consistently dispersed in the matrix. In addition, the resin covered the sepiolite surface, suggesting interaction between the surface of Sep and resin. It also shows that Sep fibres are placed between APP chunks (Figure 4.21f). APP flame retardant can be seen more in Figure 4.21g because of its higher percentages in the composition. Figure 4.21 (h, and i) represents 10% Sep in combination with 5 and 10% of APP. Sep fibres can be seen in the resin structure among APP chunks.

Figure 4.21j, Sample SP5, displays the crystallisation of the SepP in the sample. This can be seen as a bunch of crystal materials on the surface of phenolic resin in a way that recognising SepP nanoparticles in most parts of the sample is difficult. Chemical reactions separated the solid parts from the phenolic resin structure. This extent of crystallisation was mostly observed in the SP5 sample. However, agglomeration of sepiolite fibres can be seen between crystals in Figure 4.21j. In the other SepP samples, crystallisation happened in some parts; this is more significant in the SP7 and SP9 micrographs. Also, it seems that SepP nanoparticles did not preserve their core-shell structure since phosphate coating was not observed in the SepP samples. However, since there is no previous study on the SepP-phenolic resin matrix, the reason for crystallisation in SepP samples and the chemical reaction of materials are not yet fully understood. This needs further research and conducting the elemental compositions with SEM-EDS or TEM-EDS to find existing elements in the sample and analyse them.

7.7. Thermogravimetric analysis of Sep/SepP phenolic nanocomposite

Thermogravimetric analysis of Sep/SepP phenolic nanocomposite samples was investigated as explained in Chapters 3 and 5. Table 5.1 shows the specimens' number, composition, and weight loss at 850° C. Figure 5.1a shows the TGA graph of all samples.

Figure 5.2a shows the TGA graph for Samples 1 to 4. Sample 4 (15% APP) lost less weight (40.28%) than the other samples, followed by Samples 2 (50.34%), 3 (59%), and 1 (100%). It means that samples with the APP flame retardant remained with a higher residual mass compared with neat phenolic resin samples [14, 15]. There are contradicting results for thermal analysis and complete decomposition temperature of

pure phenolic resins in the literature depending on the type of resin and different curing processes. Bahramian et al. [16] studied the TGA of a resole phenolic resin at different heating rates in both air and nitrogen. Results showed that phenolic resin lost 70% weight in the nitrogen and the entire polymeric matrix was removed in the presence of atmosphere [17]. Kandola and Krishnan [18] studied the thermal stability and decomposition behaviours of different resins, and results showed that phenolic resole resin decomposed 100% at around 700° C. From Figure 5.2a, it can be said that higher percentages of APP flame retardant (15%) had higher thermal stability and thermal decomposition temperature [14].

From Figure 5.2b and Table 5.1, increasing Sep/SepP nanoparticles from 0% to 10% in the samples with a constant 5% of APP increased the mass loss percentages with an exception in Sample S8. In addition, higher percentages of nanoparticles (10%) remained more residual mass than lower percentages of them (5%). This is consistent with Alkan's and Kizilcan's work that showed higher percentages of sepiolite fibres remained more residual mass than lower percentages of them [19, 20]. Also, adding Sep/SepP nanoparticles increased the thermal stability compared with neat phenolic resin [20].

From Figure 5.2c and Table 5.1, increasing Sep/SepP nanoparticles in the samples with a constant 10% of APP decreased the weight loss percentages by 22%. However, there is an exception in Sample SP9. It also shows that combination of 10% APP with 5% nanoparticles protects the polymer by absorbing heat and creating a protective layer on the surface of the polymer [14]. Also, in Samples 4, S7, and SP7 (Figure 5.2d), with

15% of APP and 5% of nanoparticles, 15% of additives had better thermal stability and higher decomposition temperature than 20% of additives (4>S7>SP7).

In the samples with a constant 5% of nanoparticles and 5-15% of APP, samples with 10% APP lost less weight (by 44%) than the other samples, followed by 15% APP (52-64% loss), and 5% APP (76%) samples (Figure 5.2e). It means that adding APP flame retardant decreased the weight loss percentage and increased the thermal stability of the polymer [15]. The same scenario happened in the samples with a constant 10% of Sep/SepP nanoparticles and 5-10% of APP (Figure 5.2f).

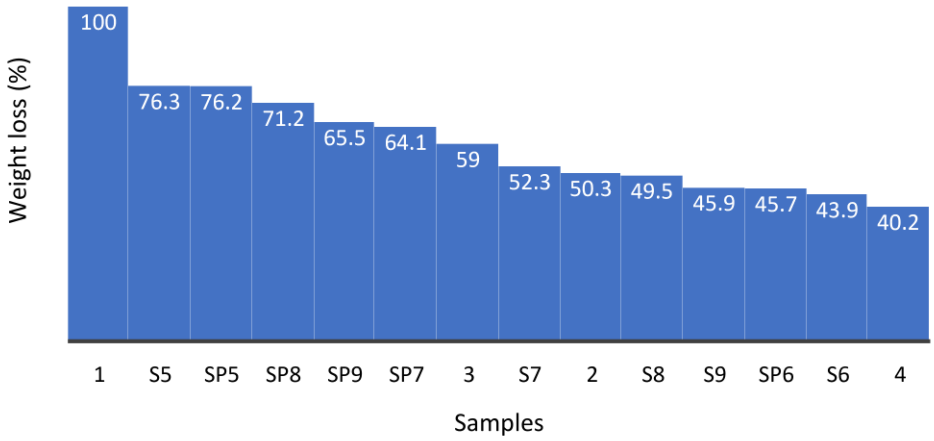

Figure 7.1. Weight loss percentages of all samples

For a better comparison between samples, weight loss percentages of all samples are shown in Figure 7.1. Results of thermogravimetric analysis of Sep/SepP phenolic nanocomposite samples showed that APP flame retardant significantly reduced the weight loss percentages and increased the thermal stability in both phenolic composite and Sep/SepP phenolic nanocomposite. For example, adding APP flame retardant from 5% to 15% into the neat phenolic composite decreased the weight loss by 20%. In addition, adding APP from 5% to 15% into 5% of Sep and SepP phenolic

nanocomposites decreased the weight loss by 31%, and 16%, respectively. This is in good agreement with the literature that APP intumescent flame retardant works in both gas and condensed phase and improves the thermal properties of polymers [14, 21]. However, the effects of Sep and SepP nanoparticles in the phenolic nanocomposite were different from APP results. It is observed that increasing SepP nanoparticles percentages (0% to 10%) into the phenolic nanocomposite increased the weight loss from 11-37% with different compositions of APP (exception: Sample SP6). On the other hand, increasing sepiolite fibres from 0-10% into the phenolic nanocomposite did not follow a constant trend and had some fluctuations. In addition, SepP samples lost more weight than Sep samples (exception: Sample S5). This may be due to the crystallisation of SepP samples and structural change of them or better dispersion of Sep fibres in the polymer.

7.8. Fire performance of 3D GFRP nanocomposite

The fire behaviour of 3D GFRP nanocomposite was evaluated using cone calorimeter tests as presented in Chapter 5. Table 5.2 and Figures 5.4-5.10 present the test results. Also, for a better comparison of the results, a summary of cone calorimeter data trends based on categorised samples is presented in Table 7.1.

Table 7.1. Summary of cone data trends for categorised samples

Samples	TTI	THR	PHRR	EHC	SEA	ML%
0% Sep/SepP, 0-15% APP	↓	↓	↓	↓	↓	↓
5% APP, 0-10% Sep/SepP	↓	↑	↑	↑	↑	↑↓
10% APP, 0-10% Sep/SepP	↓	↑	↑	↑	↑	↑
15% APP, 5% Sep/SepP	↑	↑ =	↑ =	↑↓	↑ =	↑
5% Sep/SepP, 5-15% APP	↑	↓	↓	↓	↓	↑
10% Sep/SepP, 5-10 %APP	↑↓	↓ =	↓	↓ =	↑↓	↑

According to Table 7.1, in samples without nanoparticles and containing APP (0-15%), all THR, PHRR, EHC, SEA, and ML% decreased. Samples 3 and 4 had almost the same values. This implies that the APP flame retardant reacted earlier than the phenolic resin and protected the polymer by forming a char layer on the polymer surface [14, 22]. Also, by looking through the APP percentages and results (Table 5.2), it is observed that 10% and 15% APP performed almost the same with a significant difference over samples with 0, and 5% APP.

In the samples with a constant 5% APP and 0-10% Sep/SepP nanoparticles, by increasing the Sep, and SepP nanoparticles, TTI decreased by 45% while THR, PHRR, and EHC increased between 14-20%, 8-14%, and 21-28%, respectively. Also, ML% decreased in Sep samples by 12% while it remained constant in SepP samples. In this case, the sepiolite samples behaved slightly better than SepP samples in terms of THR, PHRR, EHC, and ML%. This can be explained by the fibrous structure of sepiolite fibres [14], which may have dispersed better than the SepP nanoparticles. The same has been observed in the samples with a constant amount of 10% APP and 0-10% of Sep/SepP nanoparticles. In the samples with a constant 15% APP and 5% Sep/SepP, all fire properties increased slightly in Sep samples and remained unchanged in SepP samples. In this regard, SepP samples performed better than Sep samples. It is observed that a combination of 15% APP and 5% SepP showed a very good fire performance.

In addition, in the samples with a constant 5% of sepiolite and 5-15% of APP, by increasing the APP flame retardant, TTI increased by 55%, and 45% in the Sep and SepP samples. This is consistent with the results from Bar and Ramasamy [14], Cen

and Jiao [23], and Zhang et al. [15]. In addition, THR, PHRR, EHC, and smoke production decreased by 10-35%, 20-36%, 18-38%, and 87-91%, respectively, in the Sep and SepP samples. It shows that APP flame retardant positively affected the polymer and increased fire performance even in combination with the nanoparticles [14, 15, 21-23].

In the samples with a constant 10% of sepiolite and 5-10% of APP flame retardant, THR, PHRR, and EHC decreased in the Sep samples by 6%, 17%, and 20% while those amounts remained constant in the SepP samples except PHRR which decreased by 18%. Moreover, TTI increased in both Sep and SepP samples. It means that 10% APP showed a better fire performance than 5% APP in combination with 10% nanoparticle [15].

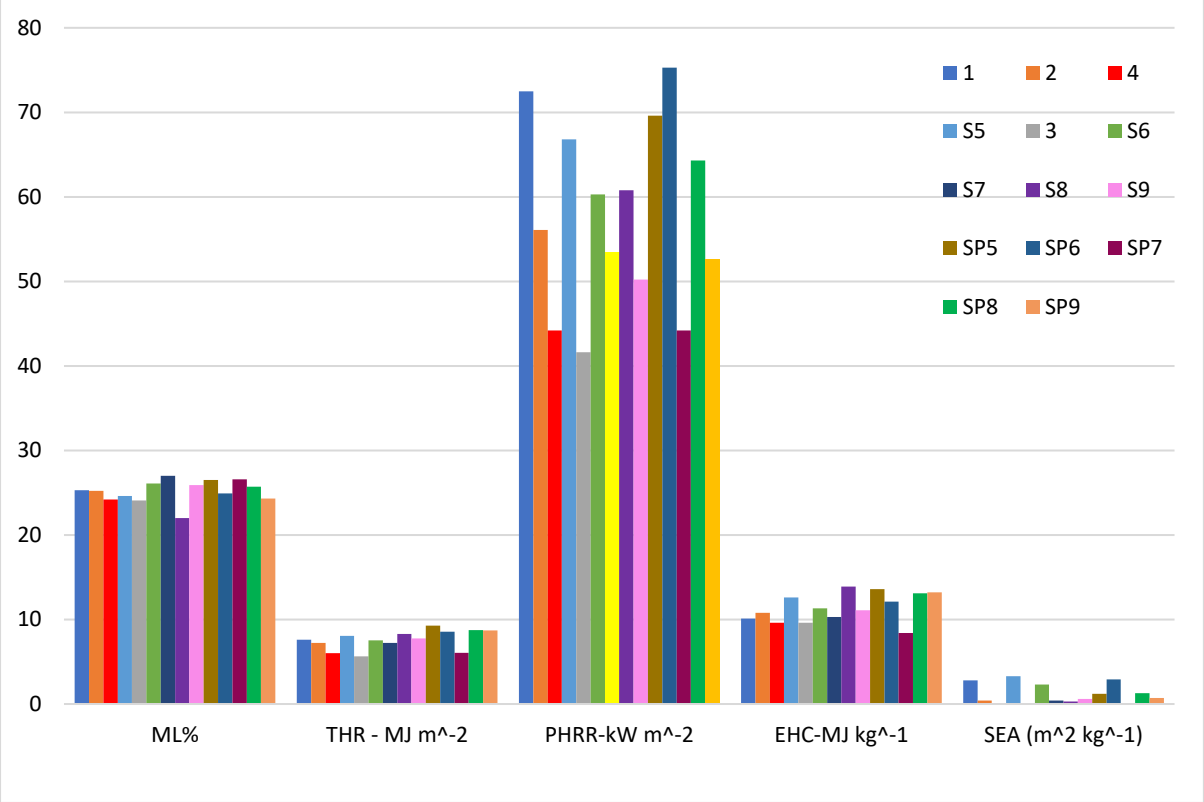

Figure 7.2. Comparison of cone calorimeter results for all compositions of 3D GFRP composite

Figure 7.2 shows the cone calorimeter test results for all compositions of 3D GFRP nanocomposite. Among Sep/SepP nanomaterial samples, SP7 showed a significantly lower amount in THR, EHC, SEA, and PHRR than the other samples. It seems that the combination of 5% SepP with 15% APP was ideal in terms of proper dispersion and interlocking with phenolic resin cross-link structure. This can be explained by the flame retardant property of SepP and it's 3d core-shell structure at high temperatures which protects the polymer at high temperatures and produces char [1]. However, the lower performance of other SepP samples compared with Sample SP7 may be due to crystallisation, chemical reaction, agglomeration, or content of APP in the sample, which needs further study. Through comparison of fire properties of all samples in Figure 7.2, Sample 3, followed by Samples 4 and SP7, showed higher fire performance (low THR, PHRR, EHC, and smoke production) than the other samples. These three samples had quite similar fire properties. It means that adding 10 or 15% APP into the phenolic resin significantly improves the flame retardancy performance [14].

The fire safety ratings of 3D GFRP compositions were studied and presented in Chapter 5. Two important parameters of fire safety of materials, namely fire growth rate (FIGRA) and fire performance index (FPI), have been calculated and presented in Table 5.2. A better understanding of full-scale fire behaviour, is obtained when the flashover (FIGRA) is combined with THR [24]. An X-Y scatterplot is provided for all material compositions in Figure 5.11. As discussed in Section 5.4, Chapter 5, all samples showed a low THR and high fire safety [24]. In terms of comparison between samples, Samples 3, 4, and SP7 showed higher fire safety than the other samples. It means that adding 10 or 15% APP in combination with 5% SepP into the phenolic resin significantly improves the fire safety of the polymer [25].

Some research has been previously undertaken to use mathematical models to predict the heat release of surface materials in the room-corner test according to cone calorimeter test outcomes [26-30]. Wickstrom and Goransson [30, 31] studied a theory for predicting the HRR of materials in a room corner test based on the ignition time and HRR history acquired from the cone calorimeter tests. They analysed the total heat release of nine products (rigid polyurethane foam, textile wallcovering on mineral wool, insulating fiberboard, expanded polystyrene, fiberboard, wood panel, paper wallcovering, particleboard, and melamine-faced particle board) and compared them with their experimental heat release curves. They showed that the proposed approach had good prediction of room-corner test heat release. Some years later, Jon Moln Teike [29] investigated a cone tools program to simplify the use of Wickstom and Goransson's model. However, those models have critical limitations. First, they only apply to homogeneous materials with no variations in the product. But more importantly, they examined the room corner test only (an indoor environment) and the behaviour of lining materials. Many of the existing models were developed for simple materials in a simple indoor fire test scenario. There is a gap in the literature on modeling techniques to predict the full-scale façade fire test, in an outdoor environment, for a wide range of materials with complex structures such as composite materials. Due to the lack of an appropriate model to predict the fire behaviour of 3D GFRP nanocomposite in a real-scale façade fire test, a simple analytical approach was developed in Chapter 5 to predict the cladding's acceptability based on full-scale façade fire cladding criteria with 3D GFRP nanocomposite cladding using only the cone calorimeter test results. The analytical approach is based on estimating from the time-temperature curve (at 5 m above opening) from the actual full-scale CSR facade

system test, the equivalent time-temperature curve of a system with 3D GFRP nanocomposite cladding. The result is then compared with the AS 5113:2016 [32] criteria 5.4.5(a). It is found that the new cladding material (3D GFRP) with the assumption of minimal heat loss meets the criteria (a) of the AS 5113:2016 [32].

To validate the above, full-scale façade fire tests with 3D GFRP nanocomposite cladding need to be conducted. The full-scale tests will also allow evaluation of other fire performance criteria such as debris mass and flaming, the temperature at cavity and unexposed face, and flame spread. Properly instrumented full-scale façade system tests should also be undertaken to develop a more robust approach, e.g. using computational fluid dynamic modelling, to allow the use of results from bench-tests such as those from the cone calorimeter tests to infer the fire performance of claddings with alternative cladding materials in full-scale façade tests.

7.9. Tensile properties of 3D GFRP nanocomposite

The tensile testing program was described in Chapter 3, and the results presented in Chapter 6. From Figure 6.1 (stress-strain curve), three regions before failure were identified: elastic phase (0.2%-1% strain), hardening phase (1.40%-3% strain), and softening phase (2.5%-5% strain). In addition, some form of initial damage is generated after the elastic phase until failure as a string of jagged peaks and small load falls because of the rupture of individual tows in almost all compositions of 3D GFRP nanocomposite. Also, tensile failure in the non-linear phase relates mostly to fibre failure in the warp yarns. The tensile properties of composites were similar to Callus et al. [33] in terms of three phases observation and Cox et al. [34] in observation of jagged peaks caused by small load falls before failure. However, this work was different

from Cox et al. [34] work in the pull-out phase. They observed a tow pull-out phase after failure which stretched the ultimate failure strain in carbon/epoxy composites while the 3D GFRP nanocomposites examined here ruptured entirely at the peak tensile stress and no pull-out was detected, which was similar to Callus et al. [33].

The ultimate tensile strength and tensile modulus of categorised samples are shown in Figures 7.3-7.8 for a better comparison between samples.

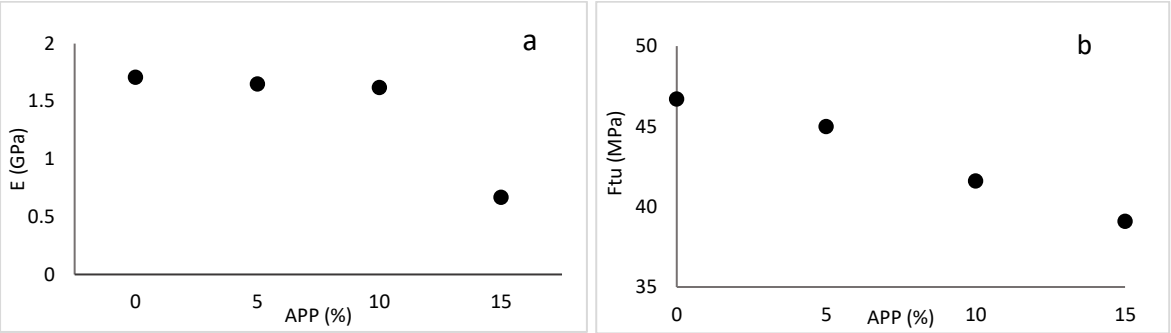

Figure 7.3. Average tensile modulus and ultimate strength of Samples 1-4: a) tensile modulus; b) ultimate strength

Effects of APP flame retardant

According to Figure 7.3, by increasing APP flame retardant from 0 to 10%, tensile modulus slightly decreased, and after 10% APP it dropped significantly. Also, by increasing APP from 0 to 15%, ultimate tensile strength decreased. The mechanical properties of fibre-reinforced polymer composite materials are significantly influenced by the adding micro-sized flame retardant fillers that is not suitable for different usage of composite materials [14]. Figure 7.4 shows samples with 5% Sep/SepP and 5-15% APP flame retardant.

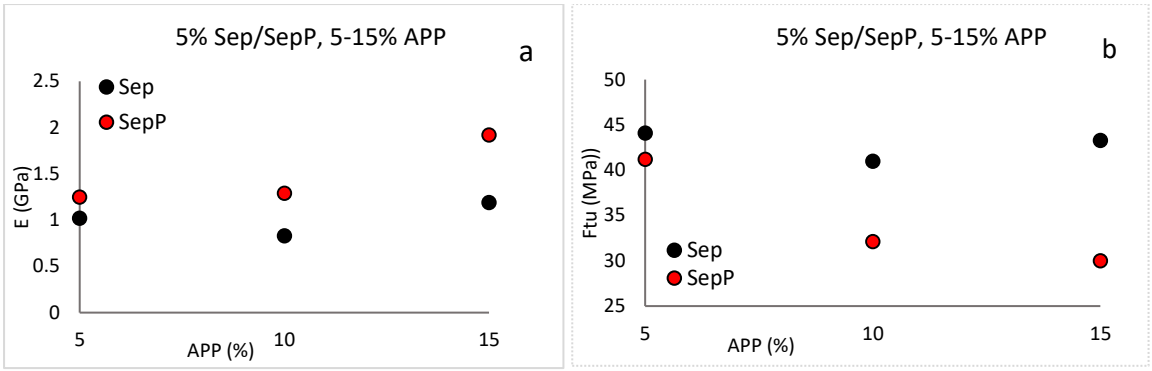

Figure 7.4. Average tensile modulus and ultimate strength of Samples S5, S6, S7, SP5, SP6, and SP7: a) tensile modulus; b) ultimate strength

In the samples with 5% Sep/SepP, by increasing APP from 5-10%, tensile modulus slightly decreased in the Sep sample while it slightly increased in the SepP sample. However, both the Sep/SepP graphs rose after 10% APP. In Figure 7.4b, increasing APP from 0% to 15% decreased the tensile strength in both Sep and SepP samples. The value was minimum at 10% of APP in the Sep sample while in the SepP sample the minimum amount was in the 15% of APP sample. In both graphs, an optimum amount of APP is 10% while tensile modulus and strength behaved differently after it. The effects of APP flame retardant in increasing tensile modulus and decreasing tensile strength are observed in Figure 7.5 with a constant 10% of Sep/SepP as well.

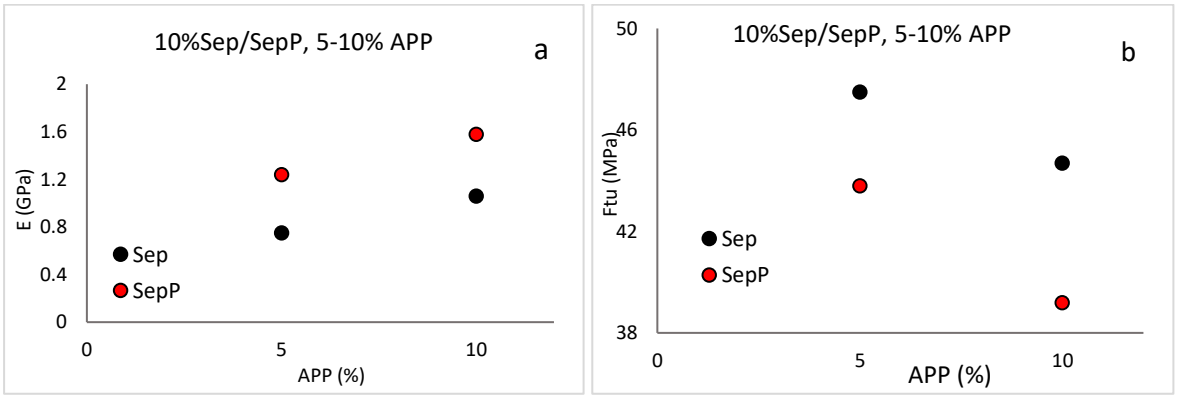

Figure 7.5. Average tensile modulus and ultimate strength of Samples S8, S9, SP8, and SP9: a) tensile modulus; b) ultimate strength

In both Figures 7.4, and 7.5, sepiolite samples showed a lower elastic modulus and higher tensile strength than the Sep samples. Research of Prabhakar et al. [35] showed that with increasing the percentage of APP from 3-9% in thermoplastic starch composites, elastic modulus slightly increased while tensile strength slightly decreased. In another study, adding APP into the sisal fibre/polypropylene composite increased the tensile modulus and decreased the tensile strength [21]. In addition, Zhang et al. [15] found that the tensile strength of the wood fibre/PP composites decreased with the addition of APP flame retardant from 0-40 phr.

Effects of Sep/SepP nanoparticles

From Figure 7.6a, in the samples with a constant 5% of APP, increasing the Sep and SepP nanoparticles from 0% to 10% decreased the elastic modulus by 54% and 25%, respectively, which was more significant in Sep samples. In terms of the tensile strength (Figure 7.6b), by increasing Sep/SepP nanoparticles from 0% to 5%, tensile strength decreased slightly in both Sep and SepP samples (<8%), and the fall was more significant in the SepP sample. By increasing the percentages of nanoparticles from 5% to 10%, the graph showed a rise which was more significant in the Sep sample than SepP. It showed that increasing the nanoparticles percentages more than 5% improves the tensile properties of the polymer.

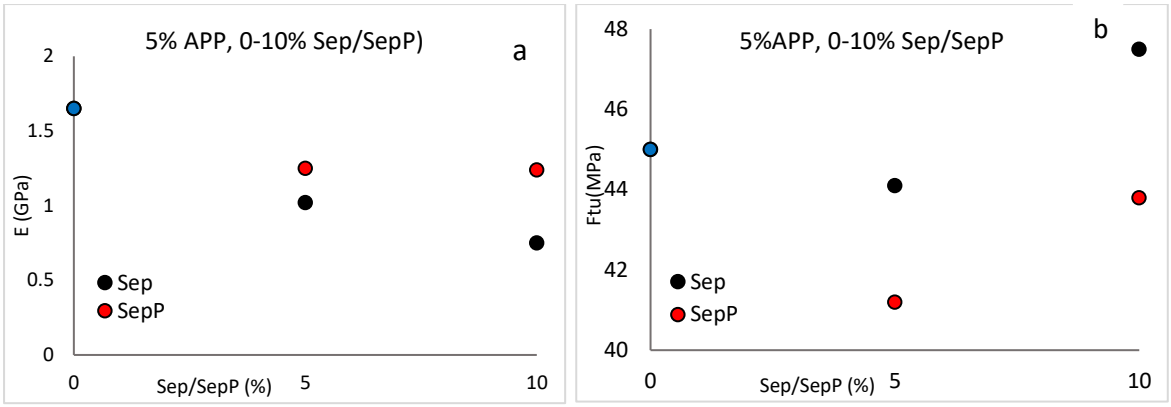

Figure 7.6. Average tensile modulus and ultimate strength of Samples 2, S5, S8, SP5, and SP8: a) tensile modulus; b) ultimate strength

The same behaviour was observed in Figure 7.7b for tensile strength in the samples with 10% of APP flame retardant. In addition, tensile modulus (Figure 7.7a) had a drop at 5% of nanoparticles and a slight rise after that.

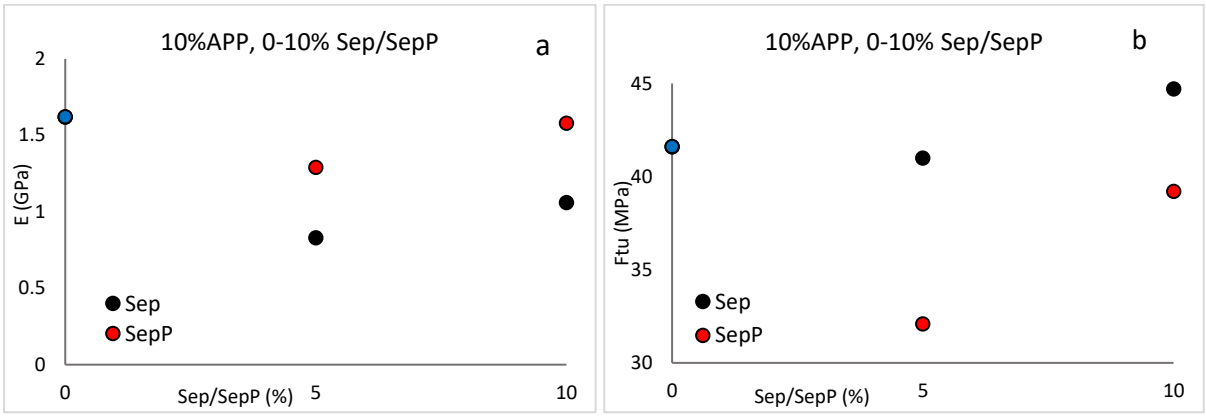

Figure 7.7. Average tensile modulus and ultimate strength of Samples 3, S6, S9, SP6, and SP9: a) tensile modulus; b) ultimate strength

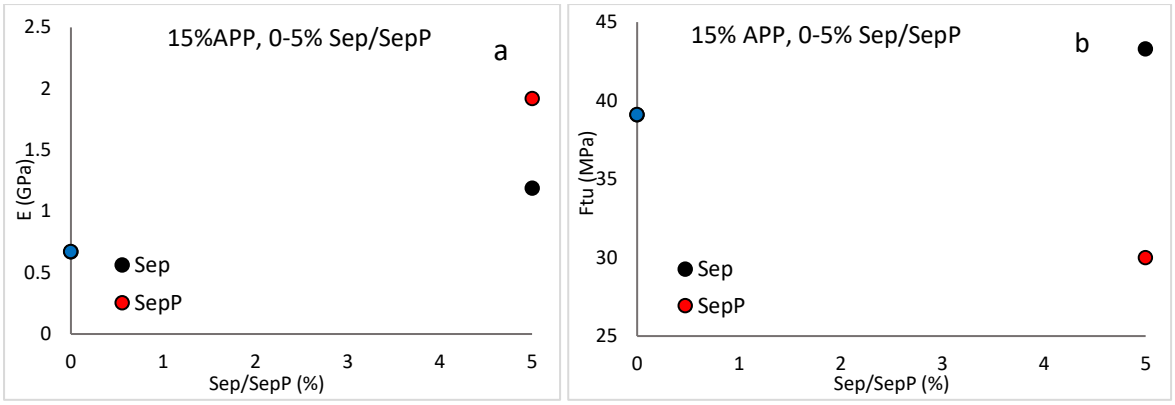

Figure 7.8. Average tensile modulus and ultimate strength of Samples 4, S7, and SP7: a) tensile modulus; b) ultimate strength

From Figure 7.8, in the samples with a constant 15% of APP, the tensile behaviour is different from 5% and 10% of APP samples. By increasing Sep and SepP nanoparticles from 0% to 5%, tensile modulus increased which is more significant in SepP samples (Figure 7.8a). Furthermore, ultimate tensile strength showed a rise in Sep samples and a drop in the SepP samples.

From the tensile test discussions, increasing APP percentage from 0% to 15% decreased the ultimate strength with and without the presence of nanoparticles. In the samples with nanoparticles, increasing APP percentages increased Young's modulus while, in the samples without nanoparticles, increasing APP percentages decreased the tensile modulus. These results are in good agreement with literature which shows deterioration of tensile properties with the addition of flame retardants in polymer composites [14, 15]. In samples containing a constant 5% APP, by increasing nanoparticles percentage from 0% to 10%, ultimate tensile strength slightly decreased in SepP samples while it increased in Sep samples. Also, elastic modulus decreased in both Sep and SepP samples. In samples containing a constant 10% APP, by increasing the nanoparticle's percentage from 0% to 10%, tensile modulus decreased while

tensile strength increased in Sep samples and decreased in the SepP samples. In samples containing a constant 15% APP, by increasing the nanoparticle's percentage from 0% to 5%, the elastic modulus increased, and the ultimate strength increased in the Sep sample while the ultimate strength decreased in the SepP sample. It was also found that higher percentages of Sep/SepP nanoparticles (10%) had a higher ultimate tensile strength than the lower percentages of them (5%).

There are contradictory results for the effects of nanomaterials on tensile properties of polymer composites in the literature [14, 36]. The tensile property highly depends on the size of the nanomaterial, its dispersion, type, content, structure, and compatibility with the matrix [15, 22, 36-38]. In the present research, Sample S8 (with 10% Sep and 5% APP) showed a significant improvement in tensile properties than the other compositions.

7.10. Comparison between fire performance and tensile properties of 3D GFRP nanocomposite samples

The previous sections showed that the APP flame retardant specifically at higher percentages significantly improved the thermal stability and fire performance of 3D GFRP nanocomposite. For instance, Samples 3, 4, and SP7 containing 10% and 15% of APP flame retardant had a better fire performance than the other samples. Also, Sample 4 (15% APP) showed the highest thermal stability and lowest weight loss in the TGA test. However, the addition of APP flame retardant contents decreased the tensile properties of 3D GFRP nanocomposite.

Sep and SepP nanoparticles, on the other hand, have not shown a significant improvement in the thermal and fire properties of the polymer except in some cases.

In general, sepiolite fibres had slightly better performance than SepP nanoparticles in thermal behaviour and fire properties of the composite except for Sample SP7 containing 5% SepP and 15% APP which showed a significant fire performance improvement among other compositions. Sepiolite fibres, regardless of APP amount, especially at higher percentages (10%) significantly improved the tensile properties of the 3D GFRP composite. For example, Sample S8 with 10% of Sep and 5% of APP improved the tensile properties of the polymer more than the other compositions.

7.11. Chapter summary

In this chapter, the results of Chapters 4, 5, and 6 were further discussed. Studying of different additives in the 3D GFRP nanocomposite showed that higher percentages of APP flame retardant (10% or 15%) improve the thermal stability, fire behaviour and fire safety while it deteriorates the tensile properties. Sep samples performed slightly better than SepP samples in both fire and tensile properties. Also, higher percentages of Sep/SepP nanoparticles (10%) showed better fire and tensile properties than the lower percentages of them (5%).

7.12. References

[1] Palacios E, Leret P, De La Mata MJ, Fernández JF, De Aza AH, Rodríguez MA et al. Self-Forming 3D Core–Shell Ceramic Nanostructures for Halogen-Free Flame Retardant Materials. ACS applied materials & interfaces. 2016;8:9462-71.
[2] Palacios E, Leret P, María J, Fernández JF, Antonio H, Rodríguez MA. Influence of the pH and ageing time on the acid aluminum phosphate synthesized by precipitation. CrystEngComm. 2013;15:3359-65.
[3] Parameswaran P, Bhuvaneswary M, Thachil ET. Control of microvoids in resol phenolic resin using unsaturated polyester. Journal of applied polymer science. 2009;113:802-10.
[4] Hamad SF, Farr N, Fei T, Shukor NF, Dean JS, Hayes SA et al. Optimizing size and distribution of voids in phenolic resins through the choice of catalyst types. Journal of Applied Polymer Science. 2019;136:48249.

[5] Natali M, Kenny J, Torre L. Phenolic matrix nanocomposites based on commercial grade resols: Synthesis and characterization. Composites science and technology. 2010;70:571-7.
[6] Munoz J-C, Ku H, Cardona F, Rogers D. Effects of catalysts and post-curing conditions in the polymer network of epoxy and phenolic resins: Preliminary results. Journal of Materials Processing Technology. 2008;202:486-92.
[7] Kahraman HT, Gevgilili H, Kalyon DM, Pehlivan E. Nanoclay dispersion into a thermosetting binder using sonication and intensive mixing methods. Journal of applied polymer science. 2013;129:1773-83.
[8] Zunjarrao S, Sriraman R, Singh R. Effect of processing parameters and clay volume fraction on the mechanical properties of epoxy-clay nanocomposites. Journal of materials science. 2006;41:2219-28.
[9] Zabihi O, Ahmadi M, Nikafshar S, Preyeswary KC, Naebe M. A technical review on epoxy-clay nanocomposites: Structure, properties, and their applications in fiber reinforced composites. Composites Part B: Engineering. 2017.
[10] Yasmin A, Abot JL, Daniel IM. Processing of clay/epoxy nanocomposites by shear mixing. Scripta materialia. 2003;49:81-6.
[11] Kawaguchi M. Dispersion stabilities and rheological properties of fumed silica suspensions. Journal of Dispersion Science and Technology. 2017;38:642-60.
[13] Yan Z, Yujian L, Qi H, Zhewen H. Effect of solvent on the chain conformation and cure behavior of phenolic resin. Journal of applied polymer science. 2008;108:3009-15.
[14] Bar M, Alagirusamy R, Das A. Flame retardant polymer composites. Fibers and polymers. 2015;16:705-17.
[15] Zhang ZX, Zhang J, Lu B-X, Xin ZX, Kang CK, Kim JK. Effect of flame retardants on mechanical properties, flammability and foamability of PP/wood–fiber composites. Composites Part B: Engineering. 2012;43:150-8.
[16] Bahramian AR, Kokabi M, Famili MHN, Beheshty MH. Ablation and thermal degradation behaviour of a composite based on resol type phenolic resin: process modeling and experimental. Polymer. 2006;47:3661-73.
[17] Ávila AF, Dias EC, Cruz DTLd, Yoshida MI, Bracarense AQ, Carvalho MGR et al. An investigation on graphene and nanoclay effects on hybrid nanocomposites post fire dynamic behavior. Materials Research. 2010;13:143-50.
[18] Kandola B, Krishnan L. Fire performance evaluation of different resins for potential application in fire resistant structural marine composites. Fire Safety Science. 2014;11:769-80.
[19] Alkan ÜB, Kızılcan N. In situ preparation of resol/sepiolite nanocomposites. Procedia-Social and Behavioral Sciences. 2015;195:2067-75.
[20] Alkan ÜB, Kızılcan N. Characterization of nanocomposite resol resins: Individual/synergist effects of alendronic acid and sepiolite. Journal of Applied Polymer Science. 2016;133.
[21] Jeencham R, Suppakarn N, Jarukumjorn K. Effect of flame retardants on flame retardant, mechanical, and thermal properties of sisal fiber/polypropylene composites. Composites Part B: Engineering. 2014;56:249-53.
[22] Shumao L, Jie R, Hua Y, Tao Y, Weizhong Y. Influence of ammonium polyphosphate on the flame retardancy and mechanical properties of ramie fiber-reinforced poly (lactic acid) biocomposites. Polymer International. 2010;59:242-8.

[23] Chen X, Jiao C. Study on flame retardance of co-microencapsulated ammonium polyphosphate and pentaerythritol in polypropylene. Journal of fire sciences. 2010;28:509-21.
[24] Petrella R. The assessment of full-scale fire hazards from cone calorimeter data. Journal of fire sciences. 1994;12:14-43.
[25] Hirschler MM. Flame retardants and heat release: review of data on individual polymers. Fire and Materials. 2015;39:232-58.
[26] Babrauskas V, Wickstrom U. The rational development of bench-scale fire tests for full-scale fire prediction. Fire Safety Science. 1989;2:813-22.
[27] Karlsson B. A mathematical model for calculating heat release rate in the room corner test. Fire Safety Journal. 1993;20:93-113.
[28] Lannon CM, Stoliarov SI, Lord JM, Leventon IT. A methodology for predicting and comparing the full-scale fire performance of similar materials based on small-scale testing. Fire and Materials. 2018;42:710-24.
[29] Moln Teike J. Improved version of Cone Tools for predictions of Room Corner Tests. 2011.
[30] Wickström U, Göransson U. Prediction of heat release rates of surface materials in large-scale fire tests based on cone calorimeter results. Journal of testing and evaluation. 1987;15:364-70.
[31] Babrauskas V, Parker WJ. Ignitability measurements with the cone calorimeter. 1986.
[32] AS 5113. Fire propagation testing and classification of external walls of buildings. 2016.
[33] Callus P, Mouritz A, Bannister MK, Leong K. Tensile properties and failure mechanisms of 3D woven GRP composites. Composites Part A: applied science and manufacturing. 1999;30:1277-87.
[34] Cox BN, Dadkhah MS, Morris W. On the tensile failure of 3D woven composites. Composites Part A: Applied Science and Manufacturing. 1996;27:447-58.
[35] Prabhakar M, Song J-I. Improved flame-retardant and tensile properties of thermoplastic starch/flax fabric green composites. Carbohydrate polymers. 2017;168:201-11.
[36] Amin MR, Al-Harthi MA, Imran S, Hussain M. Effect of Nanoparticles on Mechanical and Flame-retardant Properties of Polyether-Block-Polyamide Polymer Nanocomposites. Polymer-Plastics Technology and Engineering. 2018;57:38-45.
[37] Khoathane MC, Vorster O, Sadiku E. Hemp fiber-reinforced 1-pentene/polypropylene copolymer: the effect of fiber loading on the mechanical and thermal characteristics of the composites. Journal of Reinforced Plastics and Composites. 2008;27:1533-44.
[38] Ku H, Wang H, Pattarachaiyakoop N, Trada M. A review on the tensile properties of natural fiber reinforced polymer composites. Composites Part B: Engineering. 2011;42:856-73.

Chapter 8

Conclusions and recommendations

8.1. Introduction

In reviewing the required and the actual performance of building envelopes or façade systems, two of the most common causes of failure were corrosion of steel elements and the cladding itself, especially in a fire event. Research and standards related to the corrosion of steel elements in a façade system was comprehensively and systematically reviewed to develop practical guidance to improve the design, specification and construction of steel elements in facades. This work has been published, and presented in Appendices A and B. Thus, the main focus of the thesis turns to the fire performance of the cladding material.

Fire safety is one of the most critical performance requirements of a façade system. Fire reaction of cladding materials in the façade system determines the extent and the rate of fire spread. In a fire event, this can pose a risk to occupant safety and property loss.

The main goal of this research is to improve façade system performance through the development of a new type of cladding material with improved fire performance properties. Research to date has shown the potential for 3D GFRP phenolic nanocomposite as a base for an alternative cladding material with improved fire requirements. Thus, in support of the above goal, the three objectives are to:

1. Determine the appropriate contents mix and fabrication parameters for a new cladding panel with 3D GFRP phenolic nanocomposite;
2. Study the thermal stability and fire performance of 3D GFRP phenolic nanocomposite material samples; and
3. Investigate the tensile properties of the 3D GFRP phenolic nanocomposite material samples.

To achieve these objectives, 3D GFRP phenolic nanocomposite samples were fabricated. First, SepP synthesis was investigated, and nano structural characterisations were conducted. Then, 3D GFRP phenolic nanocomposite panels with different compositions of Sep, SepP, and APP flame retardant were fabricated. After morphological and thermal characterisations of the nanocomposite samples, the thermal stability, fire reaction, and tensile properties of 3D GFRP nanocomposite were tested according to AS/NZS 3837 [1], AS 5113 [2], and ASTM D3039 [3], respectively.

In this chapter, the main thesis findings and conclusions drawn are presented, followed by the recommendations for future research.

8.2. Major findings

8.2.1. Characterisations of SepP, and phenolic resin

The characterisation of SepP showed that its structure (3D), elements composition, phase, size, and thermal behaviour are in line with the literature and has a flame retardant potential. Morphological characterisation of phenolic resin showed micro voids that are not considered to be critical since the proposed nanocomposite will be used as a cladding material in a non-load-bearing façade system.

8.2.2. Dispersion and curing of Sep/SepP phenolic nanocomposite

The dispersion analysis and curing of SepP phenolic nanocomposite were studied with three different methods. Results show that curing time and temperature of phenolic resin in Method 3 (by using a vacuum desiccator) was appropriate. Also, a vacuum pump seems to be suitable for degassing the resin. However, it must be done at room temperature to obtain the desired structure. In terms of SepP nanoparticle dispersion in the phenolic resin, the three roll mill instrument was very useful in dispersing both Sep and SepP nanoparticles into the resin because of its power in high shear mixing of materials. It is concluded that the critical parameters to pay attention are preserving of nanomaterial structure, compatibility with other materials, dispersion control and using an appropriate high shear mixing instrument, and phenolic resin curing time and temperature control.

8.2.3. Fabrication of 3D GFRP phenolic nanocomposite

After fabrication of 3D GFRP phenolic nanocomposite, the morphological characterisation of samples showed the dispersion of APP with a diameter of less than 10 μm and sepiolite fibres. Some crystallisation happened in the SepP samples mostly in Sample SP5 (5% SepP + 5% APP + PR) due to chemical reaction and structural change of nanocomposite. This needs further study.

8.2.4. Thermal and fire performance of 3D GFRP phenolic nanocomposite

The key observations from the TGA tests are as follows:

APP micro-size flame retardant between 5-15% significantly improved the thermal stability and decomposition temperature of the polymer. Also, the better thermal

performance has been observed in the samples with 15% APP flame retardant without nanoparticles and 10% APP in combination with 5% Sep/SepP nanoparticles. It means that the optimum amount of additives that positively affected the polymer and increased thermal performance was 15% flame retardant.

From the cone calorimeter tests, the key findings are as follows:
Increasing the APP flame retardant percentage (between 0-15%) improved the fire reaction properties of 3D GFRP nanocomposite regardless of the presence of Sep/SepP nanoparticles. For instance, an increasing APP from 0-15% in the samples without nanoparticles decreased THR, PHRR, and SEA by 20%, 30%, and 96%, respectively. Also, adding APP from 5-15% in the 3D GFRP nanocomposite, with the presence of Sep/SepP, decreased the fire reaction properties between 10-87% in the Sep and 34-92% in the SepP samples.

Increasing sepiolite fibres percentages (0-10%) slightly increased the fire reaction properties of 3D GFRP nanocomposite. For example, THR increased between 14-37% in different compositions of APP while smoke production values showed some variations.

Similarly, adding SepP nanoparticles into the 3D GFRP nanocomposite increased the fire reaction properties. For instance, by increasing percentages of SepP from 0% to 10%, THR increased between 20-54% in different APP samples.

Through comparison of all samples, Sample 3 (10% APP + PR), followed by Samples 4 (15% APP + PR) and SP7 (5% SepP + 15% APP + PR), showed better fire reaction properties than the other samples. It means that adding 10% or 15% APP into the phenolic resin significantly improved the flame retardancy performance regardless of

nanoparticles. The APP flame retardant improved the fire performance of 3D GFRP nanocomposite panels more than that with sepiolite fibres and SepP nanoparticles. Among Sep/SepP samples, only Sample SP7 (5% SepP + 15% APP + PR) improved the fire reaction properties significantly and other compositions of Sep/SepP did not have any significant positive effects on the fire reaction properties of the phenolic matrix except in a few cases.

In addition, the results of FIGRA and FPI, which are used for prediction of full-scale fire behaviour from a bench-scale test and rating of fire safety, showed that all the compositions of 3D GFRP nanocomposite have FIGRA value less than 1 (good fire safety) and THR of less than 10 MJ/m^2 (very low). In terms of comparison between different compositions, Samples SP7 (5% SepP + 15% APP + PR), 3 (10% APP + PR), and 4 (15% APP + PR) showed quite similar fire safety behaviour and have lower values than other compositions.

A simple analytical approach to estimate the potential performance of an alternative cladding material in a full-scale façade system fire test was developed based on the time-temperature curve of an actual full-scale test. Results showed that the new 3D GFRP nanocomposite cladding in the CSR Inclose façade system meets the 5.4.5(a) criteria of AS 5113:2016.

8.2.5. Tensile properties of 3D GFRP nanocomposite

The tensile stress-strain curves for 3D GFRP nanocomposite at ambient temperature showed three regions, namely “elastic phase, hardening phase, and softening phase” before failure. The elastic region is between 0.2%-1% strain, the hardening region varies between 1.4%-3%, and softening region occurs between 2.5-5% strain for

different compositions of 3D GFRP nanocomposite. A string of jagged peaks and small load falls because of rupture of individual tows in the hardening phase until failure has been observed in almost all compositions.

From the tensile test, it was found that among the three flame retardants, sepiolite fibres especially in higher concentration (10%) improve the tensile properties of 3D GFRP nanocomposite while APP and SepP only improve the ductility in a few cases. The key observations are as follows:

Effects of APP: when APP (5-15%) with a combination of Sep or SepP is used in the 3D GFRP composite, tensile properties decrease. However, the presence of APP (0-15%) without nanomaterials in the 3D GFRP composite decrease the ultimate strength (by 16%) while it increases the ultimate strain (by 46%). As an example, an increasing APP from 5-15% in the 5% Sep and SepP 3D GFRP nanocomposite decreased the ultimate strength (1% and 27%) and strain (7%, 37%) while it increased Young's modulus (16%, 53%). As can be seen from the above example, those amounts are more significant in SepP samples.

Effects of Sep and SepP: increasing the percentages of Sepiolite fibres from 0-10% into the 3D GFRP composite improve the tensile properties. For example, the ultimate tensile strength increased by 5% and 14% and ultimate strain increased by 25% in different percentages of APP samples. However, adding SepP from 0-10% into the 3D GFRP composite decrease tensile properties slightly (<5%).

In comparing Sep and SepP samples, it was found that sepiolite samples show higher ultimate tensile strength (6-30%) and strain (2-39%) than SepP samples. Also, higher

percentages of Sep/SepP nanoparticles (10%) showe better tensile properties (<20% increased) than lower percentages (5%) of them.

8.3. Conclusions

The three flame retardants (Sep, SepP, and APP) improve the thermal stability and the fire performance of 3D GFRP nanocomposite panels. Among the three, the APP flame retardant influences more on improving the thermal and fire reaction properties while the sepiolite fibres influence more on improving the tensile properties of 3D GFRP nanocomposite. Preliminary results of an analytical approach to estimate the potential performance of the 3D GFRP nanocomposite as an alternative cladding material in a full-scale façade system fire test showed that the new nanocomposite cladding may meet certain criteria according to AS 5113:2016, Section 5.4.5(a). If this is validated by full-scale fire performance testing, this cladding material has the potential to offer new opportunities for the construction material industry nationally and internationally.

8.4. Recommendations and future research

The proposed next steps are to optimise the chemical and material composition for optimum performance of the nanocomposite panel, refine the fabrication process for pilot manufacturing of full-size cladding panels, and undertake full-scale fire tests of façade systems that incorporate the new material. According to the Australian National Construction Code (ABCB, volume 1, Section C, performance solutions), the external wall of a building needs to be non-combustible or avoid fire spread within a building and to adjacent buildings for most Type A or B building. Hence, the combustibility test (AS 1530.1) or full-scale fire test (AS 5113) needs to be conducted on the façade system that incorporates 3D GFRP nanocomposite. In addition, a deeper

knowledge of chemistry and material science can be useful to study the chemical reaction of SepP, APP and phenolic resin as well as understanding their structural change and crystallisation. Since the proposed cladding material may be used in different façade systems and cladding panels can be under tension after installation, the high-temperature tensile strength properties of nanocomposite should be investigated. Finally, towards potential commercialisation of 3D GFRP nanocomposite cladding, other performance properties such as cost, weather durability, compatibility with other façade materials, method of installation, and so on. need to be considered.

8.5. References

[1] AS/NZS 3837. Method of test for heat and smoke release rates for materials and products using an oxygen consumption calorimeter. 2016.
[2] AS 5113. Fire propagation testing and classification of external walls of buildings. 2016.
[3] ASTM D3039. Standard test method for tensile properties of polymer matrix composite materials. ASTM International; 2008.

Appendix A – Journal paper

Journal of Building Engineering 32 (2020) 101759

Contents lists available at ScienceDirect

Journal of Building Engineering

journal homepage: http://www.elsevier.com/locate/jobe

Corrosion protection of steel elements in façade systems – A review

Leila Soufeiani [a,*], Greg Foliente [a], Kate.T.Q. Nguyen [b], Rackel San Nicolas [a]

[a] Department of Infrastructure Engineering, Faculty of Engineering, The University of Melbourne, Melbourne, Australia
[b] School of Engineering, RMIT University, Melbourne, Australia

ARTICLE INFO

Keywords:
Façade systems
Steel corrosion
Corrosion protection
Service life

ABSTRACT

Corrosion of steel elements in a façade system may cause failure that can adversely affect building performance. In this paper we review and synthesize the scientific literature in order to provide practical guidance for engineers, designers and material/product specifiers to avoid or minimize the corrosion of steel elements in façade systems as well as to identify the challenges for future research. The review covered different types of corrosion such as atmospheric, galvanic or bimetallic, embedded, and cut-edge corrosion and how different factors affect the corrosion rate of steel. Preventing or minimising the potential for steel corrosion in a building façade involves examination of the surrounding environment, a proper design of façade system, selecting a suitable steel grade, choosing an appropriate coating, and undertaking maintenance regularly. Further research has been identified, including the development of environmentally friendly and low cost nanocoatings, and establishing locally-validated corrosion rates of steel elements. The latter can form the basis for the development of hazard zone maps that consider industrial pollutants and other local environment factors.

1. Introduction

Façade is one of most important elements in the overall aesthetics, protection and performance of a building. Façade systems consist of structural components and building envelope elements. Façade failures can occur due to inadequate strength of connection system against lateral and internal forces, water ingress, poor design, unsuitable materials, poor maintenance, corrosion, fracture, freeze-thaw, thermal damage, insufficient communications between the contractor and designer, and unsatisfactory supervised construction works [1–3]. Better understanding the potential causes of façade failures can help designers and owners to make proper decisions during design including assessments of future risks about building façade selection [2]. This can also help the owner to reduce the risk or assess the need for remediation [2]. One of the main direct or indirect causes of façade failure is corrosion of steel components. In Table 1, different applications of steel in a building's façade (as cladding, frame, connections, etc) are identified. Each of these elements, depending on the surrounding environment, are prone to degradation over time due to corrosion. For example, when steel is used as a cladding or frame, *atmospheric corrosion* may happen. Also, when two dissimilar metals are in direct contact together in presence of moisture, *galvanic corrosion* could happen. Due to the punching, welding, and cutting of the light gauge steel frame, *cut-edge corrosion* may happen. Another type is *embedded corrosion*, when steel members embedded in the wall or other construction materials may corrode and cause some serious problems such as rust jacking at window lintels, vertical cracks at corner columns, and deviated or displaced masonry [4–10]. Soluble chlorides during construction or salt water in the mortar mix may exacerbate the steel corrosion in traditional concrete or masonry walls [11]. The corrosion of steel needs the existence of moisture and oxygen simultaneously. Common atmospheric factors that may lead to steel corrosion include temperature, moisture, rain, wind velocity and solar radiation [12]. Besides, the impact and properties of the surface oxide and the impact of inclination of the surface exposed outdoors are important aspects of corrosion [13–15]. Temperature has a double influence on atmospheric corrosion rates. For a constant humidity, increasing temperature increases the rate of corrosion [16]. However, rising temperature helps rapid evaporation of humidity from a steel surface and corrosion rate decreases [17]. In indoor environments and closed air spaces, a drop in temperature accompanied by a rise in relative humidity has a significant impact on the rate of corrosion [18]. This indicates that air conditioning that reduces the temperature without extra dehumidification will speed up the corrosion rate. Also, temperature variation is more important than average temperature in corrosion [19]. The corrosion rate will drop to negligible levels at temperatures below freezing [20].

Furthermore, rainfall has the effect of either reducing or stimulating

* Corresponding author..
E-mail address: soufeiani.leila@gmail.com (L. Soufeiani).

https://doi.org/10.1016/j.jobe.2020.101759
Received 21 September 2019; Received in revised form 26 April 2020; Accepted 3 August 2020
Available online 28 August 2020

Abbreviations

SS	Stainless steel
CS	Carbon steel
MS	Mild steel
LAS	Low alloy steel
TOW	Time of wetness
HDG	Hot-dip galvanized
GS	Galvanized steel
WCS	Welded carbon steel
RH	Relative humidity
NaCl	Sodium chloride
HCl	Hydrochloric acid
N	Nitrogen
S	Sulphur
PPy	Polypyrrole
PAni	Polyaniline
MOCVD	Metal-Organic Chemical Vapour Deposition
f-CNTs	Functionalised carbon nanotubes
GO	Graphene oxide

Table 1
Façade systems including steel elements and types of corrosion [2,3,22,23].

Façade systems	Steel elements in façade	Corrosion
Masonry (brickwork, stonework)	Connections, steel stud, brackets & pins, embedded steel Connections, frame	Embedded, galvanic, cut-edge corrosion
Curtain walling	Connections, reinforcement, embedded steel	Galvanic, atmospheric
Precast concrete panels		Embedded (joints cover by mortars), atmospheric, galvanic
Insulated render	Steel stud frame, connections	Galvanic, cut-edge
Metallic cladding	Light steel frame, connection	Atmospheric, galvanic
Tiles and stone veneer panels	Light steel frame, connections	Cut-edge, galvanic, embedded
Glass & steel façade system	Frame, connections	Atmospheric, galvanic
Double-skin façade system	Steel stud, fasteners, connections	Galvanic, cut-edge, atmospheric
Hybrid system (glass with timber screening)	Frame, connections	Atmospheric, Galvanic

corrosion, based on the environment. Rain decreases corrosion by washing pollutants from the steel surface in cladding at polluted atmospheres, while the situation is reversed in less polluted areas and rain increases corrosion rate [16]. Also, prevailing wind directions and speed during rain and height of building plays an important role in distributing the rainfall [21]. Distribution of the annual rainfall is not uniform on facade and upper parts of the facades gain more rain than lower ones [21]. In addition, metal runoff (metal species washed off from the surface) is increased by rainfall which is a serious issue in atmospheric corrosion.

Moreover, corrosion rate increases with atmospheric salinity [24–29]. The chloride deposition rate is normally between 0.1 and 200 $\mu g/m^3$ per year [30]. In coastal atmospheres, deposition of chlorides strongly rely upon factors affecting the transport of ocean salt inland (e.g. local topography, wind direction, wind speed, wind sheltering islands beyond the coast, distance of the site from the sea, etc.) [19] and is between 300 and 1500 $\mu g/m^3$ per year [30]. Sulphur dioxide is another factor which accelerates the corrosion rate and the most serious one among all the atmospheric contaminants derived from industrial processes owing to its potentially high concentration in air and its effect on corrosion rate [16]. Electrolyte on the surface is acidified by sulphur dioxide gas in the atmosphere and soluble corrosion products are formed. Thus, corrosion rates are raised on many metals such as steel, zinc, stainless steel and aluminium. ISO 9223:2012 [30] categorises environments with sulphur dioxide concentrations of more than 50 $\mu g/m^3$ (yearly average) as strongly polluted environments [16]. Buildings located in the coastal areas are more prone to atmospheric corrosion than other areas. Therefore, looking at the global corrosion hazard map before designing the system may be useful. Slamova et al. [31] developed a map of atmospheric corrosion in coastal regions according to the results from geo-statistical approach and modelling. Their method was derived from ISO 9223 which is shown in Fig. 1.

The main atmospheric corrosion factors taken into account in their study are airborne salinity, humidity, and sulphure dioxide emission [31]. In addition, airborne salinity data can be estimated by simulation using suitable methods or using interpolation methods at sites where no samples are available [31].

Besides atmospheric corrosion, embedded, galvanic, and cut-edge corrosion might cause serious issues in the façade system. Fig. 2 illustrates a mild steel plate embedded in the wall behind the stone panel. Rust jacking of embedded steel reinforcing or connections leaded to displacement of masonary or concrete facades. This is one of the most common forms of façade failures [2]. Carbonation and small cover depths of reinforcement in concrete facades can cause the corrosion of reinforcement which is a deterioration mechanism. Although it seems that steel bars in concrete are protected from corrosion because of high alkalinity of concrete pore water, chloride penetration, or lowering the PH in the carbonated concrete could damage the passivity and corrosion happens [21,32]. Carbonation-induced corrosion result in uniform corrosion while chloride attack cause localised corrosion which reduce the steel diameter severely and increase the corrosion damage in a short time [21]. Corrosion of reinforcing steel bars in chloride contaminated concrete environment in terms of pitting corrosion, influence of cover depth, steel bar passivation, and subjected to different salts have been studied by several researchers [33–40].

Corrosion occurs inside the façade system when metal is part of the outer elements of a building or when joints are not properly waterproofed. Moisture can penetrate the façade through deteriorated joints and cause corrosion [4]. Water ingress and moisture penetration leading to corrosion of steel components are one of the main causes of façade failure [1,2,11]. Another consequence of the corrosion of steel in façade is spalling of the façade cladding materials. It has a major impact and involve important risks. Since façade failures are not identifiable in many cases because of “hidden” corrosion [41], remediation is difficult. Failures can have major operational and economic consequences [2]. Besides, repair of corroded components is very complicated specially in important buildings in order to preserve the significance of the building. Also, access to the hidden parts may deteriorate some visible components which may be unjustifiable or impossible for a heritage building. Fig. 3 shows glazed terracotta faience building which has aesthetic, historic, and architectural importance. This building was built around 1920’s. Cracking and spalling can be seen in the faience cladding because of corrosion of structural steel components behind and displacement of the building structure [42]. Fig. 4 shows a limestone clad façade with steel cramps behind used to fix the stones in place. The building faced an issue with corrosion of hidden fixings leading to crack in the limestone unit [42]. The focus of many past research is on steel corrosion in sea water, acidic media, or other severe environments [43–45]. However, corrosion of steel elements in the façade system is a serious issue and cause significant financial loss each year around the world [1–3,11,42].

This paper aims to review the significant scientific studies on steel corrosion in a façade system, evaluate corrosion protection methods, analyse related ISO standards and assess their limitations and gaps in order to provide guidance for practical design and construction as well as to identify future research challenges.

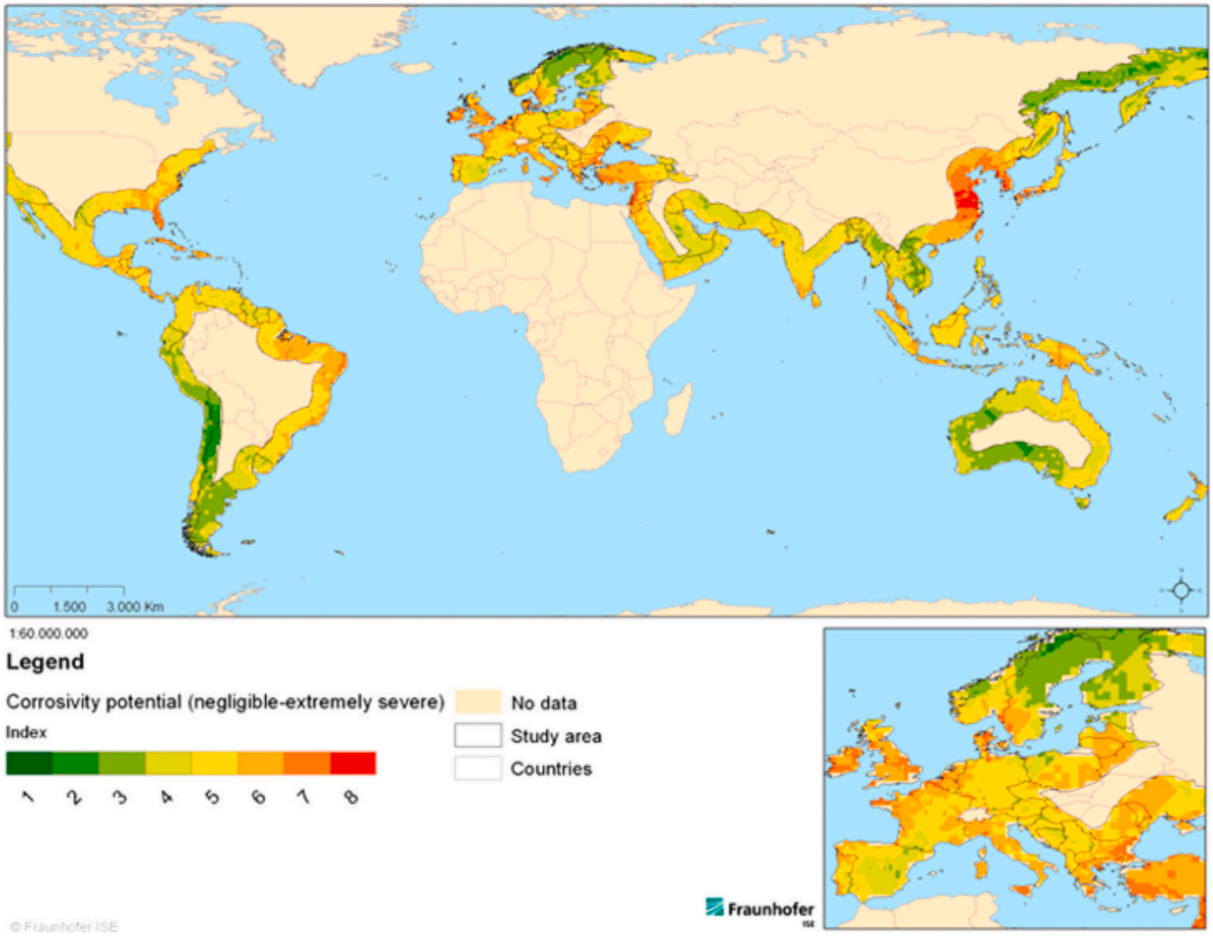

Fig. 1. Distribition of atmospheric corrosivity on the global map [31].

Fig. 2. Embedded corrosion of steel anchor plate in precast concrete wall [2].

2. Most commonly used steels in façade system

The corrosion resistance of stainless steel (SS) in atmospheric environments is higher than zinc and copper, and this is the main reason for using SS for façade systems [46].

The use of SS in the construction industry has significant advantages and it provides cost savings in the long-term by reducing maintenance costs [46]. Even though SS generally provides corrosion resistance, it may suffer from some types of corrosion in severe environments. Hence, selecting a suitable grade for a specific application is very important [47]. Studies of SS and low alloy steel (LAS) in the dynamic supercritical $CO_2/H_2O/H_2S$ system showed general and localised corrosion for LAS in the aqueous phase and localised corrosion in the SC CO_2 phase and SC $CO_2/H_2O/H_2S$ environments. However, 316 L SS showed pitting corrosion in the aqueous phase and no corrosion in the SC CO_2 phase [48]. Pitting corrosion of 304 L SS exposed to highly concentrated chloride solutions has been studied by Xie et al. [49]. The results showed that until 720 h, no change in pitting corrosion was observed and the pitting corrosion resistance was significantly affected by the chloride concentration and slightly affected by the temperature. For standard corrosion resistance, 304 alloy SS is commonly used, and 316 alloy with molybdenum can be specified for even greater protection in coastal areas or areas with high pollution levels [50]. Low carbon SS such as 304 L and 316 L are used in welded sections heavier than about 6 mm (0.25 inch) to provide corrosion resistance. However, capital costs increase in high-grade alloys [45].

Other pollutants such as NOx, O_3, climatological and geographical parameters, and organic acids (acetic and formic acids) have an influence on corrosion of carbon steel (CS) [51,52]. The source of organic acids is generally plastics, wood and paints, and they make the degradation of CS adjacent. This phenomenon is very common, for instance, when the products are packed and stocked temporarily in places close to those substances. Galloway and Likens [53], and Graedel et al. [54] found that the acetic and formic acids in rain increased acidity and

(a) Cracking of terracotta components

(b) Corrosion of embedded steel frame

Fig. 3. (a) Cracking of terracotta components, and (b) corrosion of embedded steel frame [42].

(a) Cracking of limestone unit and spalling area

(b) Corroding of fixing cramp

Fig. 4. (a, b) Cracking of limestone unit and spalling area because of corroding fixing cramp [42].

aggravated corrosion. Corrosion on CS has been seen in atmospheres with 0.5 and 10 ppm acetic acid at a relative humidity of 100% [55]. Islam et al. [56] studied the effects of surface temperature and droplet retention time (DRT) with a new technique on the corrosion rate of CS exposed to water condensation. The results indicated that droplets stay at the top of the line on the surface from 6 min to 50 min depending on the water condensation rate. Reactivity of CS plays the main role among the factors influencing the amount and type of corrosion products. This feature relies on some properties such as chemical and atmospheric composition, design, and types of structures and joints. After a long exposure time, metals lose weight and this gives information about the CS product's corrosion layers (SCPLs). Porosity, uniformity, thickness, solubility, adhesion, and other characteristics play an important role in the barrier effect of SCPLs and can remarkably influence the CS corrosion rate [20]. Much research has been conducted on the corrosion of LAS [57–60]. However, CS is commonly used in the façade system due to its low price.

3. Corrosion testing techniques

Laboratory corrosion tests (if tests are well-planned) can provide the best source of data for selecting a construction material and required information for intelligent design of a plant [61]. Commonly used laboratory methods in corrosion testing are Tafel extrapolation [62], polarization resistance (ASTM G59-97 [63]), electrochemical impedance spectroscopy (ISO 16773 [64], ASTM G106-89 [65]), frequency modulation methods [66], use of rotating disks, and cylinders [67] to study aspects of corrosion affected by solution flow, polarization methods [67] for assessing susceptibility to localised corrosion, scratch repassivation, potential-step repassivation, electrochemical noise [68] applied to pitting, potentiodynamic repassivation techniques [69] for assessing sensitization, the barnacle electrode and permeation methods for hydrogen concentration analysis, and methods for evaluating anodized layers and coatings on metals [61,70]. For evaluating the performance of coating and accelerating corrosive activity cabinet corrosion tests are recommended [61]. Commonly used cabinet tests are salt spray (fog) test (ASTM B117-16 [71]), humidity tests (corrodkote test (ISO 4541 [72]), filiform test (ASTM D2803-09 [73]), high humidity tests, corrosive gas tests), and cyclic corrosion tests (ISO 16701 [74], and ASTM D6899-03 [75]). The different types of measurement techniques (laboratory and field use) for assessing of corrosion are as follow [61]:

- Direct intrusive measurement methods: corrosion test specimens, electrical resistance, linear polarization resistance, potentiodynamic polarization, galvanic (zero resistance arnmetry), electrochemical impedance spectroscopy (EIS) [64], and electrochemical noise.
- Direct nonintrusive measurement (physical) methods for metal loss: Ultrasonic thickness measurement, Radiography, Surface activation and gamma radiometry, and Direct electrical resistance.
- Indirect intrusive measurement methods: corrosion by-products (Hydrogen probes), electrochemical methods (corrosion potential), water chemistry (pH, conductivity, dissolved oxygen, redox potential (ORP), fluid dynamics (Flow regime, flow velocity), process parameters, dewpoint (Pressure, temperature), deposition monitoring, and failure analysis (fouling).
- Indirect nonintrusive measurement methods: alkalinity, metal ion analysis, concentration of dissolved solids, gas analysis, residual oxidant, microbiological analysis, residual inhibitor, and chemical analysis.

A comprehensive research and more details on types of corrosion tests in different environments, specific metals' tests, laboratory and plant testing, corrosion-related standards, and industry's corrosion testing, are discussed in Robert Baboian's book [61]. Further corrosivity classification system introduced by the ISO can be found in section 5.

4. Corrosion protection of steel elements in facade

A proper consideration of the corrosion hazard and understanding of the surrounding environment is needed in the design of structure, including the frame that supports the façade system. The intensity of atmospheric corrosion hazard based on different zones namely coastal, microclimate, site (suburb, city centre), and industry have to be examined. Nguyen et al. [76] studied the different hazard zones and scores to examine the first year atmospheric corrosion depth for zinc and steel in Australia.

Coastal hazard zone of Australia and hazard score for coastal exposure have been shown in Fig. 5 and Table 2, respectively. Corrosivity zones in Australia has been mentioned in AS 4312–2008 [77].

After a proper system design based on the corrosivity zones, effective ways of avoiding or minimising steel corrosion in façade systems include material selection (choosing an appropriate steel alloy (matching the site hazard exposure), eliminating any one of the requirements for corrosion, reduction of the cathode and/or electrolyte activity (polarization), anode protection (passivation), changing of micro-environment, and protective coating. For avoiding or minimising corrosion, material selection and a proper design of the structure should be considered at an early stage. It is necessary to look at the primary properties such as corrosion resistance before selecting a SS grade, and also to consider that secondary properties like physical and mechanical properties. Also, the fabricability of a grade play an important role. Both short- and long-term advantages such as cost-effective fabrication and long life are gained with a suitable choice of materials [78].

A façade and its related materials have to manage water ingress and minimize water retention in the wall, therefore, they need to be durable and protected from deterioration [2,79]. RH and moisture transport in a wall can be predicted with the aid of WUFI software [80]. The hygrothermal data can also be incorporated into WUFI to study the long-term effect of moisture penetration. Also, When atmospheric factors are known for a certain application, the corrosion rate of steel products can be estimated under specific circumstances from ISO 9223 [30,81].

In terms of material selection, Austenitic stainless steels (AISI 304 and 316) have a cost of almost eight-times higher than carbon steel [82]. Therefore, the most economical method for corrosion control may be a combination of carbon steel with chemical treatments because carbon steels are highly prone to corrosion without any chemical treatment [34]. Hence, applying a protective coating can be useful. In addition, in building façades, bolts, nuts, and other parts of the structural connections should be given careful consideration when protective treatment options are developed. Ideally, their protective treatment should provide a similar performance to that specified for general surfaces.

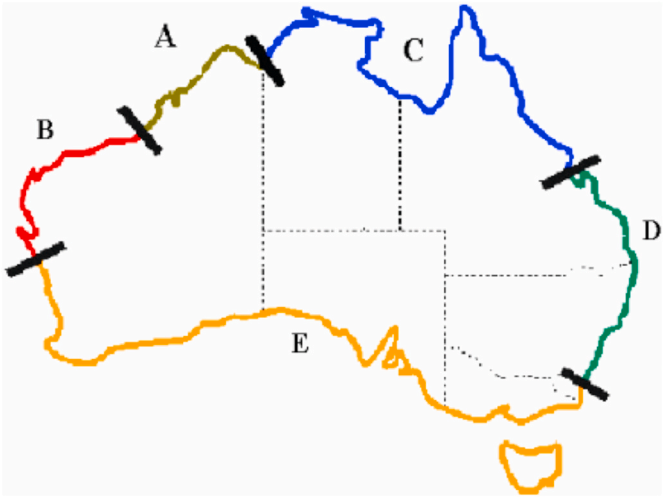

Fig. 5. Coastal hazard zones [76].

Table 2
Hazard score [76].

Coastal hazard area	Score
A	3.2
B	3.3
C	3.5
D	4.3
E	4.9

Alternatively, stainless steel fasteners may be used.

A coated steel may be used in the façade system and underneath low-alloy steel will be exposed due to cutting or punching. In these cases, a cut-edge corrosion may happen depending on the surrounded environment. Thebault et al. [83] studied the cut-edge of a galvanized steel electrochemical processes in NaCl solution by aid of numerical simulation and insitu current and PH profiles determined over the cut-edge. The results showed that in a NaCl solution, significant cathodic prevention even under cathodic polarization has been seen on the steel's area close to the zinc surface. However, no inhibitive self-healing effect and little corrosion product precipitation were monitored in the sulphate containing media. Zinc coating can protect the exposed cut-edges to some degrees and it depends on the thickness of the steel, availability of the zinc's mass in the coating next to the exposed steel, and the nature of the environment. The cut-edge corrosion is almost always neglected in Standards such as Australian Standard AS/NZS 4680:2006 [84]. Repairment of damaged areas on galvanized items after fabrication is described in the standard where the maximum allowable uncoated areas are determined in terms of area. For repair of cut edges on tube, sheet, or wire products that are galvanized prior to fabrication in other standards with galvanized products [85], there is no such requirement. Since the steel may be in the wall cavity and they are not easily accessible, a proper design at the beginning and performing cyclic corrosion test (ISO 16701) [86] might be useful.

The corrosion of reinforcement in concrete facades for 946 cases have been investigated in Finland [21]. The corrosion has been seen in four cases out of 946 contamination of chlorides mostly in upper parts of southern and western facades which get more rains. Although the corrosion damages were rare, a sufficient cover depth of concrete or hot-dip galvanizing of reinforcement may be useful [87]. In another study, determination of the chloride threshold for corrosion initiation of corrosion-resistance rebar materials has been studied and potentiostatic polarization techniques were found to be effective method [88]. In addition, surface treatment including sandblasting and wire brushing, microstructure modification through micro-alloying and heat treatment are effective ways to enhance corrosion resistance of reinforcements [89–92]. The galvanic corrosion is explained in section 3.3.1.1.

Besides the proper design and selection of a suitable steel alloy, protective coating has a significant effect in preventing of corrosion. Therefore, the most common coatings are reviewed and the practical one is highlighted.

4.1. Nano-coating

For corrosion protection of metallic surfaces, protective organic conducting polymer coatings are extensively used as a primer. For protecting steel surfaces from corrosion, adhesion of the primer coating is essential [93]. Some research has been done on using polymers as protective coatings to prevent corrosion in SS [94], MS [95], and iron [96,97]. Numerous corrosion control strategies utilise coatings of conducting polymers that consist of harmful, toxic and environmentally hazardous materials, particularly chromium mixes. New protective coating methods that make use of nanocomposites and carbon-based materials improve the corrosion resistance [93]. Contradictory behaviour have been reported on the corrosion behaviour of conducting polymers [98–101]. Conducting polymers, such as polyacetylene,

polypyrrole, polyaniline, and polythiophene have received extensive interest and had functional usage in different areas, particularly in the corrosion protection of metals [102].

The effectiveness of multilayers of polyaniline (PAni) and PAni/nanotube-TiO_2 composites on CS and WCS in 3% NaCl are compared by Pagotto et al. [103]. Results of this research showed that PAni/n-TiO_2 is a very good adherent and anticorrosive coating [103]. There are many research about superior properties of CNTs [104–109] including corrosion resistance [93]. Kumar and Gasem [110] showed the anticorrosive property of PAni/f-CNTs nanocomposite coatings on MS. Aluminium oxide coating on 304 L SS as a corrosion protection in a 0.1 M NaCl solution has been investigated by Lazar et al. [111]. Results showed that an alumina coating with a thickness in the range of 250 nm–1700 nm gives high corrosion resistance. In another study, it was shown that epoxy coating consisting of self-doped polyaniline nanofiber on MS in 3.5 wt% NaCl enhanced the anticorrosive property of composite coatings [112].

Conducting polymers and their composites do not contain toxic

Table 3
Summary of different corrosion protection coating techniques for steel against corrosion.

Material	Solution	Coating	Author and Year	Coating characterizations & tests	Results & further remarks
CS, SS	Chloride	Multilayered coatings, conducting polymers PAni and PPy	Tan & Blackwood 2003 [123]	SEM, Tafel, Rockwell scratch test[a]	-Ppy underlayer & Pani top layer (Ppy/Pani): best performance (reduced corrosion rate by a factor of 2000 & eliminate pitting corrosion), suitable for both chemical diffusion & physical barrier, best electronic barrier, strongest adhesion to SS -Multipolymer coatings: better chemical barriers
316 L SS	0.5 M NaCl	*N*-, *S*- and Cl-modified nano-TiO_2 coatings	Yun et al., 2007 [122]	XRD, SEM, ATR-IR, RS, XPS, EIS[b]	-*N*-modified TiO_2 nano-coatings: remarkable improvement in corrosion protection of steel -Addition of nitrogen improved compact structure and hydrophobic property - It is expected that the TiO_2 coatings modified by anions can be used as excellent protective coatings for metals in various applications
CS	3.5% NaCl	Bi-layered PPy doped with molybdophosphate and naphthalene disulfonate anions	Kowalski et al., 2007 [118]	GD-OES	Bi-layered coating maintains the steel in a passive state and prevents corrosion of the steels for longer time
steel	NaCl	Epoxy coatings modified by polyaniline/clay nanocomposites	Navarchian et al., 2014 [120]	FTIR, XRD, Tafel test, EIS, immersion test[c], adhesion test[d]	PANI/OMMT nanocomposite into epoxy paint: improved anticorrosion properties in comparison with PANI/MMT and neat PANI
304 L SS	0.1 M NaCl	Aluminium oxide coatings deposited by metal–organic chemical vapour deposition	Lazar et al., 2014 [111]	UV–vis, SEM, TEM, optical microscope, EIS[b]	-Corrosion protection increased when the alumina coating thickness increased -After a threshold film thickness of 500–600 nm, corrosion protection was not improved
MS	3.5 wt% NaCl	Nanocomposite coatings (PBS) contain silane functional polybenzoxazine (PB-TMOS) and SiO_2 nanoparticles	Zhou et al., 2014 [121]	FTIR, NMR, SEM, EIS[b]	SiO_2 nanoparticle content 1–5% into PB-TMOS coating: remarkable improvement in interfacial interactions at the polymer/filler interfaces resulting in a better corrosion performance
reinforcing steels	chloride-laden concrete	epoxy/polyaniline-camphorsulfonate nanocomposite (epoxy/PANI-CSA)	Pour-Ali et al., 2014 [124]	FTIR, TEM, OCP, EIS[b], RCPT[e], pull-out test[f]	-Epoxy/PANI-CSA coating: protected steel rebars during long-term immersion -Epoxy/PANI-CSA nanocomposite: good corrosion resistance and durable bond strength with concrete for steel rebars after 1 year immersion
MS	3.5% NaCl	Polyaniline/f-MWCNT nanocomposite coatings	Kumar & Gasem 2015 [110]	RS, ATR-IR, FE-SEM, EIS[b]	PANI/f-CNTs nanocomposite coatings: excellent dispersion of CNTs in pani matrix, improved mechanical properties, hardness value, and corrosion resistance
CS and WCS	3% NaCl	multilayers of polyaniline (PAni), PAni/nanotubes-TiO_2 composite	Pagotto et al., 2016 [103]	SEM, Optical microscopy, salt spray test[g]	-PAni: a layer of 2 μm showed best protection, a layer thickness up to 4.5 μm decrease in anticorrosive behaviour -PANI/n-TiO_2; showed good adherent and anticorrosive behaviour and lower porosity - PANI/n-TiO_2 on welded CS: protective layer against corrosion
MS	NaCl	Solvent-based epoxy coatings filled with GO nanosheets	Pourhashem et al., 2017 [140]	XRD, FE-SEM, EIS[b], FTIR, pull-off method[f], salt spray test[g]	Coatings produced with direct adding of 0.1 wt% GO to polymer matrix with lower viscosity: showed better adhesion, barrier properties, and corrosion protection due to quality of GO dispersion
MS	3.5 wt% NaCl	The epoxy coating consists of self-doped polyaniline nanofiber (SPANI)	Qiu et al., 2017 [112]	UV–vis, RS, X-ray photoelectron, XRD, SEM, EIS[b]	Self-doped SPANI increase anticorrosive property of composite coatings via forming a metal oxide film composed of Fe_2O_3 and Fe_3O_4.

Tafel extrapolation, Mathematical technique; XPS, X-ray photoelectron spectroscopy; GD-OES, Glow discharge optical emission microscopy; EIS, Electrochemical impedance spectroscopy; TEM, Transmission electron microscopy; OCP, Open circuit potential; SEM, Scanning electron microscopy (microbeam analysis); FE-SEM, Field emission scanning electron microscopy; XRD, X-ray diffraction; FTIR, Fourier Transforms Infrared Spectroscopy; NMR, Nuclear magnetic resonance; RS, Raman spectroscopy; RCPT, Rapid chloride ion penetration test; ATR-IR, Attenuated total reflection—infrared spectroscopy; UV–vis, Ultraviolet–visible spectroscopy.

[a] ASTM E−18 [141].
[b] ISO 16773:2016 [64].
[c] ASTM G31 [142].
[d] ASTM D3359 [143].
[e] ASTM C1202-12 [144].
[f] ASTM D4541-09 [145].
[g] ASTM B-117 [71].

substances, and this is one of their advantages over other coatings such as paint. Furthermore, other materials perform just as physical barriers, whereas both physical and electronic barrier behaviour and better protection have been seen in conducting polymers [93,113]. Among all of the conducting polymers investigated, PAni earns prime significance since it has the best mix of properties, for example, minimal cost, tailorable, superior environmental stability, and reversible electrical properties [114–116]. Since chromium-containing coatings are harmful and have environmental concerns, PAni as an anticorrosive coating is a good replacement for chromium coatings [117]. Bilayered polypyrrole coatings have been studied by Kowalski et al. [118] for corrosion prohibition of steel. Their research showed that bilayered coatings prevent corrosion of steel for a longer time period and put the steel in a passive state. Furthermore, carbon-based materials are very good in corrosion protection of metal substrates [93]. In addition, Superhydrophobic coatings which are water repellent and increase the longevity of the steel substrate, are another solution to enhance the corrosion resistance of the steel, but developing such a coating is still challenging to be achieved [119].

A series of nanocomposite coatings (PBS) containing SiO_2 nanoparticles and silane functional polybenzoxazine (PB-TMOS) for corrosion protection of MS in 3.5 wt% NaCl solution was developed by Navarchian et al. [120]. Incorporation of SiO_2 nanoparticle contents between 1 and 5% into the PB-TMOS coating improved the corrosion resistance of steel significantly [121]. Neat epoxy and epoxy/PAni samples showed less anticorrosion performance than epoxy coating modified by PAni/clay nanocomposite particles [120]. Yun et al. [122] studied the effect of nano-titania coatings with anions of nitrogen, sulphur and chlorine on 316 L SS with a dip-coating method and sol–gel process in 0.5 NaCl solution. In this study, *N*-modified TiO_2 nano coatings showed the excellent corrosion resistance. In another research study, multilayered coatings containing both polypyrrole (PPy) and conducting polymers polyaniline (PAni), on SS and CS in chloride environments have been investigated [123]. In addition, Pour-Ali et al. found that epoxy-polyaniline-camphorsulfonate nanocomposite (epoxy/PANI-CSA) coating provide good corrosion resistance and durable bond strength for reinforcing steels in chloride-laden concrete environment [124]. Table 3 summarises the research conducted in this area.

4.2. Organic coating – paint

The application of the organic coating is a cost-effective protective approach. Ecco et al. [125] studied the corrosion resistance of steel painted with waterborne acrylic coatings loaded with different combinations of cerium oxide nanoparticles. Their research showed that a paint system consisting of ceria nanoparticles has higher protection compared to that without nanoceria. Galliano and Landolt [126] studied the impacts of corrosion inhibiting additives on the performance of waterborne coating systems with different experimental methods. Armelin et al. [127] explored an epoxy paint coating with polyaniline emeraldine salt and polypyrrole composite containing carbon black as additives with accelerated immersion tests. The effective protection was seen in the steel panels with paint containing polyaniline emeraldine salt coating in 3.5% NaCl solution after 720 h of exposure. Furthermore, alkyd paints consisting of polyaniline and polyaniline derivatives on CS have been studied, and salt spray and humidity chamber tests showed that electroactive polymer coatings performed much better than conventional coatings [128].

González et al. [129] investigated corrosion resistance of polyurethane polymeric film on MS and GS in 0.5 M NaCl aqueous solution using Electrochemical Impedance Spectroscopy. Alkyd resins consisting of polyaniline as the conductive polymer showed higher corrosion protection than thermoplastic polymer coatings when applied on CS [130]. In another study, MS with polyaniline coating exposed to artificial brine and dilute hydrochloric acid environments were studied to examine the anti-corrosion performance of the polyaniline coating [131]. In a research study conducted by Mostafai and Nasirpouri [132], an epoxy coating was mixed with an organic–inorganic hybrid nanocomposite (as the corrosion inhibiting pigment). This was then applied to CS in 3.5% NaCl solution. The results demonstrated that apart from PAni, ZnO nanorods can considerably enhance the barrier and corrosion protection performance of epoxy coatings. This is because of the flaky-shaped structures of the PAni–ZnO nanocomposites [132].

Sathiyanarayanan et al. [133] used the coatings consisting of polyaniline and polyaniline–TiO_2 composite (PTC) as corrosion protection on steel in a salt fog test for 35 days and 3% NaCl for 60 days. In another study, they investigated a coating containing polyaniline glass flake composite (PGFC) as a corrosion protection on steel in 3% NaCl. Higher corrosion protection was observed in coatings containing PGFC than the glass flake containing coatings in both the immersion and salt spray tests. The reason comes back to the redox property of polyaniline [134]. In another research, they showed that polyaniline pigmented coatings can protect the steel in both acid and neutral media [135]. In 2015, Silva et al. [136] studied a smart paint for anodic protection of steel [136]. Table 4 shows a summary of research in this area. Steels consisting of five various sacrificial metal paint coatings depending on zinc, Zn–Al and Zn–Al–Mg alloys were evaluated for corrosion behaviour in both natural and accelerated environments. Steels with Zn–Al–Mg alloy coatings indicated surprisingly great blistering and edge corrosion creep resistance. Cyclic corrosion tests like the CCT-1 (ISO 11997–1 [137]) was very close to a natural exposure environment than those derived from conventional salt spray tests in the current study [138].

4.3. Inorganic coating

4.3.1. Metallic coating

Cathodic protection or metal coating is extensively used worldwide. The coating materials are usually Zn, Al, Mg, and their alloys whose electrode potentials are more negative than iron or steel [139]. The most widely used metal for metallic coating is zinc due to its superior characteristics, as described below.

4.3.2. Zinc coating and hot-dip galvanized steel

One of the main characteristics of zinc which makes it preferably suited for this activity is its availability. The most commonly used materials in the galvanizing process are zinc and steel. Iron is the fourth most available material in the earth's crust, and zinc is the 27th. Zinc is a suitable choice for corrosion protection of CS as zinc-coated steel performs very well in the atmospheric environment, particularly in façade systems [16,147].

The process of submerging iron or fabricated steel into a molten zinc bath is called hot-dip galvanizing [148]. Due to its enhanced durability, HDG components have performed very well in the Australian atmosphere for a long time, including in façade systems. Many components perform for 50–100 years [149]. Zinc will typically corrode 1/10th to 1/40th slower than iron and steel and often diminishes with time; the highest ratio is usually in high-chloride environments. The corrosion rates for zinc and zinc-iron alloy layers in a HDG coating are approximately the same [150]. Table 5 shows corrosion rates of CS and zinc in different environments.

At the beginning of each project, by introducing a proper corrosion protection system such as hot-dip galvanizing, annual costs of corrosion protection can be reduced remarkably. Hot-dip galvanizing can protect steel in different environments for more than 100 years. In addition to corrosion protection, hot-dip galvanizing is used for its durability, longevity, availability, sustainability, aesthetics, versatility, and lower initial cost [148]. Three levels of steel corrosion resistance are provided by hot-dip galvanizing: barrier protection, cathodic protection, and the zinc patina. Barrier protection describes the zinc coating as a barrier and separates the steel from the corrosive atmosphere. In cathodic or galvanic protection, zinc corrodes and acts as a sacrificial anode to cover the steel at scratches, cut edges and voids. As can be seen from Fig. 6,

Table 4
Summary of paint-coated steel against corrosion.

Material	Solution	Paint	Author and Year	Coating characterizations and tests	Results & further remarks
MS	3.5% NaCl, HCl	polyaniline coating	Lu et al., 1995 [131]	Tafel extrapolation, potentiodynamic polarization, galvanic coupling, EIS[a], Surface analysis	-Polyaniline coatings: provided significant corrosion protection to MS in severe corrosion environment -Level of protection provided by doped polyaniline is more significant for dilute acid conditions than for neutral saline conditions
LCS	Saline solution	Waterborne epoxy coating	Galliano & Landolt 2002 [126]	EIS[a], LSV, mechanical pull-off test[b], SAM	Both additives enhanced the dry adhesion and decreased blistering under cathodic polarization conditions - Experimental approach described should be useful for additive development and for coating formulation
CS	NaCl (marine), $NaHSO_3$ (Urban)	Conventional thermoplastic polymers with poly, phenoxy resin and a poly (vinyl chloride-*co*-vinyl acetate) 90/10 copolymer	Laco et al., 2005 [130]	Optical microscopy, SEM/EDS, XRD, FT-IR, NMR, SEC, field tests	Alkyd resin modified with conductive polymer have a corrosion resistance very high in comparison with thermoplastic polymer coatings
Steel	3% NaCl	Polyaniline (PAni) pigmented coating	Sathiyanarayanan et al., 2005 [135]	EIS[a], FTIR, UV–vis, OCP	-Polyaniline pigmented coatings: protect steel both in acid and neutral media, highly protective in acidic media than neutral media, passivates the iron surface and enhances its protective property
CS, GS	0.5 M NaCl	Polyurethane polymeric film	González et al., 2007 [129]	EIS[a], pull-off adhesion test[b], Microhardness test[c]	Polyurethane coating: improved anticorrosion protection and higher adhesion when applied on CS than on GS for a given film thickness
Steel	3% NaCl	Polyaniline and polyaniline–TiO_2 composite (PTC)	Sathiyanarayanan et al., 2007 [133]	FTIR, XRD, SEM, Immersion test[d], salt fog test[e], EIS[a], OCP	-PTC coating: greater corrosion protection property (50–200 mV) than Pani coating, higher resistance value -PTC better performance: due to uniform distribution of polyaniline and uniform passive film on iron surface
Steel	3% NaCl	Coating containing polyaniline glass flake composite (PGFC)	Sathiyanarayanan et al., 2008 [134]	Salt spray test[e], EIS[a], XRD, SEM, FTIR	Coating containing PGFC is able to offer higher corrosion protection than that of glass flake containing coating due to the redox property of polyaniline
LCS	3.5% NaCl	Polyaniline emeraldine salt and polypyrrole composite with carbon black as additives of an epoxy paint coating	Armelin et al., 2008 [127]	Immersion test[d], optical microscopy, SEM, FTIR, TGA	-This conducting polymer might work as both adhesion promoter and corrosion inhibitor - Conducting polymers are promising as a replacement for the hexavalent chromates as a new corrosion inhibitor for steel alloy
CS	Salt spray, humidity	Alkyd coatings containing polyaniline and polyaniline derivatives	Goncalves et al., 2011 [128]	FTIR, RS, TGA, salt spray[e], humidity chamber, EIS[a]	Protection of CS against corrosion occurs through the formation of a protective layer of oxides when using coatings obtained from paints containing electroactive polymers
CS	3.5% NaCl	Epoxy coating mixed with organic–inorganic hybrid nanocomposite	Mostafaei & Nasirpouri, 2014 [132]	XRD, FTIR, SEM, TEM, TGA, EIS[a], chronopotentiometry at OCP	-Presence of ZnO nanorods besides PAni considerably improves the barrier and corrosion resistance performance of the epoxy coating due to the flaky shaped structure of the PANI–ZnO nanocomposites -Epoxy/PANI–ZnO hybrid nanocomposite coating systems (EPZ) are crack free, uniform and compact.
Steel	H_2SO_4	Smart paint (mixing Pani with 4-chloro-3-methylphenol, a plasticiser, and solvent	Silva et al., 2015 [136]	FTIR, RS, CV, OCP, EIS[a], SEM	-Binder and the smart paint enhance the passivation of the metal substrate and increase protection abilities against corrosion -The film does not present good barrier properties
CS	0.1 M NaCl, 0.3 wt% Na_2SO_4	Waterborne acrylic coatings loaded with different combination of cerium oxide nanoparticles	Ecco et al., 2016 [125]	EIS[a], salt spray test[e], XRD, TEM	-Optimal concentration of nanoceria associated to higher corrosion protection was verified for the paint system containing 1.0 wt% -Paint systems consisting of ceria nanoparticles showed higher protection in comparison to those without nanoceria

Tafel extrapolation, Mathematical technique; SEM, Scanning electron microscopy; FE-SEM, Field emission scanning electron microscopy; SAM, Scanning acoustic microscopy; LSV, Linear sweep voltammetry; SEC, Size-exclusion chromatography; RS, Raman spectroscopy; TGA, Thermogravimetric analysis; CV, Cyclic voltammetry; OCP, Open circuit potential; Electrochemical impedance spectroscopy; XRD, X-ray diffraction analysis; TEM, Transmission electron microscopy; FTIR, Fourier-transform infrared spectroscopy; NMR, Nuclear magnetic resonance.

[a] ISO 16773:2016 [64].
[b] ASTM D4541-09 [145].
[c] ISO 14577 [146].
[d] ASTM G31 [142].
[e] ASTM B-117 [71].

Table 5
Corrosion rates (r) for the first year of exposure for steel and zinc in various corrosivity classifications [30].

Corrosivity category		Comparative corrosion rates for steel and zinc		
		Unit	Carbon steel	Zinc
C1	Very low	g/(m^2.a)	$r \leq 10$	$r \leq 0.7$
		μm/a	$r \leq 1.3$	$r \leq 0.1$
C2	Low	g/(m^2.a)	$10 < r \leq 200$	$0.7 < r \leq 5$
		μm/a	$1.3 < r \leq 25$	$0.1 < r \leq 0.7$
C3	Medium	g/(m^2.a)	$200 < r \leq 400$	$5 < r \leq 15$
		μm/a	$25 < r \leq 50$	$0.7 < r \leq 2.1$
C4	High	g/(m^2.a)	$400 < r \leq 650$	$15 < r \leq 30$
		μm/a	$50 < r \leq 80$	$2.1 < r \leq 4.2$
C5	Very high	g/(m^2.a)	$650 < r \leq 1500$	$30 < r \leq 60$
		μm/a	$80 < r \leq 200$	$4.2 < r \leq 8.4$
CX	Extreme	g/(m^2.a)	$1500 < r \leq 5500$	$60 < r \leq 180$
		μm/a	$200 < r \leq 700$	$8.4 < r \leq 25$

The classification criterion is based on the methods of determination of corrosion rates of standard specimens for the evaluation of corrosivity.
The corrosion rates, expressed in grams per square metre per year are recalculated in micrometres per year and rounded.
Corrosion rates in category CX are considered extreme. Corrosivity category CX refers to specific marine and marine/industrial environments.
Specific calculation models, guiding corrosion values and additional information on long-term corrosion behaviour, are given in ISO 9224.

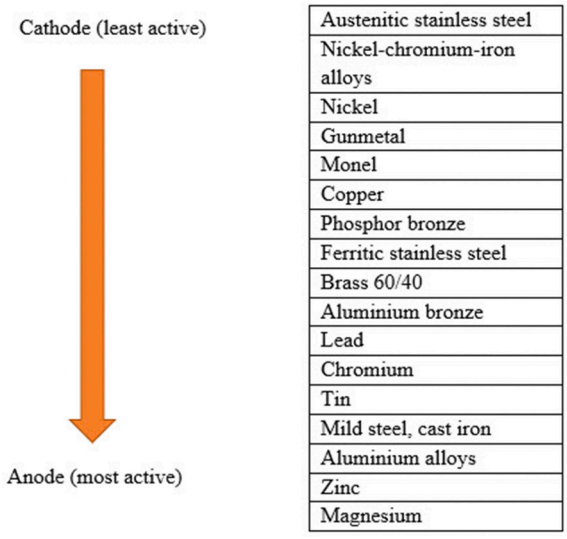

Fig. 6. Partial galvanic series showing position of zinc to other metals [19].

electrode potential of zinc is less noble than steel in many atmospheres at ambient temperatures [151]. Furthermore, zinc oxide, zinc hydroxide, and zinc carbonate will naturally form on the coating surface when galvanized coatings are exposed to both free-flowing air and moisture. This happens during natural wet and dry cycles in the environment. When zinc patina is formed completely, it will decrease the corrosion rate of zinc to around 1/30th of the corrosion rate of steel in the same environment [149,152,153]. The zinc patina is a very important parameter for longevity of galvanized steel in the atmosphere. When HDG steel is exposed in the atmosphere, its performance relies on five main parameters, namely: temperature, humidity, rainfall, sulphur dioxide (pollution) concentration in the air, and air salinity. All of these parameters are very important in the level of HDG corrosion protection on steel [148].

However, there are many conflicting finding about suitability of HDG reinforcement in concrete. While some experts argue that the suitability of HDG reinforcement against corrosion [154,155], others warn of the initial corrosion damage of coating in fresh concrete by development of hydrogen which decrease the bond strength of galvanized reinforcement in concrete [87].

Bimetallic corrosion could take place when two dissimilar metals are in direct contact to each other in presence of an electrolyte such as moisture. The bimetallic effect is the basis for the sacrificial protection that a zinc coating offers to small areas of exposed steel if the coating becomes damaged. HDG coatings will corrode preferentially to protect any metal more cathodic than zinc. The level of bimetallic corrosion that will take place will depend on a number of parameters, including the specific metals in contact, the ratio of the surface area of the two metals, and the exposure conditions. In dry internal environments, the potential for bimetallic corrosion is very low, while in external atmospheric environments, the potential increases due to the presence of water in the form of rain and condensation [150].

Normally, any potential for bimetallic corrosion may be alleviated by electrically isolating the two metals from one another. For bolted connections, this may be done using neoprene or plastic washers, while for overlapping surfaces, it may be achieved by using plastic spacers or painting one of the surfaces with a suitable paint system. Generally, HDG steel performs well in contact with most common engineering metals when in an atmospheric environment [150]. At present, the macro-environment for industrial contaminants does not have a serious impact on corrosion rates in all cities around Australia because SO_2 emissions have reduced since the 1970s [149]. However, by doubling the coating thickness, the time until the zinc is consumed and corrosion happens doubles [156]. Moreover, dropping aggressive construction materials such as cement or fresh concrete on the surface of the steel should be prevented. Corrosion behaviour of galvanized steel under wet–dry cyclic conditions with various drying periods has been studied by Yadav et al. [157].

Cycles of various wet and dry periods are experienced in real atmospheric conditions; nonetheless, there is limited information on how the diverse nature of wet and dry cycles influences the time to produce corrosion and the coating life of galvanized steel [157]. An approved method for observing atmospheric corrosion is electrochemical impedance spectroscopy [158–160]. Some research shows that galvanized steel with aluminium contents increase the corrosion resistance. It was shown that the addition more than 5% aluminium in galvanized steel in chloride solution enhanced the corrosion resistance in a short time [157]. Also, 5%–55% aluminium in galvanized steel improved the corrosion resistance compared to pure zinc with the same thickness [150].

4.3.3. Phosphating

In the phosphating process, steel is immersed into an acidic solution consisting of metal (Zn, Fe) phosphate salts. From the reaction of the steel surface with this solution, a micro-crystalline layer of phosphate is formed on the steel surface. This produces a rough surface with excellent oil-retaining characteristics. However, such compounds can be only used in dry indoor environments. Hence, they are not suitable for façade applications [16].

Apart from a suitable design and using a protective coating, steel stud walls can be prone to premature deterioration. Hence, the durability of the wall is not so much dependent on the construction specifications, but on the maintenance of the building, which should keep the environment within the wall as designed. If the envelope is not maintained, and the interior of the wall is allowed to become wet for a large portion of the year, the service life to 20% loss of section would be dramatically reduced to as low as eight years. This is the type of familiar failure mechanism who have disassembled leaking wall assemblies, revealing severely corroded studs, early in the life of a building [161]. Table 6 summarises the most common corrosion types, their causes, and prevention methods in the façade system.

Table 6
Corrosion types, their causes, and prevention methods in the façade system.

Corrosion type	Cause	Prevention
Atmospheric	Expose to RH, chloride, sulphur dioxide, other pollutants in atmosphere	System design based on hazard map, calculation of RH and moisture penetration (WUFI), estimation of corrosion rate (TOW, chloride, salinity, SO_2) (ISO 9223:1992), drainage, ventilation, material selection & protective coating
Galvanic or bimetallic	Dissimilar metals in direct contact in presence of moisture	Not using dissimilar metals (Fig. 6), electrically isolating the two metals from one another (plastic washers or painting), prevent moisture penetration
Embedded	Sustained moisture, oxygen, chlorides or PH reduced by carbonation, steelworks in contact with masonry (cement), steel reinforcing bars (carbonation, small cover depth) in concrete facades	Separating steelworks in contact with masonry, protective coating for reinforcing bars, HDG, stainless steel
Cut-edge	Cutting, punching coated steel (wet/dry condition exposure, prolong condensation, high RH)	Use HDG steel, cyclic corrosion test (ISO 16701), drainage (avoid water traps)

5. Guidelines and standards

A comprehensive classification system of corrosivity has been introduced by the ISO, which describes the combined effect of corrosivity variables on the corrosion process. A list of ISO standards relating to atmospheric corrosion is given in Table 7.

The ISO corrosivity categorisation is based on a simple assumption that corrosivity is determined by time of wetness (TOW) and levels of corrosive contaminants. Only two kinds of pollutants are considered: chloride and sulphur dioxide. For the categorisation of atmospheric corrosivity, the ISO 9223 methodology uses classes in the range of 1–5, with the most severe level at 5 [162]. Tables 8 and 9 show the classification of TOW and categorisation of chloride and sulphur dioxide, respectively. TOW amounts can be estimated from the ISO definition of TOW or measured directly with sensors. The procedure for determining chloride and sulphur dioxide deposition rates are presented comprehensively in the relevant standards (Table 9) [162].

Based on the classification of the three key variables given in the ISO chart [30,81], the applicable ISO corrosivity class can be specified. Various corrosivity classes are assigned to various types of metals. As the last step in the ISO method, the atmospheric corrosion rate can be assessed for the determined corrosivity class.

Even though the ISO technique shows a reasonable method for corrosivity categorisation, it is constrained in its accuracy. The climatic factors defining corrosivity characterisation exclude the impacts of potentially important corrosive contaminants/pollutants; for example, nitrous oxide, hydrogen sulphide, chlorine gas, acid rain and different fumes that are available in the general air or connected with a particular micro-environment. Also, the temperature is excluded as a variable, but this is a rather important exclusion, considering it is the most significant contributing component in tropical marine climates [162]. Also, the procedure does not support localised corrosion mechanisms; for example, crevice corrosion, pitting, stress corrosion cracking or intergranular corrosion [162]. In addition, the impacts of wind velocity, exposure angle, and sheltering are not considered, nor are time differences in these parameters [162].

Besides, ISO 9223 [81,163] permits the evaluation of corrosivity area in terms of corrosion rates of other metals such as zinc. Available data shows that the corrosion rates of zinc and steel could not be linked as proposed by ISO 9223, and thus, the corrosion rate of zinc has not been utilised to describe regions in AS/NZS 2312:2002 [164]. For describing corrosivity zones in Australia and New Zealand, only the real corrosion rate estimations of steel have been used, by extrapolating such outcomes to other zones with similar atmospheres and geology. Hence, corrosivity zones defined in AS/NZS 2312:2002 [164] are not equal to ISO 9223, but rather they are derived from local factors and evidences [165]. ISO 9224 [166] provides guiding values for long-term corrosion rates of zinc-coated steels which depend on a large number of exposures in many locations throughout the world; nonetheless, the method utilised in ISO 9224 [166] is not covering all the situations that can happen in real environments and service conditions. Specifically, situations that involve large changes in the environment which can cause significant increases or decreases in corrosion rates [19]. Corrosion test techniques and methods mentioned in section 3.

Table 7
List of ISO standards related to atmospheric corrosion [162].

ISO Standard	Year	Title
ISO 9223	2012	Corrosively of atmospheres: Classification, determination, and estimation
ISO 9224	2012	Guiding values of corrosion rate for each category for specific metals
ISO 9225	2012	Corrosivity of atmospheres- measurement of environmental parameters
ISO 9226	2012	Specification of corrosion rates of standard specimens

Table 8
ISO 9223:1992 Categorisation of time of wetness (TOW) [81,162].

Wetness category	TOW (%)	TOW (hours per year)	Examples of environments
T1	<0.1	<10	Indoor with climatic control
T2	0.1–3	10–250	Indoor without climatic control
T3	3–30	250–2500	Outdoor in dry, cold climates
T4	30–60	2500–5500	Outdoor in other climates
T5	>60	>5500	Damp climates

Table 9
ISO 9223:1992 Categorisation of sulphur dioxide and chloride pollution levels [81,162].

Sulphur dioxide category	Sulphur dioxide deposition rate (mgm^{-2} day)	Chloride category	Chloride deposition rate (mgm^{-2} day)
P0	≤10	S0	≤3
P1	11–35	S1	4–60
P2	36–80	S2	61–300
P3	81–200	S3	301–1500

6. Summary and conclusions

A comprehensive review of scientific studies on the corrosion of steel in the façade system, corrosion protection methods, related ISO standards and their limitations has been conducted in order to provide guidance for practical design and construction and identify further research. Different types of corrosion may occur based on the surrounding environment such as atmospheric, galvanic or bimetallic, embedded, and cut-edge corrosion in the façade system. Temperature/humidity, chloride concentration, and sulphur dioxide affect the corrosion rate of steel significantly. Moreover, the method utilised in standards do not adequately cover all the situations that can occur in real environments and service conditions.

An effective way of preventing steel elements corrosion in a building façade is examination of the surrounding environment including the consideration of corrosion hazard zones and related standards, a proper

design of façade system, selecting a suitable steel grade based on its place in the wall, choosing an appropriate coating to avoid corrosion, and do the maintenance regularly.

Practical methods for improved performance of steel elements in façade systems are summarized below:

- If the steel is exposed to the atmosphere such as cladding, external frame, and exterior fasteners in the façade system, estimation of rain, humidity, chloride, and pollutants have to be done before selecting the steel grade. Location of the building based on the hazard zone and surrounding environment play an important role in selecting a suitable steel type and grade. Depending on the material specifications for the façade system, stainless steel types 304 and 316 may be used for connections or in areas with more probability of corrosion, such as coastal areas.
- If steel components are used inside the wall, water ingress and moisture penetration through the wall should be avoided or minimised. It means that joints and outer elements must be waterproofed. Humidity and temperature could be estimated by aid of WUFI software. If the percentage of humidity was high, changing the design of façade system (for example, putting the vapour barrier after thermal insulation (from outside to inside) in rain screen façade systems will decrease the water content and humidity significantly) or selecting a higher stainless steel alloy or hot-dip galvanized steel might be useful.
- Avoid using dissimilar metals (galvanic corrosion) or close together as possible or electrically isolate one from the other.
- Avoid embedded corrosion by considering the steel surrounded environment specially presence of chlorides.
- Cutting, punching, or welding the coated steel components may change the thickness, and surface, or expose the underneath steel. Make sure the exposed area is not prone to corrosion (specially in cavities) before the installation of steel elements.
- There are a variety of protective coatings such as paint, spray, HDG, and so on. A proper coating must be chosen based on the building's location, surrounding environment, and location of steel components in the wall. Conductive polymers, epoxy paint, and PAni showed good resistance against corrosion. Furthermore, zinc coating or hot-dip galvanized steel seems to be an ideal choice in corrosive environments because of its self-healing or cathodic protection, durability, longevity, availability, sustainability, and lower initial cost. HDG steel mostly used in the façade system in Australia since it is compatible with Australian atmosphere. Furthermore, bolts, nuts, and other parts of the structural connections should be given careful consideration in protective treatments.

Much further research is needed such as the potential of corrosion on welding steel elements, repair of cut-edges that are galvanized prior to fabrication, nature of wet-dry cycles in real atmospheric condition and influence on the time to produce corrosion in cavities. In addition, real corrosion rate estimation of steel elements for describing the corrosivity zones, developing hazard zone maps which consider industrial pollutants, and tropical areas need to be investigated. Furthermore, impacts of wind velocity, exposure angle and sheltering, estimation of corrosion rate based on other pollutants such as nitrous oxide, hydrogen sulphide, chlorine gas, acid rain and different fumes that are available in the general air or connected with a particular micro-environment, need to be explored as well as environmentally friendly and low cost nano-coatings, and innovative coatings.

Declaration of competing interest

The authors declare that they have no known competing financial interests or personal relationships that could have appeared to influence the work reported in this paper.

Acknowledgements

This work was conducted with the financial support of the CRC-Project on Advanced Manufacturing of High Performance Building Envelope Systems (CRC-P54018), led by Prof Tuan Ngo, and the ARC Centre for Advanced Manufacturing of Prefabricated Housing (IC150100023), led by Prof Priyan Mendis.

References

[1] K.J. Beasley, Identification and Diagnosis of Building Façade Failures, Forensic Engineering 2009: Pathology of the Built Environment, 2010, pp. 74–84.
[2] K.J. Beasley, Latent Building Facade Failures, Forensic Engineering 2012: Gateway to a Safer Tomorrow, 2013, pp. 918–927.
[3] S. Moghtadernejad, Design, Inspection, Maintenance, Life Cycle Performance and Integrity of Building Facades, 2013.
[4] strukts, Steel Corrosion in Facades 2018.
[5] M.N. Nguyen, R.H. Leicester, C.-H. Wang, G.C. Foliente, Corrosion effects in the structural design of metal fasteners for timber construction, Structure and Infrastructure Engineering 9 (3) (2013) 275–284.
[6] G.C. Foliente, R.H. Leicester, C.-h. Wang, C. Mackenzie, I. Cole, Durability design for wood construction, For. Prod. J. 52 (1) (2002) 10–19.
[7] C. Wang, R. Leicester, G. Foliente, M. Nguyen, Timber Service Life Design Guide, Forest and Wood Products Australia Limited, 2007.
[8] L. Soufeiani, S.N. Raman, M.Z.B. Jumaat, U.J. Alengaram, G. Ghadyani, P. Mendis, Influences of the volume fraction and shape of steel fibers on fiber-reinforced concrete subjected to dynamic loading–A review, Eng. Struct. 124 (2016) 405–417.
[9] L. Soufeiani, G. Ghadyani, A.B.H. Kueh, K.T. Nguyen, The effect of laminate stacking sequence and fiber orientation on the dynamic response of FRP composite slabs, J. Build. Eng. 13 (2017) 41–52.
[10] L. Soufeiani, Dynamic Behavior of Fiber Reinforced Composite Slab Induced by Human Walking, Universiti Teknologi Malaysia, 2013.
[11] K.J. Beasley, Contemporary and traditional wall-system failures, J. Perform. Constr. Facil. 15 (2) (2001) 42–45.
[12] P.B.Y.L. Masters, in: W.H. Ailor (Ed.), Atmospheric Corrosion, John Wiley & Sons, Nueva York, 1982. EEUU.
[13] S.H. Mameng, R. Pettersson, C. Leygraf, Effect of stainless steel composition on atmospheric corrosion resistance at a marine site in dubai, Corrosion 73 (7) (2017) 880–891.
[14] L. Veleva, L. Maldonado, Classification of atmospheric corrosivity in humid tropical climates, Br. Corrosion J. 33 (1) (1998) 53–58.
[15] D. Wallinder, I.O. Wallinder, C. Leygraf, Influence of surface treatment of type 304L stainless steel on atmospheric corrosion resistance in urban and marine environments, Corrosion 59 (3) (2003) 220–227.
[16] Hilti, Crrosion Handbook, 2015.
[17] P.R. Roberge, Corrosion Engineering, McGraw-Hill, New York, NY, USA, 2008.
[18] S. Sharp, Protection of control equipment from atmospheric corrosion, Mater. Perform. 29 (1990) 43–48.
[19] AS/NZS 2312, 2: Guide to the Protection of Structural Steel against Atmospheric Corrosion by the Use of Protective Coatings: Part 2: Hot Dip Galvanizing, 2014.
[20] S. Syed, ATMOSPHERIC CORROSION OF MATERIALS, 2006.
[21] J. Lahdensivu, H. Mäkelä, P. Pirinen, Corrosion of Reinforcement in Existing Concrete Façades, Durability of Building Materials and Components, Springer2013, pp. 253-274..
[22] L. Endzhievskiy, A. Frolovskaia, Y. Petrova, Analysis of defects of overhead facade systems and other light thin-walled structures. IOP Conference Series: Materials Science and Engineering, IOP Publishing, 2017, 012046.
[23] C. Reardon, Cladding Systems, YourHome, 2013.
[24] S. Feliu, M. Morcillo, S. Feliu Jr., The prediction of atmospheric corrosion from meteorological and pollution parameters—I, Ann. Corrosion, Corrosion Sci. 34 (3) (1993) 403–414.
[25] S. Feliu, M. Morcillo, S. Feliu Jr., The prediction of atmospheric corrosion from meteorological and pollution parameters—II. Long-term forecasts, Corrosion Sci. 34 (3) (1993) 415–422.
[26] F. Corvo, Sobre el papel de los iones sulfato en la corrosión atmosférica del acero en la atmósfera salina húmeda. Pronóstico de la corrosión para zonas industriales y urbanas en la cercanía de la costa, Rev. Iberoamericana de Corrosión y Protección 19 (5) (1988) 291–292.
[27] C. Arroyave, F. Lopez, M. Morcillo, The early atmospheric corrosion stages of carbon steel in acidic fogs, Corrosion Sci. 37 (11) (1995) 1751–1761.
[28] F. Corvo, C. Haces, N. Betancourt, L. Maldonado, L. Veleva, M. Echeverria, O. De Rincón, A. Rincón, Atmospheric corrosivity in the Caribbean area, Corrosion Sci. 39 (5) (1997) 823–833.
[29] F. Corvo, T. Perez, L. Dzib, Y. Martin, A. Castañeda, E. Gonzalez, J. Perez, Outdoor–indoor corrosion of metals in tropical coastal atmospheres, Corrosion Sci. 50 (1) (2008) 220–230.
[30] ISO 9223, Corrosion of Metals and Alloys: Corrosivity of Atmospheres: Classification, European Committee for Standardization (CEN), Brussels, Belgium, 2012.
[31] K. Slamova, C. Schill, S. Wiesmeier, M. Köhl, R. Glaser, Mapping atmospheric corrosion in coastal regions: methods and results, J. Photon. Energy 2 (1) (2012), 022003.

[32] M. Babaee, A. Castel, Chloride diffusivity, chloride threshold, and corrosion initiation in reinforced alkali-activated mortars: role of calcium, alkali, and silicate content, Cement Concr. Res. 111 (2018) 56–71.
[33] D. Li, R. Wei, L. Li, X. Guan, X. Mi, Pitting corrosion of reinforcing steel bars in chloride contaminated concrete, Construct. Build. Mater. 199 (2019) 359–368.
[34] M. Otieno, J. Ikotun, Y. Ballim, Experimental investigations on the influence of cover depth and concrete quality on time to cover cracking due to carbonation-induced corrosion of steel in RC structures in an urban, inland environment, Construct. Build. Mater. 198 (2019) 172–181.
[35] M. Alonso, F. Luna, M. Criado, Corrosion behavior of duplex stainless steel reinforcement in ternary binder concrete exposed to natural chloride penetration, Construct. Build. Mater. 199 (2019) 385–395.
[36] F. Xu, Y. Xiao, S. Wang, W. Li, W. Liu, D. Du, Numerical model for corrosion rate of steel reinforcement in cracked reinforced concrete structure, Construct. Build. Mater. 180 (2018) 55–67.
[37] A. Poursaee, A. Laurent, C. Hansson, Corrosion of steel bars in OPC mortar exposed to NaCl, MgCl2 and CaCl2: macro-and micro-cell corrosion perspective, Cement Concr. Res. 40 (3) (2010) 426–430.
[38] A. Poursaee, C. Hansson, Reinforcing steel passivation in mortar and pore solution, Cement Concr. Res. 37 (7) (2007) 1127–1133.
[39] H. Torbati-Sarraf, A. Poursaee, Study of the passivation of carbon steel in simulated concrete pore solution using scanning electrochemical microscope (SECM), Materialia 2 (2018) 19–22.
[40] F. Shaheen, B. Pradhan, Influence of sulfate ion and associated cation type on steel reinforcement corrosion in concrete powder aqueous solution in the presence of chloride ions, Cement Concr. Res. 91 (2017) 73–86.
[41] N.R. Council, Research Opportunities in Corrosion Science and Engineering, National Academies Press2011.
[42] P. Johnsson, David West, Challenges in Dealing with Corrosion in Heritage Buildings, Corrosion and Prevention, 46th Annual Conference of the Australasian Corrosion Association, 2006.
[43] M. Vieira Casanova Monteiro, F. Pessu, R. Barker, J. Antônio da Cunha Ponciano Gomes, A. Neville, Analysis of the Use of Environmentally Friendly Corrosion Inhibitors for Mild Steel in a Carbon Dioxide Saturated Chloride Solution via Experimental Design, Materials and Corrosion.
[44] J.C. Guerra, A. Castañeda, F. Corvo, J.J. Howland, J. Rodríguez, Atmospheric Corrosion of Low Carbon Steel in a Coastal Zone of Ecuador: Anomalous Behavior of Chloride Deposition versus Distance from the Sea, Materials and Corrosion 1810442.
[45] M. Finšgar, J. Jackson, Application of corrosion inhibitors for steels in acidic media for the oil and gas industry: a review, Corrosion Sci. 86 (2014) 17–41.
[46] K.H. Lo, C.H. Shek, J. Lai, Recent developments in stainless steels, Mater. Sci. Eng. R Rep. 65 (4) (2009) 39–104.
[47] P. Moore, Stainless Steel Grade Selection, 2010.
[48] L. Wei, X. Pang, K. Gao, Corrosion of low alloy steel and stainless steel in supercritical CO 2/H 2 O/H 2 S systems, Corrosion Sci. 111 (2016) 637–648.
[49] Y. Xie, S. Guo, A. Leong, J. Zhang, Y. Zhu, Corrosion behaviour of stainless steel exposed to highly concentrated chloride solutions, Corrosion Eng. Sci. Technol. (2017) 1–11.
[50] J. Vilche, F. Varela, G. Acuna, E. Codaro, B. Rosales, A. Fernandez, G. Moriena, A survey of Argentinean atmospheric corrosion: I—aluminium and zinc samples, Corrosion Sci. 37 (6) (1995) 941–961.
[51] P. Brown, L. Masters, Atmospheric Corrosion, 1982. New York.
[52] S. Chawla, J. Payer, A thermodynamic perspective of copper tarnishing in moist air—SO2, Corrosion 46 (10) (1990) 860–865.
[53] J.N. Galloway, G.E. Likens, Calibration of collection procedures for the determination of precipitation chemistry, Water, Air, & Soil Pollution 6 (2) (1976) 241–258.
[54] T. Graedel, C. McCrory-Joy, J. Franey, Potential corrosion of metals by atmospheric organic acids, J. Electrochem. Soc. 133 (2) (1986) 45–453.
[55] H. Alves, M. Ferreira, The corrosion of mild steel in acetic acid-containing atmospheres, J. Electroanal. Chem. 340 (1–2) (1992) 137–144.
[56] M.M. Islam, T. Pojtanabuntoeng, R. Gubner, Condensation corrosion of carbon steel at low to moderate surface temperature and iron carbonate precipitation kinetics, Corrosion Sci. 111 (2016) 139–150.
[57] C. Jia, Y. Shao, L. Guo, Y. Liu, Incipient corrosion behavior and mechanical properties of low-alloy steel in simulated industrial atmosphere, Construct. Build. Mater. 187 (2018) 1242–1252.
[58] L. Li, M. Mahmoodian, C.-Q. Li, D. Robert, Effect of corrosion and hydrogen embrittlement on microstructure and mechanical properties of mild steel, Construct. Build. Mater. 170 (2018) 78–90.
[59] H. Torbati-Sarraf, A. Poursaee, Corrosion of coupled steels with different microstructures in concrete environment, Construct. Build. Mater. 167 (2018) 680–687.
[60] J. Shi, J. Ming, W. Sun, Passivation and chloride-induced corrosion of a duplex alloy steel in alkali-activated slag extract solutions, Construct. Build. Mater. 155 (2017) 992–1002.
[61] R. Baboian, Corrosion Tests and Standards: Application and Interpretation, ASTM international1995.
[62] E.E. Stansbury, R.A. Buchanan, Fundamentals of Electrochemical Corrosion, ASM international2000.
[63] ASTM G59-97, Standard Practice for Conducting Potentiodynamic Polarization Resistance Measurements, 2003.
[64] ISO 16773: Electrochemical Impedance Spectroscopy (EIS) on Coated and Uncoated Metallic Specimens, 2016.
[65] ASTM G106-89, Standard Practice for Verification of Algorithm and Equipment for Electrochemical Impedance Measurements, 2015.
[66] G.C. Moran, Corrosion Monitoring in Industrial Plants Using Nondestructive Testing and Electrochemical Methods: a Symposium, ASTM International1986..
[67] R. Baboian, Corrosion Tests and Standards: Application and Interpretation, American Society for Testing and Materials (ASTM), 1995.
[68] B.J. Little, J.S. Lee, R.I. Ray, Diagnosing, measuring and monitoring microbiologically influenced corrosion (MIC), Naval research lab stennis detachment stennis space center Ms oceanography div, 2011.
[69] J. Scully, R. Kelly, Methods for Determining Aqueous Corrosion Reaction Rates, 2003.
[70] J.R. Scully, D.C. Silverman, M.W. Kendig, Electrochemical Impedance: Analysis and Interpretation, ASTM Philadelphia, 1993.
[71] ASTM B117: Standard Practice for Operating Salt Spray (Fog) Apparatus.
[72] ISO 4541: Metallic and Other Non-organic Coatings- Corrodkote Test, 1995.
[73] ASTM D2803-09, Standard Guide for Testing Filiform Corrosion Resistance of Organic Coatings on Metal, 2015.
[74] ISO 16701, Corrosion of Metals and Alloys — Corrosion in Artificial Atmosphere — Accelerated Corrosion Test Involving Exposure under Controlled Conditions of Humidity Cycling and Intermittent Spraying of a Salt Solution, 2015.
[75] ASTM D6899-03, Standard Guide for Laboratory Cyclic Corrosion Testing of Automotive Painted Steel, 2010.
[76] M.N. Nguyen, R.H. Leicester, C.-H. Wang, G.C. Foliente, Service life models and design procedure of metal fasteners subjected to corrosion in timber structures, Proc. of World Conference of Timber Engineering WCTE, 2008.
[77] AS 4312, Atmospheric Corrosivity Zones in Australia, 2008.
[78] A. Steels, The Atlas Steels Technical Handbook of Stainless Steels, 2013.
[79] ISO 13823: General Principles on the Design of Structures for Durability, 2008.
[80] WUFI Team, WUFI 2D, 2017. https://wufi.de/en/software/wufi-2d/.
[81] ISO 9223, Corrosion of Metals and Alloys-Corrosivity of Atmospheres-Classification, 1992.
[82] T.C.E. Tringham, Causes and Prevention of Corrosion in Aircraft, 1958. Pitman.
[83] F. Thébault, B. Vuillemin, R. Oltra, C. Allely, K. Ogle, Protective mechanisms occurring on zinc coated steel cut-edges in immersion conditions, Electrochim. Acta 56 (24) (2011) 8347–8357.
[84] Standard 4680, Hot-Dip Galvanized (Zinc) Coatings on Fabricated Ferrous Articles, 2006.
[85] J. Robinson, Industrial Galvanizers manual (2013).
[86] ISO 16701, Corrosion of Metals and Alloys - Corrosion in Artificial Atmosphere - Accelerated Corrosion Test Involving Exposure under Controlled Conditions of Humidity Cycling and Intermittent Spraying of a Salt Solution, 2015.
[87] P. Pokorný, P. Tej, M. Kouřil, Evaluation of the impact of corrosion of hot-dip galvanized reinforcement on bond strength with concrete–A review, Construct. Build. Mater. 132 (2017) 271–289.
[88] M.F. Hurley, J.R. Scully, Threshold chloride concentrations of selected corrosion-resistant rebar materials compared to carbon steel, Corrosion 62 (10) (2006) 892–904.
[89] L. Ding, H. Torbati-Sarraf, A. Poursaee, The influence of the sandblasting as a surface mechanical attrition treatment on the electrochemical behavior of carbon steel in different pH solutions, Surf. Coating. Technol. 352 (2018) 112–119.
[90] D. Song, A. Ma, W. Sun, J. Jiang, J. Jiang, D. Yang, G. Guo, Improved corrosion resistance in simulated concrete pore solution of surface nanocrystallized rebar fabricated by wire-brushing, Corrosion Sci. 82 (2014) 437–441.
[91] D. Song, J. Jiang, W. Sun, H. Ma, J. Zhang, Z. Cheng, J. Jiang, Z. Ai, Effect of chromium micro-alloying on the corrosion behavior of a low-carbon steel rebar in simulated concrete pore solutions, J. Wuhan Univ. Technol.-Materials Sci. Ed. 32 (6) (2017) 1453–1463.
[92] H. Torbati-Sarraf, A. Poursaee, Corrosion improvement of carbon steel in concrete environment through modification of steel microstructure, J. Mater. Civ. Eng. 31 (5) (2019), 04019042.
[93] M. Ates, A review on conducting polymer coatings for corrosion protection, J. Adhes. Sci. Technol. 30 (14) (2016) 1510–1536.
[94] S. Jafarzadeh, P.M. Claesson, P.-E. Sundell, E. Tyrode, J. Pan, Active corrosion protection by conductive composites of polyaniline in a UV-cured polyester acrylate coating, Prog. Org. Coating 90 (2016) 154–162.
[95] A. Ali Fathima Sabirneeza, S. Subhashini, A novel water-soluble, conducting polymer composite for mild steel acid corrosion inhibition, J. Appl. Polym. Sci. 127 (4) (2013) 3084–3092.
[96] J. Martins, M. Bazzaoui, T. Reis, E. Bazzaoui, L. Martins, Electrosynthesis of homogeneous and adherent polypyrrole coatings on iron and steel electrodes by using a new electrochemical procedure, Synth. Met. 129 (3) (2002) 221–228.
[97] M.M. Popović, B.N. Grgur, Electrochemical synthesis and corrosion behavior of thin polyaniline-benzoate film on mild steel, Synth. Met. 143 (2) (2004) 191–195.
[98] F. Beck, R. Michaelis, F. Schloten, B. Zinger, Filmforming electropolymerization of pyrrole on iron in aqueous oxalic acid, Electrochim. Acta 39 (2) (1994) 229–234.
[99] M. Sabouri, T. Shahrabi, M. Hosseini, Improving corrosion protection performance of polypyrrole coating by tungstate ion dopants, Russ. J. Electrochem. 43 (12) (2007) 1390–1397.
[100] M. Hosseini, M. Sabouri, T. Shahrabi, Comparison between polyaniline-phosphate and polypyrrole-phosphate composite coatings for mild steel corrosion protection, Mater. Corros. 57 (5) (2006) 407–410.
[101] M. Hosseini, H. Ashassi-Sorkhabi, H. Ghiasvand, Electrochemical studies of Zn–Ni alloy coatings from non-cyanide alkaline bath containing tartrate as complexing agent, Surf. Coating. Technol. 202 (13) (2008) 2897–2904.

[102] S.A. Kumar, K.S. Meenakshi, T. Sankaranarayanan, S. Srikanth, Corrosion resistant behaviour of PANI–metal bilayer coatings, Prog. Org. Coating 62 (3) (2008) 285–292.
[103] J. Pagotto, F. Recio, A. Motheo, P. Herrasti, Multilayers of PAni/n-TiO 2 and PAni on carbon steel and welded carbon steel for corrosion protection, Surf. Coating. Technol. 289 (2016) 23–28.
[104] G. Ghadyani, L. Soufeiani, A. Öchsner, On a thickness free expression for the shear modulus of carbon nanotubes, J. Appl. Phys. 120 (17) (2016) 174302.
[105] G. Ghadyani, L. Soufeiani, A. Öchsner, On the characterization of the elastic properties of asymmetric single-walled carbon nanotubes, J. Phys. Chem. Solid. 89 (2016) 62–68.
[106] G. Ghadyani, L. Soufeiani, A. Öchsner, Angle dependence of the shear behaviour of asymmetric carbon nanotubes, Mater. Des. 116 (2017) 136–143.
[107] G. Ghadyani, A. Öchsner, Derivation of a universal estimate for the stiffness of carbon nanotubes, Phys. E Low-dimens. Syst. Nanostruct. 73 (2015) 116–125.
[108] G. Ghadyani, M. Akbarzade, A. Öchsner, On the Finite Element Modelling and Simulation of Carbon Nanotubes, Key Engineering Materials, Trans Tech Publ, 2014, pp. 55–61.
[109] G. Ghadyani, A. Oechsner, On a thickness free expression for the stiffness of carbon nanotubes, Solid State Commun. 209 (2015) 38–44.
[110] A.M. Kumar, Z.M. Gasem, In situ electrochemical synthesis of polyaniline/f-MWCNT nanocomposite coatings on mild steel for corrosion protection in 3.5% NaCl solution, Prog. Org. Coating 78 (2015) 387–394.
[111] A.-M. Lazar, W.P. Yespica, S. Marcelin, N. Pébère, D. Samélor, C. Tendero, C. Vahlas, Corrosion protection of 304L stainless steel by chemical vapor deposited alumina coatings, Corrosion Sci. 81 (2014) 125–131.
[112] S. Qiu, C. Chen, W. Zheng, W. Li, H. Zhao, L. Wang, Long-term corrosion protection of mild steel by epoxy coating containing self-doped polyaniline nanofiber, Synth. Met. 229 (2017) 39–46.
[113] P. Herrasti, F. Recio, P. Ocon, E. Fatas, Effect of the polymer layers and bilayers on the corrosion behaviour of mild steel: comparison with polymers containing Zn microparticles, Prog. Org. Coating 54 (4) (2005) 285–291.
[114] A. Pud, N. Ogurtsov, A. Korzhenko, G. Shapoval, Some aspects of preparation methods and properties of polyaniline blends and composites with organic polymers, Prog. Polym. Sci. 28 (12) (2003) 1701–1753.
[115] H. Zengin, W. Zhou, J. Jin, R. Czerw, D.W. Smith, L. Echegoyen, D.L. Carroll, S. H. Foulger, J. Ballato, Carbon nanotube doped polyaniline, Adv. Mater. 14 (20) (2002) 1480–1483.
[116] R. Sainz, A.e. Benito, M. Martinez, J. Galindo, J. Sotres, A. Baro, B. Corraze, O. Chauvet, A. Dalton, R. Baughman, A soluble and highly functional polyaniline–carbon nanotube composite, Nanotechnology 16 (5) (2005) S150.
[117] A. Özyılmaz, G. Kardaş, M. Erbil, B. Yazıcı, The corrosion performance of polyaniline on nickel plated mild steel, Appl. Surf. Sci. 242 (1) (2005) 97–106.
[118] D. Kowalski, M. Ueda, T. Ohtsuka, Corrosion protection of steel by bi-layered polypyrrole doped with molybdophosphate and naphthalenedisulfonate anions, Corrosion Sci. 49 (3) (2007) 1635–1644.
[119] A. Fihri, E. Bovero, A. Shahrani, A. Ghamdi, G. Alabedi, Recent Progress in Superhydrophobic Coatings Used for Steel Protection: A Review, Colloids and Surfaces A: Physicochemical and Engineering Aspects, 2017.
[120] A.H. Navarchian, M. Joulazadeh, F. Karimi, Investigation of corrosion protection performance of epoxy coatings modified by polyaniline/clay nanocomposites on steel surfaces, Prog. Org. Coating 77 (2) (2014) 347–353.
[121] C. Zhou, X. Lu, Z. Xin, J. Liu, Y. Zhang, Polybenzoxazine/SiO 2 nanocomposite coatings for corrosion protection of mild steel, Corrosion Sci. 80 (2014) 269–275.
[122] H. Yun, J. Li, H.-B. Chen, C.-J. Lin, A study on the N-, S-and Cl-modified nano-TiO 2 coatings for corrosion protection of stainless steel, Electrochim. Acta 52 (24) (2007) 6679–6685.
[123] C. Tan, D. Blackwood, Corrosion protection by multilayered conducting polymer coatings, Corrosion Sci. 45 (3) (2003) 545–557.
[124] S. Pour-Ali, C. Dehghanian, A. Kosari, Corrosion protection of the reinforcing steels in chloride-laden concrete environment through epoxy/polyaniline–camphorsulfonate nanocomposite coating, Corrosion Sci. 90 (2015) 239–247.
[125] L. Ecco, M. Fedel, F. Deflorian, J. Becker, B.B. Iversen, A. Mamakhel, Waterborne acrylic paint system based on nanoceria for corrosion protection of steel, Prog. Org. Coating 96 (2016) 19–25.
[126] F. Galliano, D. Landolt, Evaluation of corrosion protection properties of additives for waterborne epoxy coatings on steel, Prog. Org. Coating 44 (3) (2002) 217–225.
[127] E. Armelin, R. Pla, F. Liesa, X. Ramis, J.I. Iribarren, C. Alemán, Corrosion protection with polyaniline and polypyrrole as anticorrosive additives for epoxy paint, Corrosion Sci. 50 (3) (2008) 721–728.
[128] G. Gonçalves, A. Baldissera, L. Rodrigues, E. Martini, C. Ferreira, Alkyd coatings containing polyanilines for corrosion protection of mild steel, Synth. Met. 161 (3) (2011) 313–323.
[129] Y. González-García, S. González, R. Souto, Electrochemical and structural properties of a polyurethane coating on steel substrates for corrosion protection, Corrosion Sci. 49 (9) (2007) 3514–3526.
[130] J.I.I. Laco, F.C. Villota, F.L. Mestres, Corrosion protection of carbon steel with thermoplastic coatings and alkyd resins containing polyaniline as conductive polymer, Prog. Org. Coating 52 (2) (2005) 151–160.
[131] W.-K. Lu, R.L. Elsenbaumer, B. Wessling, Corrosion protection of mild steel by coatings containing polyaniline, Synth. Met. 71 (1) (1995) 2163–2166.
[132] A. Mostafaei, F. Nasirpouri, Epoxy/polyaniline–ZnO nanorods hybrid nanocomposite coatings: synthesis, characterization and corrosion protection performance of conducting paints, Prog. Org. Coating 77 (1) (2014) 146–159.
[133] S. Sathiyanarayanan, S.S. Azim, G. Venkatachari, Preparation of polyaniline–TiO 2 composite and its comparative corrosion protection performance with polyaniline, Synth. Met. 157 (4) (2007) 205–213.
[134] S. Sathiyanarayanan, S.S. Azim, G. Venkatachari, Corrosion protection coating containing polyaniline glass flake composite for steel, Electrochim. Acta 53 (5) (2008) 2087–2094.
[135] S. Sathiyanarayanan, S. Muthukrishnan, G. Venkatachari, D. Trivedi, Corrosion protection of steel by polyaniline (PANI) pigmented paint coating, Prog. Org. Coating 53 (4) (2005) 297–301.
[136] R.S. Silva, C. Aleman, C.A. Ferreira, E. Armelin, J.Z. Ferreira, A. Meneguzzi, Smart Paint for anodic protection of steel, Prog. Org. Coating 78 (2015) 116–123.
[137] ISO 11997-1, Paints and Varnishes – Determination of Resistance to Cyclic Corrosion Conditions – Part 1: Wet (Salt Fog)/dry/humid, 2017.
[138] R.P. Edavan, R. Kopinski, Corrosion resistance of painted zinc alloy coated steels, Corrosion Sci. 51 (10) (2009) 2429–2442.
[139] D.J. Saha, Cost Effective Ways to Protection Steel Structures from Environments.
[140] S. Pourhashem, M.R. Vaezi, A. Rashidi, M.R. Bagherzadeh, Exploring corrosion protection properties of solvent based epoxy-graphene oxide nanocomposite coatings on mild steel, Corrosion Sci. 115 (2017) 78–92.
[141] ASTM E18 - 20: Standard Test Methods for Rockwell Hardness of Metallic Materials..
[142] ASTM G31-72, Standard Practice for Laboratory Immersion Corrosion Testing of Metals, 2004.
[143] ASTM D3359: Standard Test Methods for Measuring Adhesion by Tape Test..
[144] ASTM C1202 -12, Standard Test Method for Electrical Indication of Concrete's Ability to Resist Chloride Ion Penetration, 2016.
[145] ASTM D4541 - 09: Standard Test Method for Pull-Off Strength of Coatings Using Portable Adhesion Testers..
[146] ISO 14577, Metallic Materials — Instrumented Indentation Test for Hardness and Materials Parameters, 2015.
[147] C.J. Slunder, W.K. Boyd, Zinc: its Corrosion Resistance, Australian Zinc Development Association, 1971.
[148] A.G. Association, Hot-dip Galvanizing for Corrosion Protection..
[149] G.A.o. Australia, Atmospheric Corrosion Resistance of Hot Dip Galvanized Coatings, 2012.
[150] As/NZS 2312.2, Guid to the Protection of Structural Steel against Atmospheric Corrosion by the Use of Protective coatings/Hot Dip Galvanizing, 2014.
[151] F. Goodwin, Mechanisms of Corrosion of Zinc and Zinc–5% Aluminum Steel Sheet Coatings, Zinc-Based Steel Coating Systems: Metallurgy and Performance, 1990, pp. 183–193.
[152] A.R. Marder, Effects of surface treatments on materials performance, Mater. Select. Des. 20 (1997) 1–10.
[153] A. Marder, The metallurgy of zinc-coated steel, Prog. Mater. Sci. 45 (3) (2000) 191–271.
[154] F.C. Porter, Corrosion Resistance of Zinc and Zinc Alloys, CRC Press, 1994.
[155] X.G. Zhang, Corrosion and Electrochemistry of Zinc, Springer Science & Business Media, 2013.
[156] K. Videm, R. Myrdal, The Electrochemical Behavior of Steel in Concrete and How to Evaluate the Corrosion Rate, NACE International, Houston, TX (United States), 1996.
[157] A. Yadav, A. Nishikata, T. Tsuru, Electrochemical impedance study on galvanized steel corrosion under cyclic wet–dry conditions—influence of time of wetness, Corrosion Sci. 46 (1) (2004) 169–181.
[158] A. Nishikata, Y. Ichihara, T. Tsuru, An application of electrochemical impedance spectroscopy to atmospheric corrosion study, Corrosion Sci. 37 (6) (1995) 897–911.
[159] A. Nishikata, Y. Ichihara, T. Tsuru, Electrochemical impedance spectroscopy of metals covered with a thin electrolyte layer, Electrochim. Acta 41 (7) (1996) 1057–1062.
[160] A. Nishikata, Y. Yamashita, H. Katayama, T. Tsuru, K. Tanabe, H. Mabuchi, An electrochemical impedance study on atmospheric corrosion of steels in a cyclic wet-dry condition, Corrosion Sci. 37 (12) (1995) 2059–2069.
[161] S. Thompson, Impact of stud gauge on service life–mvss wall, Durab. Build. Mater. Components 8 (1999) 1062–1069.
[162] P. Roberge, R. Klassen, P. Haberecht, Atmospheric corrosivity modeling—a review, Mater. Des. 23 (3) (2002) 321–330.
[163] ISO 9225, Corrosion of Metals and Alloys. Corrosivity of Atmospheres. Measurement of Environmental Parameters Affecting Corrosivity of Atmospheres, International Organization for Standardization, 2012.
[164] As/NZS 2312, Guide to the Protection of Structural Steel against Atmospheric Corrosion by the Use of Protective Coatings, 2002.
[165] P.a.m.c. WATTYLE, Atmospheric Environments, 2010.
[166] ISO 9224, Corrosion of Metals and Alloys - Corrosivity of Atmospheres - Guiding Values for the Corrosivity Categories, 2012.

Appendix B – Cut-edge corrosion of steel frame in the CSR Inclose rain screen façade system

Steel components used in the CSR rains screen façade system are stainless steel and Hot-dip galvanised (HDG) steel based on their locations in the wall. Therefore, they are corrosion-resistant and suitable in Australian climate. Steel frame is located between plasterboard and sheathing layers inside wall and made from HDG steel. Some parts of HDG Steel frame is cut due to punching (wall connections). Hence, a small part of HDG steel which is called cut-edge is exposed. Estimation of HDG steel cut-edge corrosion is the purpose of this section.

Among atmospheric parameters effecting corrosion, Sulphur dioxide has only a minor effect on steel corrosion in Australia and New Zealand and can be ignored except close to recognised point sources [1]. Since the studied steel frame is located inside wall, and is not exposed to weather, effects of sulphur dioxide and chloride are ignored based on ISO 9223: 2012 [2]. However, moisture/temperature is the main parameter influencing corrosion. Hence, moisture penetration, relative humidity, and temperature are investigated by aid of WUFI 1D and WUFI 2D software. "WUFI is a software which can calculate the transient coupled one and two-dimensional heat and moisture transport in walls and other multi-layers components of a building exposed to natural weather. WUFI® software uses the latest findings regarding vapor diffusion and moisture transport in building materials." [3].

In the first model wall layers consist of cladding, air gap, mineral wool, membrane (vapour barrier), rigid sheathing, steel frame, and plasterboard in the WUFI 1D modelled to examine moisture penetration within wall layers. Also, vertical, and

horizontal joints are modelled in the WUFI 2D to study probability of moisture penetration through theses connections. In order to model connection elements to WUFI software, all connection elements changed to closed polygons in the AutoCAD software to be understandable by WUFI. Figure B1 (“a” to “e”) illustrates CSR rain screen façade system’s detail, AutoCAD drawings, and WUFI modelling.

“Copyright materials”

Figure B1. CSR Inclose (panelised rain screen façade system’s detail), AutoCAD drawings: a) Inclose system; b) vertical joint section; c) horizontal joint section; d) vertical joint in AutoCAD; e) horizontal joint in AutoCAD.

WUFI simulation has been done to estimate the rate of cut-edge corrosion based on the moisture and relative humidity in the wall. Figures B2 and B3 show WUFI 1D and WUFI 2D modelling.

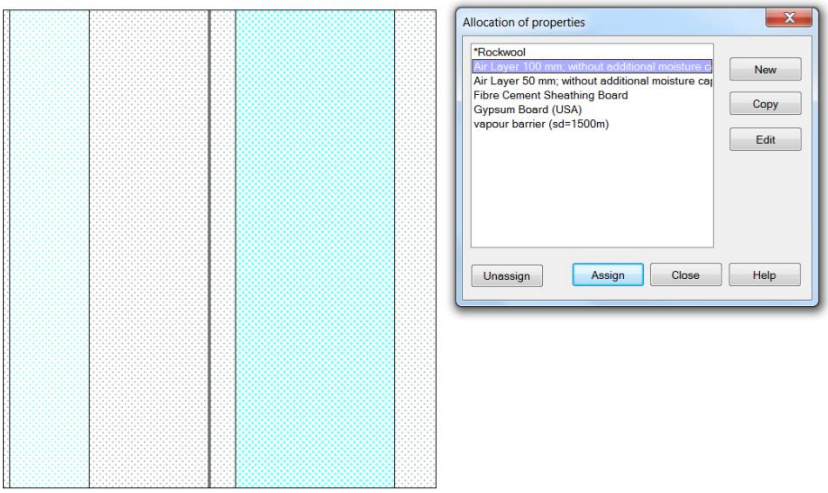

Figure B2. WUFI 1D model – Inclose wall layers

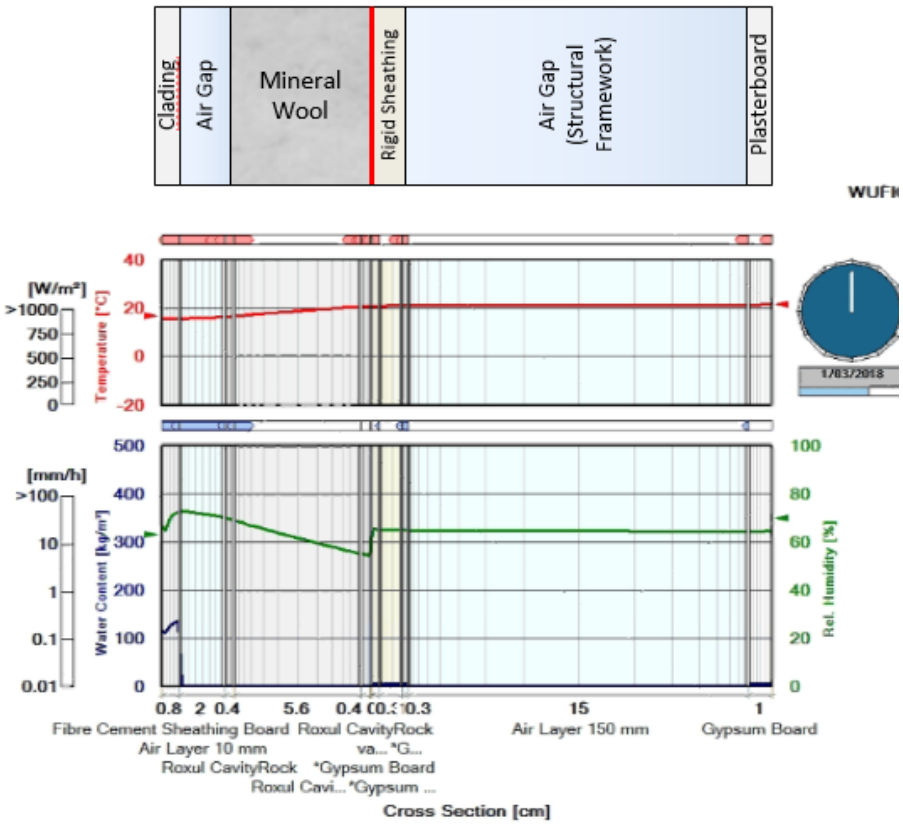

Figure B3. WUFI 2D, temperature, relative humidity, and water content within Inclose wall layers

Results of WUFI 1D showed that percentage of moisture in the steel frame layer is only 0.13% and by this low amount of moisture corrosion will not occur. WUFI 2D simulation for wall connections showed that relative humidity stands below 80%. Based on the ANSI/ASHRAE Standard 160-2016, "the 30-day running average of hourly values of surface relative humidity of the metal shall remain less than 80% in order to avoid corrosion". Hence, by considering to this standard, the model showed corrosion may not happen in the steel frame in CSR Inclose system.

Another estimation of corrosion rate is based on the equation (1) in ISO 9223:2012 [2].

$$r_{corr} = 1.77\ P_d^{0.52} \exp(0.020\ RH + \ F_{st}) + 0.102 S_d^{0.62} \exp(0.033RH + 0.040T) \quad \text{equation 1}$$

$$f_{st} = 0.150(T - 10)\ when\ T \ll 10℃\ ; otherwise - 0.054\ (T - 10)$$

$$N = 128, R^2 = 0.85$$

r_{corr} : is first-year corrosion rate of metal, expressed in micrometres per year (µm/a);
T: is the annual average temperature, expressed in degrees Celsius (°C);
RH: is the annual average relative humidity, expressed as a percentage (%);
Pd: is the annual average SO_2 deposition, expressed in milligrams per square metre per day [mg/ (m^2.d)];
Sd: is the annual average Cl^- deposition, expressed in milligrams per square metre per day [mg/(m^2.d)].

By substituting relative humidity and temperature from WUFI result and very low amount for chloride and sulphur dioxide from Table B.2 from ISO 9223:2012 [2], corrosion rate estimated less than 10 g/m^2a which is categorised as C1 : very low corrosivity [2]. Therefore, steel frame in CSR Inclose façade system does not need corrosion protection.

References

[1] WATTYLE Protective and marine coatings. Atmospheric environments. 2010.
[2] ISO 9223, Corrosion of Metals and Alloys: Corrosivity of Atmospheres: Classification. European Committee for Standardization (CEN): Brussels, Belgium; 2012.
[3] WUFI Team. WUFI 2D. 2017. https://wufi.de/en/software/wufi-2d/.

Appendix C: Conference paper

USE OF RESOLE SEPIOLITE-PHOSPHATE NANOCOMPOSITE FOR BUILDING FACADES

L. Soufeiani[1*], K. Nguyen[2], and G. Foliente[1]

[1] Department of Infrastructure Engineering, The University of Melbourne, Melbourne, Australia

[2] School of Engineering, RMIT University, Melbourne, Australia

Corresponding author (soufeiani.leila@gmail.com)

Keywords: Phenolic resin, Sepiolite-phosphate, Nanocomposite

ABSTRACT

COMBUSTIBILITY OF CLADDING MATERIALS IN THE FAÇADE SYSTEM IS THE MAIN ISSUE IN THE PREFABRICATED BUILDING ENVELOPES AS COMBUSTIBLE MATERIALS SPREAD THE FIRE RAPIDLY. INVESTIGATION OF NEW NANOCOMPOSITE MATERIAL TO BE REPLACED THE EXISTING COMBUSTIBLE CLADDING'S MATERIAL IS THE PURPOSE OF THE CURRENT STUDY. SEPIOLITE-PHOSPHATE (SEPP) HAS BEEN MADE AND DIFFERENT CONTENTS OF IT (3%, 5%, AND 10%) SYNTHESIZED WITH RESOLE PHENOLIC RESIN IN ORDER TO STUDY THE DISPERSION OF THE SEPP NANOPOWDERS IN THE PHENOLIC RESIN NANOCOMPOSITE. HELIUM ION MICROSCOPE (HIM) AND SCANNING ELECTRON MICROSCOPE (SEM) SHOWED THAT THE SEPP HAS BEEN MADE SUCCESSFULLY AND THE SEPP 3% HAD A BETTER DISPERSION IN THE PHENOLIC NANOCOMPOSITE.

1 INTRODUCTION

Building facades have the greatest level of failure as a building element [173, 174]. Recent catastrophic events with façade fires such as the Grenfell Tower fire (UK, 2017) and the Lacrosse Building fire (AU, 2014) have raised the awareness of fire safety in building facades and the increasing need for innovative façade materials which meet both structural and fire safety requirements [175, 176]. For this purpose, Nanocomposite materials are ideal due to their superior properties [71, 177, 178].

Among thermosetting resins which are used industrially, phenol-formaldehyde resins are mainly used due to their extensive application in wood adhesives, laminates, coatings, moldings, thermal insulation materials, and composites [54, 86]. Phenolic nanocomposite has a three dimensional (3D) molecular structure even before curing. Owing to the difficulties in synthesizing phenolic composite, not much research has been carried out [86, 179, 180]. Due to its high thermal stability with good smoke and fire resistance, phenolic resins (PRs) are attractive in structural applications at high temperatures [21]. Among existing nanomaterials, Sepiolite, ($Mg_8Si_{12}O_{30}(OH)_4(H_2O)_4 \cdot 8H_2O$) which is a nanoclay fiber and has a large specific surface area (about 320 m^2/g) [75] has been used in nanocomposites because of its needle-like structure, high surface area, and good ability of dispersion [78, 181, 182]. Palacious et al. [74] made Sepiolite-phosphate (SepP) with direct synthesis of aluminum phosphate on sepiolite nanofibers. They used sepiolite as a support to control the agglomeration and size of phosphate nanoparticles (halogen-free flame retardant) [74], and developed a new three-dimensional rigid supported phosphate structure during the thermal treatment. They concluded that the SepP has the potential to be used as a flame retardant [74].

Due to outstanding properties of phenolic resin and SepP's 3D structure at high temperatures, the authors propose resole/SepP nanocomposite as a prospective alternative for building facades cladding owing to the above mentioned advantages. Resole/SepP nanocomposite will be used in the glass fiber reinforced polymer nanocomposite for façade application.

In this study, SepP has been made with the precipitation synthesis method [74] to examine its characteristics and dispersion in the phenolic resin for flame retardant applications. In order to evaluate the morphology of the SepP, Helium Ion Microscopy (HIM) has been conducted due to its better resolution at high magnification over SEM. Then, different contents of SepP (3wt%, 5wt%, and 10wt%) in the phenolic resin were used to produce resole-SepP nanocomposite. After curing process, Scanning Electron Microscopy (SEM) has been carried to determine the dispersion of SepP in the phenolic resin, and its morphological characterization.

2 Materials and Preparation

2.1 Materials

Sepiolite powders (>95%, Pangel S9) were supplied from TOLSA S.A. Aluminum hydroxide, Hydrochloric acid 37%, Ortho-phosphoric acid 85%, and Ammonia solution 28-30% were purchased from MERCK. Phenolic resin and catalyst were purchased from Hexion Pty Ltd.

2.2 Experimental details

To obtain the 6% sepiolite, 6gr of sepiolite powder was dispersed in deionized water under high shear mixing for 5 minutes. Then HCl solution was added to adjust the pH around 2 under stirring. In addition, 2.33gr of $Al(OH)_3$ was dissolved in the aqueous solution of 17.33 gr of H_3PO_4 (Al/P:1/3 molar ratio), and stirred at room temperature to obtain a uniform solution. Then, this uniform solution was added to the initial sepiolite dispersion, and stirring was continued for 30 minutes. Thereafter, a NH_4OH solution was added dropwise to the solution until pH of 4.8 to produce the phosphate precipitation. Then, synthesized powders were filtered under vacuum, washed with deionized water, and dried at 80^{o}C for several hours. The final product is SepP nanopowders. Then morphological characterization has been conducted with Helium Ion Microscope (HIM- Zeiss Orion NanoFab).

In the next step, SepP with different contents by phenolic resin (PR) weight (3wt%, 5wt%, and 10wt%) was added to the PR with 5 minutes stirring at temperature 80 °C followed by 10 minutes sonication in the same temperature. Then, 5% catalyst was added to the SepP-PR and stirred for 2 minutes under room temperature to mix and turn the color of the solution to a lighter color. Thereafter, putting the sample in the oven for one hour at 80 °C. The phenol with viscosity 180-270 cPs, PH: 7-8, and water content 14-16%, and a catalyst with viscosity 150-350 cP and water content 20-28% was used in this study. Then, the PR structure was observed with scanning electron microscope (SEM-FEI Hitachi) in order to study the characterization of the nanocomposite. Table 1 shows composition of samples.

Table 1: Composition of samples

No	SepP	Phenolic resin	Catalyst
1	-	100%	5%
2	3%	100%	5%
3	5%	100%	5%
4	10%	100%	5%

3 Results and Discussion

3.1 Morphological characterization of the sepiolite-phosphate (SepP) composites

In order to observe the dispersion state of the phosphate on the sepiolite fibers, Helium Ion Microscop (HIM- Zeiss Orion NanoFab) characterization was carried out on the SepP composite. Figure 1 shows HIM micrograph of SepP composite.

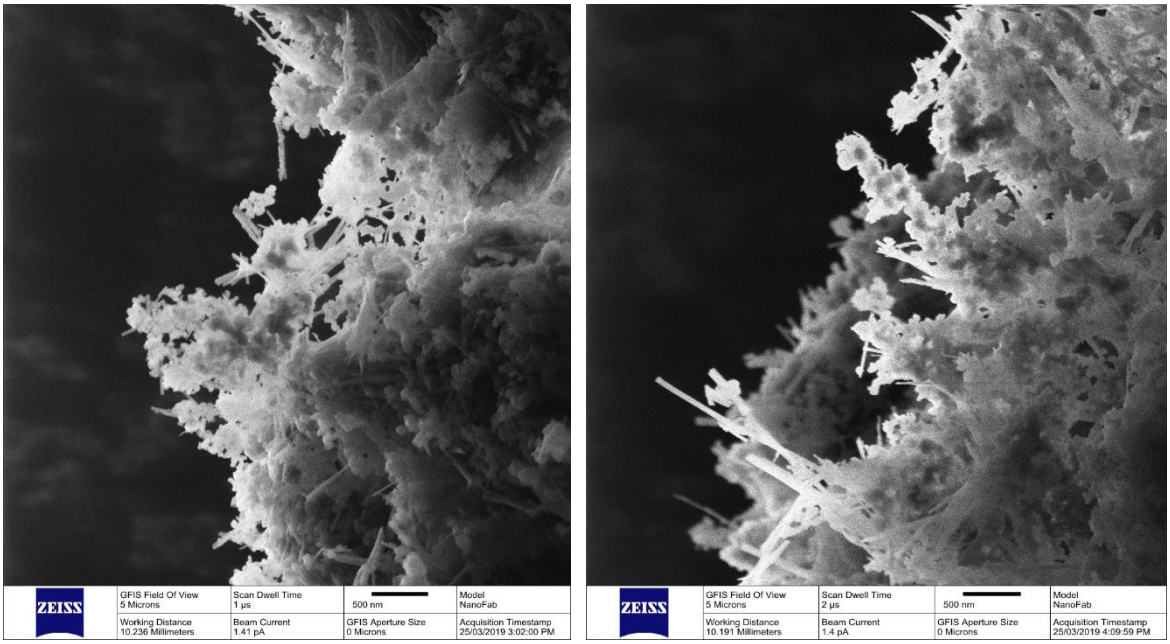

Figure 1: Micrograph of SepP composite: Uniform distribution of phosphate nanoparticles on the surface of sepiolite fibers. Fibers are fully covered by phosphate nanoparticles

From Figure 1, it can be seen that the phosphate particles covered the sepiolite fibers surface and distributed uniformly. The figure shows the typical geometry of sepiolite fibers which are 15-50 nm in diameter, and phosphate nanoparticles which are 40-80 nanometers. The micrograph displays a uniform distribution of phosphate on the sepiolite fibers surface.

3.2 Morphological characterization of SepP phenolic nanocomposite

SEM analysis was conducted to understand the phenolic resin structure and distribution of SepP nanoparticles in polymeric phenolic resin matrix. As seen in Figure 2, there are microvoids on the phenolic resin surface with diameter of less than 5 micrometers with an average diameter of 3.85 micrometers. The microvoid measurements are shown in Table 2.

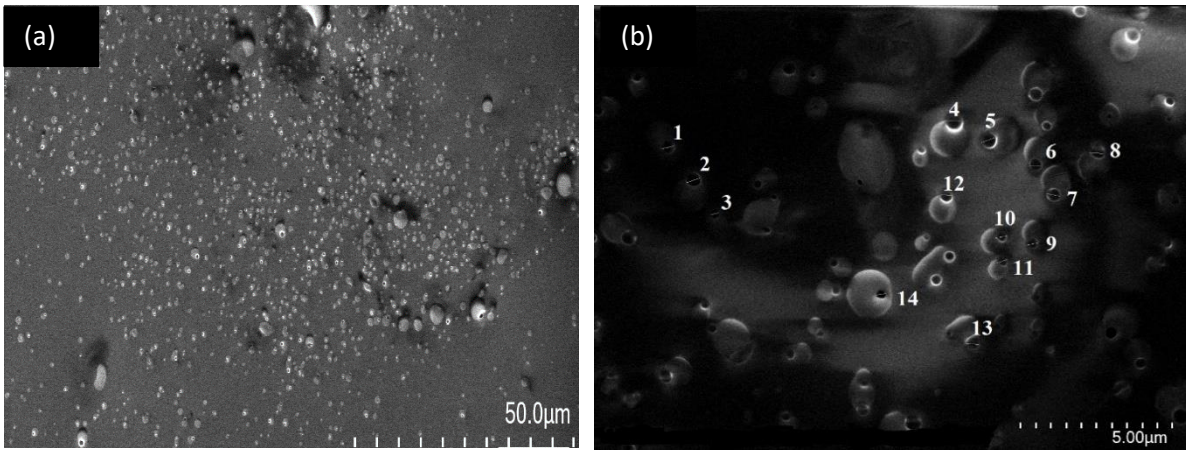

Figure 2: Phenolic resin structure: (a) microvids. (b) microvoids diameter measurements which are less that 5 micrometers

Table 2: Phenolic resin microvoids diameters

Voids	Label	Area	Diameter (µm)
1		0.624	4.055
2		0.713	4.578
3		0.401	2.481
4		0.757	4.975
5		0.713	4.594
6		0.557	3.582
7		0.668	4.254
8		0.668	4.383
9		0.579	3.669
10		0.557	3.632
11		0.49	3.147
12		0.535	3.389
13		0.646	4.184
14		0.468	3.011
	Mean	0.598	3.852

The emergence of microvoids is due to the release of by-product water molecules in the phenolic resin during polymerization. Water vapor bubbles getting trapped in the sample during curing and form macro and microvoids [95]. To reduce the number of defects and eliminate volatiles in the phenolic resin, an accurate temperature control and gradual heating is needed [122]. However, this type of porosity may decrease the structural strength. This may not be critical in the present study because the proposed nanocomposite will be used as a fire-resistant cladding material which is not load bearing.

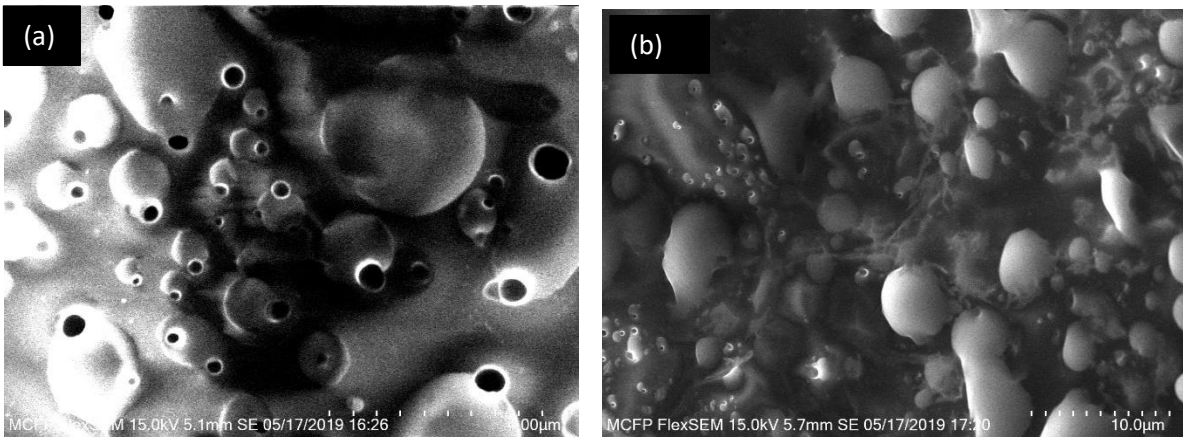

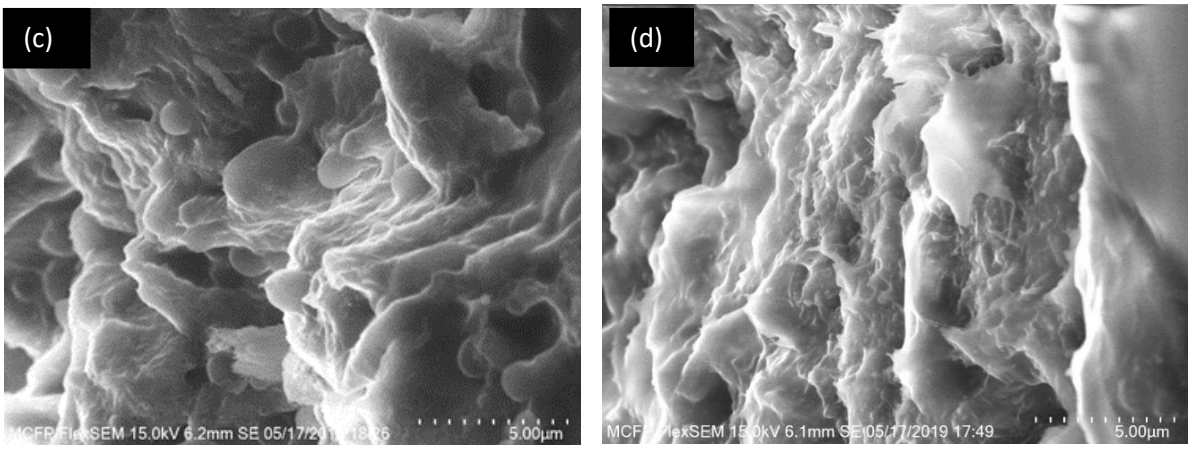

Figure 3: (a) PR structure. (b) SepP (3%)-PR nanocomposite. (c) SepP(5%)-PR nanocomposite. (d) SepP(10%)-PR nanocomposite

Figure 3 (a) shows the micrograph of phenolic resin and Figure 3 (b, c, and d) shows different contents of SepP nanopowders in the phenolic resin structure. It can be seen that the SepP nanopowders are not dispersed uniformly and agglomeration can be seen mostly for SepP5% and 10%. Further investigation on SepP agglomeration in the phenolic resin with HIM will be conducted and presented in the conference.

4. Conclusion

The investigation of SepP in the phenolic resin has been carried out for the first time in this research. HIM showed that the SepP nanopowders formed effectively and phosphate nanoparticles uniformly covered the surface of sepiolite fibers. SEM micrograph of phenolic resin showed its porous structure due to evaporation of the water. Different contents of SepP in the phenolic resin have been investigated and SEM micrograph showed that 3% of SepP had a better dispersion in the nanocomposite. The next step will be high shear mixing of resole-SepP nanocomposite to prevent agglomeration and make a uniform dispersion. The proposed phenolic nanocomposite will be used with 3D glass fibers to make a 3DGFRP nanocomposite for façade application.

ACKNOWLEDGEMENTS

This work was conducted with the financial support of the CRC-Project on Advanced Manufacturing of High Performance Building Envelope Systems (CRC-P54018) and ARC Centre for Advanced Manufacturing of Prefabricated Housing (IC150100023). Also, it was performed in part at the Materials Characterization and Fabrication Platform (MCFP) at the University of Melbourne and the Victorian Node of the Australian National Fabrication Facility (ANFF).

REFERENCES

[1] K.T. Nguyen, P. Weerasinghe, P. Mendis, T. Ngo, J. Barnett, Performance of modern building façades in fire: a comprehensive review, *Electronic Journal of Structural Engineering* 16, 2016, pp. 69-86.
[2] T.D. Ngo, Q.T. Nguyen, P. Tran, Heat release and flame propagation in prefabricated modular unit with GFRP composite facades, *Building Simulation*, Springer, 2016, pp. 607-616.
[3] P. Hayes, How Lacrosse and Grenfell have dramatically altered the litigation and regulatory landscape, *Journal of Building Survey, Appraisal & Valuation* 7(1), 2018, pp. 48-60.
[4] J. Anderson, L. Boström, R. Jansson McNamee, Fire Safety of Façades, 2017.
[5] Q. Nguyen, P. Mendis, T. Ngo, C. Nguyen, D. Bhattacharyya, Effects of nanoclay on fire performance of hybrid nano composites, *The 19th International Conference on Composite Materials.*
[6] A.R. Bahramian, Pyrolysis and flammability properties of novolac/graphite nanocomposites, *Fire Safety Journal*, 61, 2013, pp. 265-273.
[7] M.Á. Cárdenas, D. García-López, A. García-Vilchez, J.F. Fernández, J.C. Merino, J.M. Pastor, Synergy between organo-bentonite and nanofillers for polymer based fire retardant applications, *Applied Clay Science*,45(3), 2009, pp. 139-146.
[8] H.G. Dodiuk, Sidney H., *Handbook of thermoset plastics*, Elsevier, 2014.
[9] Ü.B. Alkan, N. Kızılcan, In situ preparation of resol/sepiolite nanocomposites, *Procedia-Social and Behavioral Sciences*, 195, 2015, pp. 2067-2075.
[10] N. Kızılcan, G. Özkaraman, In situ preparation of resol/clay nanocomposites, *Journal of Applied Polymer Science*, 129(5), 2013, pp. 2966-2976.
[11] M. López, M. Blanco, M. Martin, I. Mondragon, Influence of cure conditions on properties of resol/layered silicate nanocomposites, *Polymer Engineering & Science*, 52(6), 2012, pp. 1161-1172.
[12] T. NGUYEN, Fire performance of GFRP facade systems, 2015.
[13] G. Tartaglione, D. Tabuani, G. Camino, Thermal and morphological characterisation of organically modified sepiolite, *Microporous and Mesoporous Materials*, 107(1-2), 2008, pp. 161-168.
[14] Y. Liu, J. Zhao, C.-L. Deng, L. Chen, D.-Y. Wang, Y.-Z. Wang, Flame-retardant effect of sepiolite on an intumescent flame-retardant polypropylene system, *Industrial & Engineering Chemistry Research*, 50(4), 2011, pp. 2047-2054.
[15] N.A. Mohd Zaini, H. Ismail, A. Rusli, Short Review on Sepiolite-Filled Polymer Nanocomposites, *Polymer-Plastics Technology and Engineering*, 56(15), 2017, pp. 1665-1679.
[16] A. Zotti, A. Borriello, A. Martone, V. Antonucci, M. Giordano, M. Zarrelli, Effect of sepiolite filler on mechanical behaviour of a bisphenol A-based epoxy system, *Composites Part B: Engineering*, 67, 2014, pp. 400-409.
[17] E. Palacios, P. Leret, M.J. De La Mata, J.F. Fernández, A.H. De Aza, M.A. Rodríguez, F. Rubio-Marcos, Self-Forming 3D Core–Shell Ceramic Nanostructures for Halogen-Free Flame Retardant Materials, *ACS applied materials & interfaces*, 8(14), 2016, pp. 9462-9471.
[18] C. Kaynak, C.C. Tasan, Effects of production parameters on the structure of resol type phenolic resin/layered silicate nanocomposites, *European polymer journal*, 42(8), 2006, pp. 1908-1921.
[19] J.-C. Munoz, H. Ku, F. Cardona, D. Rogers, Effects of catalysts and post-curing conditions in the polymer network of epoxy and phenolic resins: Preliminary results, *Journal of Materials Processing Technology*, 202(1-3), 2008, pp. 486-492.

Appendix D – Declarations of a thesis with publications

D1. Declaration for Publication #1

Declaration for a thesis with publication

THE UNIVERSITY OF MELBOURNE

PhD and MPhil students may include a primary research publication in their thesis in lieu of a chapter if:

- The student contributed greater than 50% of the content in the publication and is the "primary author", ie. the student was responsible primarily for the planning, execution and preparation of the work for publication
- The student has approval to include the publication in their thesis from their Advisory Committee
- It is a primary publication that reports on original research conducted by the student during their enrolment
- The initial draft of the work was written by the student and any subsequent editing in response to co-authors and editors reviews was performed by the student
- The publication is not subject to any obligations or contractual agreements with a third party that would constrain its inclusion in the thesis

Students must submit this form, along with *Co-author authorisation forms* completed by each co-author, when the thesis is submitted to the Thesis Examination System: *https://tes.app.unimelb.edu.au/*. If you are including multiple publications in your thesis you will need to complete a separate form for each publication. Further information on this policy is available at: *gradresearch.unimelb.edu.au/preparing-my-thesis/thesis-with-publication*

A. PUBLICATION DETAILS *(to be completed by the student)*

Full title	Corrosion protection of steel elements in façade systems–a review	
Authors	Leila Soufeiani, Greg Foliente, Kate TQ Nguyen, Rackel San Nicolas	
Student's contribution (%)	70%	
Journal or book name	Journal of Building Engineering	
Volume/page numbers	v. 32, p. 101759	
Status	☐ Accepted and In press ■ Published ☐ In progress	Date accepted/ published 28/08/2020

B. STUDENT'S DECLARATION

I declare that the publication above meets the requirements to be included in the thesis

Student's name	Student's signature	Date *(dd/mm/yy)*
Leila Soufeiani		18/10/2020

C. PRINCIPAL SUPERVISOR'S DECLARATION

I declare that:

- the information above is accurate
- The advisory committee has met and agreed to the inclusion of this publication in the student's thesis
- All of the co-authors of the publication have reviewed the above information and have agreed to its veracity
- 'Co-Author Authorisation' forms for each co-author are attached.

Supervisor's name	Supervisor's signature	Date *(dd/mm/yy)*
Lu Aye	Lu Aye Digitally signed by Lu Aye Date: 2020.11.05 13:37:13 +11'00'	05/11/20

The University of Melbourne
CRICOS Provider Number: 00116K

Last Updated 19 October 2017

D2. Co-author authorisation for publication #1

Co-author authorisation form

THE UNIVERSITY OF MELBOURNE

All co-authors must complete this form. By signing below co-authors agree to the listed publication being included in the student's thesis and that the student contributed greater than 50% of the content of the publication and is the "primary author" ie. the student was responsible primarily for the planning, execution and preparation of the work for publication.

In cases where all members of a large consortium are listed as authors of a publication, only those that actively collaborated with the student on material contained within the thesis should complete this form. This form is to be used in conjunction with the *Declaration for a thesis with publication form*.

Students must submit this form, along with the *Declaration for thesis with publication form*, when the thesis is submitted to the Thesis Examination System: *https://tes.app.unimelb.edu.au/*

Further information on this policy and the requirements is available at:
gradresearch.unimelb.edu.au/preparing-my-thesis/thesis-with-publication

A. PUBLICATION DETAILS *(to be completed by the student)*

Full title	Corrosion protection of steel elements in façade systems – A review	
Authors	Leila Soufeiani, Greg Foliente, Kate TQ Nguyen, Rackel San Nicolas	
Student's contribution (%)	70%	
Journal or book name	Journal of Building Engineering	
Volume/page numbers	v. 32, p. 101759	
Status	☐ Accepted and In-press ■ Published ☐ In progress	Date accepted/published 28/08/2020

B. CO-AUTHOR'S DECLARATION *(to be completed by the collaborator)*

I authorise the inclusion of this publication in the student's thesis and certify that:

- the declaration made by the student on the *Declaration for a thesis with publication form* correctly reflects the extent of the student's contribution to this work;
- the student contributed greater than 50% of the content of the publication and is the "primary author" ie. the student was responsible primarily for the planning, execution and preparation of the work for publication.

Co-author's name	Co-author's signature	Date *(dd/mm/yy)*
Greg Foliente		08/10/20

The University of Melbourne
CRICOS Provider Number: 00116K

Last Updated 19 October 2017

Co-author authorisation form

THE UNIVERSITY OF MELBOURNE

All co-authors must complete this form. By signing below co-authors agree to the listed publication being included in the student's thesis and that the student contributed greater than 50% of the content of the publication and is the "primary author" ie. the student was responsible primarily for the planning, execution and preparation of the work for publication.

In cases where all members of a large consortium are listed as authors of a publication, only those that actively collaborated with the student on material contained within the thesis should complete this form. This form is to be used in conjunction with the *Declaration for a thesis with publication form*.

Students must submit this form, along with the *Declaration for thesis with publication form*, when the thesis is submitted to the Thesis Examination System: *https://tes.app.unimelb.edu.au/*

Further information on this policy and the requirements is available at:
gradresearch.unimelb.edu.au/preparing-my-thesis/thesis-with-publication

A. PUBLICATION DETAILS *(to be completed by the student)*

Full title	Corrosion protection of steel elements in façade systems – A review	
Authors	Leila Soufeiani, Greg Foliente, Kate TQ Nguyen, Rackel San Nicolas	
Student's contribution (%)	70%	
Journal or book name	Journal of Building Engineering	
Volume/page numbers	v. 32, p. 101759	
Status	☐ Accepted and In-press ■ Published ☐ In progress	Date accepted/published 28/08/2020

B. CO-AUTHOR'S DECLARATION *(to be completed by the collaborator)*

I authorise the inclusion of this publication in the student's thesis and certify that:

- the declaration made by the student on the *Declaration for a thesis with publication form* correctly reflects the extent of the student's contribution to this work;
- the student contributed greater than 50% of the content of the publication and is the "primary author" ie. the student was responsible primarily for the planning, execution and preparation of the work for publication.

Co-author's name	Co-author's signature	Date *(dd/mm/yy)*
Kate Nguyen	Kate Nguyen	28/10/2020

Co-author authorisation form

THE UNIVERSITY OF MELBOURNE

All co-authors must complete this form. By signing below co-authors agree to the listed publication being included in the student's thesis and that the student contributed greater than 50% of the content of the publication and is the "primary author" ie. the student was responsible primarily for the planning, execution and preparation of the work for publication.

In cases where all members of a large consortium are listed as authors of a publication, only those that actively collaborated with the student on material contained within the thesis should complete this form. This form is to be used in conjunction with the *Declaration for a thesis with publication form*.

Students must submit this form, along with the *Declaration for thesis with publication form*, when the thesis is submitted to the Thesis Examination System: *https://tes.app.unimelb.edu.au/*

Further information on this policy and the requirements is available at:
gradresearch.unimelb.edu.au/preparing-my-thesis/thesis-with-publication

A. PUBLICATION DETAILS *(to be completed by the student)*

Full title	Corrosion protection of steel elements in façade systems – A review	
Authors	Leila Soufeiani, Greg Foliente, Kate TQ Nguyen, Rackel San Nicolas	
Student's contribution (%)	70%	
Journal or book name	Journal of Building Engineering	
Volume/page numbers	v. 32, p. 101759	
Status	☐ Accepted and In-press ■ Published ☐ In progress	Date accepted/published 28/08/2020

B. CO-AUTHOR'S DECLARATION *(to be completed by the collaborator)*

I authorise the inclusion of this publication in the student's thesis and certify that:

- the declaration made by the student on the *Declaration for a thesis with publication form* correctly reflects the extent of the student's contribution to this work;
- the student contributed greater than 50% of the content of the publication and is the "primary author" ie. the student was responsible primarily for the planning, execution and preparation of the work for publication.

Co-author's name	Co-author's signature	Date *(dd/mm/yy)*
Rackel San Nicolas		28/10/20

The University of Melbourne
CRICOS Provider Number: 00116K

Last Updated 19 October 2017

D3. Declaration for publication #2

Declaration for a thesis with publication

THE UNIVERSITY OF MELBOURNE

PhD and MPhil students may include a primary research publication in their thesis in lieu of a chapter if:

- The student contributed greater than 50% of the content in the publication and is the "primary author", ie. the student was responsible primarily for the planning, execution and preparation of the work for publication
- The student has approval to include the publication in their thesis from their Advisory Committee
- It is a primary publication that reports on original research conducted by the student during their enrolment
- The initial draft of the work was written by the student and any subsequent editing in response to co-authors and editors reviews was performed by the student
- The publication is not subject to any obligations or contractual agreements with a third party that would constrain its inclusion in the thesis

Students must submit this form, along with *Co-author authorisation forms* completed by each co-author, when the thesis is submitted to the Thesis Examination System: *https://tes.app.unimelb.edu.au/*. If you are including multiple publications in your thesis you will need to complete a separate form for each publication. Further information on this policy is available at: *gradresearch.unimelb.edu.au/preparing-my-thesis/thesis-with-publication*

A. PUBLICATION DETAILS *(to be completed by the student)*

Full title	Use of resole sepiolite-phosphate nanocomposite for building facades	
Authors	Leila Soufeiani, Kate TQ Nguyen, Greg Foliente	
Student's contribution (%)	75%	
Journal or book name	ICCM22	
Volume/page numbers	p. 2480-2486	
Status	☐ Accepted and In press ■ Published ☐ In progress	Date accepted/ published: August 2019

B. STUDENT'S DECLARATION

I declare that the publication above meets the requirements to be included in the thesis

Student's name	Student's signature	Date *(dd/mm/yy)*
Leila Soufeiani		18/10/2020

C. PRINCIPAL SUPERVISOR'S DECLARATION

I declare that:

- the information above is accurate
- The advisory committee has met and agreed to the inclusion of this publication in the student's thesis
- All of the co-authors of the publication have reviewed the above information and have agreed to its veracity
- 'Co-Author Authorisation' forms for each co-author are attached.

Supervisor's name	Supervisor's signature	Date *(dd/mm/yy)*
Lu Aye	Lu Aye Digitally signed by Lu Aye Date: 2020.11.05 13:41:13 +11'00'	05/11/20

The University of Melbourne
CRICOS Provider Number: 00116K

Last Updated 19 October 2017

D4. Co-author authorisation for publication #2

Co-author authorisation form

THE UNIVERSITY OF MELBOURNE

All co-authors must complete this form. By signing below co-authors agree to the listed publication being included in the student's thesis and that the student contributed greater than 50% of the content of the publication and is the "primary author" ie. the student was responsible primarily for the planning, execution and preparation of the work for publication.

In cases where all members of a large consortium are listed as authors of a publication, only those that actively collaborated with the student on material contained within the thesis should complete this form. This form is to be used in conjunction with the *Declaration for a thesis with publication form*.

Students must submit this form, along with the *Declaration for thesis with publication form*, when the thesis is submitted to the Thesis Examination System: *https://tes.app.unimelb.edu.au/*

Further information on this policy and the requirements is available at:
gradresearch.unimelb.edu.au/preparing-my-thesis/thesis-with-publication

A. PUBLICATION DETAILS *(to be completed by the student)*

Full title	Use of resole sepiolite-phosphate nanocomposite for building facades	
Authors	Leila Soufeiani, Kate TQ Nguyen, Greg Foliente	
Student's contribution (%)	75%	
Journal or book name	ICCM22	
Volume/page numbers	p. 2480-2486	
Status	☐ Accepted and In-press ■ Published ☐ In progress	Date accepted/published August 2019

B. CO-AUTHOR'S DECLARATION *(to be completed by the collaborator)*

I authorise the inclusion of this publication in the student's thesis and certify that:

- the declaration made by the student on the *Declaration for a thesis with publication form* correctly reflects the extent of the student's contribution to this work;
- the student contributed greater than 50% of the content of the publication and is the "primary author" ie. the student was responsible primarily for the planning, execution and preparation of the work for publication.

Co-author's name	Co-author's signature	Date *(dd/mm/yy)*
Kate Nguyen	Kate Nguyen	28/10/2020

The University of Melbourne
CRICOS Provider Number: 00116K

Last Updated 19 October 2017

Co-author authorisation form

THE UNIVERSITY OF MELBOURNE

All co-authors must complete this form. By signing below co-authors agree to the listed publication being included in the student's thesis and that the student contributed greater than 50% of the content of the publication and is the "primary author" ie. the student was responsible primarily for the planning, execution and preparation of the work for publication.

In cases where all members of a large consortium are listed as authors of a publication, only those that actively collaborated with the student on material contained within the thesis should complete this form. This form is to be used in conjunction with the *Declaration for a thesis with publication form*.

Students must submit this form, along with the *Declaration for thesis with publication form*, when the thesis is submitted to the Thesis Examination System: *https://tes.app.unimelb.edu.au/*

Further information on this policy and the requirements is available at:
gradresearch.unimelb.edu.au/preparing-my-thesis/thesis-with-publication

A. PUBLICATION DETAILS *(to be completed by the student)*

Full title	Use of resole sepiolite-phosphate nanocomposite for building facades	
Authors	Leila Soufeiani, Kate TQ Nguyen, Greg Foliente	
Student's contribution (%)	75%	
Journal or book name	ICCM22	
Volume/page numbers	p. 2480-2486	
Status	☐ Accepted and In-press ■ Published ☐ In progress	Date accepted/published August 2019

B. CO-AUTHOR'S DECLARATION *(to be completed by the collaborator)*

I authorise the inclusion of this publication in the student's thesis and certify that:

- the declaration made by the student on the *Declaration for a thesis with publication form* correctly reflects the extent of the student's contribution to this work;
- the student contributed greater than 50% of the content of the publication and is the "primary author" ie. the student was responsible primarily for the planning, execution and preparation of the work for publication.

Co-author's name	Co-author's signature	Date *(dd/mm/yy)*
Greg Foliente		08/10/20

Appendix E – List of electronic files

Thermal characterisation of Sep/SepP (Chapter 4)

- TGA_Sep_SepP.xlsx

Thermogravimetric analysis of Sep/SepP phenolic composite- Samples 1-14 (Chapter 5)

- tga_ 1.xlsx
- tga_2.xlsx
- tga_3.xlsx
- tga_4.xlsx
- tga_S5.xlsx
- tga_S6.xlsx
- tga_S7.xlsx
- tga_S8.xlsx
- tga_S9.xlsx
- tga_SP5.xlsx
- tga_SP6.xlsx
- tga_SP7.xlsx
- tga_SP8.xlsx
- tga_SP9.xlsx
- tga_processed data_all samples.xlsx

Cone calorimeter test results of 3D GFRP nanocomposite (Chapter 5)

- Cone_raw data_1.xlsx
- Cone_raw data_2.xlsx
- Cone_raw data_3.xlsx
- Cone_raw data_4.xlsx
- Cone_raw data_S5.xlsx
- Cone_raw data_S6.xlsx
- Cone_raw data_S7.xlsx

- Cone_raw data_S8.xlsx
- Cone_raw data_S9.xlsx
- Cone_raw data_SP5.xlsx
- Cone_raw data_SP6.xlsx
- Cone_raw data_SP7.xlsx
- Cone_raw data_SP8.xlsx
- Cone_raw data_SP9.xlsx
- Cone_processed data_all samples.xlsx

Tensile test results of 3D GFRP nanocomposite (Chapter 6)

Composition 1

- tensile_raw data_1_1.xlsx
- tensile_raw data_1_2.xlsx
- tensile_raw data_1_3.xlsx
- tensile_raw data_1_4.xlsx
- tensile_raw data_1_5.xlsx

Composition 2

- tensile_raw data_2_1.xlsx
- tensile_raw data_2_2.xlsx
- tensile_raw data_2_3.xlsx
- tensile_raw data_2_4.xlsx
- tensile_raw data_2_5.xlsx

Composition 3

- tensile_raw data_3_1.xlsx
- tensile_raw data_3_2.xlsx
- tensile_raw data_3_3.xlsx
- tensile_raw data_3_4.xlsx
- tensile_raw data_3_5.xlsx

Composition 4

- tensile_raw data_4_1.xlsx
- tensile_raw data_4_2.xlsx
- tensile_raw data_4_3.xlsx
- tensile_raw data_4_4.xlsx
- tensile_raw data_4_5.xlsx

Composition S5

- tensile_raw data_S5_1.xlsx
- tensile_raw data_S5_2.xlsx
- tensile_raw data_S5_3.xlsx
- tensile_raw data_S5_4.xlsx
- tensile_raw data_S5_5.xlsx

Composition S6

- tensile_raw data_S6_1.xlsx
- tensile_raw data_S6_2.xlsx
- tensile_raw data_S6_3.xlsx
- tensile_raw data_S6_4.xlsx
- tensile_raw data_S6_5.xlsx

Composition S7

- tensile_raw data_S7_1.xlsx
- tensile_raw data_S7_2.xlsx
- tensile_raw data_S7_3.xlsx
- tensile_raw data_S7_4.xlsx
- tensile_raw data_S7_5.xlsx

Composition S8

- tensile_raw data_S8_1.xlsx
- tensile_raw data_S8_2.xlsx
- tensile_raw data_S8_3.xlsx
- tensile_raw data_S8_4.xlsx

- tensile_raw data_S8_5.xlsx

Composition S9

- tensile_raw data_S9_1.xlsx
- tensile_raw data_S9_2.xlsx
- tensile_raw data_S9_3.xlsx
- tensile_raw data_S9_4.xlsx
- tensile_raw data_S9_5.xlsx

Composition SP5

- tensile_raw data_SP5_1.xlsx
- tensile_raw data_SP5_2.xlsx
- tensile_raw data_SP5_3.xlsx
- tensile_raw data_SP5_4.xlsx
- tensile_raw data_SP5_5.xlsx

Composition SP6

- tensile_raw data_SP6_1.xlsx
- tensile_raw data_SP6_2.xlsx
- tensile_raw data_SP6_3.xlsx
- tensile_raw data_SP6_4.xlsx
- tensile_raw data_SP6_5.xlsx

Composition SP7

- tensile_raw data_SP7_1.xlsx
- tensile_raw data_SP7_2.xlsx
- tensile_raw data_SP7_3.xlsx
- tensile_raw data_SP7_4.xlsx
- tensile_raw data_SP7_5.xlsx

Composition SP8

- tensile_raw data_SP8_1.xlsx
- tensile_raw data_SP8_2.xlsx
- tensile_raw data_SP8_3.xlsx

- tensile_raw data_SP8_4.xlsx
- tensile_raw data_SP8_5.xlsx

Composition SP9

- tensile_raw data_SP9_1.xlsx
- tensile_raw data_SP9_2.xlsx
- tensile_raw data_SP9_3.xlsx
- tensile_raw data_SP9_4.xlsx
- tensile_raw data_SP9_5.xlsx
- Tensile_processed data_all samples_all compositions.xlsx